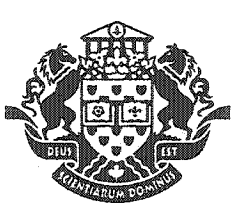

Université d'Ottawa • University of Ottawa

Université d'Ottawa · University of Ottawa

FACULTÉ DES ÉTUDES SUPÉRIEURES ET POSTDOCTORALES

FACULTY OF GRADUATE AND POSTDOCTORAL STUDIES

Luc PIGEON

AUTEUR DE LA THÈSE - AUTHOR OF THESIS

M. Sc. (Earth Sciences)

GRADE - DEGREE

Department of Earth Sciences

FACULTÉ, ÉCOLE, DÉPARTEMENT - FACULTY, SCHOOL, DEPARTMENT

TITRE DE LA THÈSE - TITLE OF THE THESIS

Mineralogy, Petrology and Petrogenesis of Syenitic Rocks of the Porcupine-Destor Fault Zone Near Matheson, Ontario

A. E. Lalonde

DIRECTEUR DE LA THÈSE - THESIS SUPERVISOR

K. Hattori

CO-DIRECTEUR DE LA THÈSE - THESIS CO-SUPERVISOR

EXAMINATEURS DE LA THÈSE - THESIS EXAMINERS

K. Benn

E. Cameron

R. Taylor

J.-M. De Koninck, Ph.D.

LE DOYEN DE LA FACULTÉ DES ÉTUDES SUPÉRIEURES ET POSTDOCTORALES

SIGNATURE

DEAN OF THE FACULTY OF GRADUATE AND POSTDOCTORAL STUDIES

Mineralogy, petrology and petrogenesis of syenitic rocks of the Porcupine-Destor fault zone near Matheson, Ontario.

Luc Pigeon

A thesis submitted to the School of Graduate Studies and Research in partial fulfillment of the requirements for the degree of M. Sc. in Geology.

Ottawa-Carleton Geoscience Centre
University of Ottawa

Your file Votre référence
ISBN: 0-612-89904-7
Our file Notre référence
ISBN: 0-612-89904-7

Abstract

The mineralogy, petrology and petrogenesis of a representative suite of late Archean syenitic intrusions emplaced along the Porcupine-Destor fault zone near Matheson, Ontario in the southern Abitibi greenstone belt are studied using a combined approach involving field work, petrography, mineral chemistry and, major and trace element geochemistry. Members of the Matheson suite are from east to west: Iris, Garrison, Emens, Ludgate and Pangea intrusions. The Iris, Emens, Ludgate and Pangea intrusions are mostly composed of syenitic rocks with compositions ranging from alkali-feldpsar quartz-syenite to melasyenite. Textures range from equigranular to porphyritic. Iris and Pangea intrusions also contain related mafic rocks. The Garrison intrusion is composed of hornblende quartz-monzonite. All intrusions but one have hypersolvus feldspar assemblages; the exception being Garrison intrusion, which displays a subsolvus feldspar assemblage. The occurrence of late aegirine-augite, magnesioriebeckite and widespread albite replacement, especially in rocks from Ludgate and Iris intrusions, indicates that late or post-magmatic sodium-rich fluids variably affected the rocks.

Two magmatic series were identified based on silica-saturation properties and alkali-contents. The first, comprised of Emens and Ludgate intrusions, is composed of silica- undersaturated to -saturated potassic to ultrapotassic rocks; and the second, comprised of Iris, Ludgate and Garrison intrusions, is composed of silica-oversaturated sodic rocks. Moderate to high large ion lithophile elements contents and prominent negative Nb-Ta-Ti anomalies in normalized diagrams characterizes both series. Similarly, both suites display fractionated rare earth element patterns without negative Eu anomalies.

Rare earth element modelling confirms that the mafic rocks and syenites of Iris intrusion are cogenetic and are linked through fractionation of apatite, titanite, diopside, amphibole and feldspar. The U-shaped rare earth element patterns of the syenites are a direct consequence

of this fractionation. Rocks from the Matheson suite are analogous to those of the Kirkland Lake suite, also of the southern Abitibi greenstone belt. Both suites share several geological and geochemical traits, which indicates that they were formed through similar petrogenetic processes. A geochemical parallel with the Roman province of Italy also exists.

The petrography and geochemistry of the potassic rocks indicate that the parent magmas are mantle-derived and that the observed geochemical traits of the potassic series are directly related to subduction processes. Although the petrogenesis of the sodic suite still remains to be clearly established, it is likely that these rocks have the same petrogenesis has the potassic suite but acquired their sodic character through intense albitization. Alternatively, both suites could be derived from a source that underwent heterogeneous potassic and sodic metasomatism.

Sommaire

La minéralogie, pétrologie et pétrogenèse de cinq intrusions syénitiques d'âge Archéen tardif sont étudiées. Les plutons, ci-après nommés la suite de Matheson, ont été introduits en bordure de la zone de faille Porcupine-Destor près de Matheson en Ontario, située dans la ceinture de roches vertes de l'Abitibi du sud. L'étude utilise une approche combinée qui incorpore des relevés de terrain, pétrographie, chimie des minéraux et géochimie des éléments majeurs et traces des roches entières. Les intrusions membres de la suite de Matheson sont de l'est vers l'ouest : Iris, Garrison, Emens, Ludgate et Pangea. Ces intrusions sont géographiquement associées à plusieurs gisements aurifères. Les intrusions Iris, Emens, Ludgate et Pangea sont composées principalement de roches syénitiques alors que l'intrusion Garrison est composée surtout de monzonite quartzifère. Des roches mafiques sont aussi présentes dans les intrusions Iris et Pangea. Les roches ont des textures qui varient d'équigranulaire à porphyrique. Toutes les intrusions, à l'exception d'une, possèdent un assemblage de feldspath hypersolvus. Seulement l'intrusion Garrison démontre un assemblage de feldspath subsolvus. La présence de minéraux sodiques tardifs tel que l'aegyrine-augite et le magnésioriebeckite, en plus d'une abondance de plages tardives d'albite, indiquent que les roches ont été variablement affectées par des fluides enrichies en sodium tardi- ou post-magmatiques. Ceci est surtout le cas pour les intrusions Ludgate et Iris.

Les propriétés de saturation en silice et les teneurs en éléments alcalins ont permis d'identifier deux séries magmatiques. La première, comprenant les intrusions Emens et Pangea, est composée de roches potassiques à ultrapotassiques sous-saturées à saturées, alors que la seconde, comprenant les intrusions Iris, Ludgate et Garrison, est composée de roches sodiques sur-saturées. Les deux séries sont caractérisées par des teneurs modérées à élevées en éléments lithophiles à fort rayon et par des diagrammes normalisés qui ont des anomalies Nb-Ta-Ti négatives

prononcées. De plus, les deux suites ont des courbes d'éléments terres-rares fractionnées ne démontrant aucunes anomalies négatives en Eu.

La modélisation à l'aide des éléments terres-rares confirme que les roches mafiques et syénitiques de l'intrusion Iris sont cogénétiques et qu'elles sont reliées par le fractionnement de l'apatite, la titanite, le diopside, l'amphibole et le feldspath. Le fractionnement de ces minéraux est aussi responsable de la forme courbée en U des patrons d'éléments terres-rares des roches syénitiques de cette intrusion. Les roches de la suite de Matheson sont analogues à celles de la suite de Kirkland Lake qui est également située dans la ceinture de roches vertes de l'Abitibi du sud. Les deux suites ont en commun plusieurs traits géologiques et géochimiques qui laissent entendre qu'elles ont été formées par des processus pétrogénétiques semblables. Un parallèle géochimique existe aussi avec les roches potassiques de la province romaine d'Italie.

La pétrographie et géochimie des roches potassiques indiquent que les magmas parentaux de ces roches proviennent du manteau et que leurs traits géochimiques ont été directement acquis des processus de subduction. Quoique la pétrogenèse de la suite sodique reste à être définie de façon plus précise, il est probable que ces roches ont une pétrogenèse identique à la série potassique mais que leur caractère sodique ait été acquis suite à une albitisation intense. En contrepartie, les deux suites pourraient provenir d'une source ayant subit un métasomatisme hétérogène potassique et sodique.

Acknowledgements

To my supervisor, Dr. André E. Lalonde (University of Ottawa), I would like to express my sincere and outmost gratitude. His patience, enthusiasm, wisdom and constant encouragement over the past three years reflect his reputation as a great Professor and a superb Supervisor. Thank You.

Dr. Kéiko Hattori (U.O.), my co-supervisor, is thanked for reviewing Chapter 4 (geochemistry) of the thesis. Her comments and recommendations considerably improved the final product.

Ben Berger and Dr. John Ayer of the Ontario Geological Survey (OGS) are thanked for the numerous productive discussions in the field and after, and for providing the author with all the logistic support to conduct this study.

George Mrazek (U.O.) is thanked for the preparation of polished thin sections and for his help during sample preparation. Dave Crabtree and the members of the Geosciences Laboratories of the OGS are thanked for carrying the whole-rock geochemical analyses and performing all the electron microbe analyses.

I would like to thank my field assistant Robert Jones for his help throughout the summer of 1999. Brian Luinstra (U.O.), Christine Vaillancourt (OGS), Dr. Keith Benn (U.O.) and Dr. Anthony Fowler (U.O.) are thanked for their input and help during fieldwork. Hugues Longuépé (Université du Québec à Chicoutimi) is thanked for his help at mapping the volcanic rocks of Iris intrusion. Mélanie Plouffe is thanked for acting as my field assistant during one week of the summer.

To my parents, Paulette and Vincent, I would like to express my outmost gratitude for their unending moral and financial support throughout my graduate studies. To my aunt, Pauline Pigeon, who sacrificed a lot of time, energy and money during my graduate studies, I am forever indebted. I thank my girlfriend, Mélanie Plouffe, for her support, encouragement, patience and love during the past, and sometimes difficult, three years.

I dedicate this thesis to my:

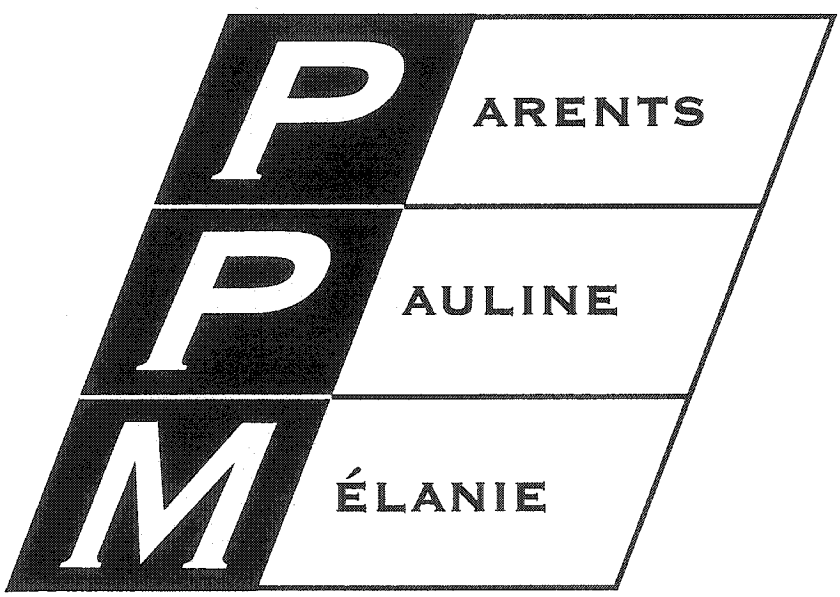

Their support will never be forgotten.

Table of contents

List of figures

List of tables

Introduction

A close spatial association between gold mineralization and syenitic intrusions has long been recognized in Archean greenstone belts, and in particular in the Abitibi greenstone belt of the Superior province in Canada (e.g., Wyman & Kerrich, 1988; Fyon et al., 1989; Kerrich, 1989; Levesque & Hattori, 1989; Edgar et al., 1991; Rowins et al., 1993; Duuring et al., 2000; Robert, 2001). One well-known locality, exemplifying the economic importance of this type of association, is the Kirkland Lake gold camp in Ontario. Although most mines are now closed, Kirkland Lake has historically been one of the most productive gold camps of the world. The economic importance of this type of association has prompted several studies on the possible genetic link between gold mineralization and alkaline intrusions, on the role of the Kirkland Lake-Larder Lake fault at focusing both gold and intrusions, and on the nature of syenitic magmatism in general (e.g., Cameron & Hattori, 1987, Cameron, 1988, 1993; Smith & Sutcliffe, 1988, Ben Othman et al., 1990; Sutcliffe et al., 1990; Hattori, 1993; Rowins et al., 1993; Levesque, 1994; Fang & Zhang, 1995; Wilkinson et al., 1999).

A similar type of association exists to the north of Kirkland Lake along the Porcupine-Destor fault zone (PDFZ) near Matheson, Ontario. The geological setting of this area is surprisingly similar to the one of Kirkland Lake. Several small syn- to post-tectonic syenitic intrusions intrude the volcanic rocks along a narrow corridor that includes and is parallel to the PDFZ. Their age of 2680 Ma (i.e., Garrison intrusion; Corfu et al., 1989) and style of emplacement are similar to the intrusions from Kirkland Lake. Furthermore like Kirkland Lake, they are in close spatial association with several small Au deposits (e.g., Buffonta and Hislop) or active mines (e.g., Holt-McDermott and Holloway).

Despite the similarities with the Kirkland Lake camp, few geological studies are available for this part of the PDFZ. This prompted the Ontario Geological Survey (OGS) to fund several projects in the Matheson area (i.e., this study, Ropchan, 2000; Luinstra, 2002) in order to

better understand the intimate association of gold, PDFZ and syenites, and at the same time, to establish a parallel with the Kirkland Lake camp in the hope of stimulating gold exploration.

The purpose of this project is to describe the mineralogy, geochemistry and petrogenesis of a suite of syenitic rocks that occur near the PDFZ in Guibord, Michaud, Garrison and Harker townships (Figure 1.1). A thorough characterization of these intrusions will demonstrate that they are in fact very similar to those of Kirkland Lake.

In view of the fact that there are no detailed studies of these intrusions and that there is only a few recent geochemical analyses published (e.g., Berger & Amelin, 1999), emphasis is placed on characterizing the petrography and mineral chemistry of the various rock units, including comprehensive major, trace and rare earth elements analyses of the rocks. The petrogenesis of the intrusions and possible genetic relationship between the members of the intrusive suite is explored in light of the results and compared with other alkaline rocks of similar composition or geodynamic setting.

A suite of five intrusions was sampled in this study. The intrusions are from east to west: 1) Iris, 2) Garrison, 3) Emens, 4)Ludgate, and 5)Pangea (Figure 1.1). Fieldwork for this project extended from early June to the end of August 1999 while employed by the Ontario Geological Survey (OGS) under the supervision of Ben Berger and Dr. John Ayer. A portion of this time was spent producing a detailed geological map of the Iris intrusion. Field mapping was done at a scale of 1:100 with the final product, attached at the end of the thesis, at a scale of 1:295. Since mapping was performed before the era of metre-scale GPS accuracy, several days were spent establishing a large grid on the outcrop for precise positioning. The grid was divided into 5 metre increments and extended over all the outcrop surface area. Over forty samples of the different rock units of the map area and beyond were collected for a wide array of elemental analysis

including major, trace, rare earth, gold and platinum group elements. Samples of Ludgate and Garrison intrusions were also collected in the field by the author. Since Emens and Pangea intrusions do not outcrop at the surface, several drill holes were logged during the summer in order to get an accurate representation of the various lithologies of these intrusions. Drill core sampling for these intrusions is as extensive as what was performed at Iris intrusion. Over 50 polished thin sections were made from rocks of all the intrusions and over 100 mineral analyses were performed on these samples. All whole-rock and mineral analyses were funded by the OGS. Access to drill core from Emens and Pangea intrusions was made possible courtesy of Moneta-Porcupine Mines and Pangea Goldfields respectively. Similarly, Mr. Alex Perron made sampling of the Iris and Garrison intrusions possible while Pentland Firth Ventures granted access to the Ludgate intrusion. The collaboration of these companies is gratefully acknowledged.

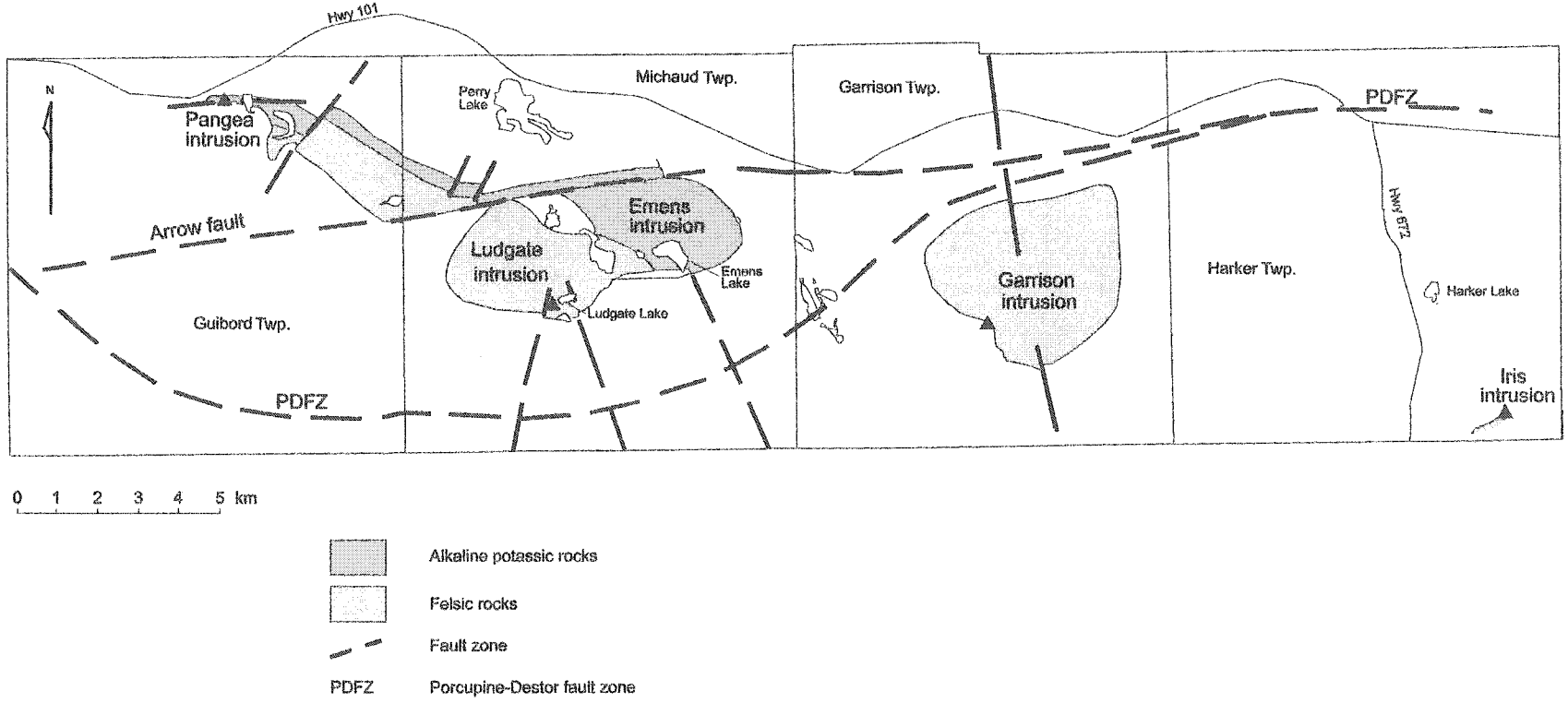

Figure 1.1 Location map of the study area with respect to the major deformation zones of the area (courtesy of Ben Berger, OGS).

Chapter 1

Regional geology of the Superior province and Abitibi greenstone belt

I. Geology of the Superior province
II. Geology of the Abitibi greenstone belt
III. Geology of the study area

I. Geology of the Superior province

The Superior province is the largest Archean craton in the world covering over 1.5 million square kilometres (Hoffman, 1989). It extends from Manitoba in the west to Québec in the east, with a major portion of the province (565 000 km^2) located in Ontario (Thurston, 1991).

The Superior province in bounded to the south by the Proterozoic Southern province (Bennett et al., 1991), to the east by the Proterozoic Grenville province (Wynne-Edwards, 1972; Easton, 1992), to the northeast (Labrador trough) and northwest by the mostly Archean Churchill province and to the west and north by Phanerozoic basins (Nelson & Johnson, 1966; Sanford et al., 1968; Roksandic, 1987; Norris, 1993).

In general, the Superior province is composed of east-northeast trending domains of heterogeneous lithologies, ages and deformation/metamorphism intensities. These domains are interpreted to be accreted remains of Archean continental and oceanic crust (Card, 1990). These contrasting domains prompted the further subdivision of the Superior province into subprovinces based on the predominant lithologies. Card (1990) identified four broad types of subprovinces : 1) volcano-plutonic, 2) metasedimentary, 3) gneissic/plutonic and 4) high-grade gneiss.

The volcano-plutonic subprovinces are by far the more economically important since they host most of the base and precious metal deposits. They are composed predominantly of greenstone belts (metamorphic volcanic and related sedimentary and intrusive rocks) and granitic rocks. The metamorphic grade in these subprovinces is generally low (sub-greenschist to greenschist facies).

The metasedimentary type subprovinces are composed of shale and sandstone metamorphosed to various degrees. The metamorphic grade is usually low (greenschist) on the subprovinces margins and more intense in the interior (amphibolite to granulite facies).

The gneissic/plutonic type is composed of tonalitic gneisses and granitoid intrusions. The metamorphic grade is usually high (upper amphibolite to granulite facies).

The high-grade gneiss subprovinces are composed of gneisses (sedimentary and plutonic origin) cut by tonalitic, granodioritic and syenitic intrusions (Percival & Card, 1985). The metamorphic grade of the subprovinces is high (upper amphibolite to granulite facies).

II. Geology of the Abitibi greenstone belt

The Abitibi greenstone belt (Goodwin & Ridler, 1970; Jensen & Langford, 1985; Hodgson, 1983) is the largest greenstone belt in the world, covering an area of over 85 000 km^2 (Card, 1990). The belt is located in the southeastern part the Superior province (Figure 1.2). It is characterized by a high ratio of supracrustal to intrusive rocks and a generally low metamorphic grade.

The Abitibi greenstone belt has a long history of mineral exploration and mining. It is one of the gold most productive greenstone belts in the world, with over 3700 metric tons of gold mined in the past 80 years (Colvine et al., 1988). The belt is also rich in base metal deposits of the volcanogenic massive sulphide type and the komatiite-associated Ni-Cu-PGE type. Amongst the base metal deposits, the Kidd Creek Pb-Zn mine is classified as a world-class deposit.

The Abitibi greenstone belt is bound to the south by the Ramsey-Algoma granitoid complex (Card, 1979), the Cobalt embayment (Bennett et al., 1991) and the Pontiac subprovince (Figure 1.2). To the north, the belt is bound by the Opatica subprovince; to the east by the Grenville province (Easton,1992), and to the west by the Ivanhoe Lake cataclastic zone, part of the Kapuskasing structural zone (Percival and Card, 1983).

Dimroth et al. (1983b) subdivided the Abitibi greenstone belt into two distinct belts: the northern belt and the southern belt (Figure 1.3). The northern belt is characterized by abundant tonalite-trondhjemite-granodiorite intrusions, anorthosite complexes and minor ultramafic units (Dimroth et al., 1983b). The regional metamorphic facies of the northern belt is normally greenschist or higher (Dimroth et al., 1983b). Only a small part of the northern belt is exposed in Ontario (Figure 1.3).

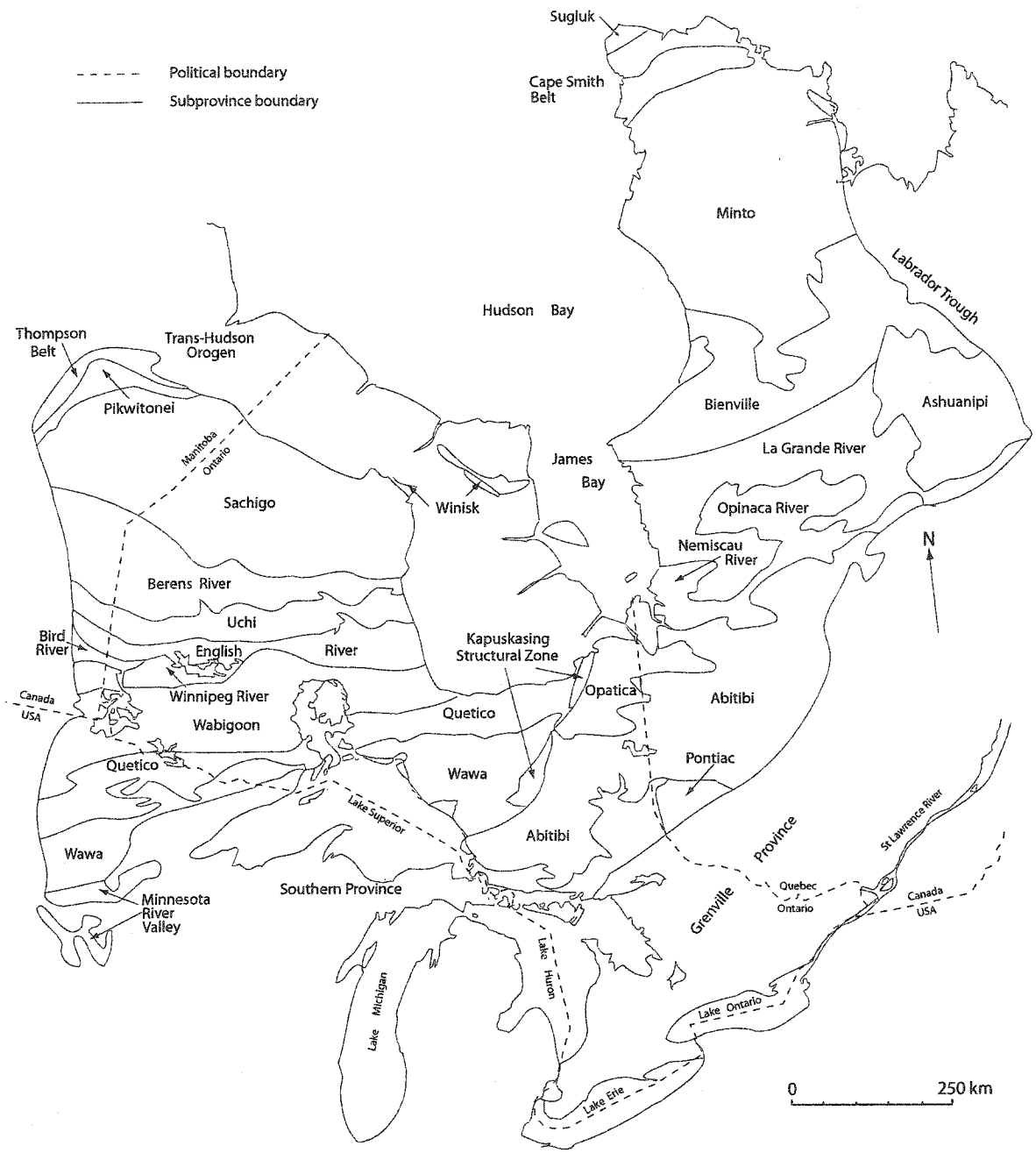

Figure 1.2 Subdivision of the Superior province into subprovinces (modified from Thurston, 1991).

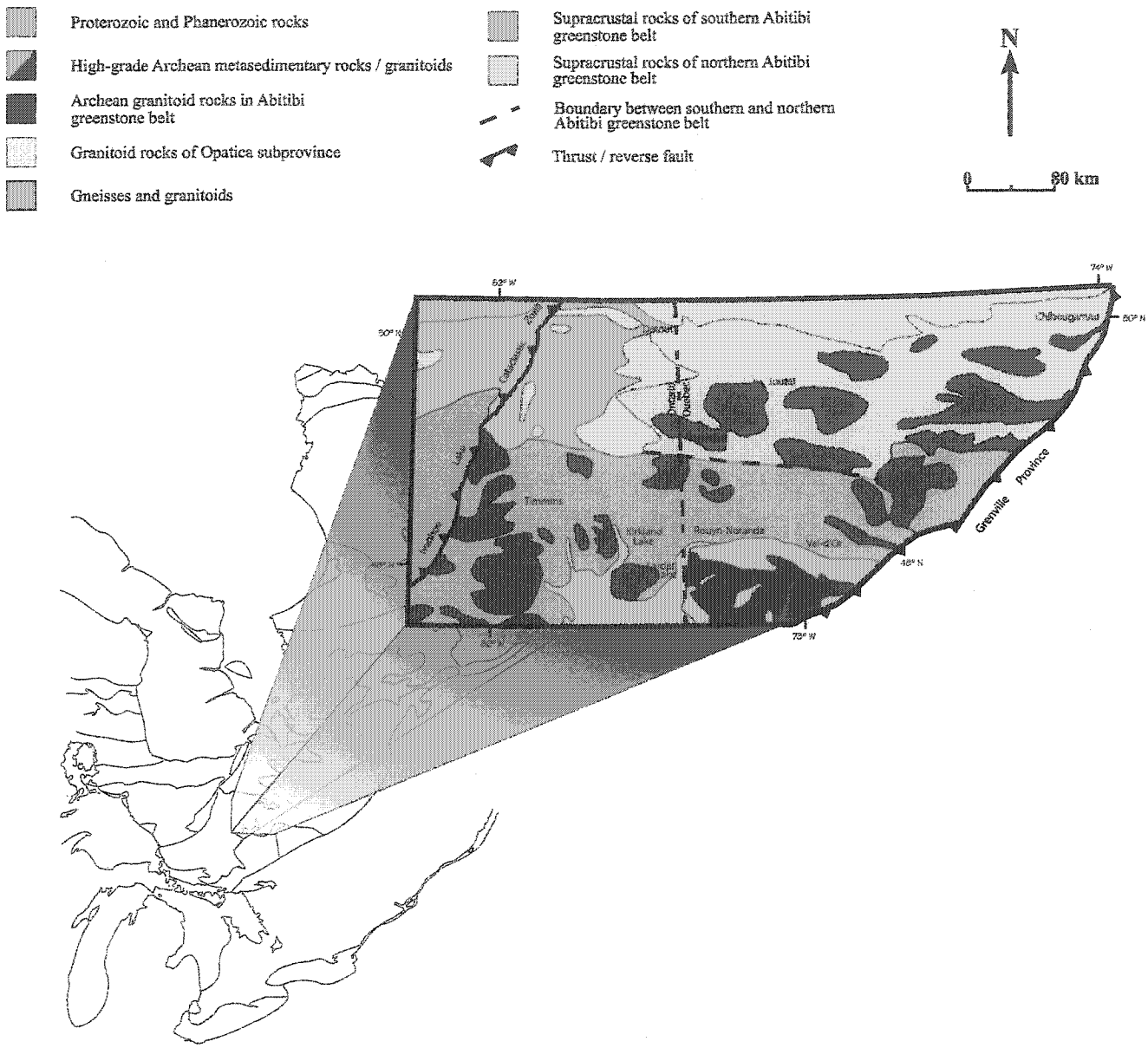

Figure 1.3 Subdivision of the Abitibi greenstone belt into two distinct belts: the northern belt and the southern belt (modified from Dimroth et al., 1983b).

The genesis of the southern Abitibi greenstone belt can be simplified into three major and broad events. 1) The extrusion of volcanic rocks and the deposition of syn-volcanic sedimentary rocks, and the intrusion of syn-volcanic peridotitic to granodioritic rocks between ~2.75 and ~2.70 Ga (Corfu et al., 1989). 2) The intrusion, between ~2.70 and ~2.68 Ga, of large tonalitic and granodioritic batholiths that were later foliated, and followed by the emplacement of more massive granodiorite, granite, feldspar ± quartz porphyry and syenite intrusions (Corfu et al., 1989). 3) The deposition of syn- and post- intrusion alluvial-fluvial sedimentary rocks (Hyde, 1980) with coeval extrusion and intrusion of alkaline rocks (Cooke & Moorhouse, 1969).

The southern belt was subjected to episodes of regional deformation prior to and after the deposition of the sedimentary and alkaline volcanic rocks. The regional metamorphic grade is generally low (subgreenschist facies) but is higher (amphibolite facies) near some intrusions (Jolly, 1978, 1980; Powell et al., 1995).

The Abitibi greenstone belt supracrustal rocks are divided into distinct units called assemblages. Thurston (1991) defines an assemblage as "stratified volcanic and/or sedimentary rock units built during a discrete interval of time in a common depositional or volcanic setting." Jackson and Fyon (1991) subdivided the Abitibi greenstone belt into 54 different lithotectonic assemblages. These subdivisions were based on a model suggesting that the Abitibi belt was formed by the superposition of allochthonous assemblages. However, recent work by Corfu (1993), Heather (1998) and Ayer et al. (1999, 2002) has established that inherited zircons with ages similar to those of underlying assemblages are present in all assemblages apart for the Pacaud and Kinojevis. This evidence is not consistent with an allochthonous model and it suggests to these authors that the lithostratigraphic units of the Abitibi greenstone belt were deposited in autochthonous successions. In light of this evidence, Ayer et al. (2002) published a revision of the stratigraphy of the belt. The new stratigraphy now comprises seven volcanic and

two sedimentary assemblages. The following is a brief review of these new assemblages taken from Ayer et al. (1999, 2002).

Pacaud assemblage

The Pacaud assemblage is composed of tholeiitic mafic volcanic rocks with lesser amounts of komatiite and calc-alkaline intermediate to felsic volcanic rocks. The assemblage age ranges from about 2750 to 2735 Ma.

Deloro assemblage

The Deloro assemblage is composed of mafic to felsic calc-alkaline volcanic rocks, and commonly with regionally extensive iron oxide formations. The assemblage ranges in age from 2730 to 2724 Ma.

Stoughton-Roquemaure assemblage

The Stoughton-Roquemaure assemblage is composed of thick Mg- and Fe-rich tholeiitic basalt sequences with local komatiites and felsic volcanic rocks. The assemblage ranges in age from about 2723 to 2720 Ma.

Kidd-Munro assemblage

The Kidd-Munro assemblage consists mainly of basalt and komatiite but calc-alkaline basalt to rhyolite and tholeiitic rhyolitic volcanic rocks are also present. The age of these rocks ranges from 2719 to 2710 Ma.

Tisdale assemblage

The Tisdale assemblage consists of tholeiitic basalts and rhyolites, komatiites and intermediate to felsic calc-alkaline volcanic rocks. The assemblage ranges in age from 2710 to 2703 Ma.

Kinojevis assemblage

The Kinojevis assemblage is composed of a thick sequence of tholeiitic mafic volcanic rocks and a minor amount of thin felsic flows and clastic sedimentary horizons. The Kinojevis has a narrow age range of 2702-2701 Ma.

Blake River assemblage

The Blake River assemblage is composed of calc-alkaline mafic to intermediate volcanic rocks in the Ontario portion but also contain tholeiitic basalt and rhyolites in Québec (Jackson & Fyon, 1991). The assemblage age ranges from 2701 to 2697 Ma.

Porcupine assemblage

The Porcupine assemblage is composed of wacke, siltstone and mudstone with a predominantly distal environment. Local turbidity current deposits and conglomerates indicate a more proximal setting. The Porcupine assemblage was deposited after 2696 Ma (Bleeker & Parrish, 1996).

Timiskaming assemblage

The Timiskaming assemblage is predominantly composed of narrow bands of clastic sedimentary rocks and alkaline to calc-alkaline volcanic rocks. The sedimentary rocks consist of polymictic conglomerates and sandstones deposited in subaerial-fan, fluvial and deltaic environments (Mueller et al., 1994). The assemblage age ranges from 2687 to 2675 Ma.

The formation of structures in the southern Abitibi greenstone belt can be divided into three broad events (Jackson & Fyon, 1991): 1) pre-cleavage folds, 2) structures related to batholith emplacement, and 3) syn- to post- Timiskaming structures. Of the three events, the syn- to post-Timiskaming structures are the most prominent. The Porcupine-Destor fault zone (Green et al., 1990; Jackson et al., 1990) and the Cadillac-Larder Lake shear zone (Hamilton, 1986; Toogood &

Hodgson, 1986; Robert, 1990) cut the southern belt in a easterly direction for several hundreds of kilometres (Figure 1.3).

There is evidence that the steeply south-dipping Porcupine-Destor fault zone first underwent a vertical south-over-north slip (Green et al., 1990). Later reactivation produced a component of sinistral horizontal slip (Hodgson et al., 1990), while Piroshco and Kettles (1991) identified a still later dextral horizontal slip reactivation on the deformation zone.

In Ontario, the Cadillac-Larder Lake shear zone is steeply south-dipping and contains steeply south-plunging stretching lineations (Jackson & Fyon, 1991). These characteristics (dip and lineation directions) and older-to-the-south on younger-to-the-north relationship all suggest that the main displacement of the Cadillac-Larder Lake shear zone was reverse and south-side up (Hamilton, 1986).

Numerous tectonic models have been proposed for the Abitibi greenstone belt (Goodwin, 1977; Dimroth et al., 1983a; Jensen and Langford, 1985; Hodgson, 1986; Ludden et al. 1986; Hodgson & Hamilton, 1989). Early models were dominantly based on vertical tectonics (Ayer et al., 1999, 2002). These models explained the stratigraphy by the development a large scale geosynclinal basin formed as a result of rifting, crustal subsidence and cyclical volcanism (Goodwin, 1977; Jensen & Langford, 1985). Later, plate tectonic models were introduced. These models hypothesized that the Abitibi greenstone belt was formed by lithotectonic assemblages that were developed in different geodynamic environments. These assemblages were then juxtaposed in their present positions by various tectonic processes. This most likely occured along active continental margins (Jackson et al., 1994; Mueller et al., 1997; Calvert & Ludden, 1999).

As previously mentioned, Heather (1998) and Ayer et al. (1999, 2002) have suggested a stratigraphy-based model, in which they hypothize that the lithostratigraphic units of the belt were deposited in autochthonous successions. They interpret that the present distribution of units is the result of interplay of multiphase folding and faulting.

III. Geology of the study area

The intrusions that were studied are located in Harker, Garrison, Guibord and Michaud Townships (Figure 1.1). These townships were previously mapped by Satterly (1947, 1949), Prest (1951), Troop (1989, 1990) and more recently by Berger and Amelin (1999). Two recent thesis projects were also done in this area. Ropchan (2000) studied the petrography and geochemistry of alteration zones associated with gold mineralization at the Holloway mine in nearby Holloway Township while Luinstra (2002) studied the geology, structure and gold mineralization within the Porcupine-Destor fault zone. This brief summary of the local geology is mostly inspired by the work of Berger and Amelin (1999).

Most of the area of these townships is covered by overburden (Quaternary sand and gravel). However, a wealth of archived data obtained by private company diamond drill core and airborne geophysical data facilitated the geological mapping and the interpretation of the unexposed areas (Berger & Amelin, 1999 and references therein).

Five assemblages of Achean metavolcanic and metasedimentary rocks were identified in the study area. Using the classification introduced by Ayer et al. (1999, 2002), these assemblages are: 1) Kidd-Munro, 2) Porcupine, 3) Tisdale, 4) Kinojevis and, 5) Timiskaming. A brief description of each assemblage is given below. For simplicity the prefix "meta" will be omitted in the following paragraphs. However, the reader should keep in mind that most rocks of the area, which are not located within the Pocupine-Destor fault zone, have generally only undergone either prehnite-pumpellyite, or greenschist facies metamorphism (Fowler et al., 2002).

The Kidd-Munro assemblage is composed of ultramafic, mafic and intermediate volcanic rocks. The mafic volcanic rocks are predominently pillowed or massive although some hyaloclastite,

pillow breccias and variolitic units are also present. A recent study of the variolitic rocks of the area by Fowler et al. (2002) adresses the subject of variole genesis. The stratigraphy is generally north younging, however south-facing pillows occur in Garrison Township (i.e., Troop, 1990).

Rocks from the Porcupine assemblage are restricted to the northeastern part of Guibord township. The assemblage is composed of clastic and a minor amount of chemical sedimentary rocks. Turbidites displaying Bouma sequences are common. The predominence of siltstone and mudstone in the turbidites indicate that they were formed in a distal facies.

The Tisdale assemblage consists of mafic and ultramafic volcanic rocks. Ultramafic rocks with spinifex, flow breccia and cumulate textures are interleaved with talc-chlorite-carbonate schist and mafic volcanic rocks in Guibord and Michaud Townships. Ultramafic flows and schists also occur north of the Garrison intrusion in Garrison Township. These flows also extend into Harker Township. Pillowed and massive mafic volcanic flows are common in central Michaud Township. Variolitic mafic volcanic flows of high magnesium basalts are found in western Guibord Township.

The Kinojevis assemblage is predominently composed of massive and pillowed mafic volcanic rocks. Several clastic interflow sedimentary rocks also occur. Variolitic mafic volcanic flows are abundant. The Kinojevis assemblage consistently youngs to the south.

The Timiskaming assemblage consists of subaerial sedimentary rocks and syenitic intrusive rocks. The sedimentary rocks are usually in close spatial association with the Porcupine-Destor fault zone and occur as an arcuate band that extends from central Garrison through Michaud and Guibord Townships. The sedimentary rocks are composed of polymictic conglomerates, sandstone and mudstone. Iron formation and jasper clasts, which are characteristic of Timiskaming

conglomerates, occur within these conglomerate and sandstone beds, as well as ultramafic, mafic and syenitic clasts. The higher proportion of sandstone and mudstone over conglomerates, and the small average clast sizes, coupled with the absence of large scale cross-bedding indicate that deposition occured in a low energy fluvial environment. Numerous alkalic intrusive rocks ranging in composition from pyroxenite/hornblendite to syenite and granite intrude the country rock as plutons, dykes, sills and cupolas. It is a representative suite of these intrusions that concern this study. Their characteristics will be discussed in-depth in the following chapters.

Jurassic/Cretacious kimberlite dykes and plugs occur at the New Buffonta pit of Garrison intrusion in Garrison Township. Kimberlite was also reported in western Michaud and eastern Guibord Townships.

Gold mineralization occurs throughout the study area. Gold was extracted from the Buffonta, New Buffonta, Garrcon and Jonpol deposits in Garrison Township. Several potentially economic deposits are outlined in close proximity to three intrusions that are part of this study i.e., Pangea, Ludgate Lake and Moneta-Porcupine deposits in Guibord and Michaud Townships. Holloway and Holt-McDermott mines are the only active gold producers in the immediate vicinity of the study area. Gold mineralization in the area is usually closely associated with alkalic rocks and subsidiary faults or shear zones of the Porcupine-Destor fault zone. Gold mineralization can be hosted within sheared syenites (i.e., Ludgate Lake deposit), within variolitic basalts at the periphery of alkalic intrusions (i.e., Buffonta, New Buffonta and Pangea deposits) or within hydrothermally altered Timiskaming conglomerates (i.e., Moneta-Porcupine deposit).

The Porcupine-Destor fault zone is the dominant structure in the area. It is interpreted to fan west of the Garrison intrusion into a number of discrete west-, southwest- and northwest-striking faults. Another major structure called the Arrow fault splays from the main Porcupine-Destor

fault zone northeast of the Garrison intrusion at the boundary between Harker and Garrison Townships, and reconnects with the Porcupine-Destor fault in western Guibord Township (Figure 1.1). North-northwest to north-northeast striking faults offset the main Porcupine-Destor fault in Michaud Township, and appear to terminate at the contact with the Ludgate and Emens intrusions.

Chapter 2

Petrography and mineralogy of the intrusive rocks

I. Introduction

Iris intrusion

THE Iris intrusion is located approximately 4 km east of Highway 672 at the boundary of Harker Township (Figure 1.1). The mineral rights of the area that covers the intrusion are owned by Mr. Alex Perron, a local prospector. The Iris intrusion is a small intrusion with a total surface area of only ~0.5 km^2. It is very well exposed (Figure 2.0 & 2.1). The exceptional exposure is the result of numerous exploration surveys conducted over the area. Several thousand square metres of the intrusion were stripped of overburden and washed with high-powered water pumps. The intrusion is composed of numerous distinct mafic and felsic units. Five major rock units were identified while mapping the intrusion: 1) pyroxene-bearing hornblendite, 2) monzodiorite, 3) alkali-feldspar quartz-syenite, 4) alkali-feldspar porphyritic syenite and 5) antiperthite syenite. A detailed geological map of the Iris intrusion exposure is attached at the back of the thesis while a smaller version of this map is presented as Figure 2.3.

Garrison intrusion

The Garrison intrusion is the largest of the five intrusions in the area and is also well exposed. It is located approximately 2.5 km south of the intersection of Garrison Creek with Highway 101 in Garrison Township (Figure 1.1). The site visited, called New Buffonta, is also owned by Mr. Alex Perron and is located at the southwestern margin of the intrusion. Past exploration ventures have left numerous stripped areas and one large open pit that is now flooded (Figure 2.2). Medium-grained hornblende quartz-monzonite is the major rock unit in the Garrison intrusion.

Emens intrusion

The Emens intrusion is located northeast of the Ludgate Lake syenite, approximately 2 km southeast of Perry Lake in Michaud Township (Figure 1.1). The southwestern portion of this intrusion is in contact with the Ludgate Lake syenite. The Emens intrusion, which does not

outcrop at the surface, was sampled only in drill core owned by Moneta-Porcupine Mines Ltd. Two major units were identified in the available core: 1) alkali-feldspar phenocrystic biotite-syenite and 2) alkali-feldspar syenite.

Ludgate intrusion

The northern tip of the Ludgate intrusion is located approximately 2 km south of Perry Lake in Michaud Township (Figure 1.1). The site visited is owned by Pentland Firth Ventures Ltd and is at the southern boundary of the intrusion. It consists of a stripped outcrop of about 30 m by 80 m in dimensions. The principal rock type found on the property is coarse-grained alkali-feldspar quartz-syenite.

Pangea intrusion

The Pangea intrusion is located approximately 1 km southeast of the intersection of Little Pike River with Highway 101 in Guibord Township and extends about 2 km into Michaud Township (Figure 1.1). The Pangea intrusion, like the Emens, does not outcrop at the surface and was only sampled from drill core originally owned by Pangea Goldfields Inc. Three petrographic units were identified from these drill cores: 1) medium-grained melasyenite with extensive textural and compositional variation, 2) pyroxene-bearing hornblendite and 3) coarse-grained alkali-feldspar syenite.

Note that all the rock units in this study are classified according to the recommendations of the IUGS Subcommission on the Systematics of Igneous Rocks reported by Streckeisen (1976). All of the above mentioned rock units are described below.

Figure 2.0 View of the Iris exposure, looking towards the north from a distance of ~250 m.

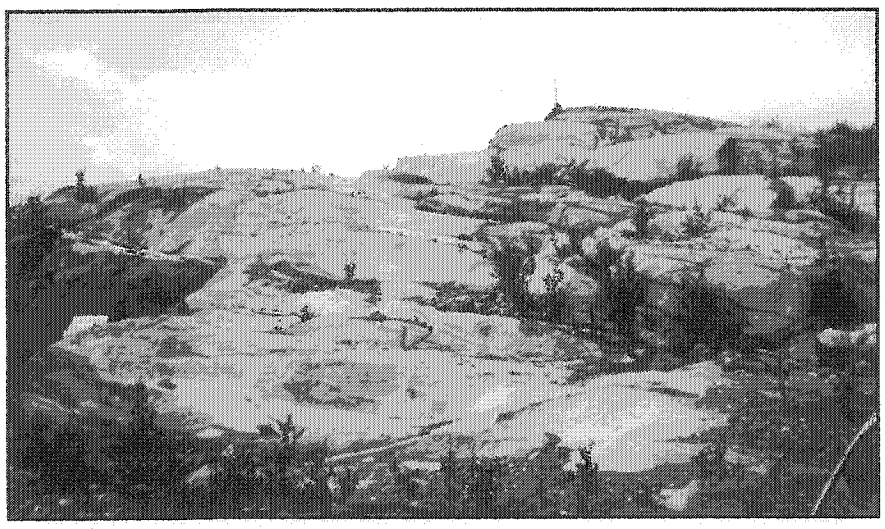

Figure 2.1 View of the cleaned exposure of the Iris intrusion.

Figure 2.2 Abandoned open-pit at the New Buffonta property within the Garrison intrusion.

II. Iris intrusion

A. Pyroxene-bearing hornblendite

Pyroxene-bearing hornblendite (hereinafter called hornblendite) is the principal mafic rock unit at the Iris intrusion. The hornblendite unit is located on the southern and southeastern rim of the intrusion (Figure 2.3), in sharp contact with the coarse-grained alkali-feldspar syenite unit, and is crosscut by 0.5 to 2 m thick xenolith-rich monzonite dykes, 1 to 3 cm thick fractures filled with blue asbestiform amphibole (Figure 2.4) and numerous small (5-15 mm) albite veins (Figure 2.5). The hornblendite unit is interpreted, on the basis of cross-cutting relationships seen on outcrop surfaces, to be the oldest unit of the Iris intrusion.

The hornblendite rock consists of a fine- to medium-grained green matrix composed of anhedral albite, anhedral to subhedral diopside and magnetite, and 40 to 50 % dark green to black 0.5 to 1.5 cm anhedral to subhedral pargasite and magnesiohastingsite megacrysts (Table 2.1; Figure 2.6, 2.7 & 2.8); chapter 3 for mineral chemistry). The modal abundances reported in this chapter are visual estimates of minerals identified in thin section. The rock contains zones of various sizes that are only composed of large amphibole and albite crystals (figure 2.9). Some of these zones contain elongated euhedral amphibole crystals that have albite filled cores (Figure 2.10 & 2.11). The occurence of this texture, which is similar to hopper pyroxenes and olivines, is believed to reflect rapid disequilibrium crystal growth from volatile-rich fluids. The rock is also locally massive, coarse-grained and equigranular. On a weathered surface, the hornblende megacrysts are commonly in positive

Mineral	Modal%
Amphibole megacrysts	40-50
Diopside	15-20
Albite	15-20
Magnetite	5-10
Apatite	5
Chlorite	5
Titanite	1
Secondary calcite	tr.
Epidote	tr.

Table 2.1 Range of modal composition of the pyroxene-bearing hornblendite unit.

Figure 2.3 Detailed map of the Iris intrusion. See also larger map included at the end of the thesis.

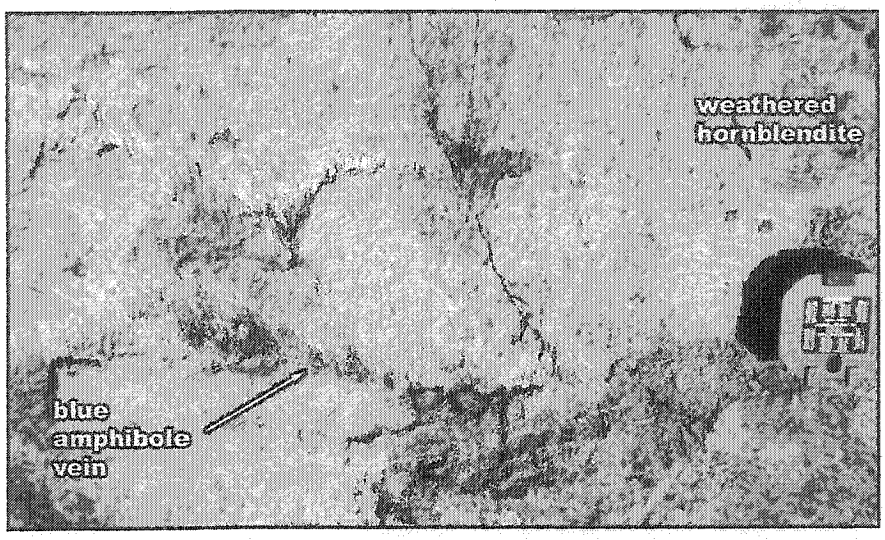

Figure 2.4 Vein of blue amphibole cross-cutting the pyroxene-bearing hornblendite unit.

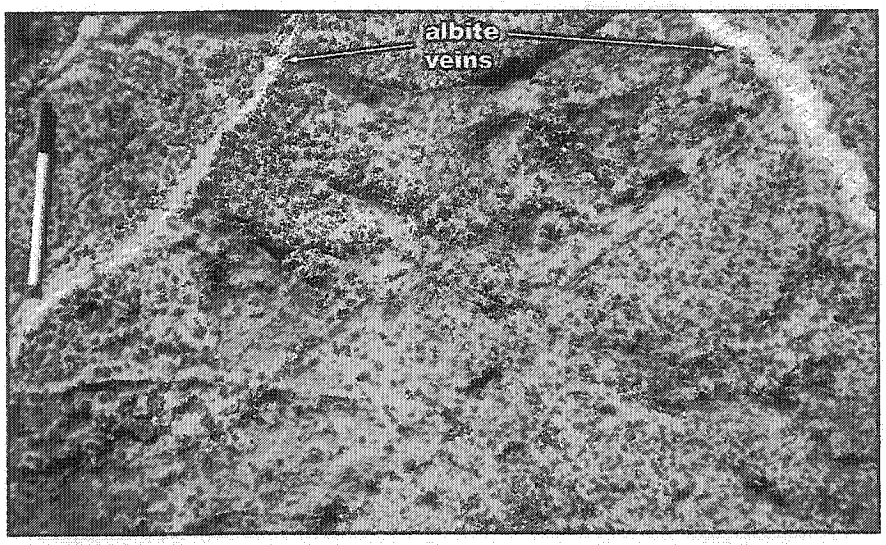

Figure 2.5 Small albite veins cross-cutting the pyroxene-bearing hornblendite unit.

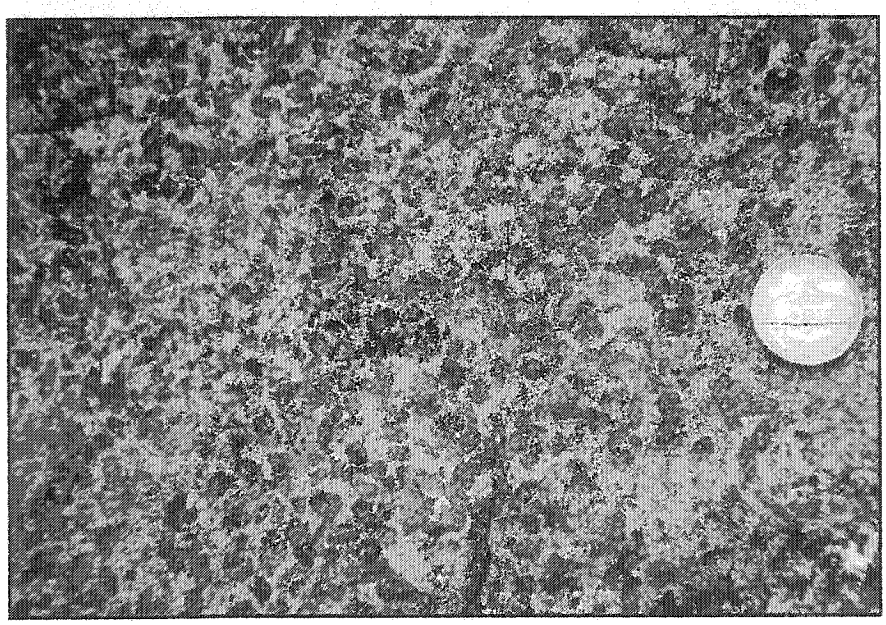

Figure 2.6 Fresh surface of the pyroxene-bearing hornblendite rock. The hornblende megacrysts are dark green to black.

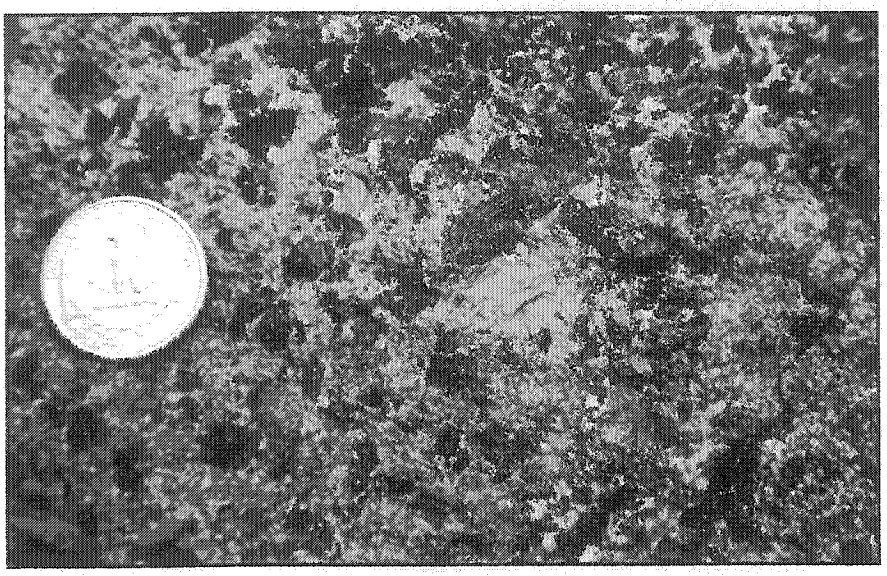

Figure 2.7 Close-up of a fresh surface of the pyroxene-bearing hornblendite. The hornblende megacrysts are dark green to black. The matrix, composed of albite, diopside, apatite and magnetite is greenish-gray. Larger albite crystals are white to pale gray.

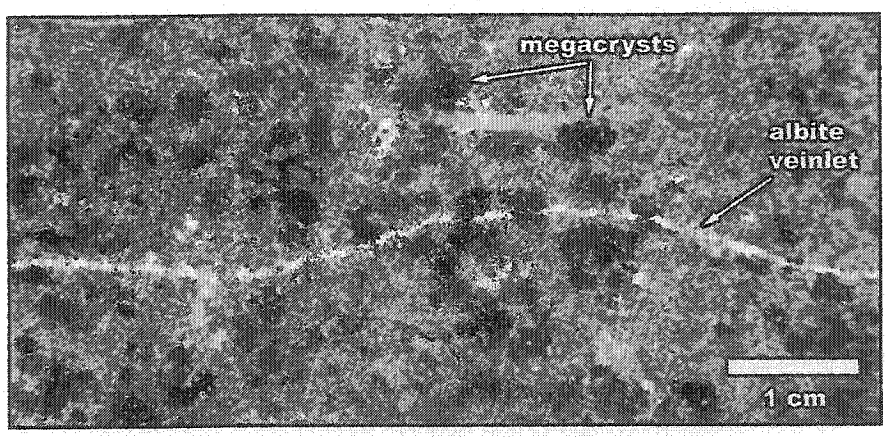

Figure 2.8 Close-up of a fresh surface of a pyroxene-bearing hornblendite slab. See above for description. A white albite veinlet is cross-cutting the sample.

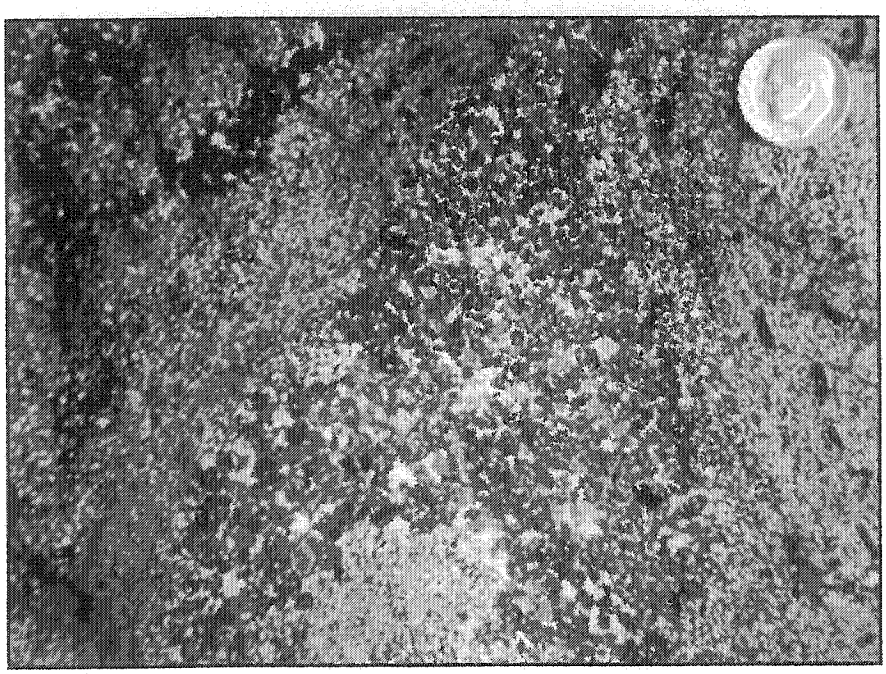

Figure 2.9 Local grain-size variations are commonly observed in the pyroxene-bearing hornblendite unit. The minerals of these zones are interpreted to have crystallized from volatile-rich pockets.

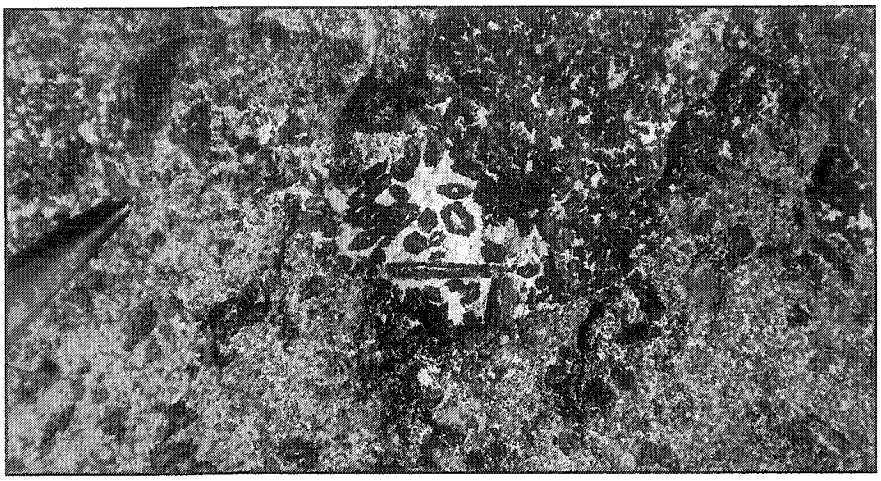

Figure 2.10 Local grain-size variations are commonly observed in the pyroxene-bearing hornblendite unit. Also visible are euhedral amphiboles with albite-filled cores. The occurence of this texture is believed to reflect rapid disequilibrium crystal growth from a volatile-rich environment.

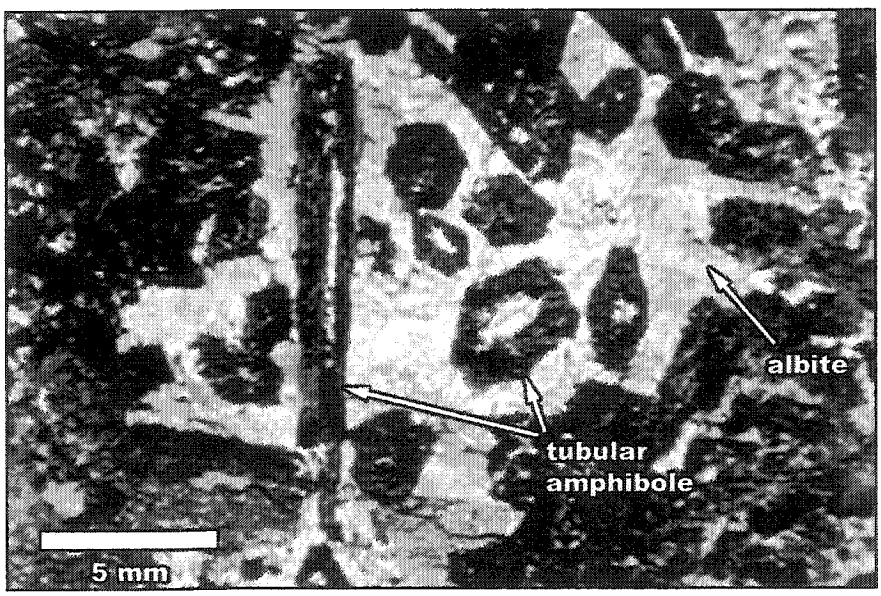

Figure 2.11 Close-up of the euhedral amphibole. See above for description.

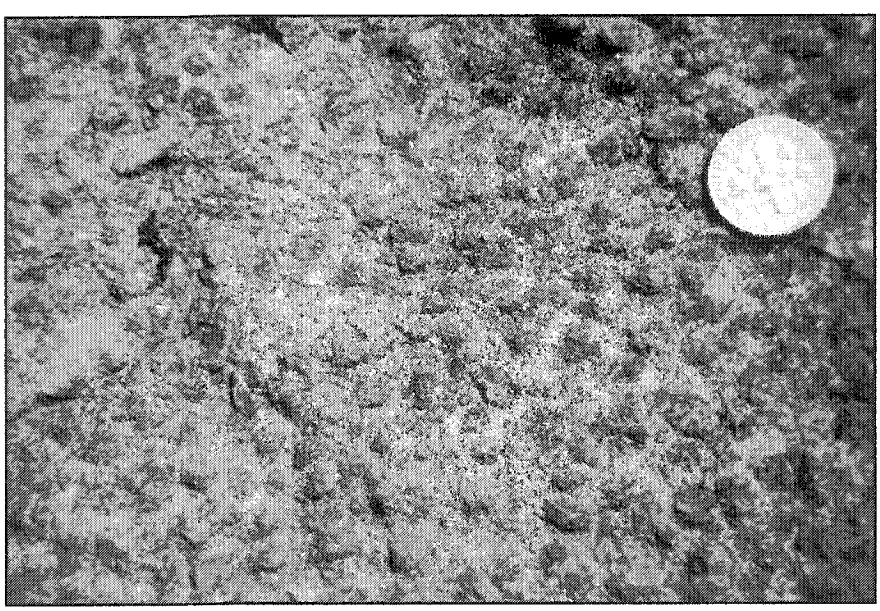

Figure 2.12 Weathered surface of the pyroxene-bearing hornblendite unit. Amphibole megacrysts are in positive relief producing a rough, knobby surface.

relief, producing a rough knobby surface (Figure 2.12). Usually, the matrix is slightly chloritized.

Under the microscope, pargasite and magnesiohastingsite megacrysts display light olive green to dark olive green to brownish-orange pleochroic colors. They are sometimes zoned, the zoning consisting in variations in the pleochroism along the rims of the megacrysts (Figure 2.13). Most large megacrysts are subhedral but smaller ones are commonly euhedral (Figure 2.13). They contain numerous small inclusions of apatite, magnetite and diopside suggesting that the megacrysts formed late in the paragenetic sequence. (Figure 2.13, 2.14 & 2.15). The megacrysts are usually fresh but alteration to chlorite is observed.

Diopside is present in the matrix as anhedral to subhedral crystals but euhedral crystals displaying pyroxene basal sections or long-prismatic shapes are also common (Figure 2.16). The diopside crystals are small (0.2-0.4 mm) however, the long axis of some prismatic crystals may reach up to 7 mm in length. They are light green with little or no pleochroism. Diopside is commonly twinned (Figure 2.16 & 2.17). In these crystals, the twinning plane is parallel to the long axis. The occurence of lamellar twinning is common in diopside (Nesse, 1991). Diopside is generally fresh but larger crystals have amphibole alteration rims that are probably the result of the interaction of late hydrous fluidswith the rims of the pyroxene crystals.

Albite crystals are anhedral and usually display good albite twinning (Figure 2.18). The Na-rich composition of this feldspar was confirmed using optical extinction angle measurements and electron microprobe analyses. They are turbid, producing a distinctive dark gray color. Albite is interstitial to diopside, magnetite, apatite and titanite crystals (Figure 2.18 & 2.19). This texture suggests that albite crystallized late in the sequence either from residual melts or from postmagmatic Na-rich fluids.

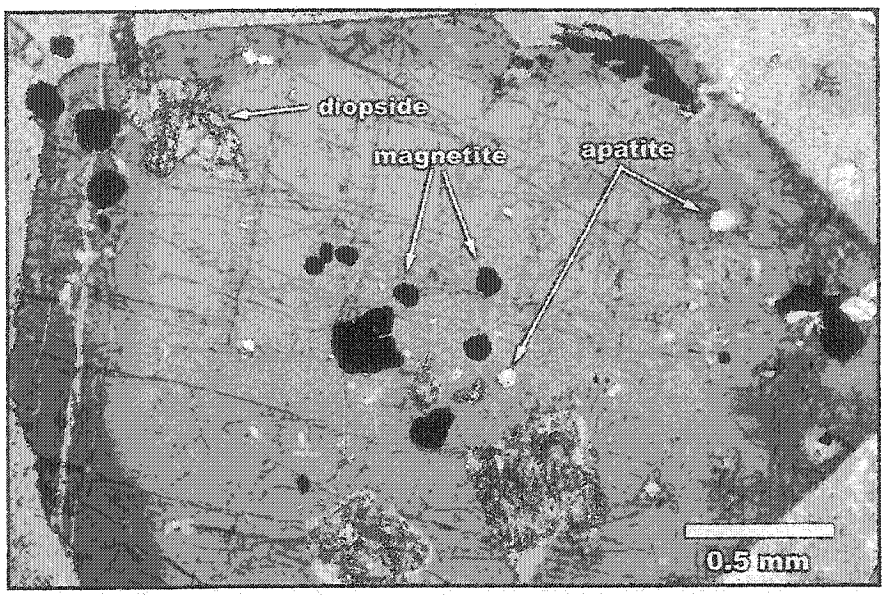

Figure 2.13 Euhedral zoned amphibole crystal containing apatite, diopside and magnetite inclusions. Parallel polars.

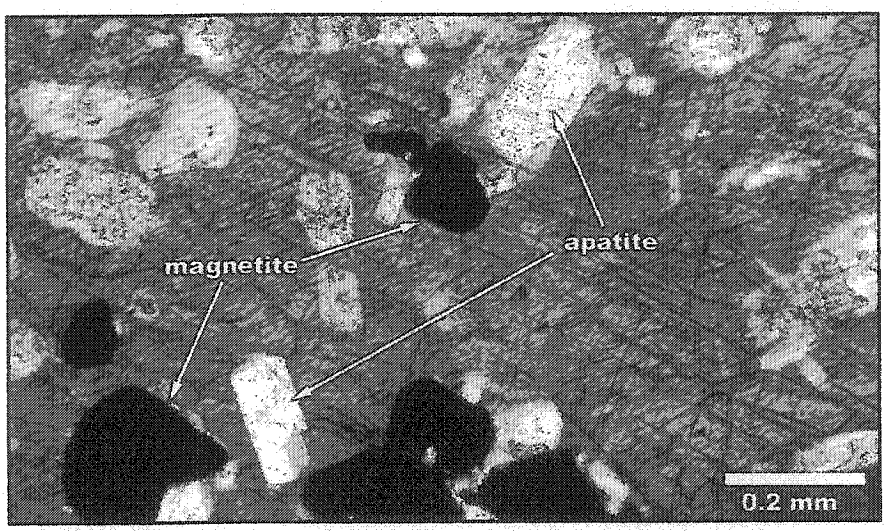

Figure 2.14 Close-up of apatite and magnetite inclusions in an amphibole megacryst. Parallel polars.

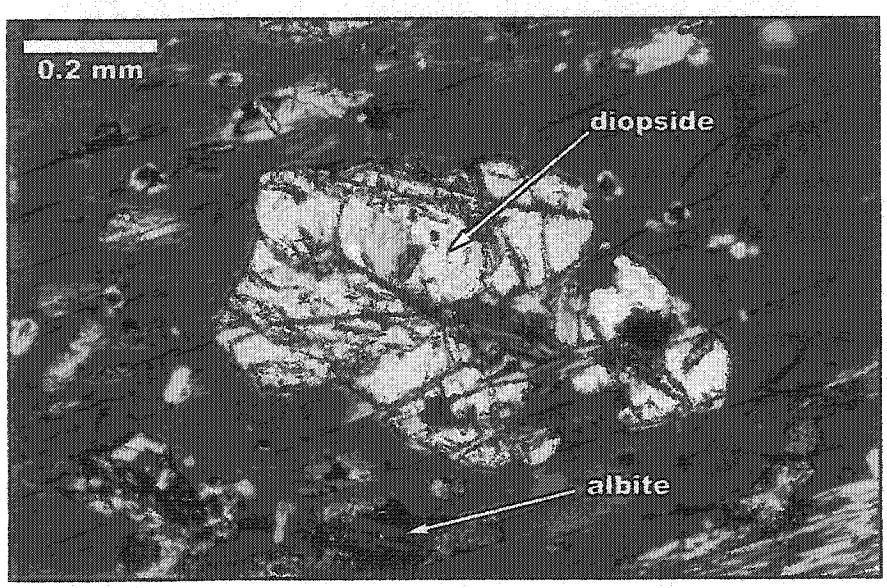

Figure 2.15 Close-up of a diopside and albite inclusion in an amphibole megacryst. Crossed polars.

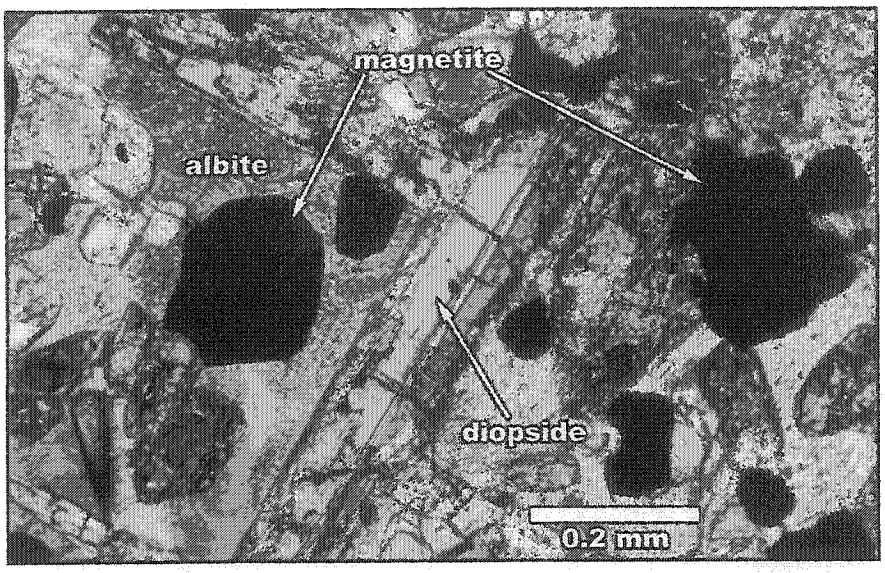

Figure 2.16 Euhedral long-prismatic twinned diopside crystal. Also visible are magnetite crystals and interstitial albite. Crossed polars.

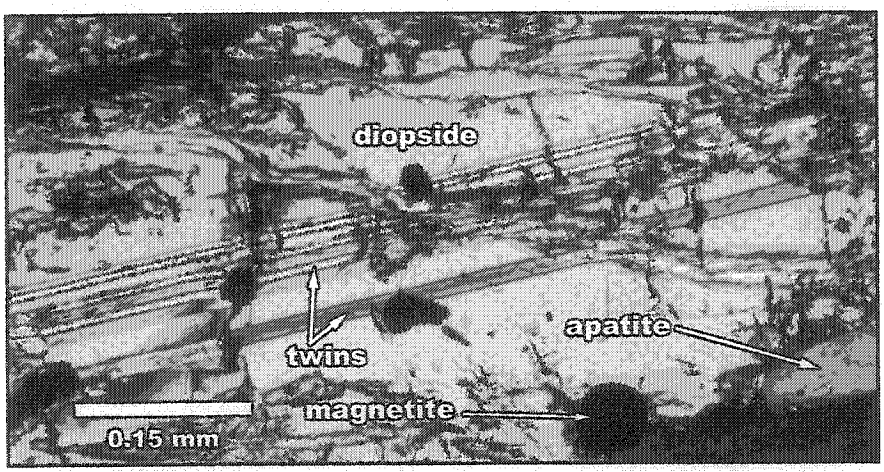

Figure 2.17 Close-up of a twinned diopside crystal containing magnetite inclusions. Crossed polars.

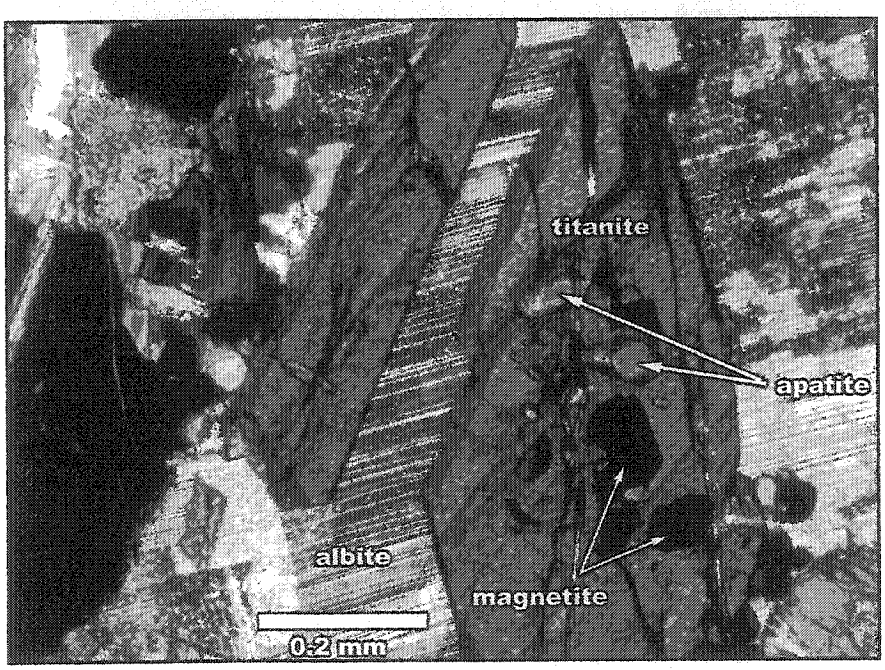

Figure 2.18 Albite-twinned interstitial albite and euhedral titanite containing apatite and magnetite inclusions. Crossed polars.

Magnetite is ubiquitous and is present in high proportions (Table 2.1) making the rock extremely magnetic. Magnetite crystals are usually anhedral to subhedral and 0.1 to 0.4 mm in size. Smaller magnetite crystals are also found as inclusions in megacrystic pargasite and magnesiohastingsite, diopside and titanite crystals (Figure 2.13, 2.14, 2.17 & 2.18). Some magnetite is also intimately associated with chlorite.

Apatite crystals are usually small (0.1-0.3 mm), anhedral to subhedral and ubiquitous. They are also commonly included in the megacrystic amphibole and in titanite crystals (Figure 2.13, 2.14 & 2.18). Titanite is less common but ubiquitous. Titanite crystals display subhedral to euhedral rhombic sections (wedge). The crystals vary in size from 0.4 to 0.8 mm. They commonly contain small magnetite and apatite inclusions (Figure 2.18).

B. Monzodiorite

The monzodiorite unit is the least exposed of the Iris intrusion. It is only found in the southeast corner of the intrusion (Figure 2.3), where it is in sharp contact with the coarse-grained syenite, medium-grained syenite and hornblendite units. The monzodiorite unit is crosscut by the coarse-grained syenite unit and monzonite dykes.

The monzodiorite rock is medium-grained, equigranular and is composed of anhedral black hastingsite, anhedral dark green diopside, anhedral light gray albite and light pinkish-gray perthite (Figure 2.20; Table 2.2). It does not display any major variation in modal composition or texture. The rock is more altered than the hornblendite. Pervasive chloritization is the principal alteration but local epidotization is also common.

Mineral	Modal%
Albite	20-25
Perthite	20-25
Diopside	20-25
Hastingsite	15-20
Chlorite	5-10
Magnetite	5
Epidote	1
Titanite	tr.
Apatite	tr.

Table 2.2 Range of modal composition of the monzodiorite unit.

The principal components of the monzodiorite rock are albite and perthite (Table 2.2). Stained slabs of monzodiorite confirmed that albite is equally or slightly more abundant than perthite.

Under the microscope, albite crystals are anhedral, dark gray to rusty-brown and 0.4 to 0.8 mm in size. Albite twinning was observed in a few of crystals (Figure 2.21). A minor amount of secondary albite was also observed. The secondary albite is anhedral, clear and is commonly rimming turbid albite crystals.

The perthite crystals are anhedral, dark gray and 0.4 to 0.8 mm in size. The high turbidity of the crystals prevented an accurate examination of the exsolution domains but the crystals appear to be composed of 50 to 60 % K-domains. No twinning was visible within the domains.

Diopside crystals are anhedral to subhedral and pale green. They generally do not display pleochroism. Diopside crystals that show basal sections are usually 0.4 to 0.6 mm in size while those with prismatic sections can be up to 1 mm in length (Figure 2.22). Diopside with basal sections is commonly twinned (Figure 2.23) or rimmed by hastingsite (Figure 2.22 & 2.23). Magnetite and apatite are common as inclusions in the diopside.

Hastingsite crystals are anhedral, vary in size from 0.2 to 0.5 mm and display light green to brownish-green pleochroic colors (Figure 2.24). The occurrence of this amphibole, as rims on diopside, suggests that it crystallized late in the crystallization sequence from an H_2O-enriched magma. Larger hastingsite crystals frequently have numerous inclusions of magnetite and apatite, and are often partially altered to chlorite.

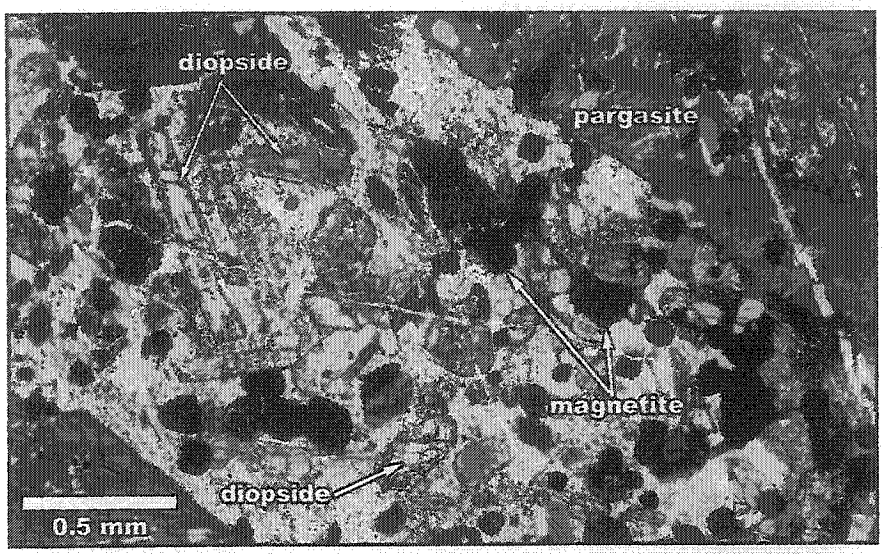

Figure 2.19 Interstitial turbid albite. Also visible are diopside, magnetite, apatite and amphibole crystals. Crossed polars.

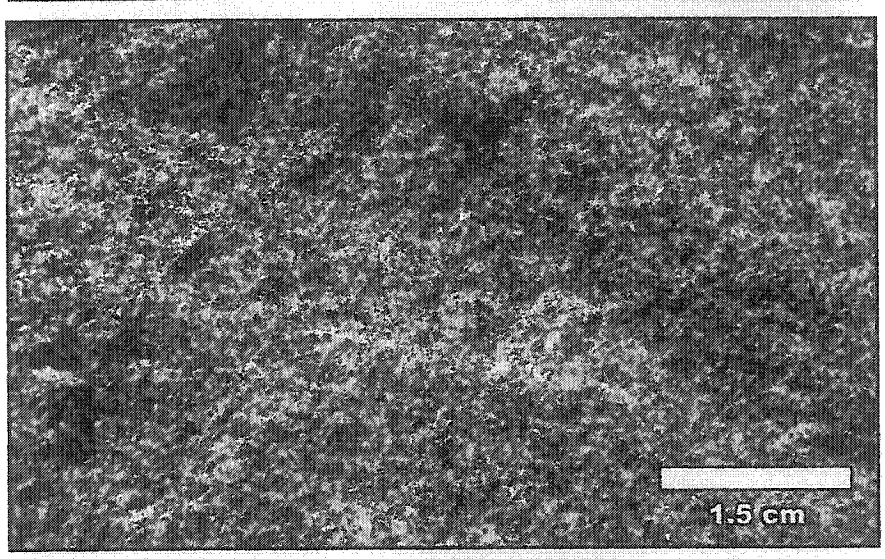

Figure 2.20 Fresh surface of a monzodiorite sample.

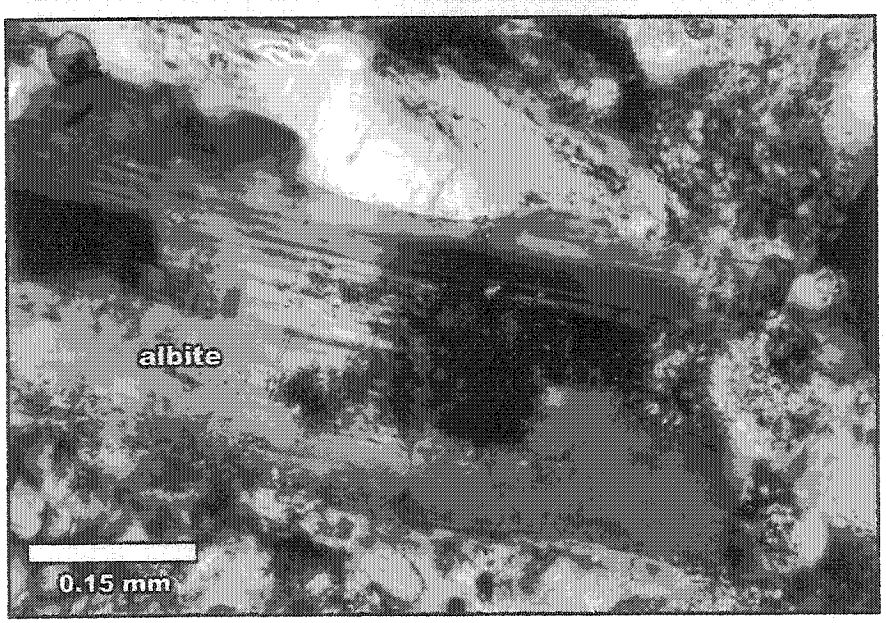

Figure 2.21 Albite- and Carlsbad-twinned albite crystal with a turbid core. Crossed polars.

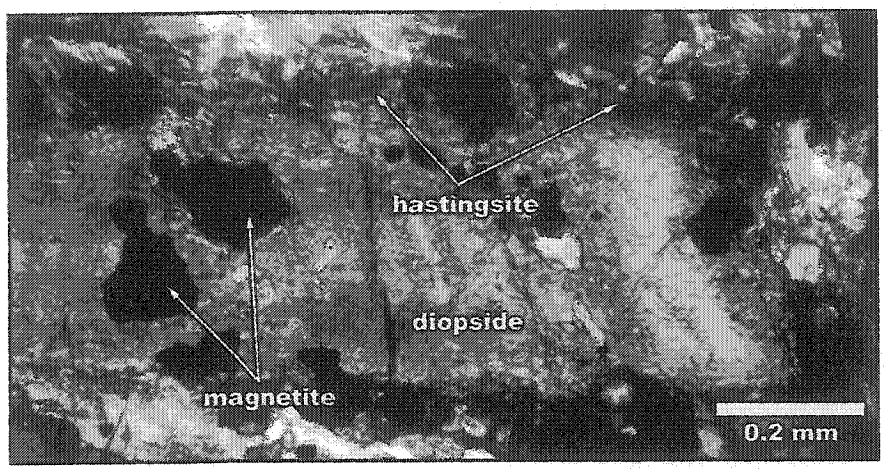

Figure 2.22 Long prismatic diopside crystal rimmed by hastingsite. Magnetite inclusions are visible. Crossed polars.

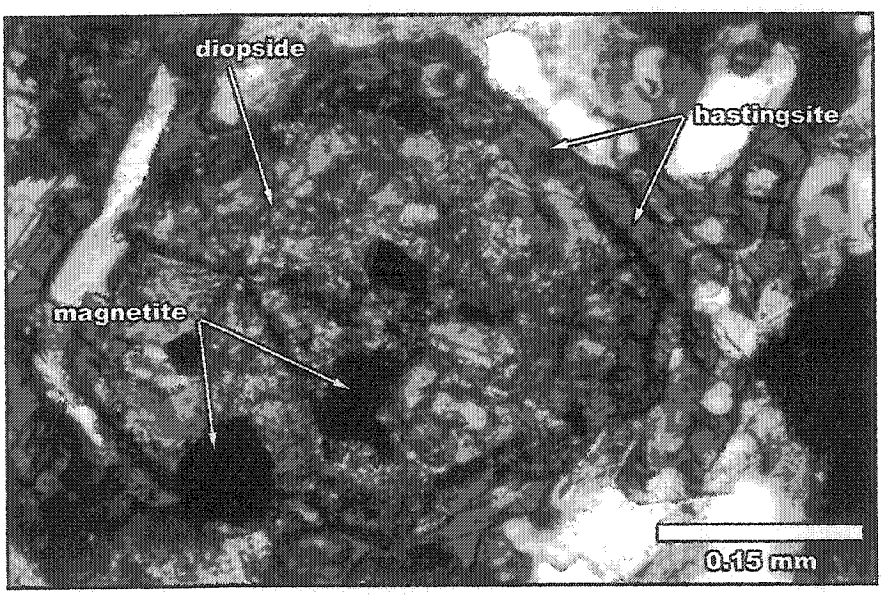

Figure 2.23 Twinned diopside crystal displaying a basal section. The crystal is rimmed by hastingsite. Magnetite inclusions are visible. Crossed polars.

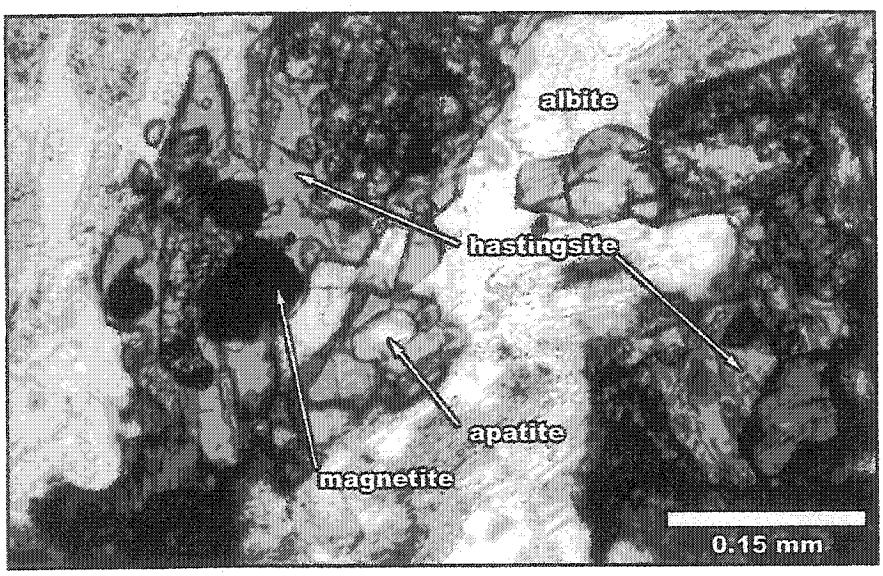

Figure 2.24 Anhedral hastingsite with magnetite and apatite inclusions. Parallel polars.

Magnetite is ubiquitous in the monzodiorite rock. It occurs as small anhedral crystals ranging in size from 0.1 to 0.3 mm. Apatite crystals are usually subhedral to euhedral and 0.1 to 0.2 mm in size. Both magnetite and apatite are commonly included in diopside and hastingsite.

C. Alkali-feldspar quartz-syenite

The alkali-feldspar quartz-syenite unit (hereinafter AF Qz-syenite) is the principal rock unit of the Iris intrusion. It represents about 80 % of the exposed intrusion. Field relationships indicate that the AF Qz-syenite is the latest unit of the intrusion. It is in sharp contact with all the other units except for the alkali-feldspar porphyritic unit where the contact is sharp in some areas and gradational in others.

The AF Qz-syenite is composed of light pink to reddish-pink to sometimes brick red perthite that is commonly zoned and a minor amount of quartz, chlorite and magnetite (Figure 2.25 & 2.26; Table 2.3). This rock displays a hypersolvus feldspar assemblage. Perthite crystals are generally subhedral, tabular and 1 to 3 cm long. Large perthite crystals are often compositionally zoned, displaying white to light gray cores, and alternating pinkish-gray and reddish-pink zones (Figure 2.26). This compositional zoning is readily visible on slabs stained by potassium cobaltinitrate (Figure 2.27) and in thin section (Figure 2.28 & 2.29).

Mineral	Modal%
Perthitic feldspar	85-90
Albite	2-3
Microcline	1-3
Quartz	5
Chlorite	3-5
Magnetite	tr.
Titanite	tr.
Hematite	tr.

Table 2.3 Range of modal composition of the alkali-feldspar quartz-syenite unit.

Under the microscope, the zoning consists of alternating Na- and K-rich zones displaying antiperthitic and perthitic textures respectively (Figure 2.30). Pure albite zones are also common. Cores of the zoned feldspars are commonly composed of albite with good albite twinning.

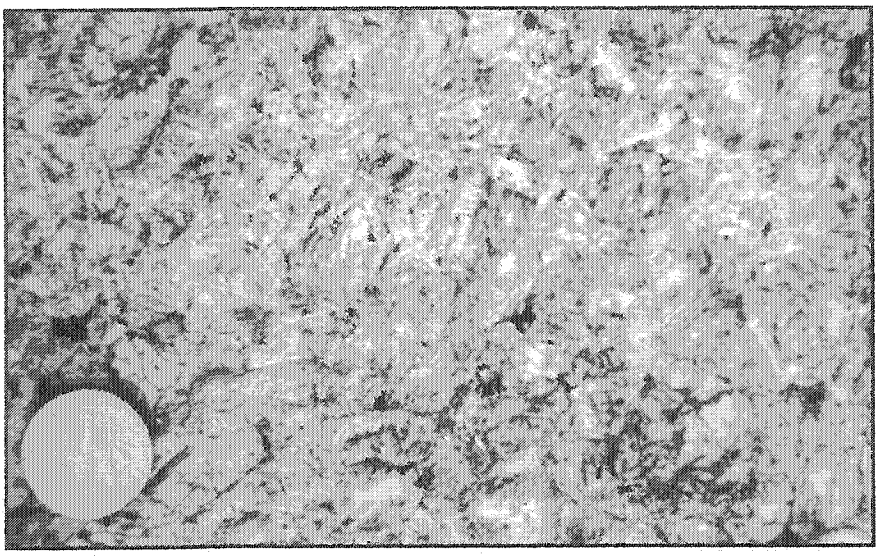

Figure 2.25 Light pink alkali-feldspar quartz-syenite rock.

Figure 2.26 Reddish-pink alkali-feldspar quartz-syenite rock. Zoned perthite crystals are visible.

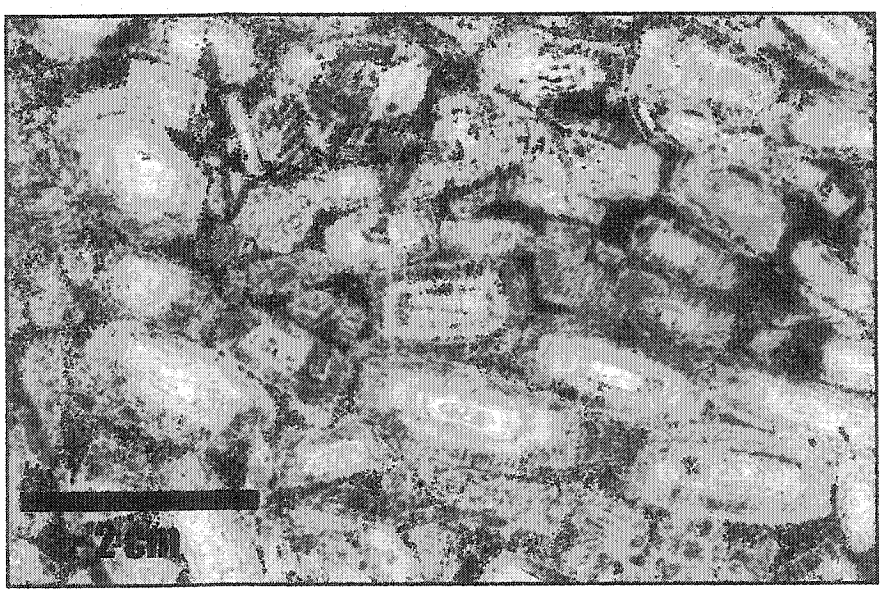

Figure 2.27 Slab of the alkali-feldspar quartz-syenite rock stained by potassium cobaltinitrate in order to identify K-feldspar. Zoning in the perthite crystals is clearly visible. Image courtesy of Dr, Gary Beakhouse, Ontario Geological Survey.

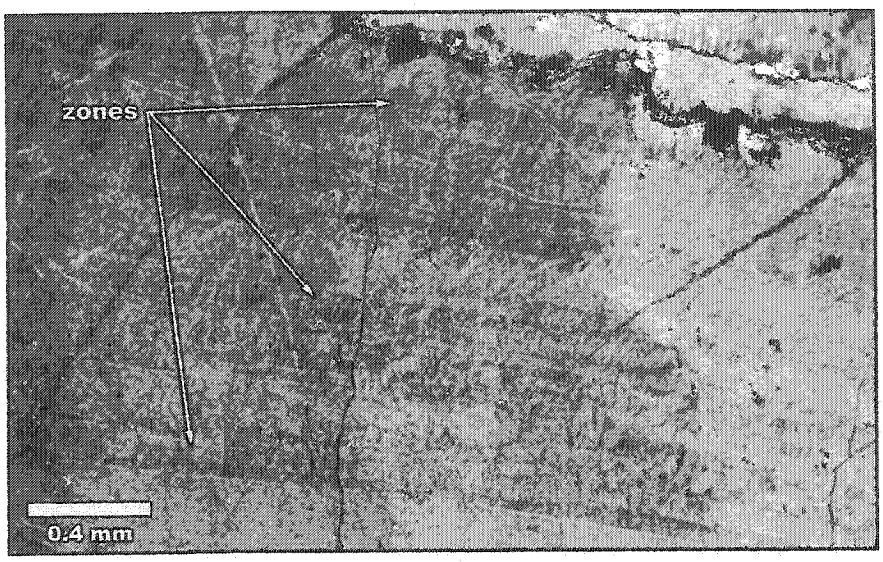

Figure 2.28 Rim of a perthite crystal displaying alternating perthite and antiperthite zones. Crossed polars.

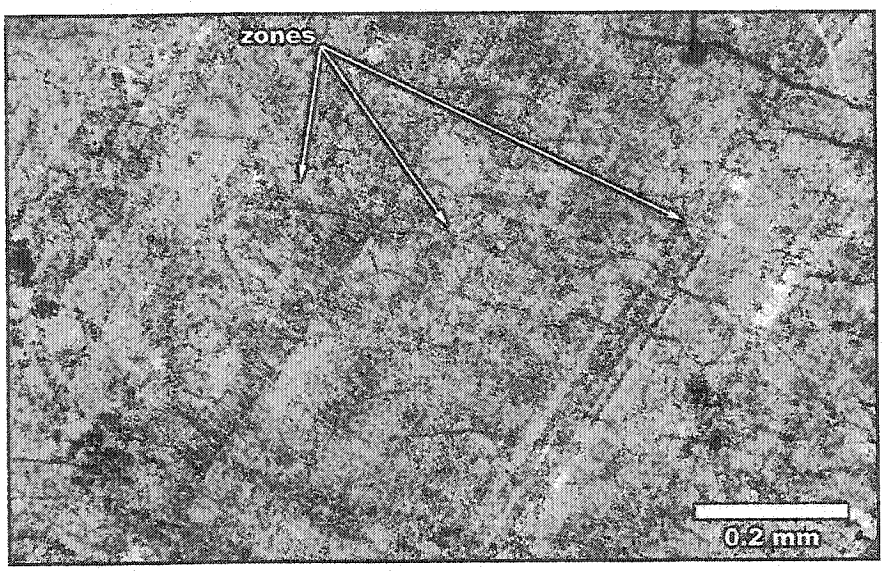

Figure 2.29 Perthite crystal displaying alternating perthite and antiperthite zones. Crossed polars.

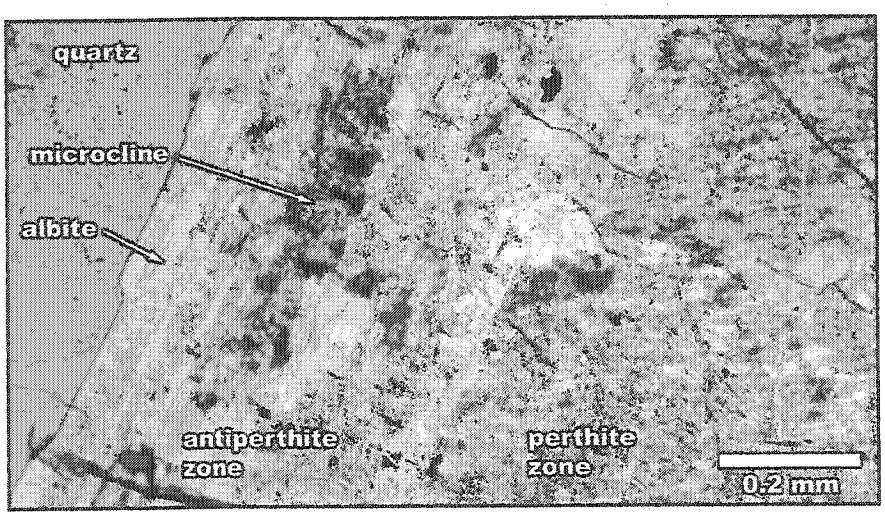

Figure 2.30 Perthite crystal containing antiperthitic and perthitic zones. Crossed polars.

The antiperthitic zones are generally composed of 20 to 30 % K-domains whereas the perthitic domains are usually composed of 50 to 60 % K-domains. Antiperthitic zones are more abundant than the perthitic ones. These observations are consistent with the whole-rock chemistry of the AF Qz-syenite, which is enriched in Na compared to K (Chapter 4 for rock chemistry). Patch perthite (Anderson, 1928) is a common texture in the perthite. Potassium domains commonly display tartan twinning and the Na-domains less frequently display albite twinning. A minor amount of distinct antiperthite grains were identified (Figure 2.31). They are usually composed of 20 to 30 % small tartan twinned K-domains. Film microperthite (Anderson, 1928) is common in small (0.5-1 mm) anhedral unzoned crystals (Figure 2.32). In these crystals, the exsolution domains are usually homogeneously distributed and are 1 to 3 μm thick and 50 to 100 μm long. Because of these characteristics, the film microperthite crystals were good candidates for wide beam electron microprobe analysis. These analyses revealed that K and Na are almost equally abundant in the microperthitic feldspar (Chapter 3 for mineral chemistry). No twinning was optically visible within the individual domains of these crystals. The perthite of the AF Qz-syenite is usually turbid. The intensity of this turbidity is normally a function of the degree of hematization of the rock. In highly hematized samples, the perthite crystals are highly turbid and display a brown to rusty-brown color.

Numerous perthite crystals have irregular and peculiar exsolution textures. One particular microperthitic feldspar crystal is composed of thin albite exsolution lamellae similar to film microperthite. However, the lamellae are not parallel and are producing a strange zigzag texture (Figure 2.33 & 2.34). The change in orientation of the lamellae may be the result of unseen crystal dislocations or twinning. Another strange exsolution texture produces a «cross-hatch like» pattern in a perthitic feldspar crystal (Figure 2.35). In these crystals, the albite exsolution lamellae have two different orientations that intersect at angles of about 60° and 120°. The lamellae have varying thickness and are irregularly shaped. The two sets of lamellae appear to

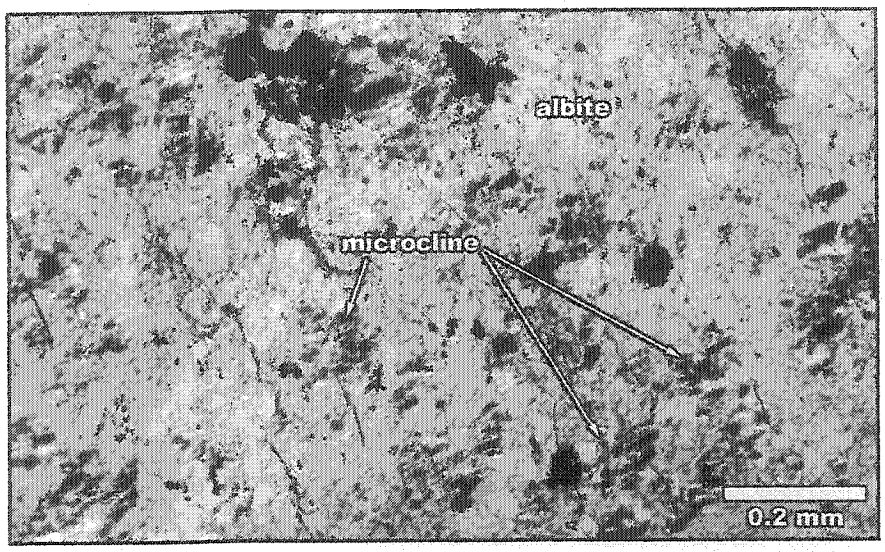

Figure 2.31 Antiperthite crystal with tartan-twinned K-domains. Crossed polars.

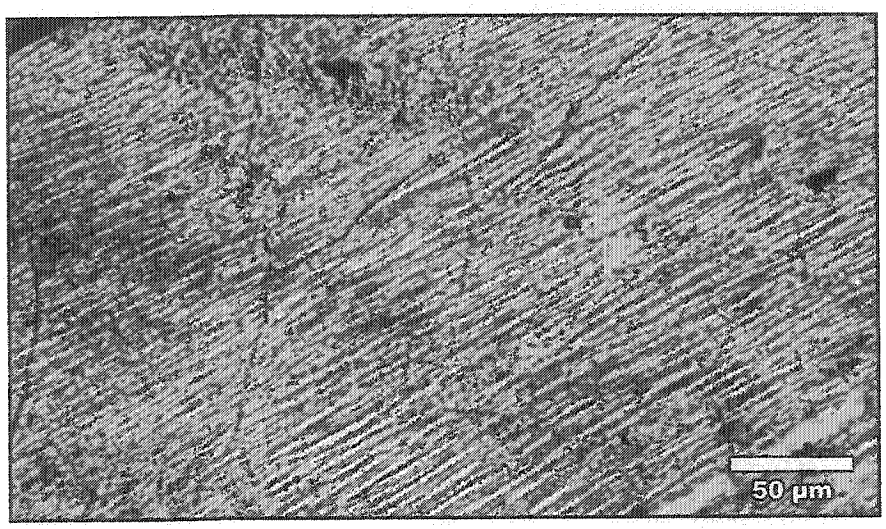

Figure 2.32 Film microperthite crystal. Extinct domains are potassic. Crossed polars.

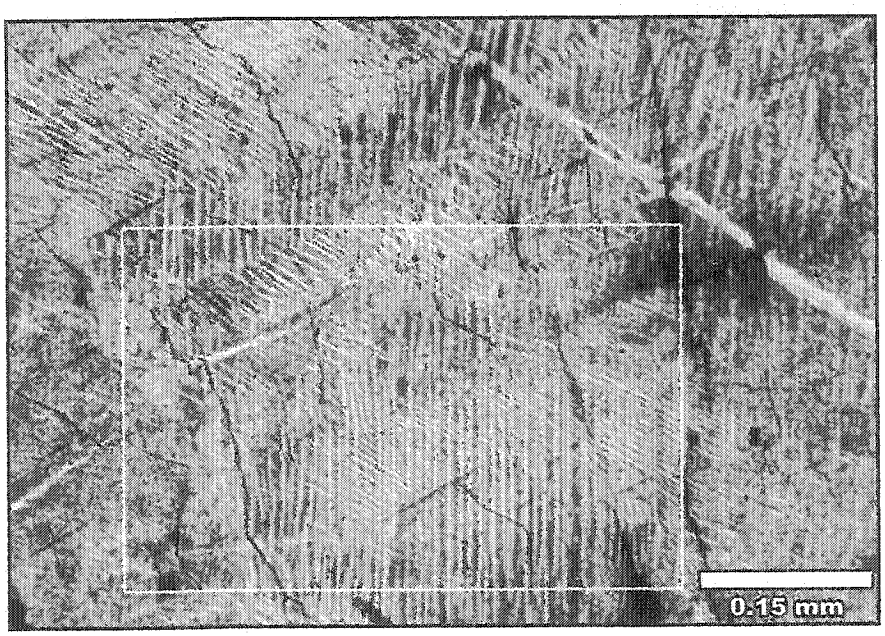

Figure 2.33 Irregular exsolution texture in a perthite crystal. See text for description. A close-up view of the area within the rectangle is available in the next figure. Crossed polars.

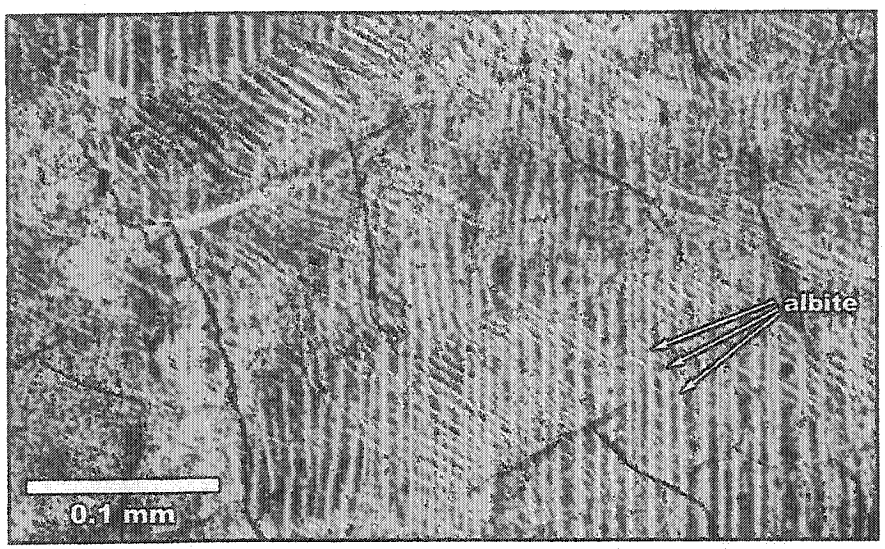

Figure 2.34 Close-up view of the previous figure. See text for description. Crossed polars.

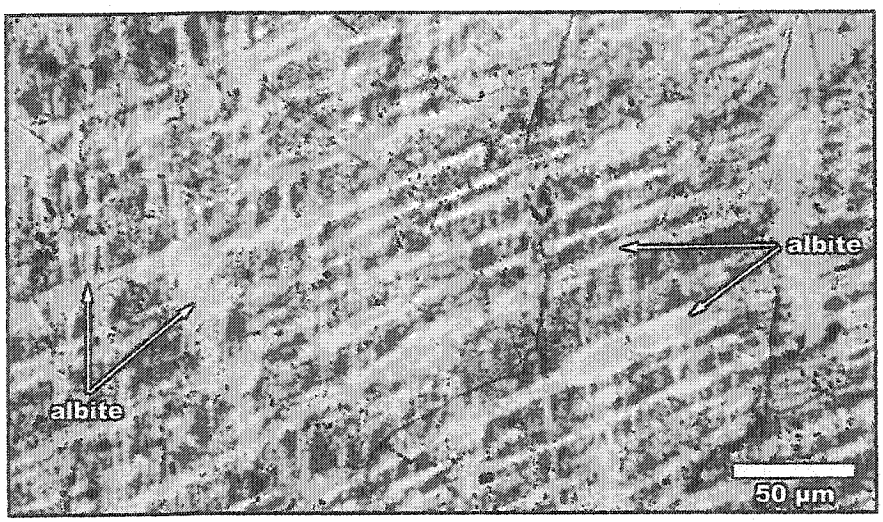

Figure 2.35 Irregular exsolution texture in a perthite crystal producing a «cross-hatch like» pattern. This texture may result from an extreme coarsening of a braid perthite. Crossed polars.

react at their intersection points, suturing the lamellae together. This texture may result from an extreme coarsening of braid perthite. Grain-boundary interactions commonly occur between perthitic feldspar crystals. The most common interaction is the «swapped rims» type (Voll, 1960), in which grain-boundary migration occurs producing a concentration of albite-rich phase forming complex sutured or interlocking grain boundaries (Smith & Brown, 1988; Figure 2.36 & 2.37). This texture is considered to result from the late-stage action of water on high-angle grain-boundary migration of albite exsolved from pertithic feldspars (Parsons, 1980).

Albitization is common in the AF Qz-syenite. In fact, most antiperthite crystals are likely the result of this type of alteration. Evidence supporting this is visible in Figures 2.30 and 2.31 where the irregular shapes of K-domains produce a texture similar to patch perthite. This probably results from extensive replacement of perthite by albite during alteration; leaving only small irregular zones of the original grain. Albite-filled fractures within crystals and clear albite rims on perthite and antiperthite crystals are also taken as evidence for late albitization.

The AF Qz-syenite also contains a minor amount of anhedral light gray interstitial quartz, chlorite, hematite and pyrite (Table 2.3). Chlorite and hematite are more abundant in zones where they are interstitial to the perthitic feldspar crystal. Hematite is also probably responsible for the common turbid nature of most of the perthitic feldspar. Pyrite is disseminated through the rock; it is however slightly enriched in localized zones.

Field observations

Numerous shallow-dipping quartz veins and more steeply dipping cataclastic gouge or quartz filled fracture systems crosscut the AF Qz-syenite. Quartz veins are usually striking south-southwest and dip from 30° to 45° (Figure 2.38). Their thickness varies from 1 to 30 cm and are commonly 15 to 40 m long. Scheelite-bearing quartz veins have been reported (Hawke, 1993)

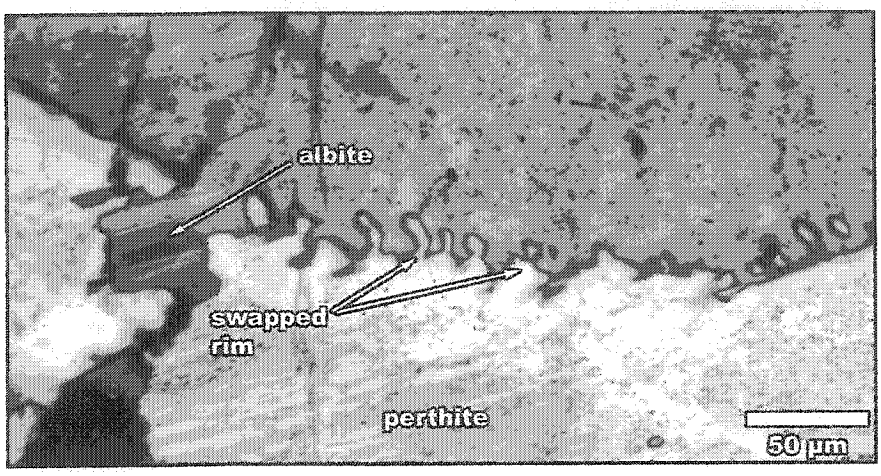

Figure 2.36 Swapped-rim texture at the boundary of two perthite grains. Crossed polars.

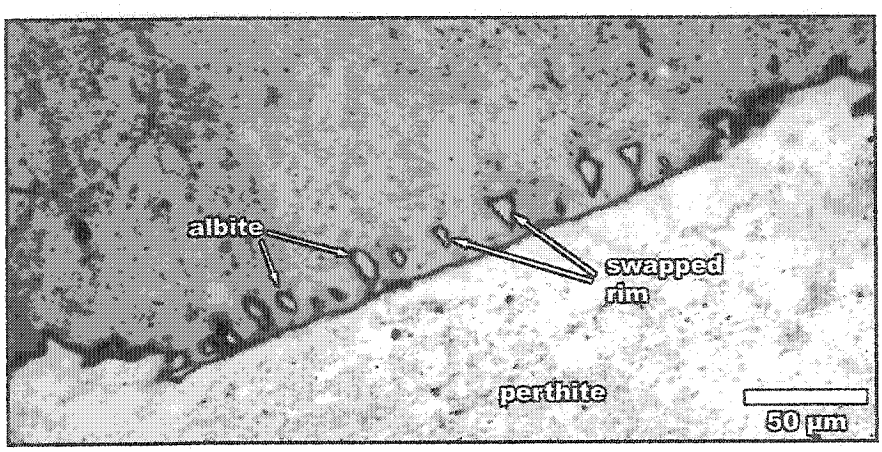

Figure 2.37 Swapped-rim texture at the boundary of two perthite grains. Crossed polars.

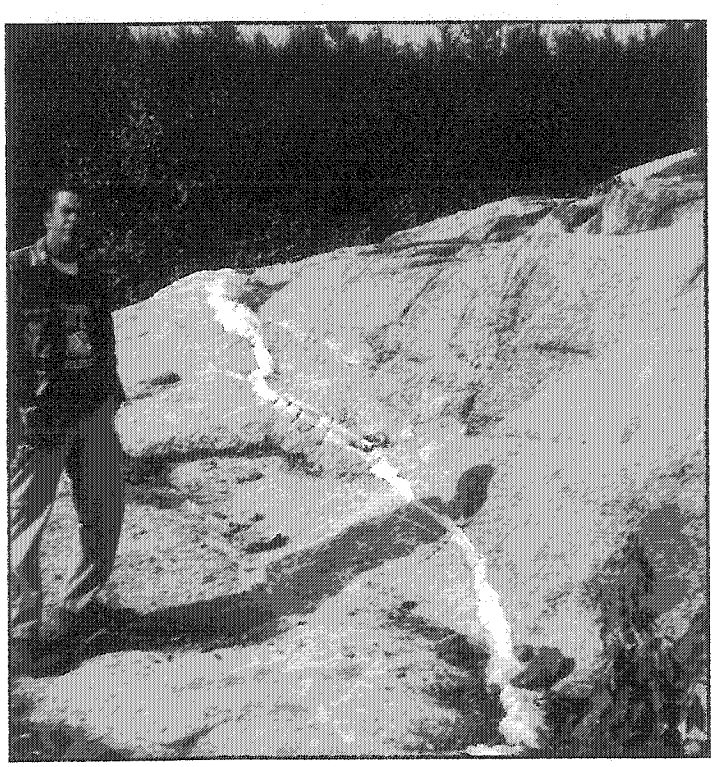

Figure 2.38 Shallow-dipping quartz vein cross-cutting the alkali-feldspar quartz-syenite.

but were not observed by the author. The fracture systems are more widely distributed than the quartz veins. They are usually 5 to 10 m wide and contain numerous large-scale parallel quartz- and/or gouge-filled fractures (Figure 2.39) and small-scale gouge-filled fractures (Figure 2.40). The large-scale fractures are generally 2 to 6 cm thick and 2 to 20 m long but one large gouge-filled fracture is at least 200 meters long. The small-scale fractures are characterized by very small (often less than 1 mm) gouge-filled fractures that cross-cut individual feldspar crystals (Figure 2.40). Three general orientations of fracture systems were identified, however, only one of them is widespread and present at large scale. The more common fracture system is usually striking northwest and dipping between 55° to 70° (Figure 2.39).

The AF Qz-syenite unit exhibits local compositional and textural variations. These variations are usually present as zones of varying size and shape (15 cm to several metres). The most common of these zones are composed of a varying amount (5-10 %) of interstitial dark green to black mixture of chlorite and hematite (Figure 2.41), although one particular zone is enriched in interstitial material compared to the others (Figure 2.42). For the purpose of identification, these zones were labeled during field work as IMS («interstitial mafic segregation») however no genetic interpretations are implied. IMS zones are distributed throughout the unit with no apparent preferential location. The perthite crystals of one large IMS zone are aligned, forming a trachytic texture interpreted to result from primary magmatic flow alignment (Figure 2.43). Perthite crystal alignment is also common in the «regular» syenite.

Pyrite-rich zones are also common in the AF Qz-syenite unit. These irregular-shaped zones vary in size from 1 to 10 m and are found throughout the unit. The larger zones appear to be more common on the southern side of the exposed intrusion. The pyrite zones are characterized by a higher concentration (2-4 %) of subhedral to euhedral interstitial pyrite (Figure 2.44). Most

Figure 2.39 Parallel quartz-filled cataclastic fractures cross-cutting the alkali-feldspar quartz-syenite.

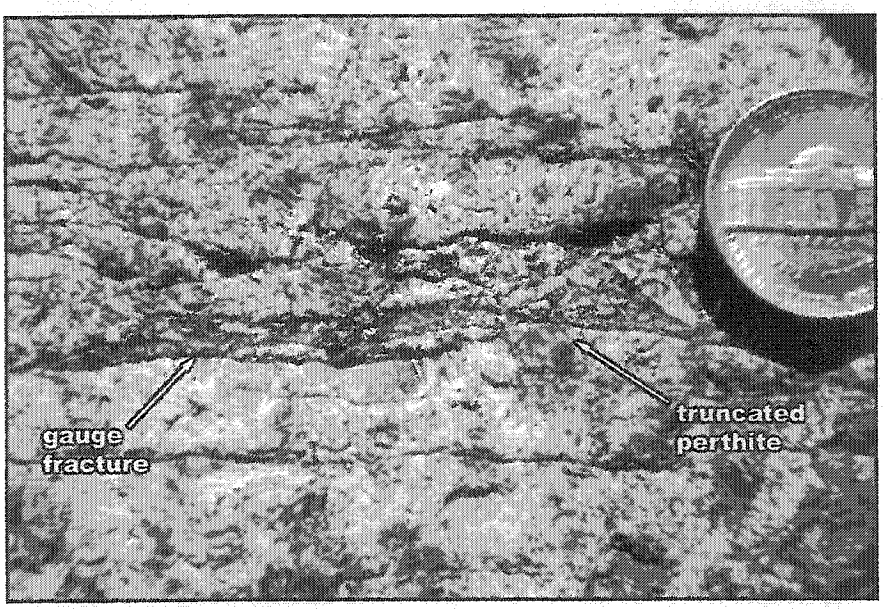

Figure 2.40 Small scale gauge-filled cataclastic fractures cross-cutting individual perthite crystals.

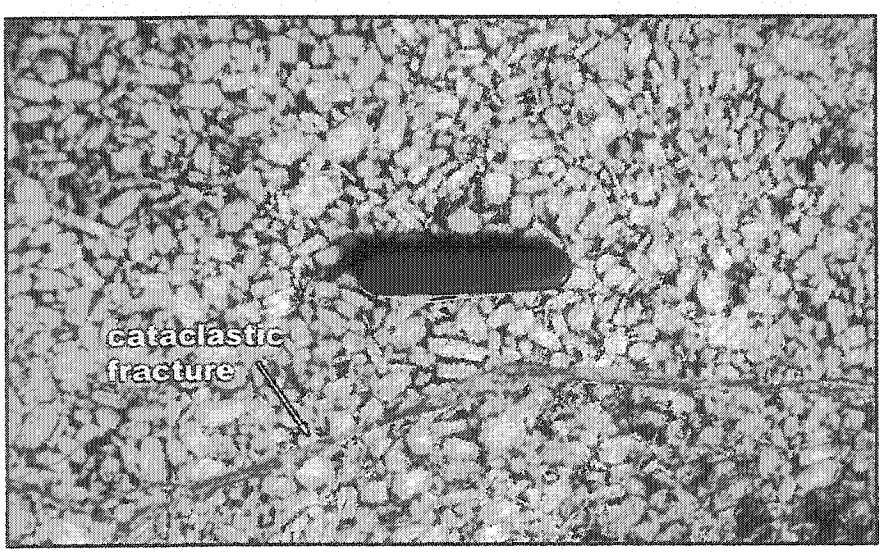

Figure 2.41 Zone composed of an increased proportion of interstitial chlorite and hematite.

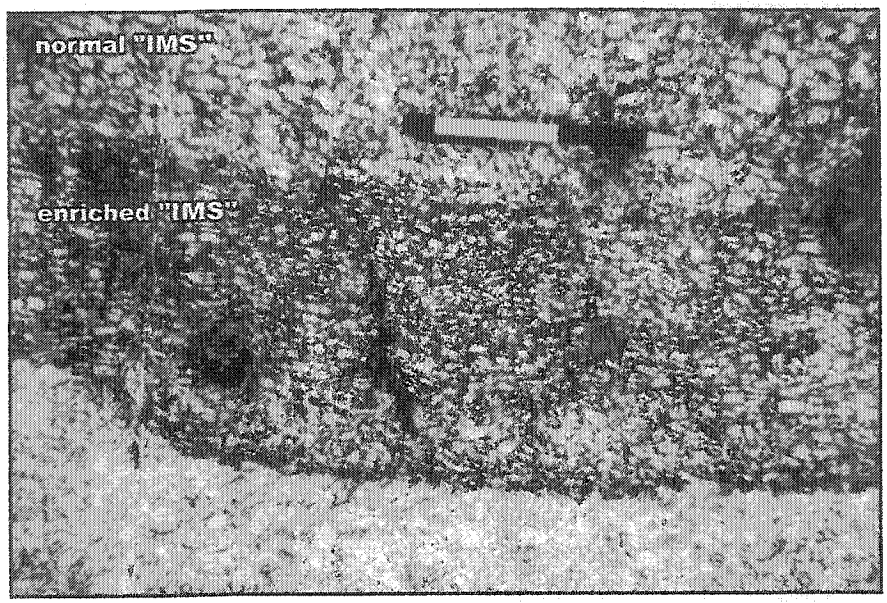

Figure 2.42 Zone composed of an increased proportion of interstitial chlorite and hematite. Primary (magmatic) crystal alignment is also visible in the more mafic zone.

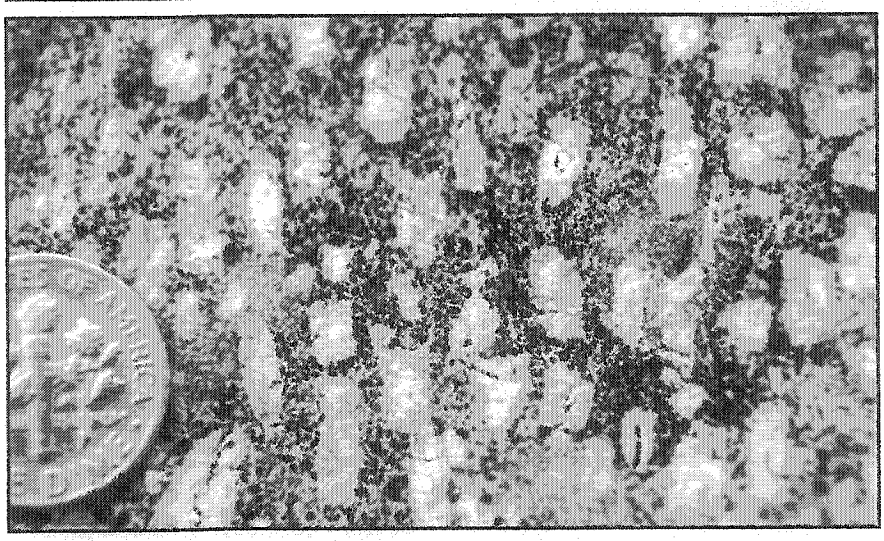

Figure 2.43 Primary (magmatic) alignment of perthite crystals.

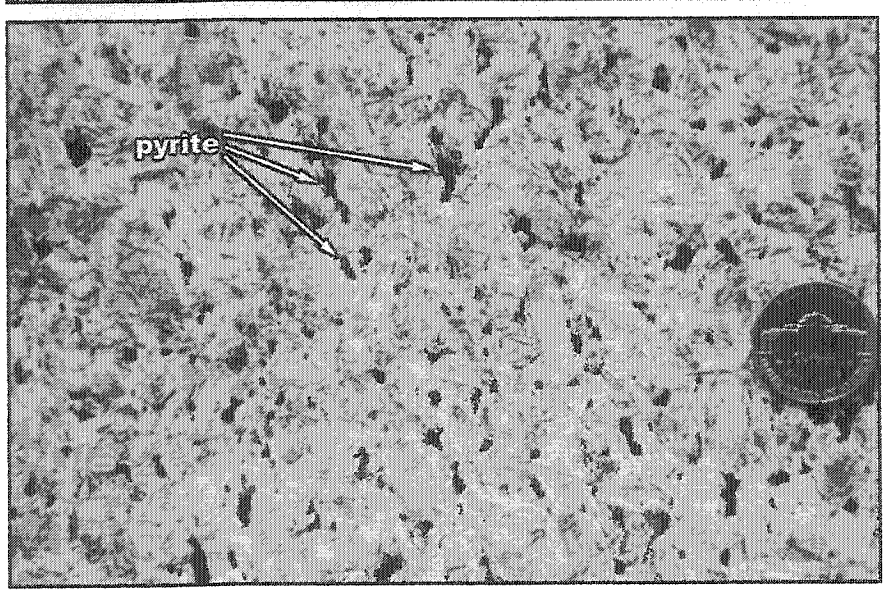

Figure 2.44 Zone containing an increased proportion of interstitial pyrite.

pyrite-rich zones are easily identifiable on the outcrop since they have a rusty-orange weathering color (Figure 2.45).

Color variations within the unit are common. The rock is usually light pink colored (Figure 2.25) but darker shades of pink and reddish-pink are common (Figure 2.26). These color variations reflect the intensity of hematization of the AF Qz-syenite unit.

D. Alkali-feldspar porphyritic syenite

The alkali-feldspar porphyritic syenite (hereinafter AFP syenite) unit is found only in the northeast section of the intrusion (Figure 2.3). The unit is both in sharp and gradational contact with the AF Qz-syenite, and is crosscut by the same quartz veins and fracture systems described in the AF Qz-syenite.

Mineral	Modal%
Alkali-feldpsar megacrysts	40-50
Albite	30-40
Perthitic feldspar	10
Quartz	3-5
Chlorite	3-5
Microcline	tr.
Magnetite	tr.
Pyrite	tr.
Secondary calcite	tr.

Table 2.4 Range of modal composition of the alkali-feldspar porphyritic syenite unit.

The AFP syenite is usually composed of 0.8 to 2.5 cm long subhedral tabular perthitic feldspar phenocrysts that are hosted in a medium-grained matrix of anhedral to subhedral pinkish-gray albite, anhedral pink perthitic feldspar and a minor amount of quartz and chlorite (Figure 2.46; Table 2.4).

The perthite megacrysts are commonly zoned. The zoning is clearly visible in hand samples and is characterized by alternating pinkish-gray and reddish-pink zones with gray to pinkish-gray cores. Staining revealed that the pinkish-gray zones were sodic and that the darker reddish-pink zones are more potassic.

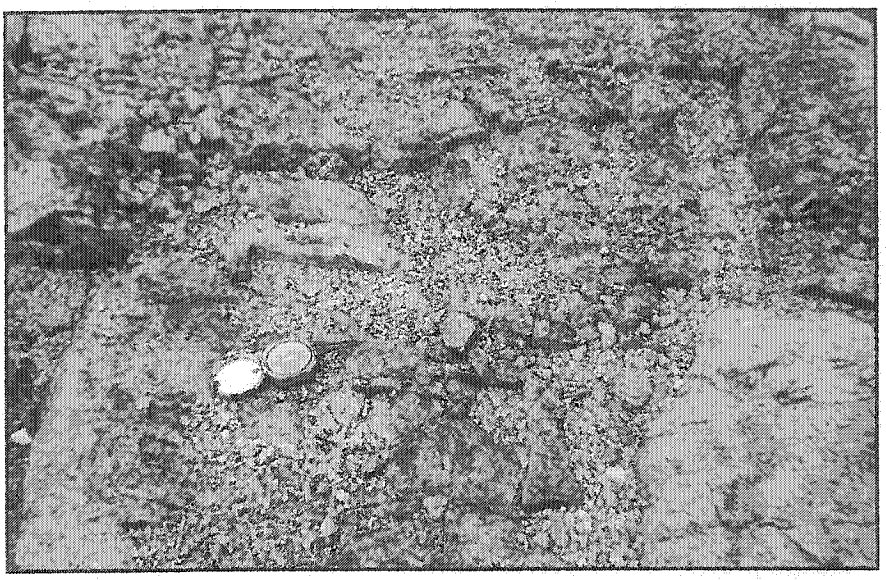

Figure 2.45 Characteristic rusty color of pyrite-rich zone.

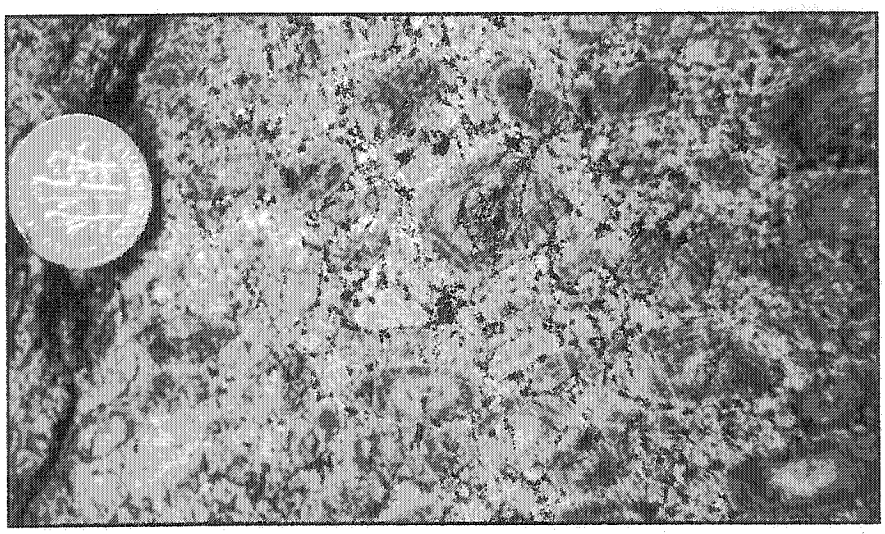

Figure 2.46 Alkali-feldspar porphyritic syenite rock. Perthite megacrysts are commonly zoned.

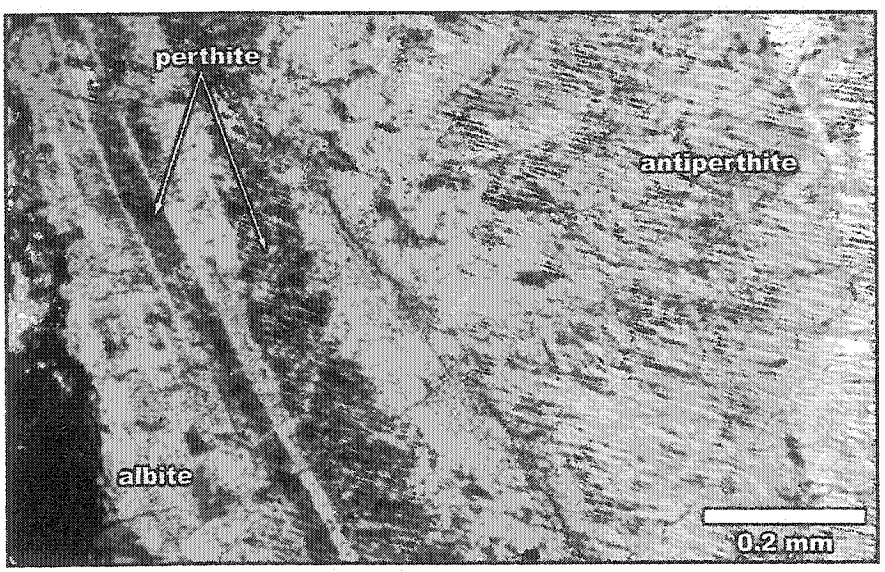

Figure 2.47 A perthite megacryst composed of a sodic antiperthitic core and a thinly zoned rim of perthite and albite. Crossed polars.

Cores of the megacrysts are composed of antiperthite displaying a texture similar to film microperthite (Anderson, 1928; Figure 2.47). The antiperthite cores are contain 70 to 80 % Na-domains that are slightly turbid. The Na-domains are thicker (6-30 μm) than the K-domains (1-5 μm). The potassic and sodic domains do not display any visible twinning. The rims of the megacrysts contain two types of zones: Na-rich and K-rich. The Na-rich zones are composed of albite with a minor amount of exsolved K-domains ($\sim$5 %) and have irregular thickness that can vary from 50 to 250 μm. The K-rich zones are composed of perthite and are smaller than the albite zones with thickness between 40 to 120 μm. Perthite from these zones contains 20 to 30 % Na-domains that commonly display film microperthite texture (Anderson, 1928). Fine scale exsolution textures of the perthite zones are however commonly masked by intense hematization.

In one particular sample (LMP-116), some megacrysts are composed of albite. These megacrysts are the same size and shape as the perthite megacrysts. They display good albite and Carlsbad twinning (Figure 2.48). All the albite megacrysts have oscillatory extinction and high turbidity. These megacrysts are likely completely albitized perthite megacrysts.

The matrix of the AFP syenite is principally composed of albite and perthite. Matrix perthite crystals are generally anhedral to subhedral and 0.5 to 1.5 mm in size. They are commonly zoned and highly turbid (Figure 2.49). The zoned crystals have a highly turbid and often altered perthitic feldspar core surrounded by zones of albite and perthitic to antiperthitic feldspar (Figure 2.50). The bulk composition is however generally Na enriched. The crystals sometimes display Carlsbad twinning. Albite is the most common mineral in the matrix. The crystals are anhedral, 0.5 to 1 mm in size and are always turbid. They commonly display albite and Carlsbad twinning. Larger (1-4 mm) subhedral to euhedral elongated rectangular crystals are also present. They are, however, less common than the anhedral albite. These crystals are generally highly turbid (Figure 2.51) and contain numerous inclusions of hematite and white mica. The crystals

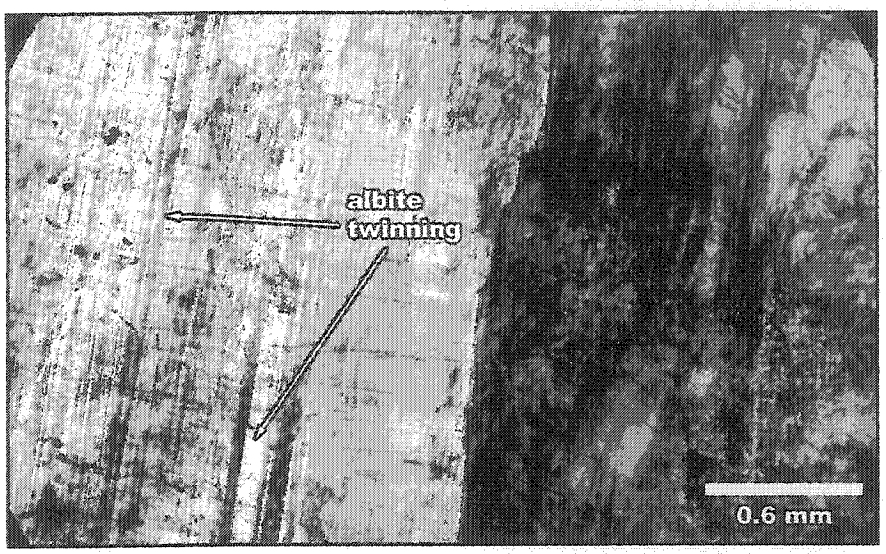

Figure 2.48 Albite megacryst from the alkali-feldspar porphyritic syenite. This crystal displays albite and Carlsbad twinning. Crossed polars.

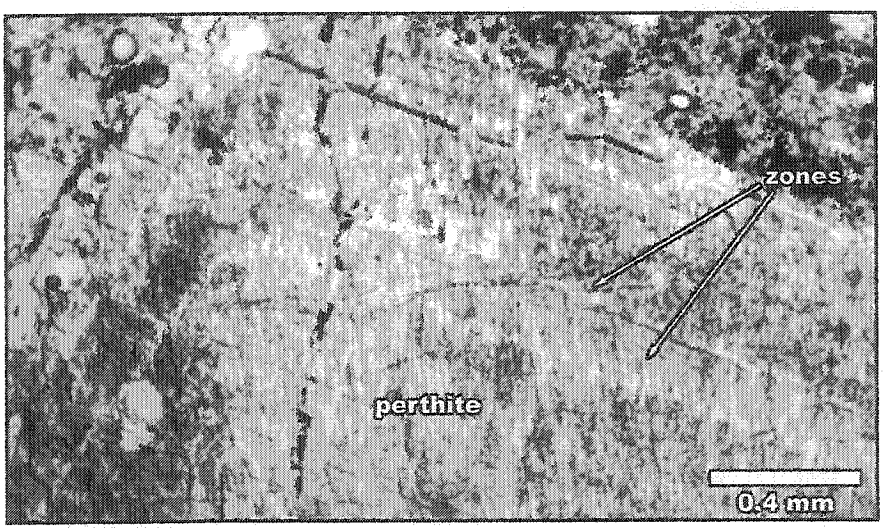

Figure 2.49 Turbid perthite crystal displaying compositional zoning. Arrows point toward Na-rich zones. Parallel polars.

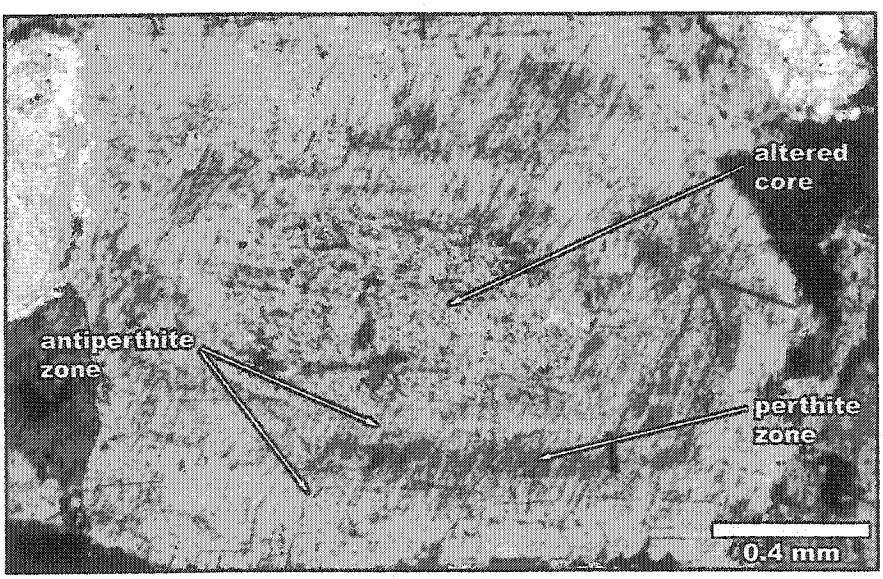

Figure 2.50 Matrix perthite with a highly turbid core and alternating perthite and anti-perthite zones. Crossed polars.

usually display good albite and Carlsbad twinning. A layer of clear albite is commonly rimming the turbid crystals (Figure 2.51).

The matrix also contains a minor amount of chlorite, magnetite, microcline, pyrite and quartz (Table 2.4). Chlorite and magnetite are anhedral, 0.2 to 0.4 mm in size and are usually closely associated. Microcline crystals are anhedral, 1 to 2 mm in size and display tartan twinning.

E. Antiperthite syenite

The medium-grained antiperthite syenite unit (hereinafter called A-syenite) is located on the southwestern margin of the Iris intrusion in sharp contact with the main coarse-grained quartz-syenite unit (Figure 2.52). Numerous sub-angular to sub-rounded xenoliths of basalt, hornblendite and monzodiorite were found in this unit, indicating that the medium-grained syenite postdates the two mafic units of the intrusion. The abundance and size of xenoliths is highest near contacts (Figure 2.53) and decreases with distance away from the contacts (Figure 2.54). A few xenoliths of the A-syenite were identified in the AF Qz-syenite.

Mineral	Modal%
Antiperthitic feldspar	50-65
Albite	30-45
Chlorite	4-5
Magnetite	1
Secondary calcite	tr.
Apatite	tr.
Muscovite	tr.
Quartz	tr.
Titanite	tr.

Table 2.5 Range of modal composition of the antiperthite syenite unit.

The rock is composed of 1-3 mm long, pinkish-gray to light pink anhedral to subhedral albite and antiperthite crystals forming a matrix that is hosting 10 to 15 % larger phenocrysts composed of subhedral to euhedral, 4 to 6 mm long, albite and antiperthite (Figure 2.55; Table 2.5). In this rock, the larger phenocrysts have the same composition and texture as the albite to antiperthitic feldspar

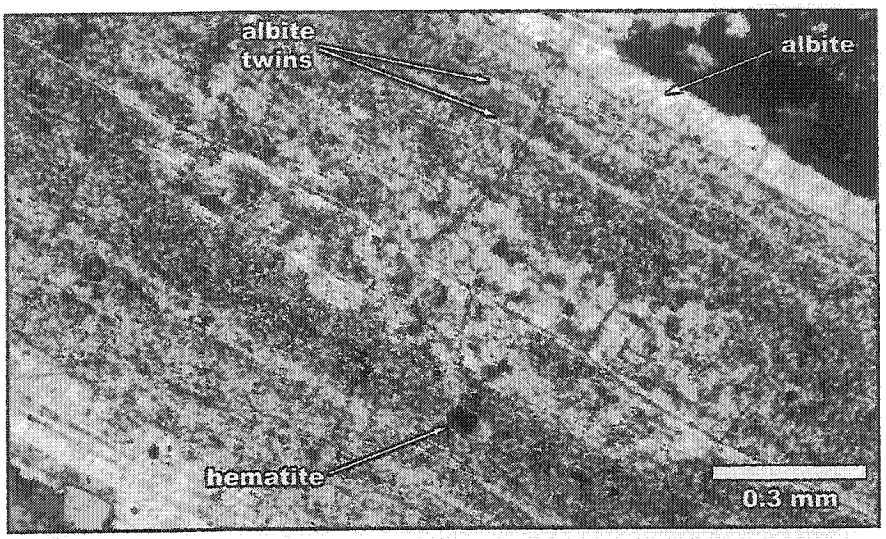

Figure 2.51 Highly turbid elongated rectangular albite crystal from the alkali-feldspar porphyritic syenite. It contains numerous white mica and hematite inclusions. Clear late-magmatic albite is rimming the turbid crystal. Crossed polars.

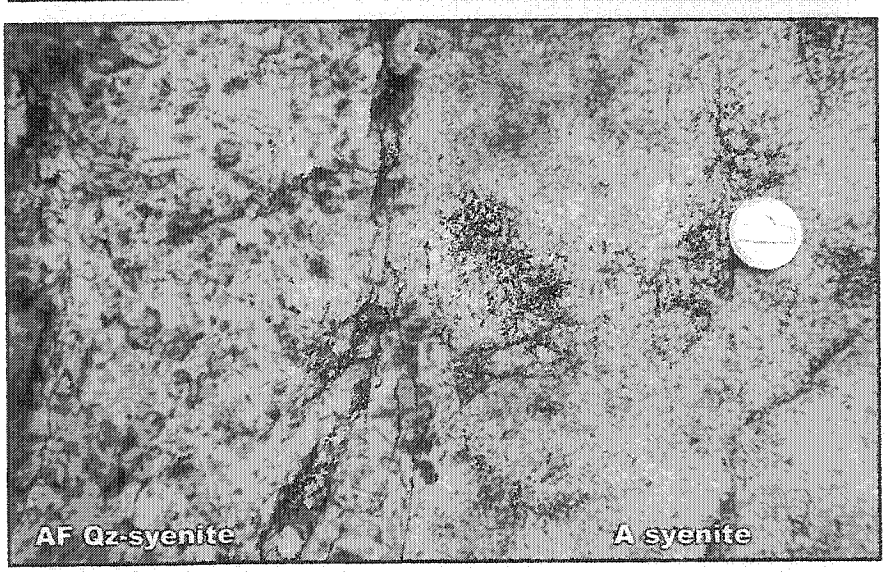

Figure 2.52 Sharp contact between the alkali-feldspar quartz-syenite and antiperthite syenite units.

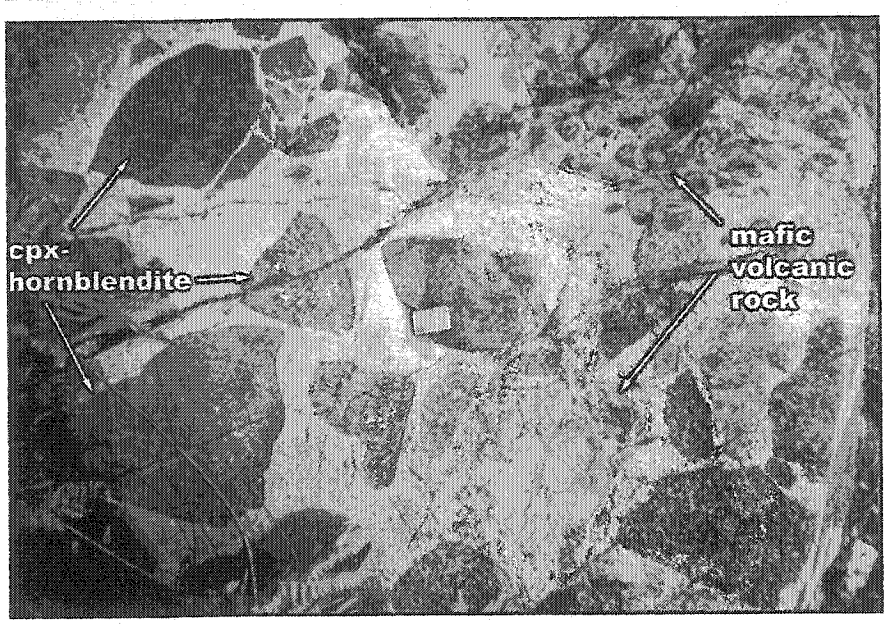

Figure 2.53 The antiperthite syenite contains large sub-angular xenoliths of mafic volcanic and pyroxene-bearing hornblendite rocks. The size and abundance of these xenoliths decreases with increasing distance from the geological contact. This image was taken only a few metres away from the contact between the antiperthite syenite and the pyroxene-bearing hornblendite.

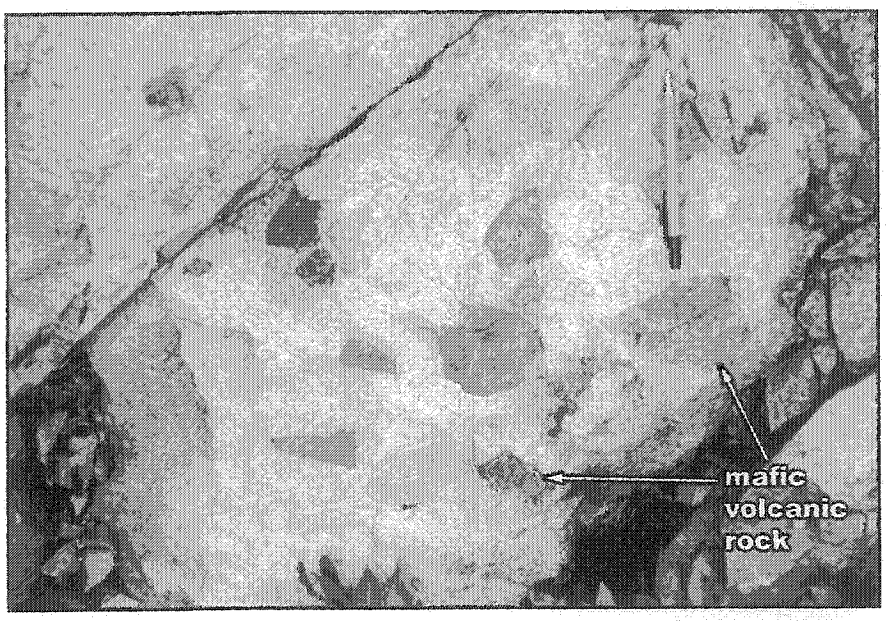

Figure 2.54 Mafic volcanic rock xenoliths found in the antiperthite syenite unit. This image was taken several metres away from the contact between the antiperthite syenite and the surrounding mafic volcanic country rocks.

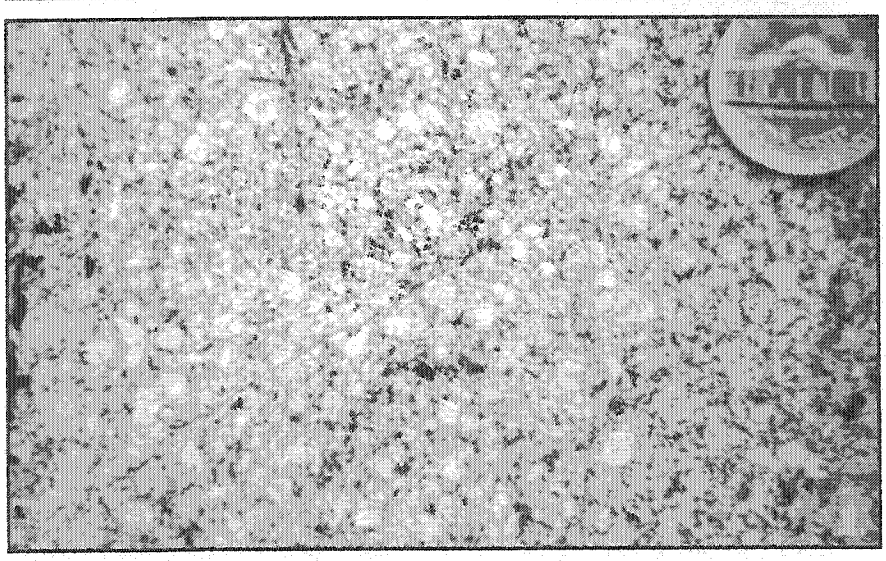

Figure 2.55 Close-up of the antiperthite syenite rock. Antiperthite phenocrysts are light pinkish-gray color.

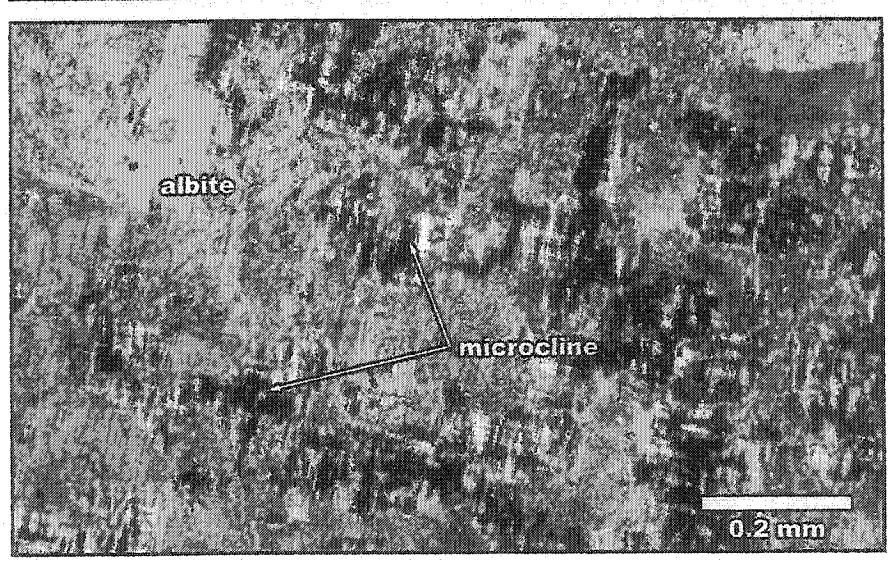

Figure 2.56 Antiperthite crystal displaying tartan-twinned K-domains. The K-domains are producing a texture similar to patch perthite. Crossed polars.

crystals (except size and shape) forming the matrix. Therefore, the following description applies for both phenocrysts and matrix.

The antiperthite crystals are composed of 20 to 30 % K-domains forming a texture similar to patch perthite (Anderson, 1928; Figure 2.56). Potassic domains generally display good tartan twinning (Figure 2.56 & 2.57) and are irregularly shaped and distributed within the crystals (Figure 2.57). However, in some cases, the exsolved K-domains are more abundant in zones of some antiperthite crystals (Figure 2.58). Antiperthitic feldspar crystals are commonly zoned. The zoning generally consists of a highly turbid antiperthite core and a less turbid albite-twinned rim that is almost entirely composed of albite (Figure 2.59). More complex zoning also occurs in antiperthitic feldspar crystals (Figure 2.58 & 2.60). These crystals contain an antiperthitic feldspar core surrounded by alternating K-rich and Na-rich zones. The K-rich zones contain a higher density of potassic exsolution domains whereas the Na-rich zones are either composed of pure albite or antiperthite. Anthiperthite crystals are usually highly turbid, giving them a dark brown color under parallel polars. Clear to lightly turbid albite commonly rims the turbid crystals. White mica alteration patches are also common in the cores of zoned antiperthitic feldspar crystals. As discussed in the AF Qz-syenite section, most antiperthite crystals are likely albitized perthite. Irregular patchy textures such as in Figures 2.56, 2.57 and 2.59 support this interpretation.

Albite is generally less abundant than the antiperthitic feldspar (Table 2.5). Albite textures are similar than the antiperthitic feldspar crystals. Matrix albite usually occurs as anhedral crystals whereas phenocrystic albite occurs as subhedral to euhedral crystals. Albite phenocrysts are usually rectangular shaped with a long axis reaching up to 6 mm in length. Albite crystals display good albite twinning and are also commonly Carlsbad twinned. Zoning is sometimes visible within large albite crystals. In these crystals, the zoning is usually the results of variations in

the intensity of the turbidity within the zones. Some thin zones display minor or no turbidity whereas other zones are highly turbid. Unzoned crystals are highly turbid. Clear or slightly turbid secondary postmagmatic albite rims antiperthite and primary albite crystals.

Apatite, chlorite, magnetite and titanite are common accessory minerals. A minor amount of secondary calcite veinlets and patches are present throughout the rock. Apatite and calcite are closely associated.

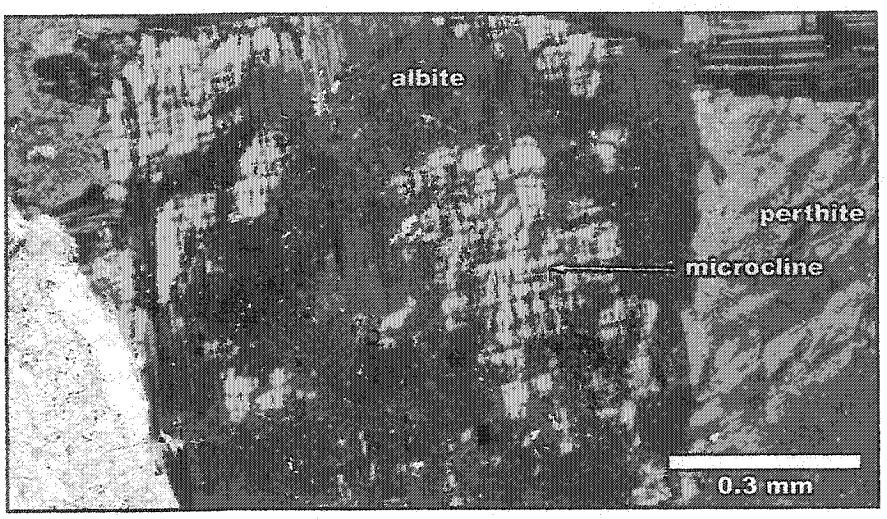

Figure 2.57 Irregularly shaped and distributed K-domains in an antiperthite crystal. This texture likely results from the albitization of a microcline crystal. K-domains display tartan twinning. Crossed polars.

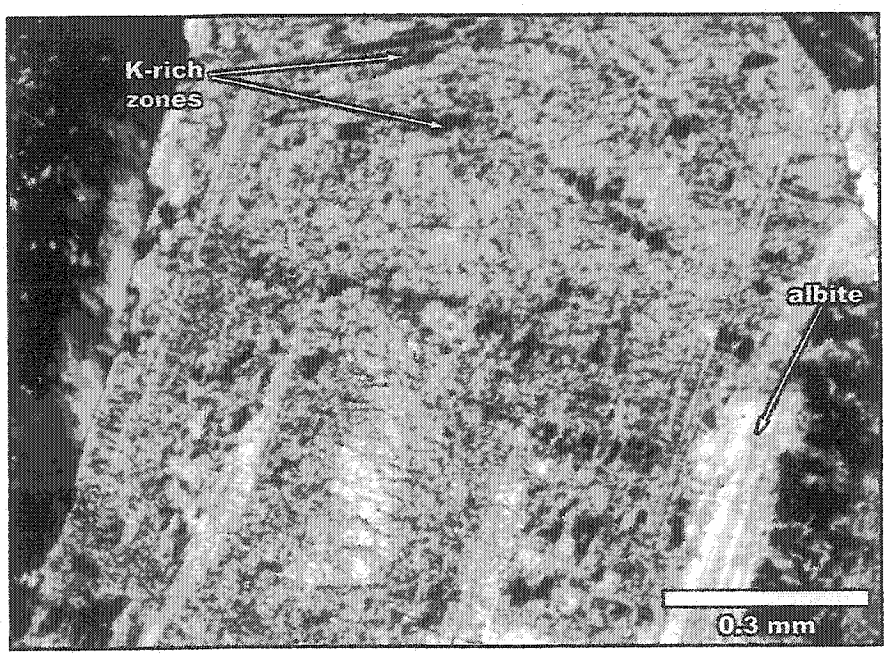

Figure 2.58 Antiperthite crystal containing tartan-twinned K-rich zones. Crossed polars.

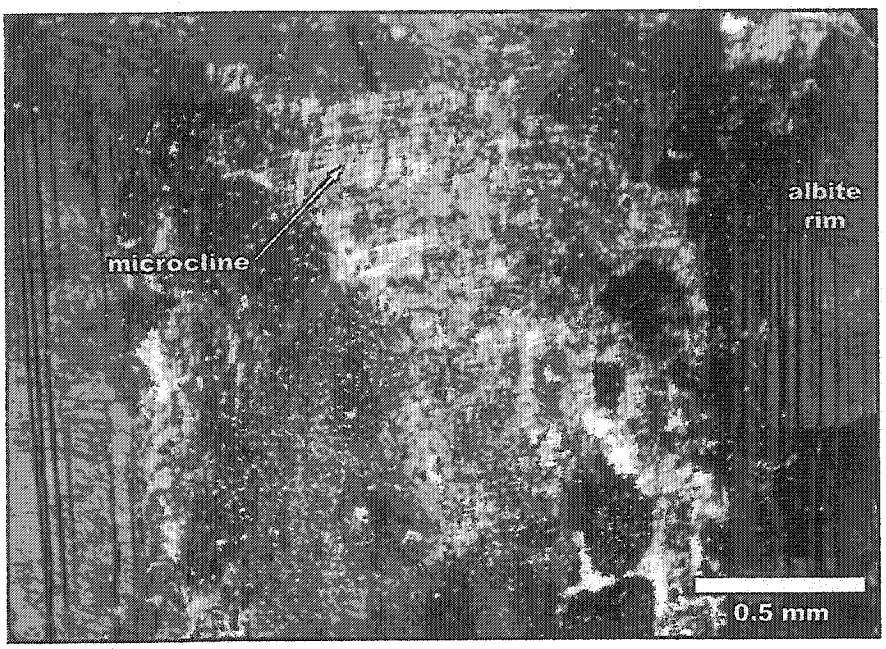

Figure 2.59 Zoned antiperthite crystal composed of a turbid antiperthite core and a clear albite-twinned albite rim. Crossed polars.

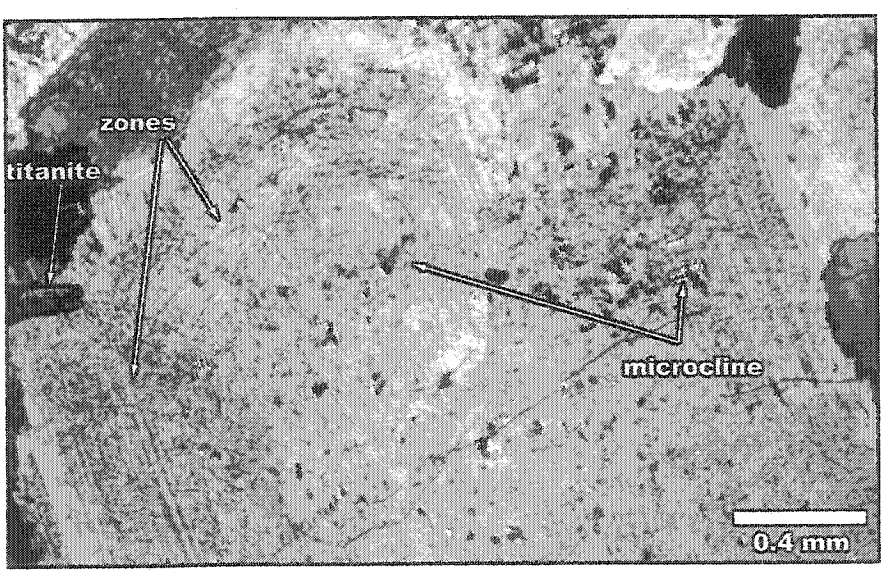

Figure 2.60 Zoned antiperthite crystal containing tartan-twinned K-domains. Crossed polars.

III. Emens intrusion

A. Alkali-feldspar porphyritic biotite-syenite

The Alkali-feldspar porphyritic biotite-syenite is a common rock type in the drill core from the Emens intrusion. The alkali-feldspar porphyritic biotite-syenite (hereinafter called AFP biotite-syenite) contains large subhedral to euhedral, 1 to 3 cm long, tabular perthite megacrysts that are hosted in a dark, medium-grained matrix composed of dark green to black anhedral phlogopite, anhedral light pink to purplish-gray to dark gray perthitic feldspar and a minor amount of light gray albite (Table 2.6; Figure 2.61, 2.62, 2.63 &2.64).

Mineral	Modal%
Alkali-feldspar megacrysts	50-60
Phlogopite	10-20
Perthite (matrix)	10-15
Albite	5-10
Andradite	3-5
Secondary calcite	5
Chlorite	5
Apatite	1
Titanite	tr.
Magnetite	tr.
Pyrite	tr.
Chalcopyrite	tr.
Allanite[1]	tr.
Barite[1]	tr.
Bastnasite[1]	tr.
Bornite[1]	tr.
Chalcocite[1]	tr.

Table 2.6 Range of modal composition of the alkali-feldspar porphyritic biotite-syenite unit. [1] The occurrence of these minerals is inferred from the energy spectra obtained on the EDS unit of the electron microprobe.

The megacrysts display various colors from white to light pink to reddish-pink. The perthite megacrysts have a patch perthite texture and are composed of 30 to 40 % sodic domains. The sodic domains are usually irregularly shaped and vary in size from 60 to 150 μm, and commonly display albite twinning (Figure 2.65). Potassic domains do not exhibit any twinning. The megacrysts are commonly twinned according to the Carlsbad law (Figure 2.66). They contain small 0.3 to 0.4 mm clusters of inclusions of albite, biotite and chlorite (Figure 2.67). The megacrysts are always highly turbid (Figure 2.67) and also contain patches of white mica alteration. Perthite is also present in the matrix. Crystals are anhedral and vary in size from 0.5 to 1.5 mm.

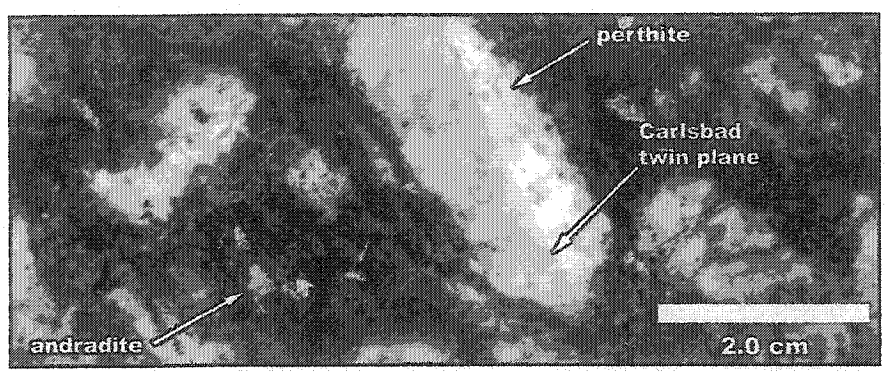

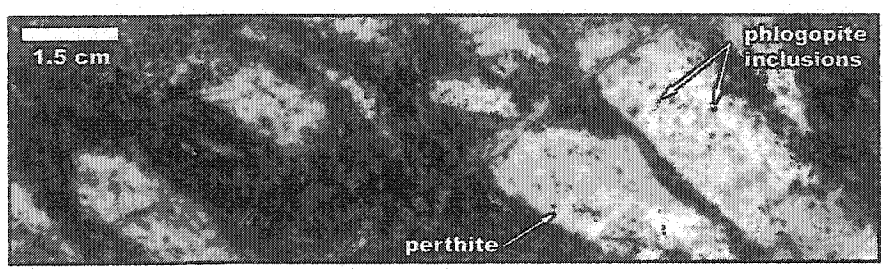

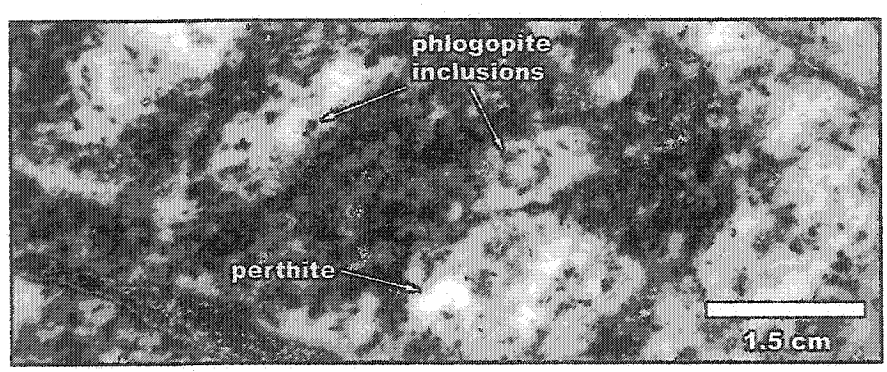

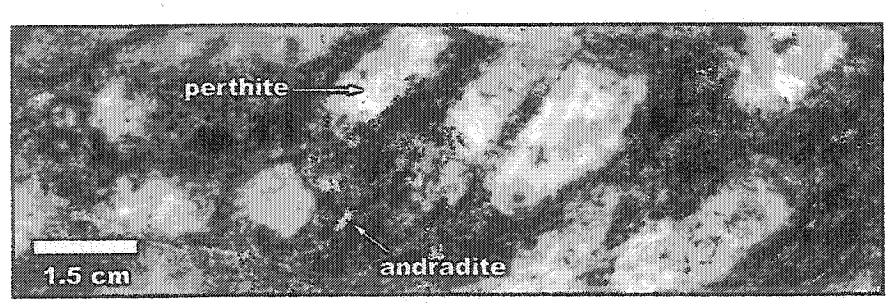

Figures 2.61, 2.62, 2.63 & 2.64 The alkali-feldspar porphyritic biotite-syenite rock. The rock contains subhedral to euhedral, 1 to 3 cm long, tabular perthite megacrysts that are hosted in a dark, medium- to coarse-grained matrix composed of dark green to black anhedral phlogopite, anhedral light pink to purplish-gray to dark gray perthite and a minor amount of light gray albite. The perthite megacrysts commonly contain phlogopite inclusions.

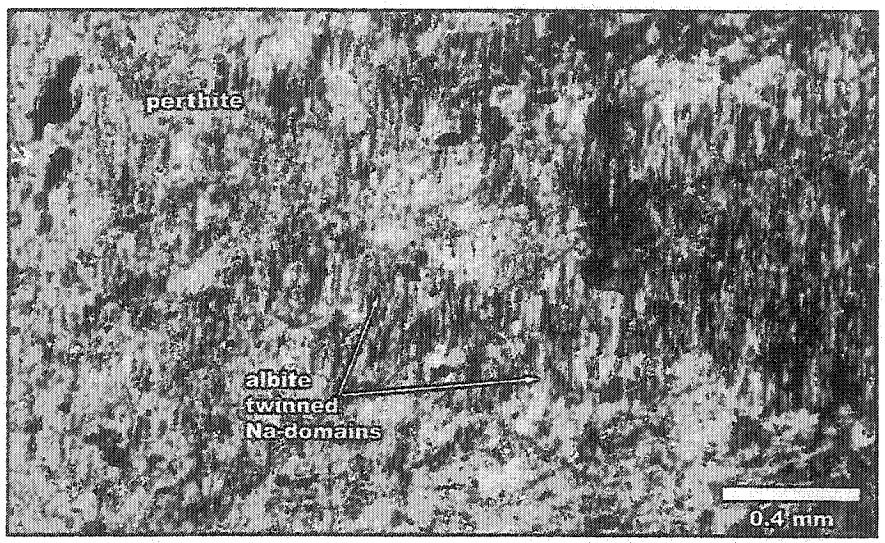

Figure 2.65 Perthite crystal displaying albite-twinned Na-domains. Crossed polars.

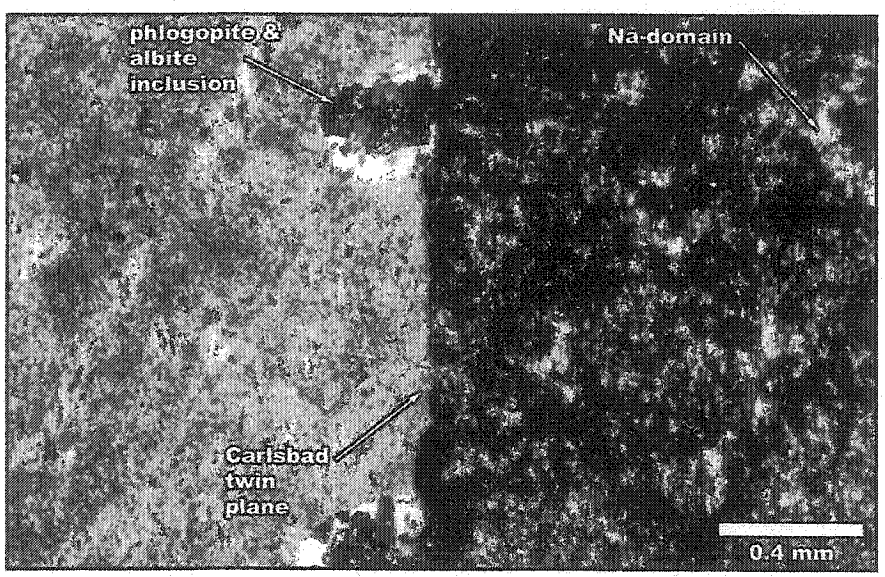

Figure 2.66 A Carlsbad-twinned perthite crystal containing small inclusion-rich zones of albite, phlogopite and chlorite. Crossed polars.

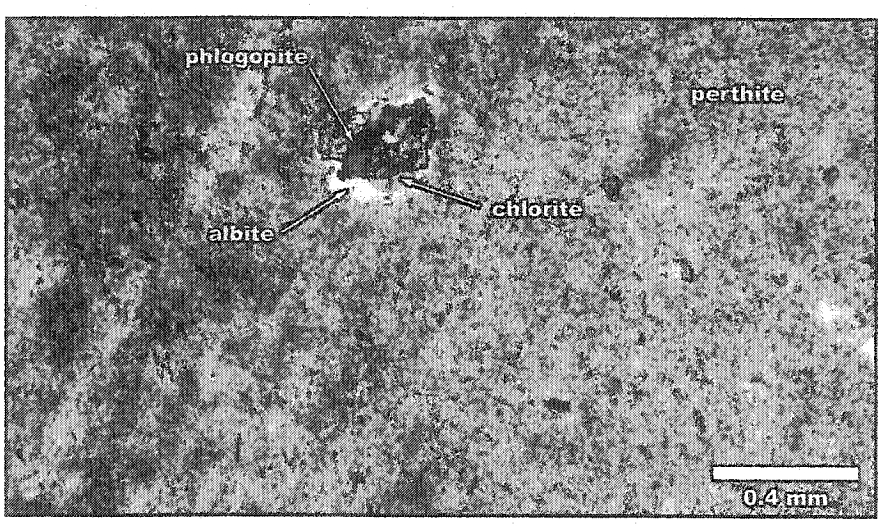

Figure 2.67 Same image as above but in parallel polars. The inclusion-rich zone is clearly visible.

The high turbidity of the matrix perthite prevented an accurate estimation of its composition. However, variations in the intensity of the turbidity suggest that the crystals are the same composition as the megacrysts (30-40 % Na-domains).

Mica is the most abundant ferromagnesian mineral in the porphyritic syenite (Table 2.6). All the mica crystals studied from the AFP biotite-syenite rock, apart for one exception, are phlogopite in the sense of the IMA nomenclature for the mica group [i.e. Fe/(Fe+Mg) < 0.5; chapter 3]. Only one crystal was identified as annite (Fe/(Fe+Mg) = 0.510). Phlogopite most frequently occurs as anhedral crystals that vary in size from 0.5 to 1.5 mm. Pleochroism varies from tan to light green to dark green. The crystals are usually fresh but alteration to chlorite is observed (Figure 2.68). Rusty-brown pleochroic halos are seen around apatite and monazite inclusions (Figure 2.69, 2.70 & 2.71). In the matrix, phlogopite is associated with andradite, titanite and chlorite.

Aegirine-augite was identified in two highly altered AFP biotite-syenite samples, although these samples contained a higher proportion of altered mafic minerals (i.e. LMP-045 & LMP-084). Aegirine-augite occurs as small (0.1-0.15 mm) anhedral crystals that are associated with chlorite (Figure 2.72). They are light green and do not display any pleochroism.

Albite is a late magmatic mineral in the AFP biotite-syenite. It occurs as small 0.2 to 0.5 mm anhedral clear crystals that display good albite twinning. Albite crystals are found in the matrix and in small carbonate and muscovite veins.

Titanian-andradite or melanite (Chapter 3 for mineral chemistry) is a ubiquitous component of the AFP biotite-syenite (Table 2.6). Fresh melanite crystals are anhedral, 0.3 to 1 mm in size and display light brown to dark brown colors (Figure 2.69 & 2.73). Euhedral pseudomorphs of garnet

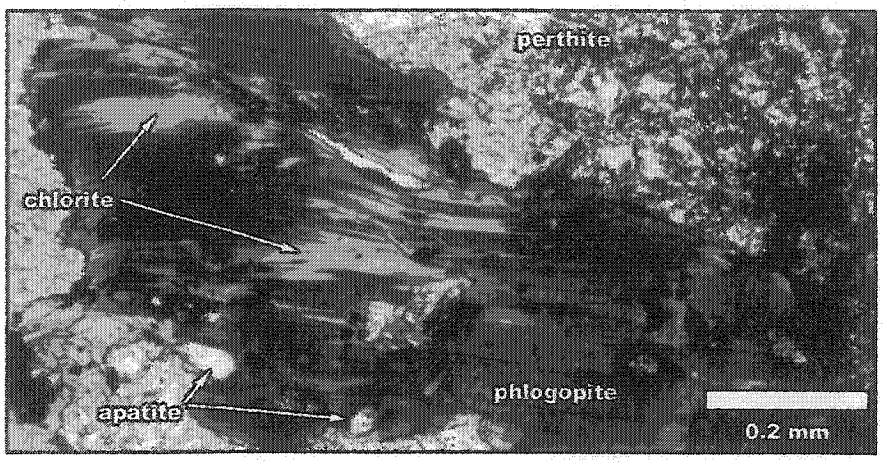

Figure 2.68 Anhedral phlogopite crystal partially altered to chlorite along {001}. Parallel polars.

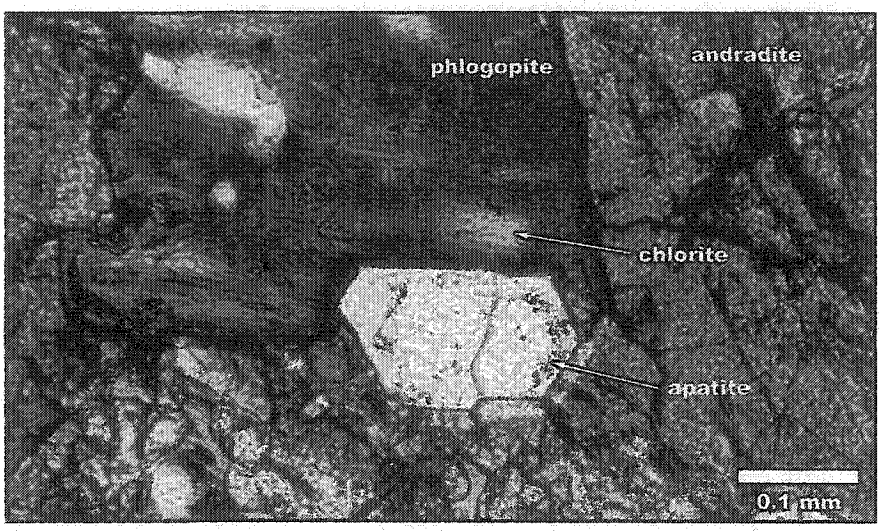

Figure 2.69 Euhedral apatite crystal surrounded by a pleochroic halo in the partially altered phlogopite crystal. Titanian-andradite is also visible. Parallel polars.

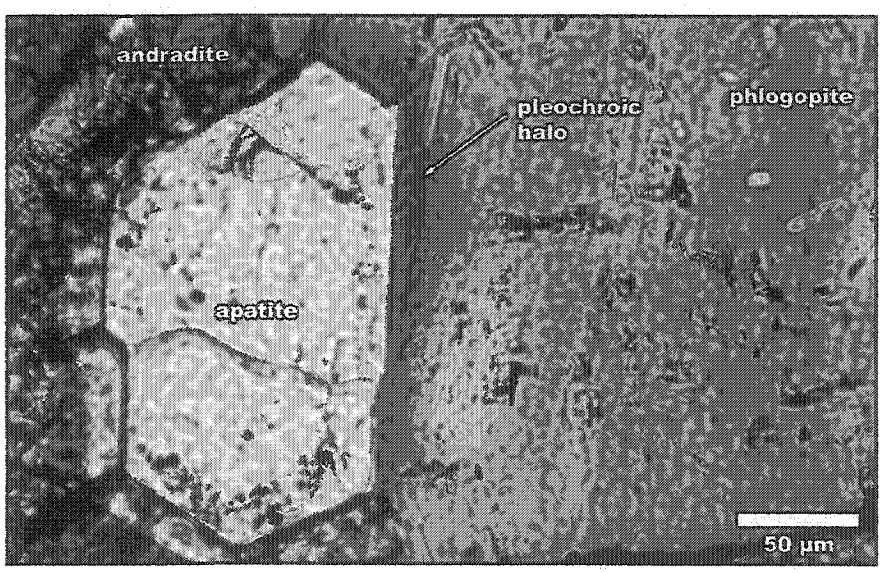

Figure 2.70 Close-up of the apatite crystal described above. The pleochroic halo is clearly visible. Parallel polars.

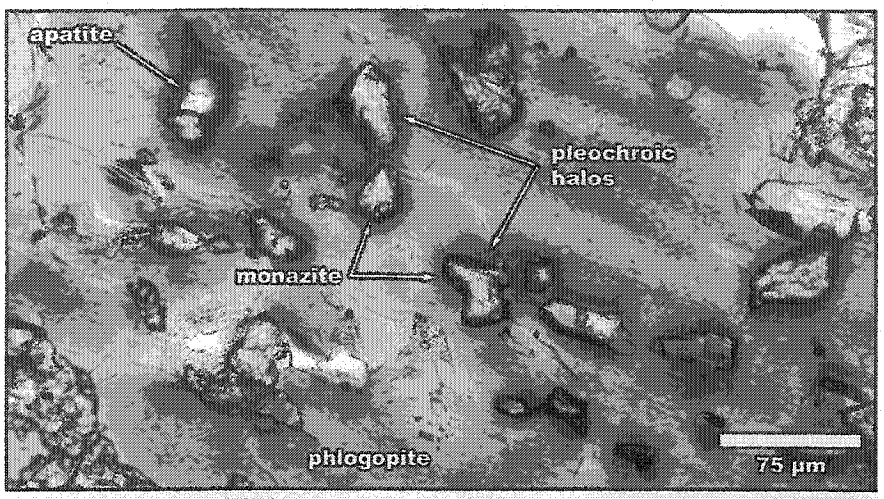

Figure 2.71 Apatite and monazite inclusions encircled by pleochroic halos in the host phlogopite crystal. Parallel polars.

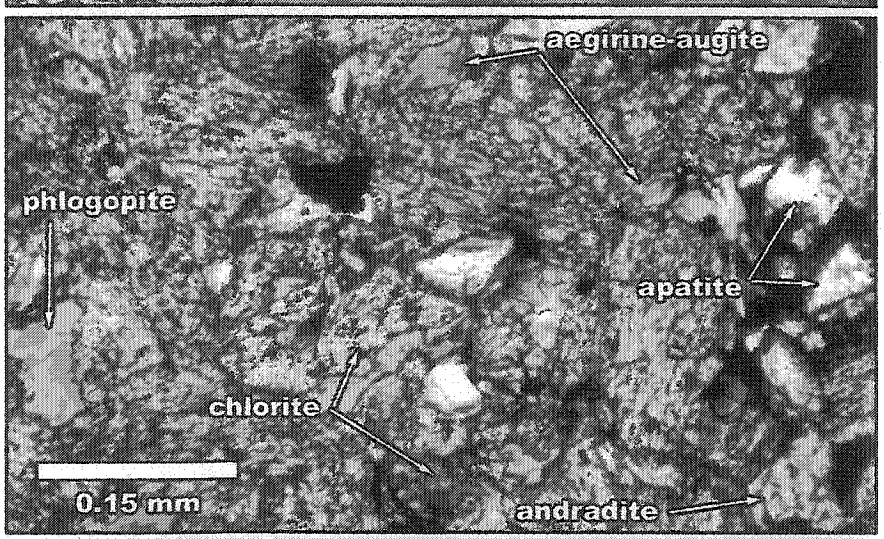

Figure 2.72 Small aegirine-augite crystals in a mass of chlorite and phlogopite. Parallel polars.

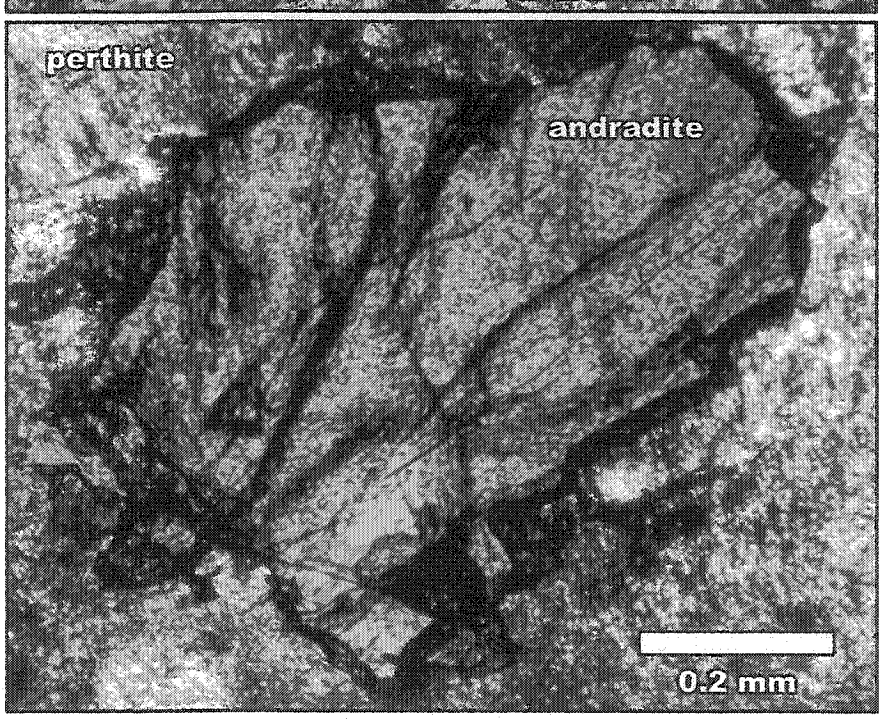

Figure 2.73 Anhedral titanian-andradite crystal surrounded by turbid perthite. Parallel polars.

are observed (Figure 2.74). These pseudomorphs are composed of phlogopite, magnetite, titanite and chlorite. Andradite containing appreciable amounts of titanium is a common mineralogical feature of alkaline igneous rocks (Deer et al., 1996).

B. Alkali-feldspar syenite

The alkali-feldspar syenite (hereinafter called AF syenite) is a rock commonly observed in the drill core of Emens intrusion. This hypersolvus syenite is composed of 0.5 to 2 cm long anhedral to subhedral light pink to purplish-pink to dark purplish-gray perthite (Figure 2.75 & 2.76) and traces of accessory minerals. The rock is highly leucocratic, with a color index always less than 10 (Table 2.7). The perthite phenocrysts are sometimes zoned. The zoning is visible in hand samples and is characterized by dark purplish-gray cores and light pink to purplish-pink rims (i.e., extent of turbidity).

Mineral	Modal%
Perthite	90-95
Phlogopite	2-5
Chlorite	3-5
Epidote	tr.
Magnetite	tr.
Pyrite	tr.
Titanite	tr.
Secondary muscovite	tr.
Secondary calcite	tr.

Table 2.7 Range of modal composition of the alkali-feldspar syenite unit.

Perthite crystals display patch and vein textures (Anderson, 1928; Figure 2.77). They are generally composed of 20 to 30 % Na-domains that are 25 to 50 μm thick and 250 to 750 μm long. These domains are commonly albite twinned (Figure 2.78). The potassic domains are more turbid than the sodic ones (Figure 2.80). Only a minor amount of these are tartan twinned (Figure 2.79). Perthite crystals displaying dark purplish-gray color in hand samples are more turbid than the light colored ones. This feature is also evident in zoned crystals, which have a more turbid core compared to the rim producing, in hand sample, a dark core and light colored rim. Perthite crystals commonly contain anhedral inclusions of albite that vary in size from 35 to 150 μm (Figure 2.81).

Mica is not common in the AF syenite (Table 2.7). Phlogopite crystals are anhedral, 0.1 to 0.3 mm in size and display tan to dark green to brownish-green pleochroic colors. Crystals are usually partially to totally altered to chlorite. Epidote, magnetite, pyrite and titanite are all minor but ubiquitous components of the AF syenite rock (Table 2.7).

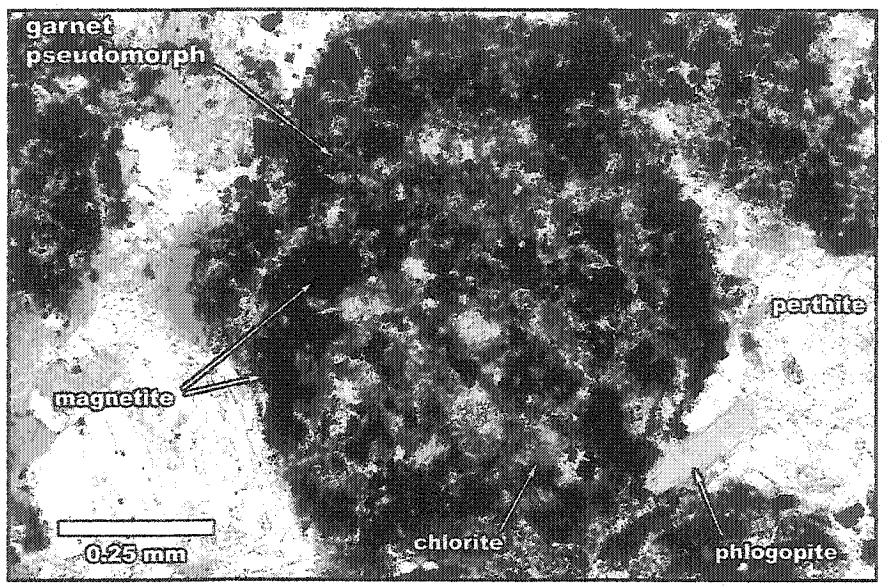

Figure 2.74 Euhedral pseudomorph of melanite garnet composed of magnetite and chlorite. Apatite, albite and phlogopite are also present. Parallel polars.

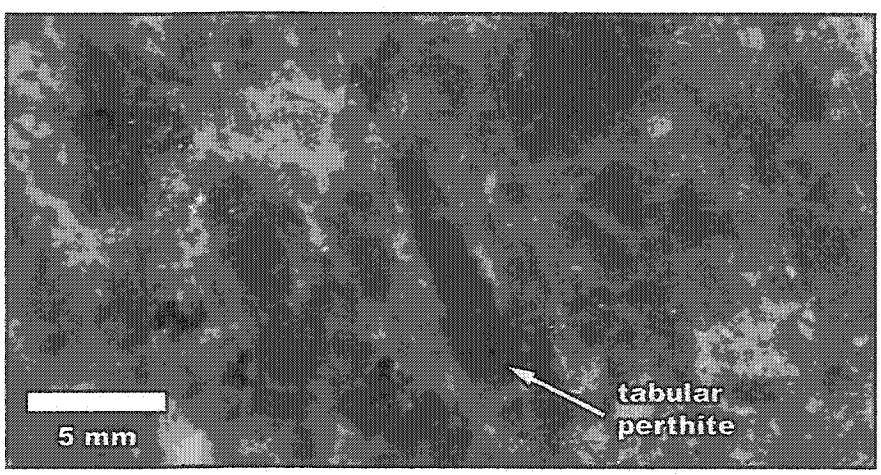

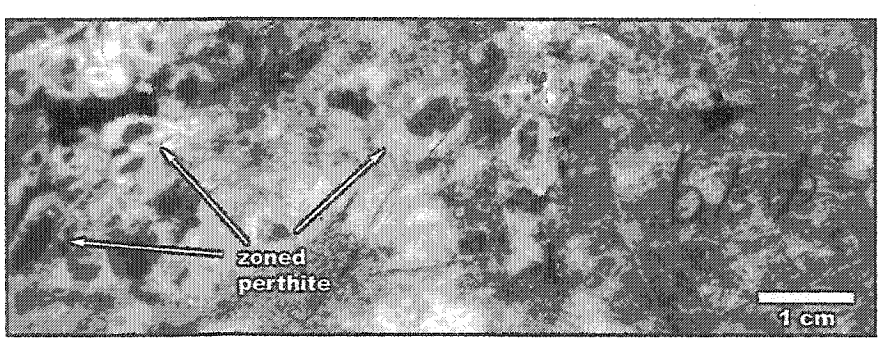

Figures 2.75 & 2.76
Alkali-feldspar syenite rock. The rock is composed of 0.5 to 2 cm long, anhedral to subhedral light pink to purplish-pink to dark purplish-gray perthite. Perthite crystals are commonly zoned.

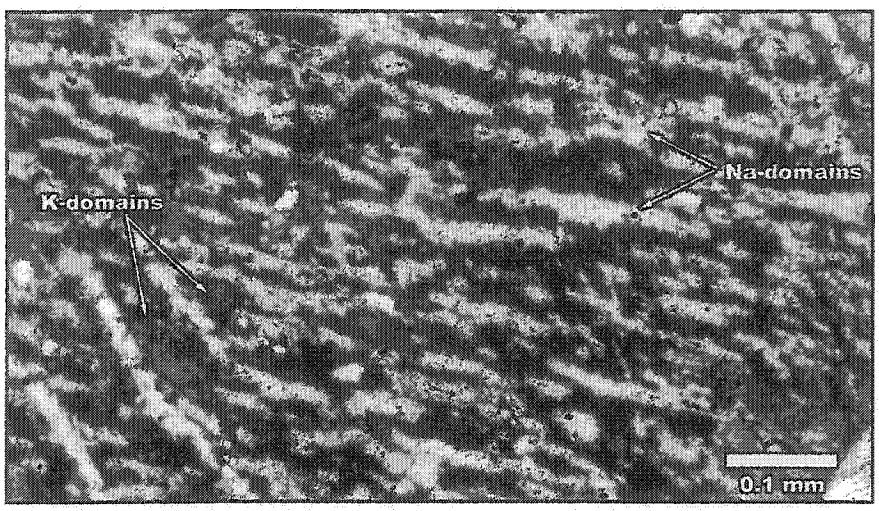

Figure 2.77 Vein perthite. K-domains are extinct. Crossed polars.

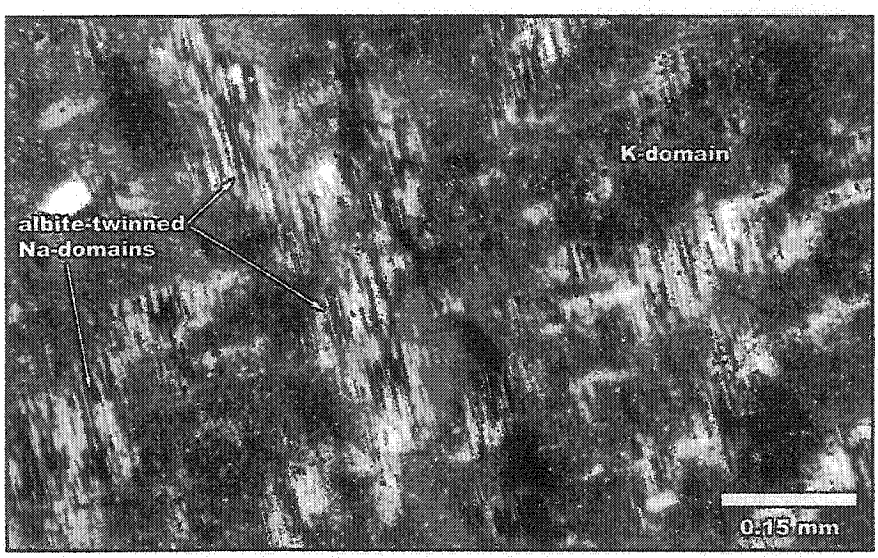

Figure 2.78 Patch perthite with turbid K-domains and albite-twinned Na-domains. Crossed polars.

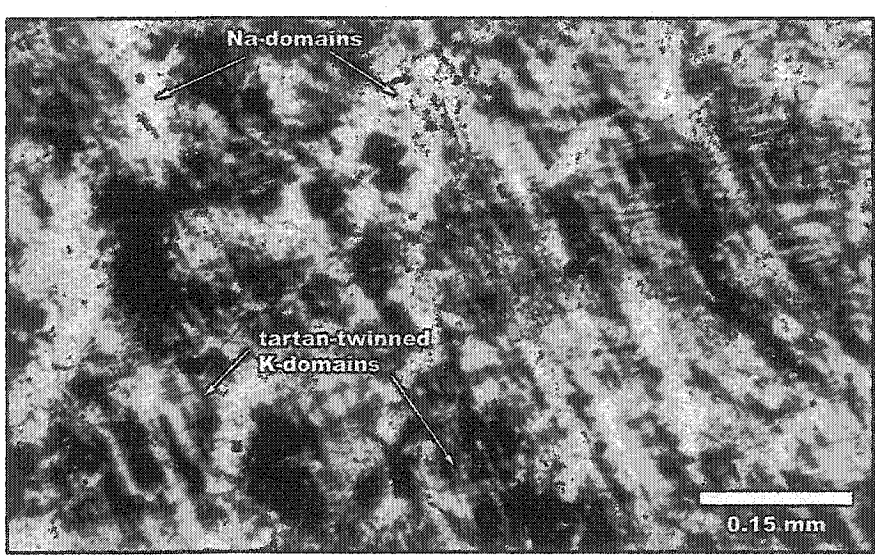

Figure 2.79 Vein perthite with tartan-twinned K-domains. Crossed polars.

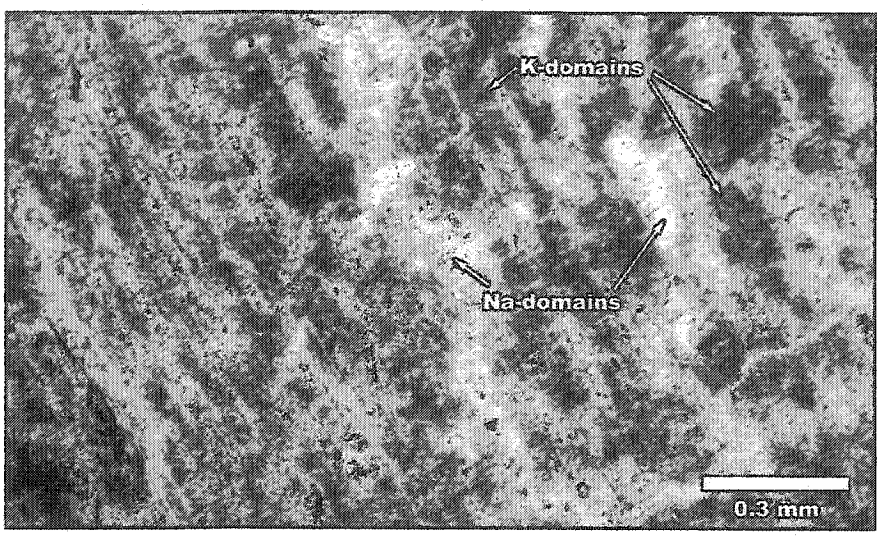

Figure 2.80 Highly turbid K-domains in a perthite crystal. Parallel polars.

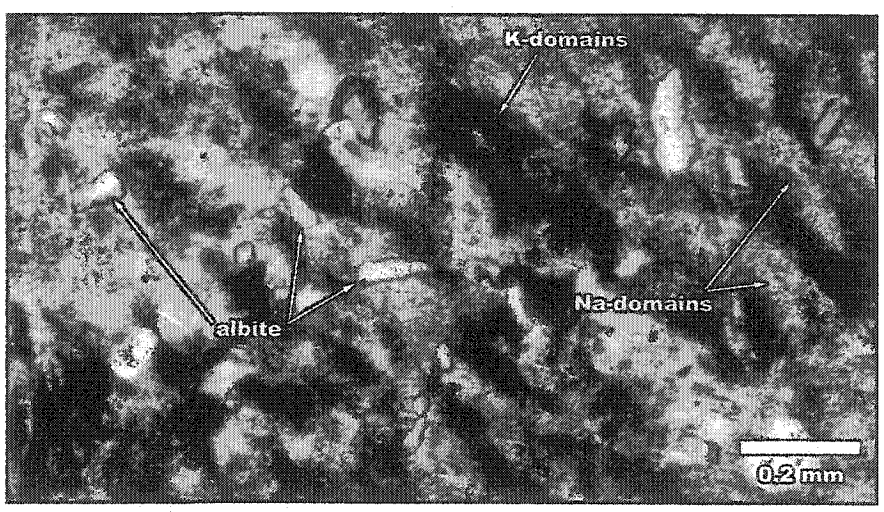

Figure 2.81 Clear albite inclusions in a perthite crystal. Crossed polars.

IV. Pangea intrusion

A. Pyroxene-bearing hornblendite

Pyroxene-bearing hornblendite is a common rock type in the drill core from the Pangea intrusion. The pyroxene-bearing hornblendite (hereinafter called hornblendite) has a close spatial association with the melasyenite unit; contacts between the two units are usually gradational making it difficult to identify the limits of each unit. Thin dykes of syenite and melasyenite crosscut the hornblendite unit.

The hornblendite is composed of a fine-grained green matrix with variable contents of 0.2 to 1.0 cm anhedral to subhedral dark green to black amphibole megacrysts, which have compositions varying between magnesiohastingsite and tschermakite (Figure 2.82; chapter 3 for mineral chemistry). The modal composition of the hornblendite rock is given in Table 2.8.

Mineral	Modal%
Amphiboles	30-45
Diopside	10-25
Chlorite	10-15
Albite	2-15
Phlogopite	1-5
Magnetite	1-5
Apatite	1-5
Ilmenite	1-5
Titanite	1
Secondary calcite	tr.
Pyrite	tr.

Table 2.8 Range of modal composition of the pyroxene-bearing hornblendite unit.

In thin section, the megacrysts display tan to light green to brownish-orange pleochroism. They contain numerous small inclusions of apatite, opaque oxides (magnetite and ilmenite) and turbid albite (Figure 2.83 & 2.84). The presence of these inclusions suggests that the megacrysts were formed later in the crystallization sequence. Furthermore, the rock commonly contains zones ranging in size from 5 to 25 cm with larger albite and amphibole megacrysts that were probably formed by late volatile-rich fluids. Similar zones are observed in the hornblendite unit of the Iris intrusion

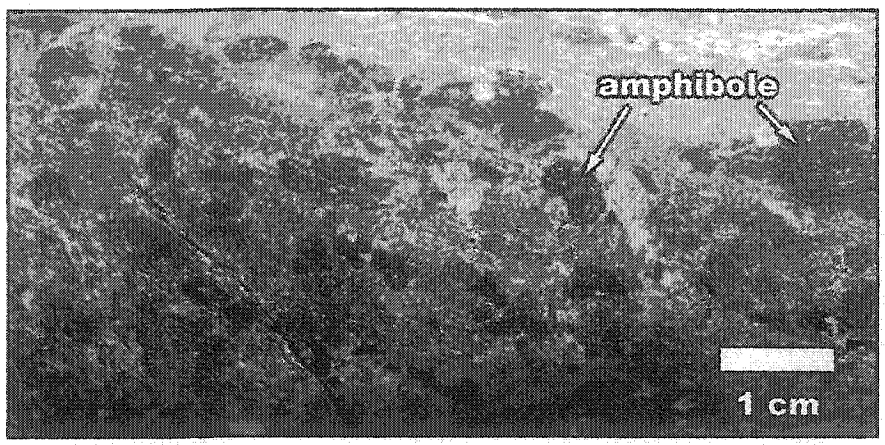

Figure 2.82 The pyroxene-bearing hornblendite rock. The rock is composed of a fine-grained green matrix with variable contents of 0.2 to 1.0 cm anhedral to subhedral dark green to black amphibole megacrysts, which have compositions varying between magnesiohastingsite and tschermakite.

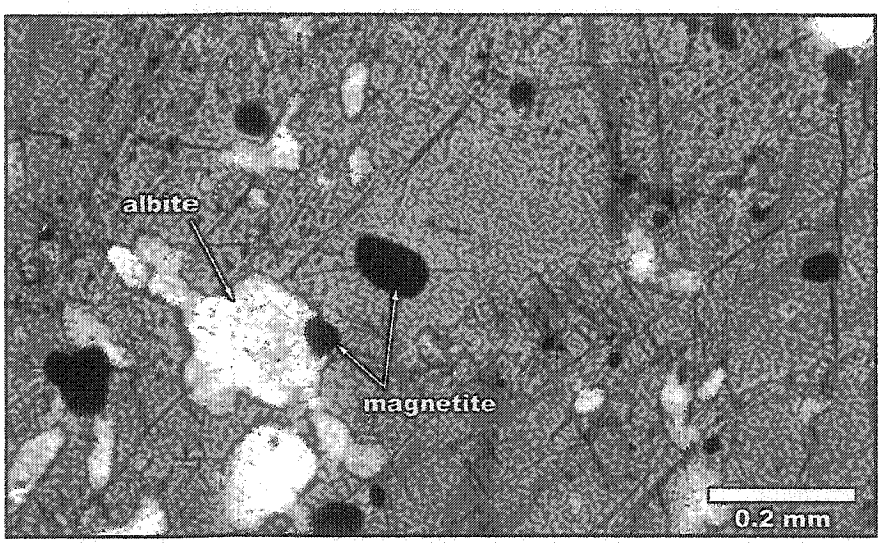

Figure 2.83 Albite and magnetite inclusions in an amphibole megacryst. Parallel polars.

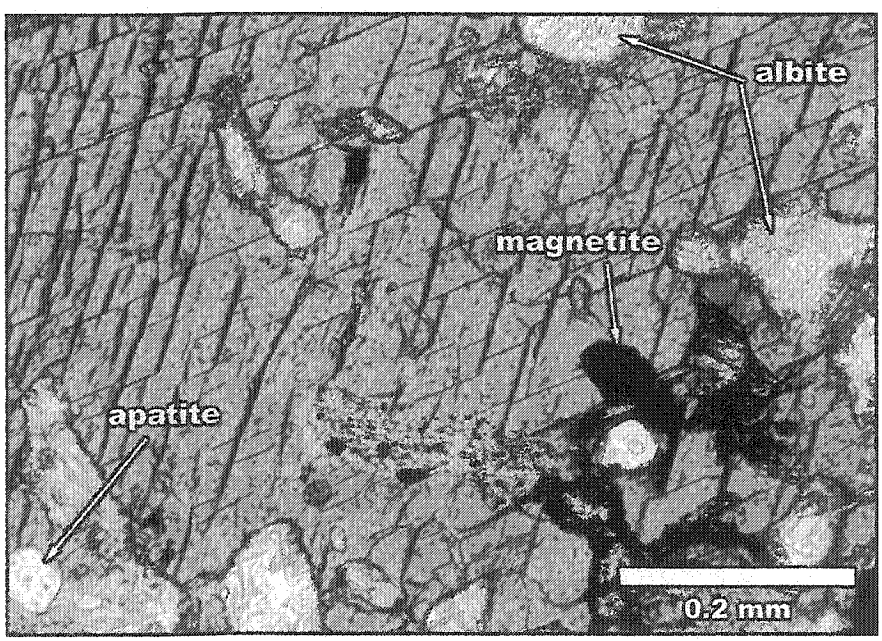

Figure 2.84 Albite, apatite and magnetite inclusions in an amphibole megacryst. Parallel polars.

(Figure 2.9). The megacrysts are partially altered to chlorite and, in some samples, totally altered to phlogopite (Figure 2.85).

The matrix is composed of amphiboles, chlorite, diopside, alkali feldspar and, depending on the sample, phlogopite (Table 2.8). Amphiboles identified in the matrix were hastingsite, ferrotschermakite and actinolite (chapter 3 for mineral chemistry). Hastingsite and ferrotschermakite occur as small (~0.3-0.5 mm) anhedral crystals displaying light to dark olive green pleochroism (Figure 2.86). Actinolite is fibrous and displays colorless to pale yellow-green to pale blue-green pleochroism (Figure 2.87). All amphiboles in the matrix are partially altered to chlorite.

Diopside crystals are anhedral to subhedral, tan to light green color and display little or no pleochroism. Large mostly unaltered crystals are commonly rimmed by a layer of chlorite (Figure 2.88). Small anhedral diopside crystals are also found in the center of actinolite clusters (Figure 2.87), suggesting that the actinolite replaced the primary diopside.

Mica content in hornblendite samples is variable. Some samples contain up to 20 % mica while others only have minor amounts (1-5 %). All the mica crystals from the hornblendite rock, apart for one exception, are phlogopite (chapter 3 for mineral chemistry). A single grain was identified as annite. Primary phlogopite occurs as anhedral crystals (0.5-1 mm) that are commonly rutilated. Two types of rutile inclusions were identified: (1) acicular and (2) anhedral to subhedral rusty-red crystals (Figure 2.89). Pleochroism varies from light olive green to dark green to brown. In general, mica is fresh but alteration to chlorite is common.

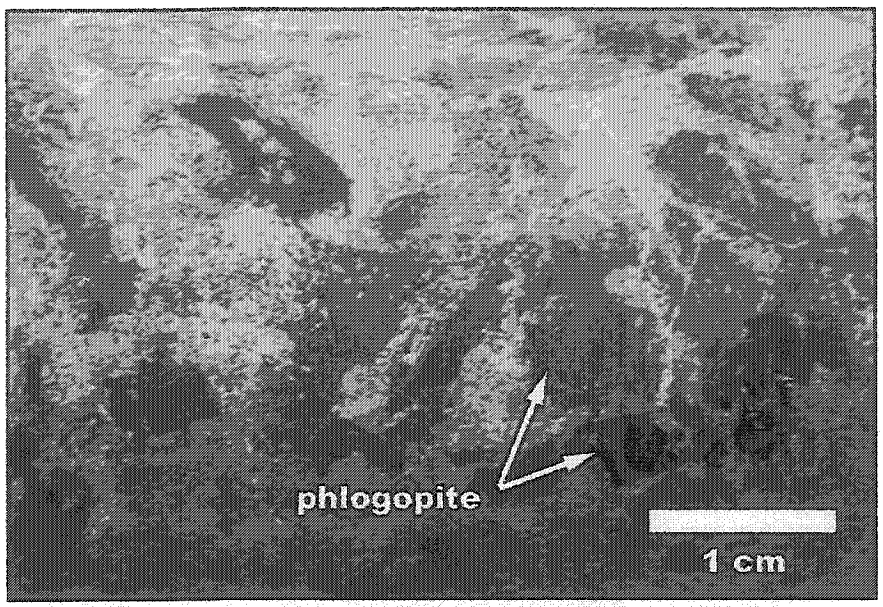

Figure 2.85 Altered hornblendite rock. The megacrysts are completely altered to phlogopite.

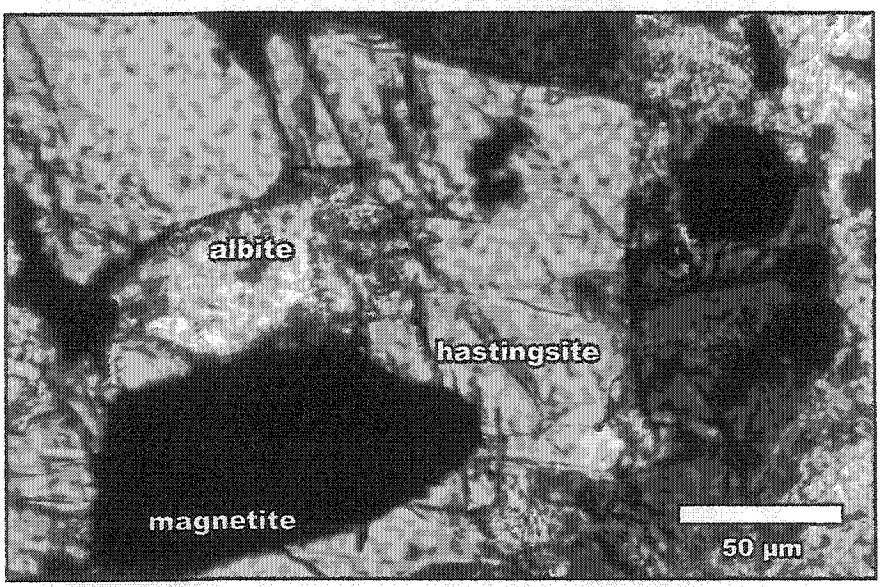

Figure 2.86 Anhedral hastingsite crystal associated with albite and magnetite. Parallel polars.

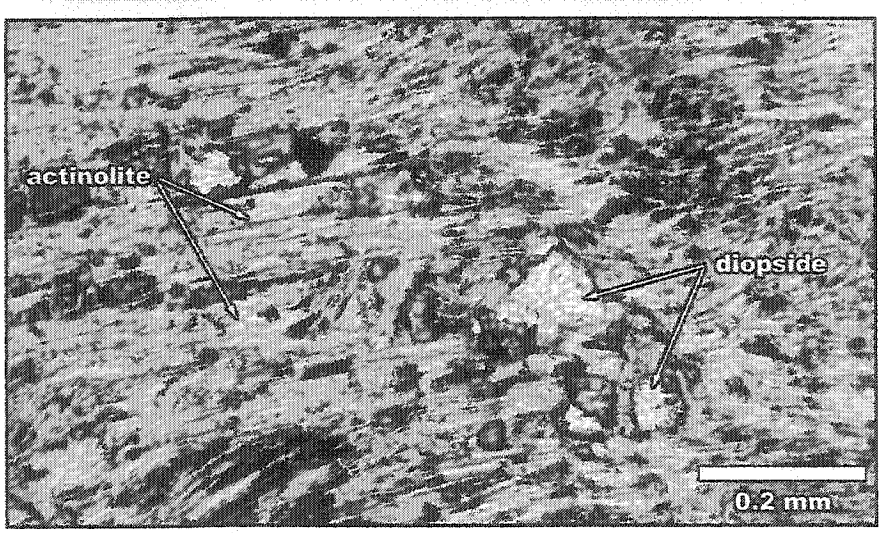

Figure 2.87 Anhedral diopside crystal surrounded by a mass of actinolite. Parallel polars.

Albite occurs in the matrix as small (0.2-0.6 mm) anhedral and highly turbid crystals that are present in small irregular shaped zones. The highly turbid nature of the albite makes it difficult to observe twinning. However, some crystals displayed the characteristic albite twinning.

Chlorite is the most common alteration mineral found in the matrix (Table 2.8). It is partially or totally replacing actinolite, phlogopite and the amphibole megacrysts. Chlorite also rims diopside crystals (Figure 2.88). Chlorite is anhedral and usually displays yellowish-green to green pleochroism colors and is intimately associated with magnetite.

Apatite, ilmenite, magnetite and titanite are the common accessory minerals in the hornblendite unit (Table 2.8). Subhedral to euhedral crystals (0.5-2 mm) of magnetite and ilmenite are found in the matrix but magnetite is also present as inclusions in amphibole megacrysts (Figure 2.83 & 2.84). Most specimens of hornblendite have high magnetic susceptibility. Ilmenite is present as small exsolution lamellae in magnetite crystals or vice versa, as discrete crystals with magnetite exsolution (Figure 2.90). Apatite crystals are anhedral to subhedral and generally 0.5 to 2.0 mm in size. Titanite is a ubiquitous mineral and occurs as subhedral to euhedral crystals. Although pyrite is not particularly abundant in this rock, there are a few relatively small (~ 1-1.5 mm) zones that are composed mostly of altered anhedral albite, anhedral to subhedral pyrite and, anhedral magnetite and ilmenite. In these zones, magnetite appears to rim both albite and pyrite, although magnetite is also included in some pyrite crystals (Figure 2.91).

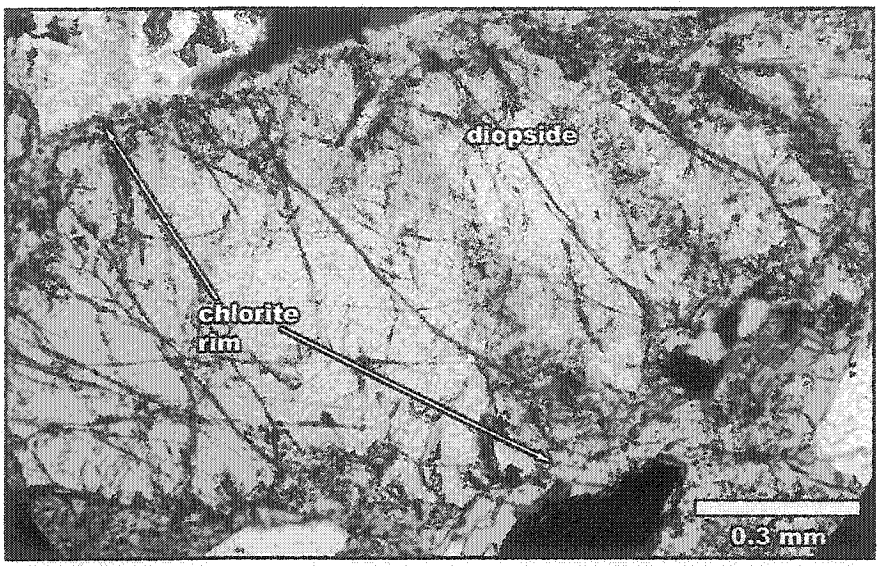

Figure 2.88 Diopside crystal rimmed by chlorite. Parallel polars.

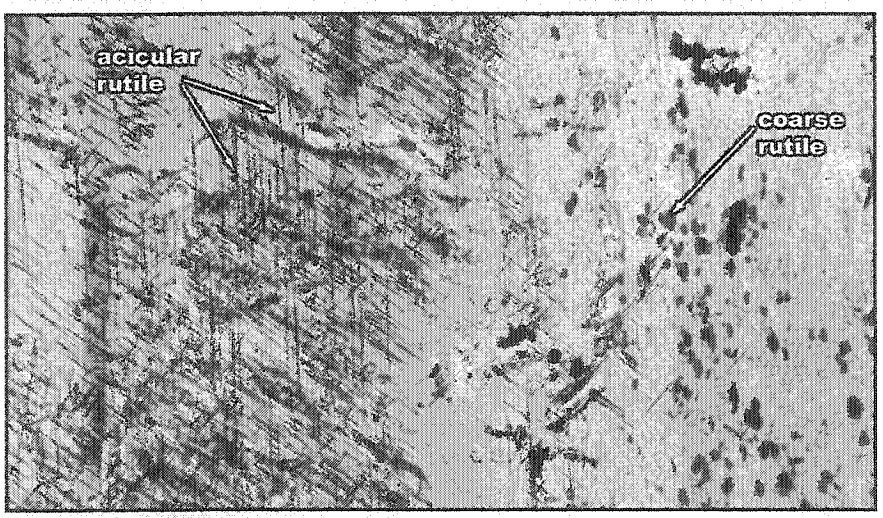

Figure 2.89 Phlogopite containing acicular and rusty-red rutile inclusions. Parallel polars.

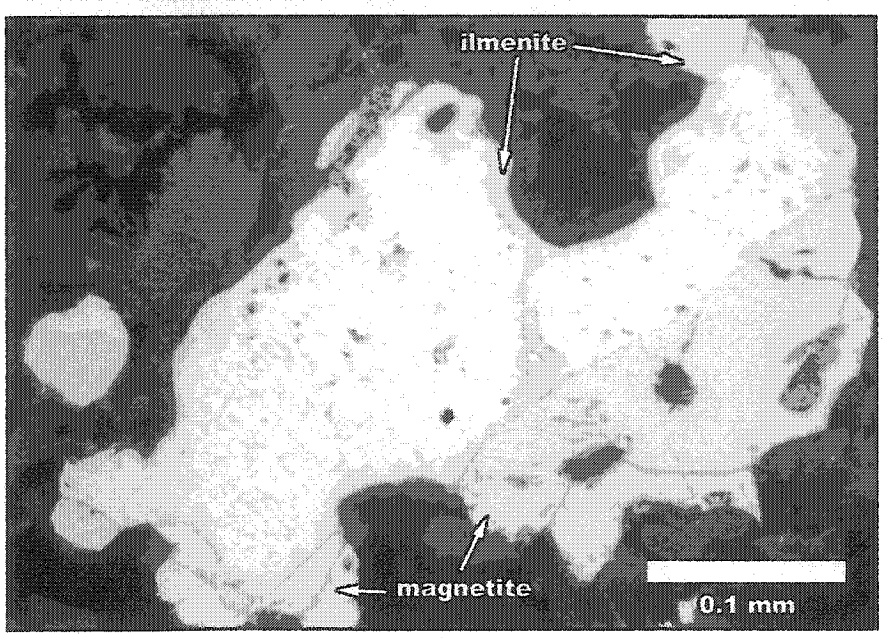

Figure 2.90 Ilmenite exsolution in a magnetite crystal. Reflected light with parallel polars.

B. Melasyenite

Melasyenite is the most common rock unit observed in the drill core of the Pangea intrusion. The thickness of the melasyenite unit in drill core varies between 15 to 75 m. As previously described, melasyenite is in close spatial association with the pyroxene-bearing hornblendite. The two units usually display gradational contacts, suggesting contemporaneous emplacement. Dykes of felsic aplite, syenite, biotite-rich lamprophyre and minor veins of blue amphibole crosscut the melasyenite unit.

The melasyenite has heterogeneous modal composition and textures but is usually medium- to coarse-grained and equigranular (Figure 2.92) or slightly porphyritic (Figure 2.93 & 2.94). The range of modal mineralogy is given in Table 2.9. When porphyritic, the melasyenite has a medium-grained matrix composed of anhedral perthite and anhedral to subhedral amphibole. The perthite megacrysts are anhedral to subhedral and vary in size from 2 to 10 mm. The color of the matrix and megacrysts is variable and is a function of the intensity of hematization. In the least hematized samples, the perthite megacrysts are light gray to pinkish-gray color while they are reddish-pink in the more hematized samples. Zones of grain size variations are common. In most of these zones, the rock is composed of 1 to 2 mm long prismatic subhedral to euhedral dark green amphibole and anhedral to subhedral light pink perthite of similar size. However, some zones contain large euhedral (1.0-1.5 cm) long prismatic green amphibole that are hosted in an albite matrix. These

Mineral	Modal%
Perthite	45-60
Amphiboles	15-30
Chlorite	10-15
Albite	2-5
Phlogopite	2-5
Epidote	2-5
Magnetite	1-5
Apatite	1-2
Diopside	1-2
Titanite[1]	1-2
Andradite[1]	tr.
Pyrite	tr.
Secondary calcite	tr.

Table 2.9 Range of modal composition of the melasyenite unit.
[1] locally enriched.

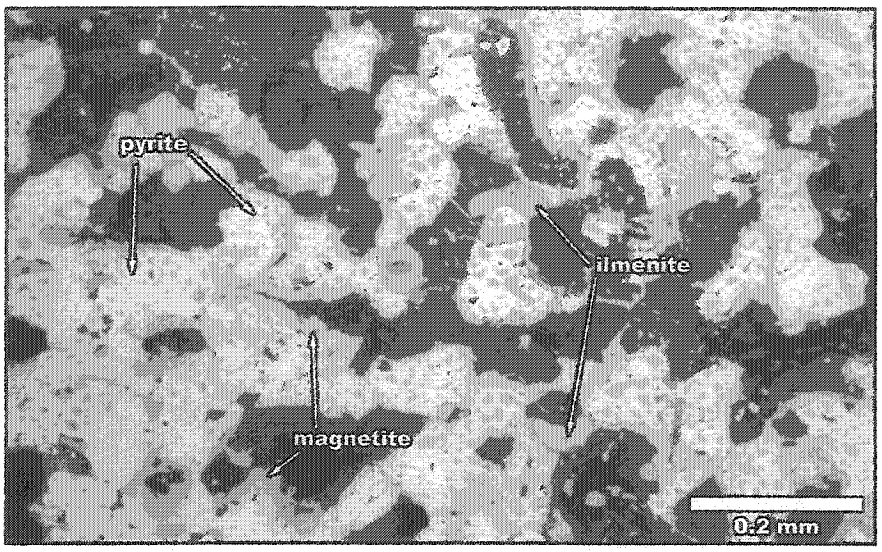

Figure 2.91 Association of pyrite, ilmenite and magnetite. Magnetite appears to rim pyrite. Reflected light with parallel polars.

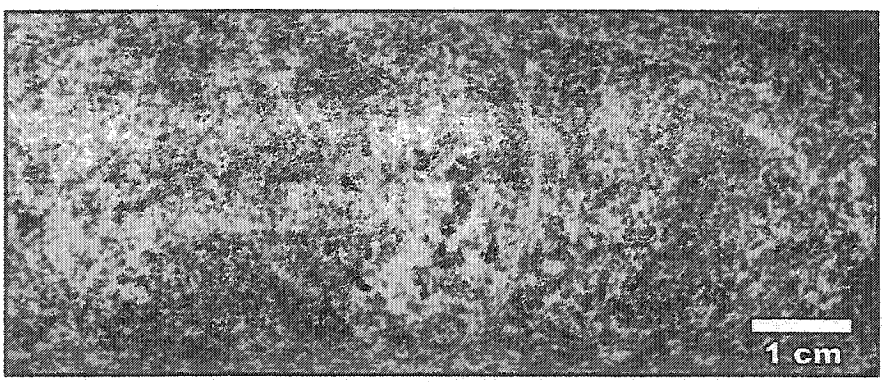

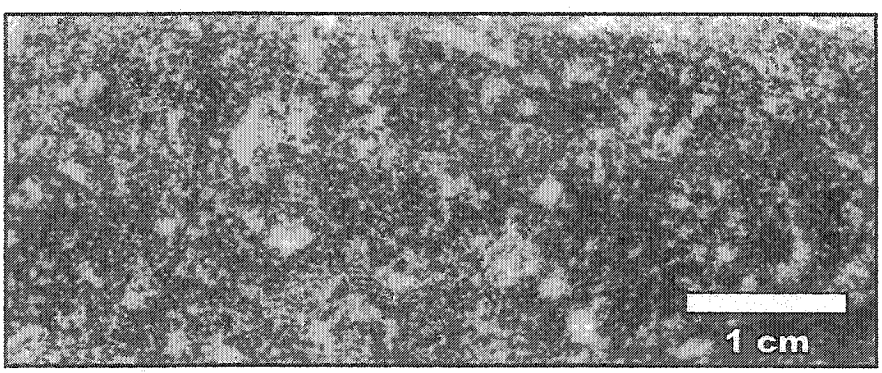

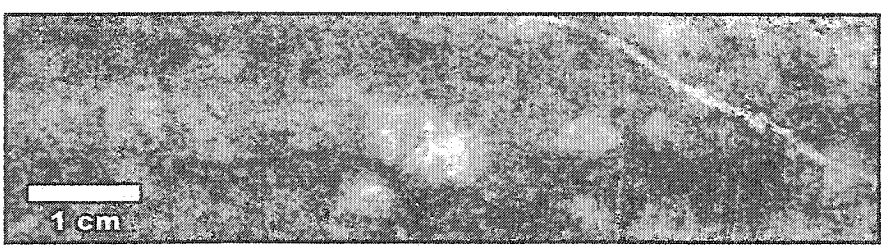

Figures 2.92, 2.93 & 2.94 The melasyenite rock. The unit is heterogeneous in composition and textures but is usually medium- to coarse-grained and equigranular or slightly porphyritic. When porphyritic, the melasyenite has a medium-grained matrix composed of anhedral perthite and anhedral to subhedral amphibole. The perthite megacrysts are of various sizes from 2 to 10 mm.

zones are also enriched in subhedral to euhedral, 0.5 to 3 mm long crystals of magnetite (Figure 2.95).

Under the microscope, perthite crystals are highly turbid (Figure 2.96) with patches of sericite alteration. The turbidity of the perthite is interpreted to result from myriads of microscopic opaque inclusions (probably hematite) within the crystals. The inclusions give the characteristic brown to rusty-brown «dirty» appearance to the feldspar. Patch perthite (Anderson, 1928) is a common texture. Exsolution domains are usually visible under crossed polars (Figure 2.97). Potassium-rich domains dominate (60-70 %) over the sodium-rich domains. Twinning within the individual Na-rich and K-rich domains was not observed. However, Carlsbad twinning is common in the larger perthite crystals.

Actinolite is the most common amphibole in the melasyenite unit (chapter 3 for mineral chemistry), and is the result of pyroxene alteration. It completely replaces 0.3 to 0.8 mm euhedral crystals of pyroxene that display distinctive pyroxene basal sections (Figure 2.98). The actinolite displays light tan to light olive green pleochroism. Actinolite also occurs as anhedral clusters in the matrix of the fine-grained melasyenite. These clusters of actinolite often have a fibrous habit, irregular extinction and are partially to almost completely altered to chlorite. Although not abundant, magnesiohastingsite is present in some samples (Figure 2.99). It is anhedral, 0.2 to 1.0 mm long and has pleochroism that varies from light olive green to dark green.

Phlogopite is a ubiquitous mineral in the melasyenite unit (Table 2.9). It occurs as small (0.5-1 mm) anhedral crystals or subhedral to euhedral sheets that are 3 to 4 mm in length. Pleochroism varies from light olive green to dark green to brown and bird's eye extinction is common. The larger phlogopite crystals contain numerous acicular inclusions of rutile and less

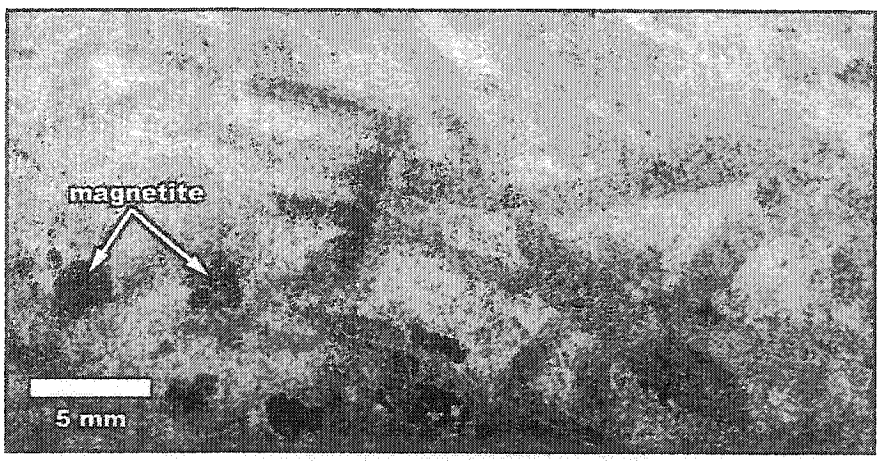

Figure 2.95 Zone composed of large euhedral long prismatic green amphibole that are hosted in an albite matrix. These zones are also enriched in magnetite.

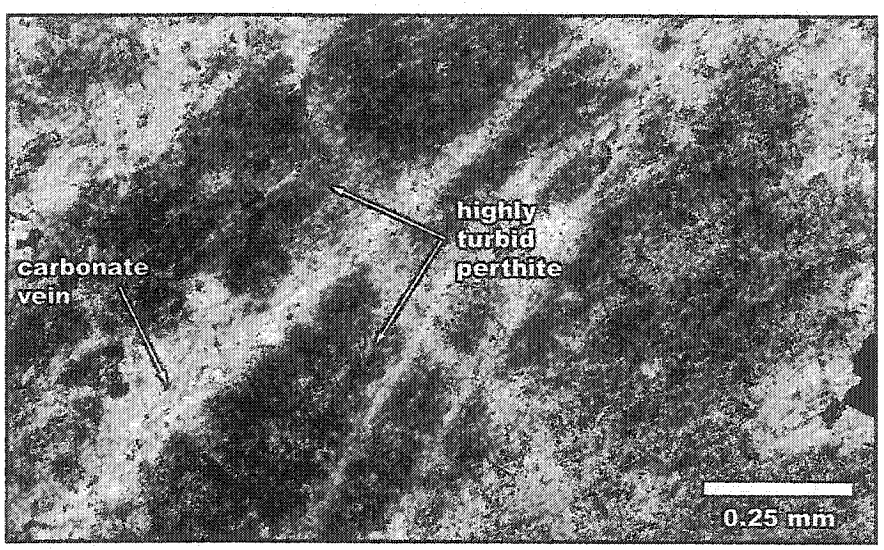

Figure 2.96 Highly turbid perthite in the melasyenite. Parallel polars.

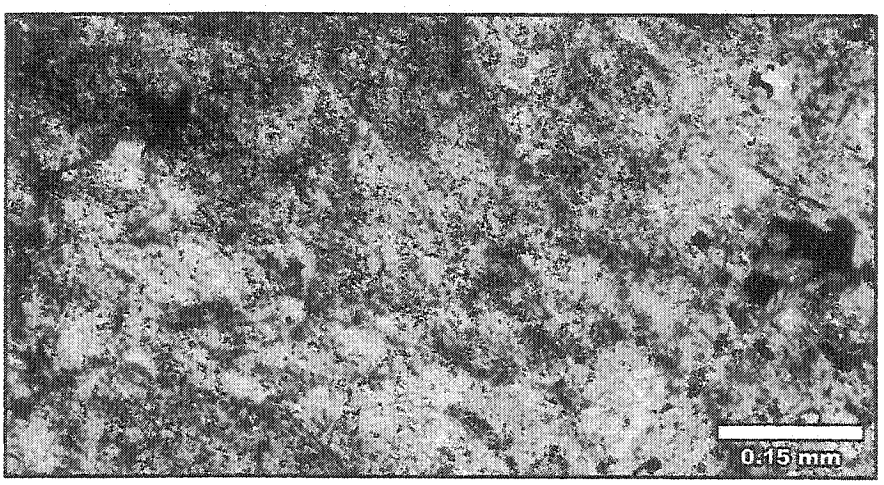

Figure 2.97 Turbid patch perthite. Crossed polars.

frequently inclusions of apatite (Figure 2.100). In general, the crystals are fresh but chlorite alteration is present.

Fresh diopside is not common in the Pangea melasyenite unit (Table 2.9). When present, it is found in partially altered crystals that display subhedral to euhedral basal sections (Figure 2.98). The diopside is tan to light green colored with minor or no pleochroism and displays high birefringence colors.

Titanite, magnetite, pyrite and apatite are accessory minerals in the melasyenite (Table 2.9). Titanite is ubiquitous and sometimes locally highly enriched. One specimen contained 30 to 40 % titanite (Figure 2.101). It occurs as euhedral crystals of various sizes (0.5-5 mm) with rhombic sections. Titanite crystals are commonly twinned. Magnetite is ubiquitous and disseminated throughout the rock. It occurs as subhedral to euhedral crystals ranging in size from 0.5 to 1.5 mm. Apatite is also common, crystals are subhedral and 0.2 to 1 mm in size, and found as inclusions in biotite crystals (Figure 2.100).

Subhedral to euhedral titanian-andradite or melanite was identified in one sample (Figure 2.102; Chapter 3 for mineral chemistry). The crystals vary in size from 0.5 to 2.0 mm and are light brown to dark brown. They commonly contain inclusions of albite, apatite and titanite. Titanian-andradite was also identified in the rocks from Emens intrusion. Titanian-andradite is common in alkaline igneous rocks (Deer et al., 1996).

A particular fine-grained melasyenite unit, intersected in hole G95-101, contains numerous xenoliths of a highly magnetic mafic volcanic rock and fine- to medium-grained hornblendite. The xenoliths range in size from 1 to 20 cm. They are mostly sub-rounded, occasionally sub-angular, and have greenish-gray to green cores and dark green to black reaction rims (Figure 2.103). Also

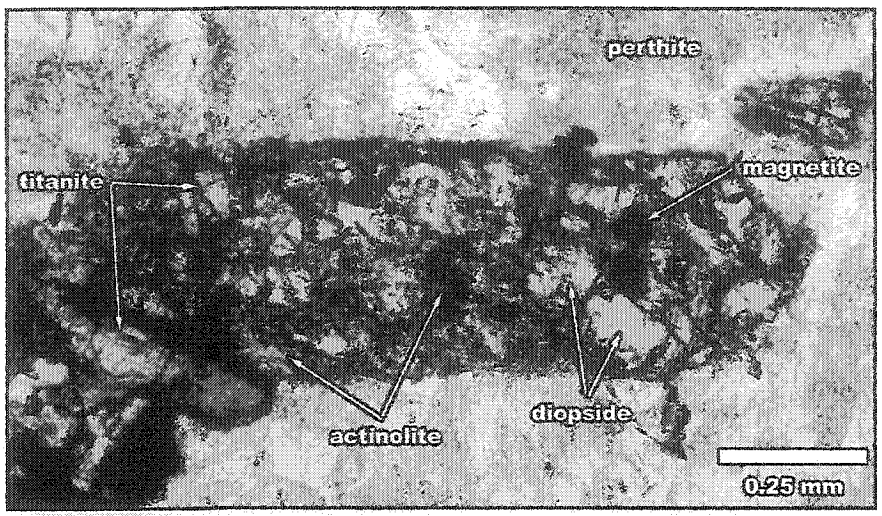

Figure 2.98 Altered diopside crystal displaying a basal section. Parallel polars.

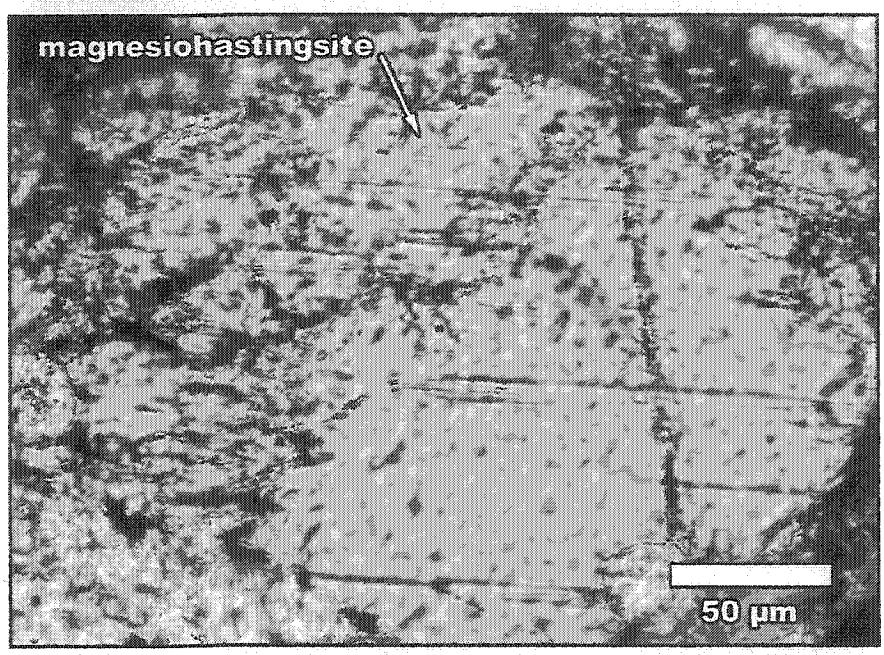

Figure 2.99 Small anhedral magnesiohastingsite crystal found in the matrix. Parallel polars.

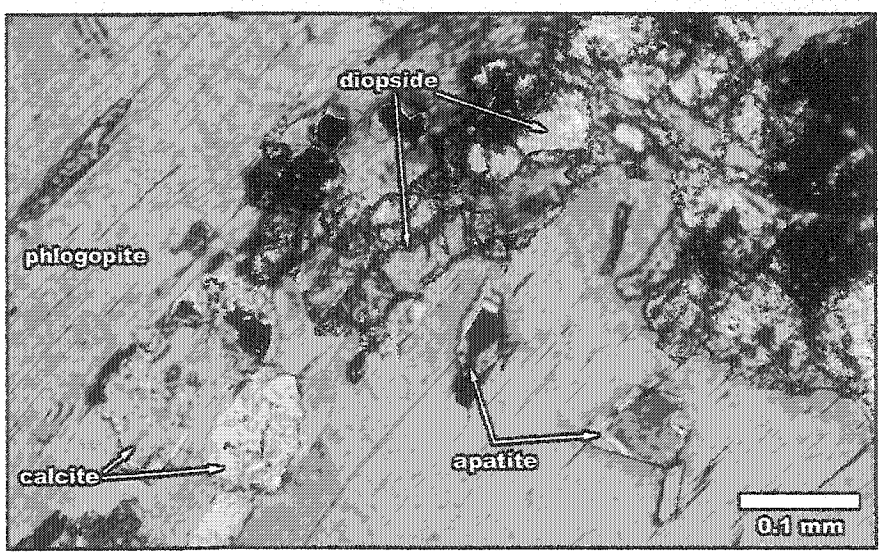

Figure 2.100 Phlogopite crystal containing apatite, calcite and diopside inclusions. Crossed polars.

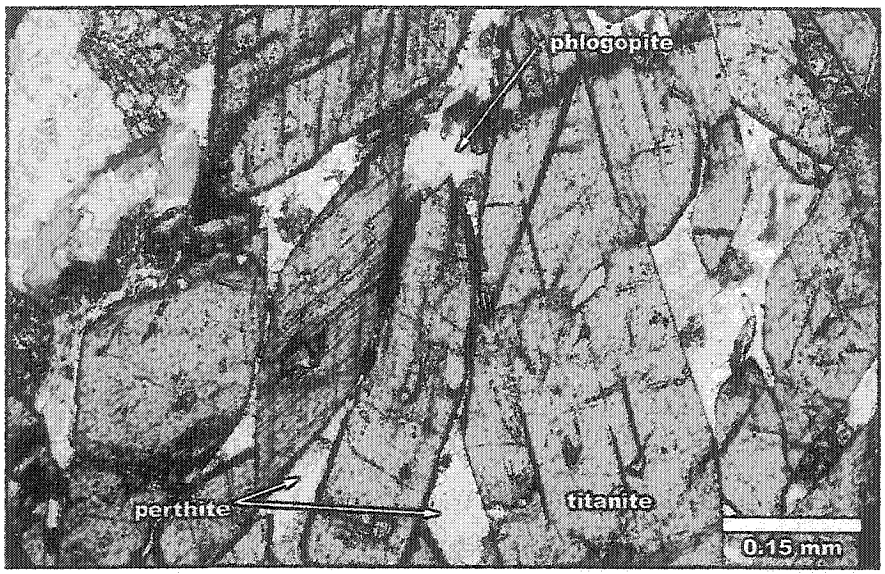

Figure 2.101 Zone highly enriched in euhedral titanite crystals. Parallel polars.

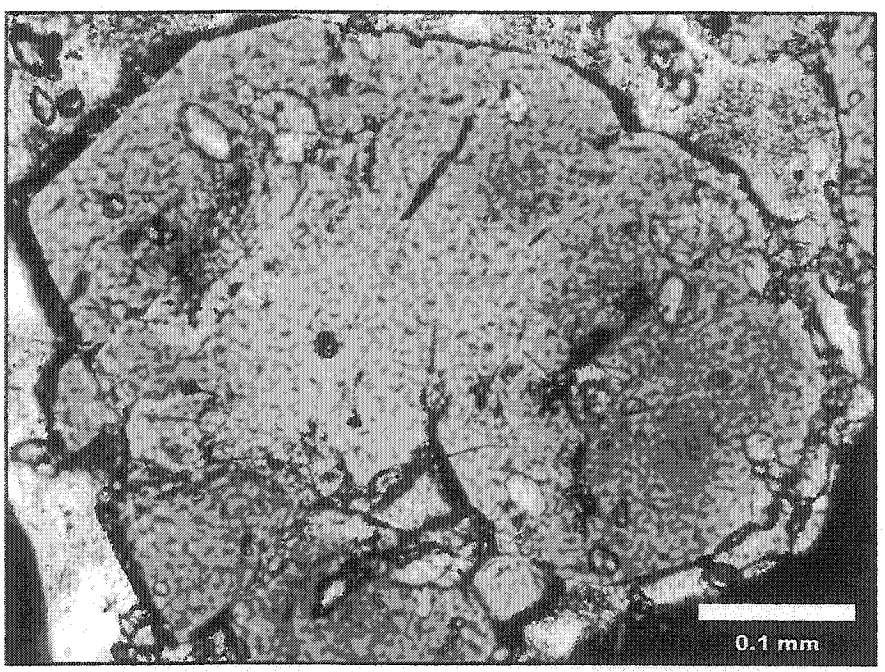

Figure 2.102 Subhedral titanian-andradite crystal. Parallel polars.

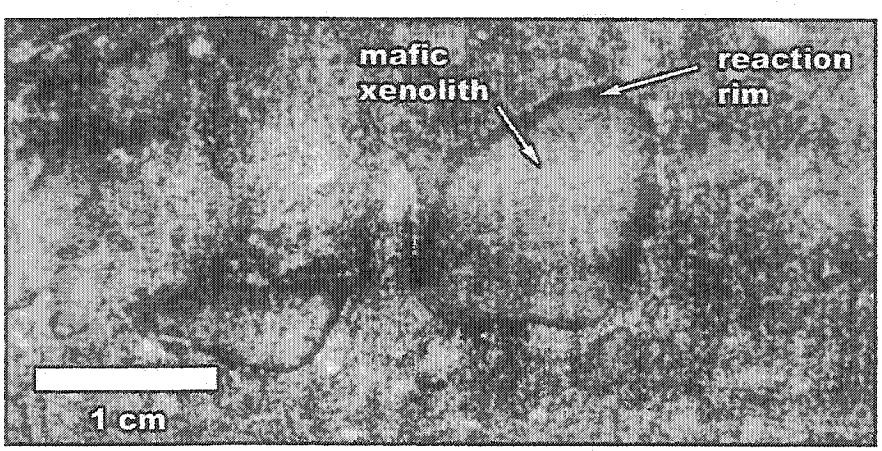

Figure 2.103 Rounded xenolith of mafic volcanic rock with a dark green to black reaction rim.

in this unit, are subhedral to euhedral phenocrysts of pseudoleucite with trapezohedral outlines (Figure 2.104 & 2.105). Pseudoleucite is the alteration product of leucite. It is composed of a mixture of microcrystalline nepheline, orthoclase and analcime (Klein & Hurlburt, 1993). The phenocrysts vary in size from 1 to 10 mm but several larger crystals (1-3 cm) were observed. The pseudoleucite phenocrysts are white to light gray colored and account for 2 to 5 % of the mode. The presence of pseudoleucite in this rock is of great significance and provides insights on the composition of the magma since leucite only crystallizes in silica undersaturated and highly K-enriched magmas (Deer et al., 1996).

C. Alkali-feldspar syenite

The alkali-feldspar syenite is the least abundant rock type in the Pangea intrusion diamond drill core. The alkali-feldspar syenite (hereinafter called AF syenite) is most frequently found as dykes of various thickness (0.2-5 m) that crosscut the pyroxene-bearing hornblendite and melasyenite units. The syenite unit was rarely observed in gradational contact with the melasyenite unit.

The AF syenite rock is composed of medium- to coarse-grained anhedral light pink to purplish-pink perthite (Figure 2.106) and sometimes contains minor 0.5 to 2 mm long, subhedral to euhedral prismatic green to dark green altered amphibole and dark brown to black, 0.5 to 1.5 mm, anhedral phlogopite (Table 2.10). The AF syenite is locally porphyritic with subhedral to euhedral, 1 to 3 cm tabular phenocrysts of perthite (Figure 2.107). The megacrysts are of various colors from light gray to light pink to light orange. The AF syenite rock displays numerous colors from light pink to light purple to brick-red. The color variation within this unit is a function of the intensity of hematization of the rock. Hematization is the most common alteration but epidote and sericite nodules and carbonate veins are also present.

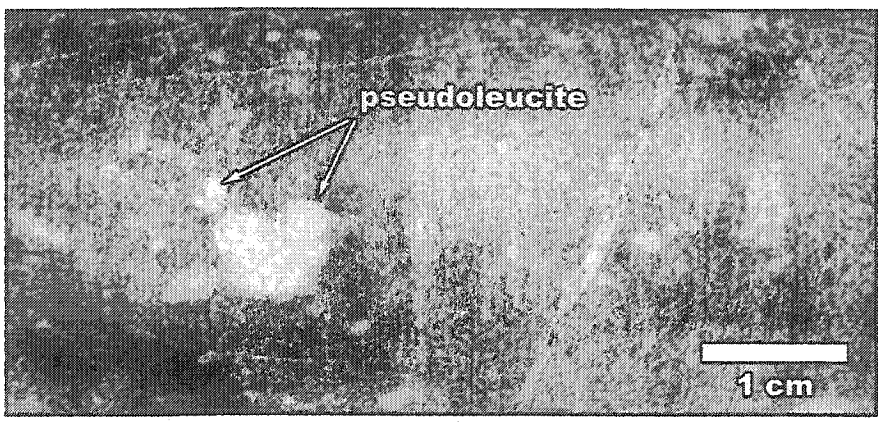

Figure 2.104 Pseudoleucite crystals in a fine-grained melasyenite.

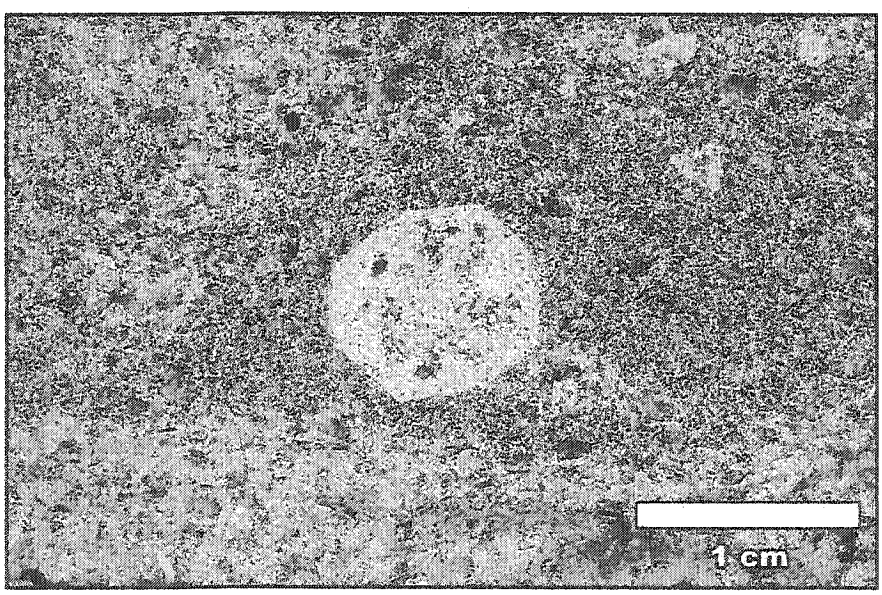

Figure 2.105 Pseudoleucite crystals in a fine-grained melasyenite. Parallel polars. (courtesy of Ben Berger, Ontario Geological Survey)

Mineral	Modal%
Perthite	80-85
Actinolite	2-5
Chlorite	5-10
Phlogopite	1-5
Albite	1-2
Magnetite	1-2
Titanite	1-2
Pyrite	1-2
Epidote	1
Garnet	tr.
Muscovite	tr.
Secondary calcite	tr.
Monazite	tr.

Table 2.10 Range of modal composition of the alkali-feldspar syenite unit.

Under the microscope, perthite crystals are turbid, anhedral and 2 to 6 mm in size. They display a patch perthite texture and are composed of 50 to 60 % potassic domains that range from 10 to 30 μm across (Figure 2.108). Vein perthite is also common (Figure 2.109). Some vein perthite crystals have albite zones that cross-cut the exsolution lamellae (Figure 2.109). This texture likely results from albitization along fractures in the perthite. Sodic domains of some perthite megacrysts display albite twinning (Figure 2.110). Potassic domains generally do not exhibit any twinning. However, they are generally more turbid than the sodic ones. The perthite megacrysts are of similar composition than the smaller perthite crystals of the unit. They are commonly twinned according to the Carlsbad law (Figure 2.111) and are also rimmed by clear secondary anhedral albite showing good albite twinning. A minor amount of subhedral albite crystals is also present. These crystals are 0.2 to 0.6 mm long and rectangular shaped. They are turbid but albite twinning was usually visible.

Amphibole is usually almost completely altered to chlorite. Only small remnants of actinolite are preserved within the mass of chlorite. They actinolite displays pale green to green pleochroism. Phlogopite displays light yellow to dark olive green pleochroic colors. It is partially to completely altered to chlorite (Figure 2.112). Chlorite is intimately associated with small (0.1-0.2 mm) anhedral crystals of magnetite.

Garnet was identified in one sample (i.e. lmp-180). It is tan to light brown and interstitial to euhedral perthite laths (Figure 2.113).

Epidote, magnetite, pyrite and titanite are all minor but ubiquitous components of the syenite rock. Titanite was observed as inclusions in some perthite megacrysts (Figure 2.111). Anhedral calcite and muscovite occur in small pockets or veinlets.

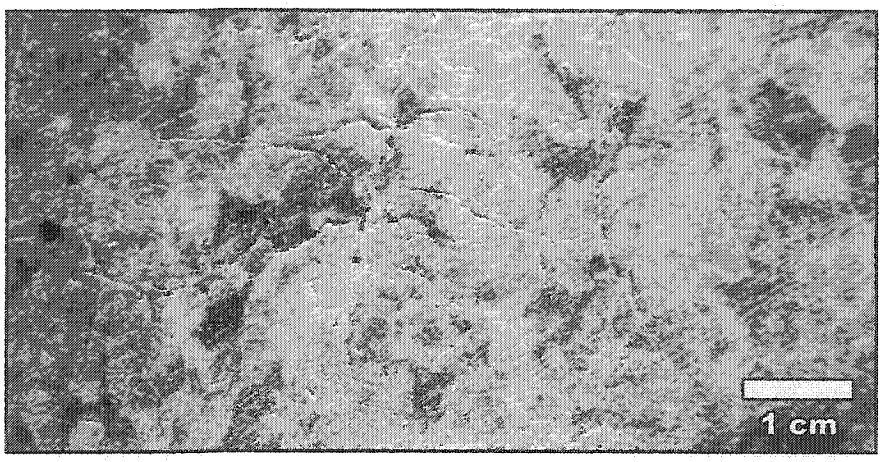

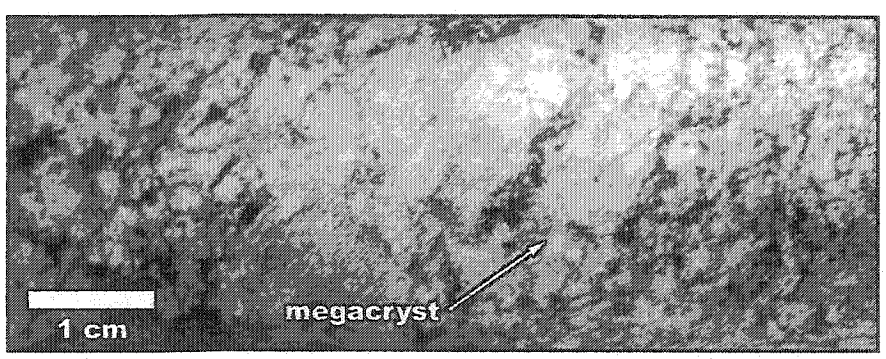

Figures 2.106 & 2.107
The alkali-feldspar syenite rock. The rock is composed of medium- to coarse-grained anhedral light pink to purplish-pink perthite and sometimes contains minor 0.5-2 mm long, subhedral to euhedral, prismatic green to dark green altered amphibole and dark brown to black, 0.5-1.5 mm, anhedral phlogopite. The AF syenite is locally porphyritic with subhedral to euhedral, 1-3 cm tabular megacrysts of perthite.

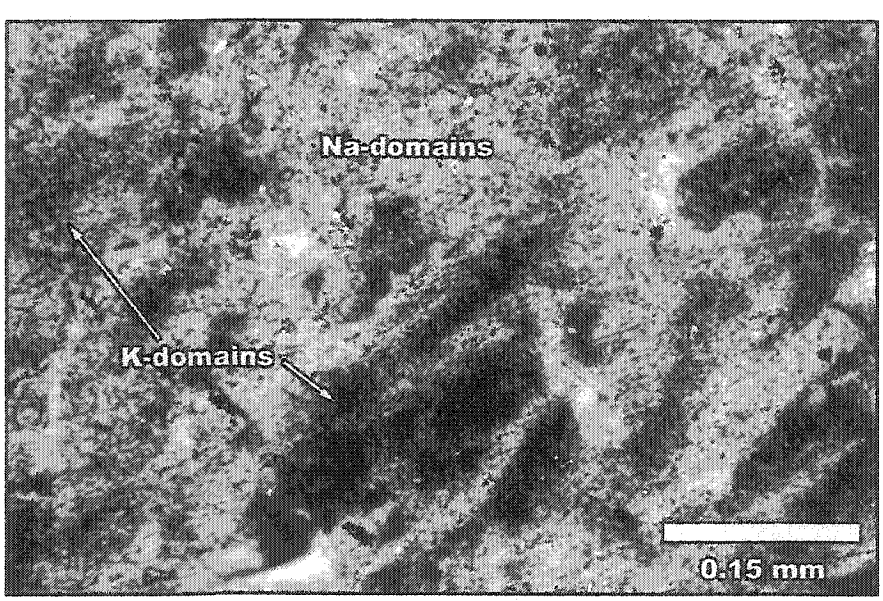

Figure 2.108 Turbid patch perthite. K-domains are extinct. Crossed polars.

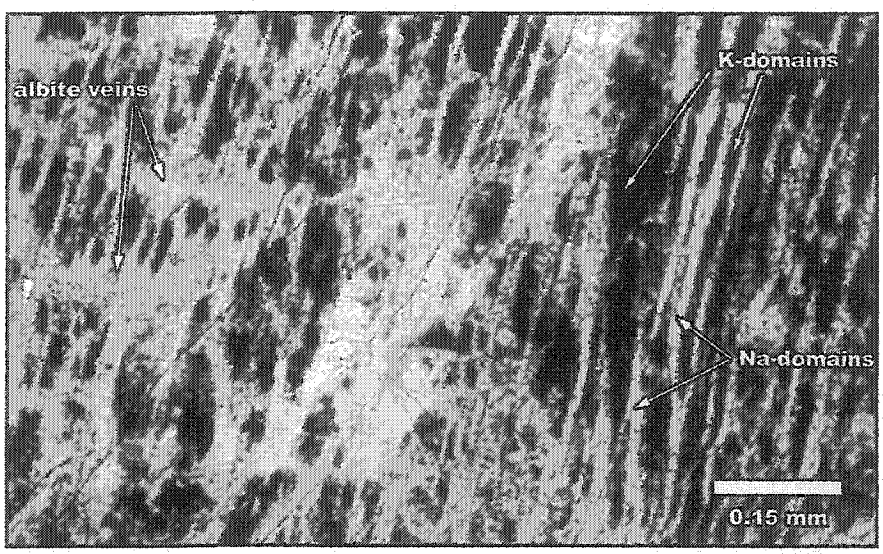

Figure 2.109 Vein perthite with cross-cutting thick albite veins. They likely result from albitization along fractures in the perthite grain. K-domains are extinct. Crossed polars.

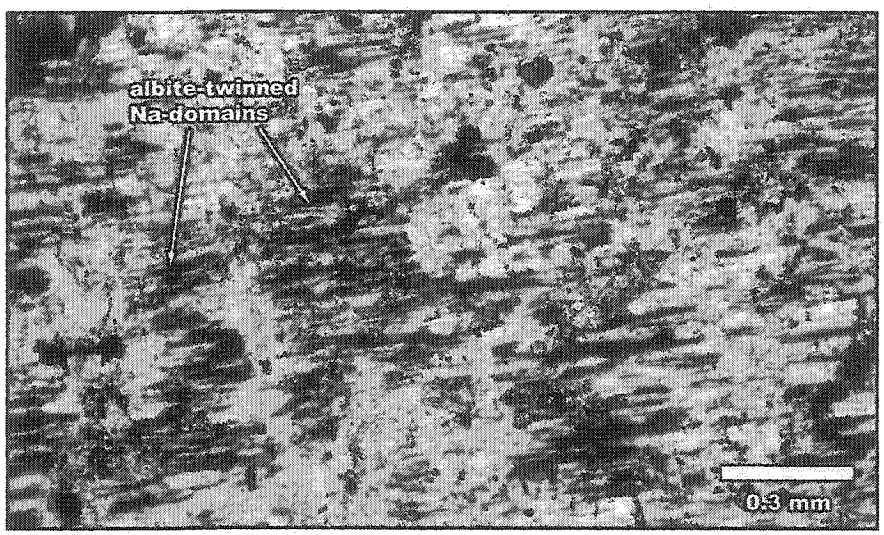

Figure 2.110 Patch perthite containing albite-twinned Na-domains. Crossed polars.

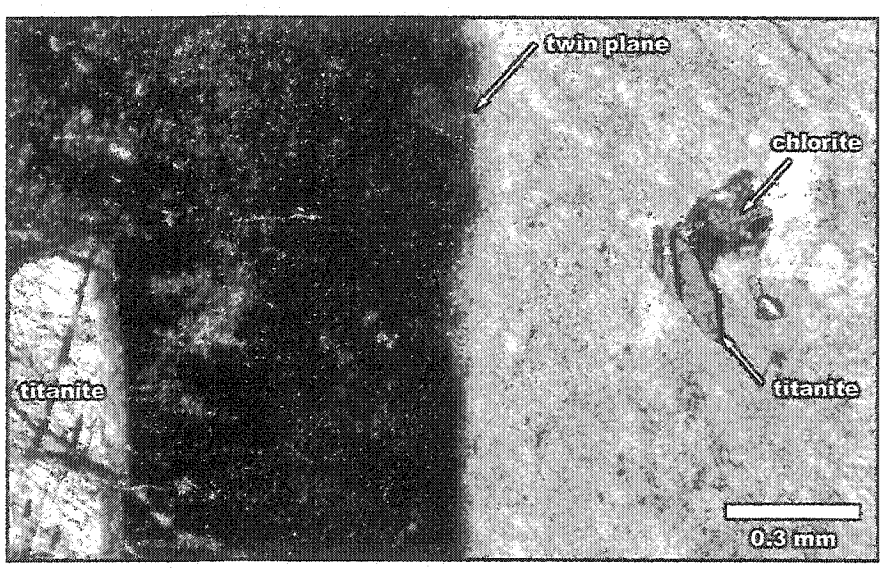

Figure 2.111 Carlsbad-twinned perthite megacryst. The crystal contains titanite and chlorite inclusions. Crossed polars.

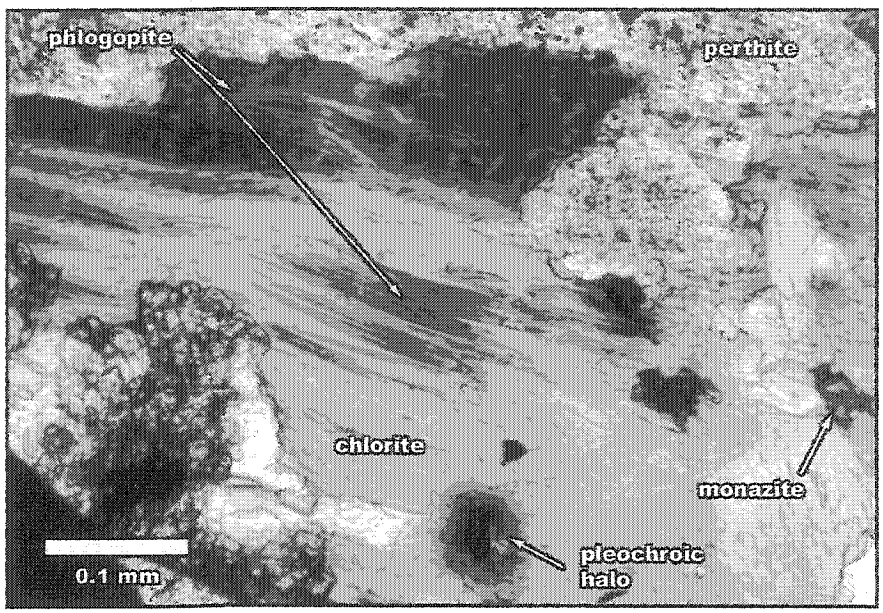

Figure 2.112 Anhedral phlogopite crystal almost completely altered to chlorite. Monazite inclusions are circled by pleochroic halos. Parallel polars.

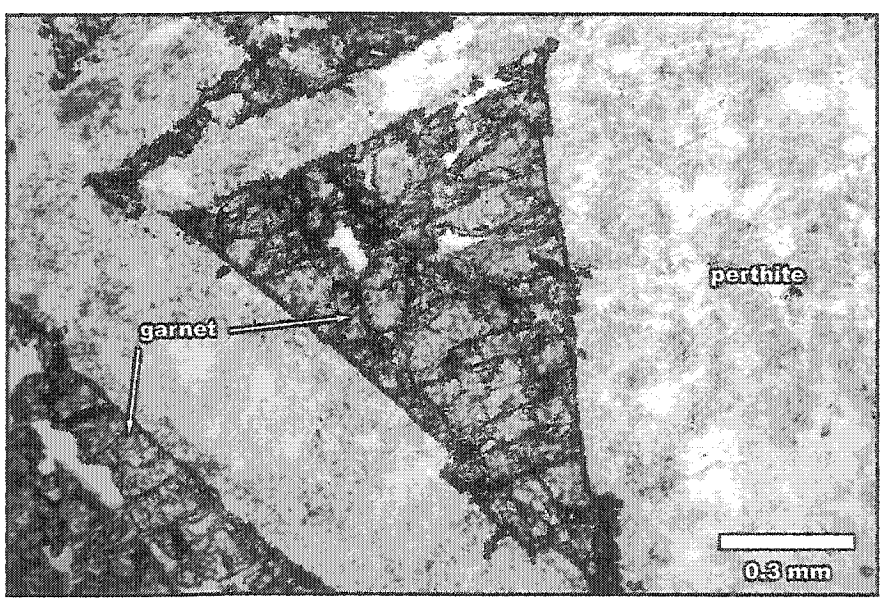

Figure 2.113 Garnet crystals interstial to turbid perthite laths. Parallel polars.

V. Garrison intrusion

A. Hornblende quartz-monzonite

The Garrison intrusion is composed of medium-grained, equigranular hornblende quartz-monzonite containing a variable amount of quartz and magnesiohornblende (Figure 2.114; Table 2.11). The rock is light pink colored and is usually fresh but light hematization is common. Occasionally the rock is porphyritic and contains subhedral to euhedral phenocrysts of perthite and/or anhedral to subhedral phenocrysts of magnesiohornblende (Chapter 3 for mineral chemistry). The perthitic feldspar phenocrysts are white to light gray, 3 to 4 mm in size and usually display rectangular sections. The magnesiohornblende phenocrysts are dark green to black and have a prismatic shape with long axes that can reach up to 6 mm. Small purple zones are visible in some specimens (Figure 2.115). These zones result from a local concentration of very fine disseminated fluorite.

Mineral	Modal%
Perthite	40-50
Albite	30-40
Quartz	5-15
Magnesiohornblende	5-10
Magnetite	1
Titanite	1
Apatite	tr.
Fluorite	tr.
Pyrite	1-2
Aegirine-augite	tr.
Magnesioriebeckite	tr.
Richterite	tr.

Table 2.11 Range of modal composition of the hornblende quartz-monzonite unit.

Perthite is the major component of the rocks of the Garrison intrusion (Table 2.11). It occurs as subhedral phenocrysts and anhedral to subhedral crystals in the matrix. Exsolution domains are usually well developed and easily visible under crossed polars. Vein perthite (Anderson, 1928) is the most common perthitic feldspar present (Figure 2.116) however, minor patch perthite (Anderson, 1928) and braid perthite (Goldich & Kinser, 1939) are also present. Potassic domains are more abundant (60-70 %) than the Na-domains. The K-domains commonly display tartan twinning

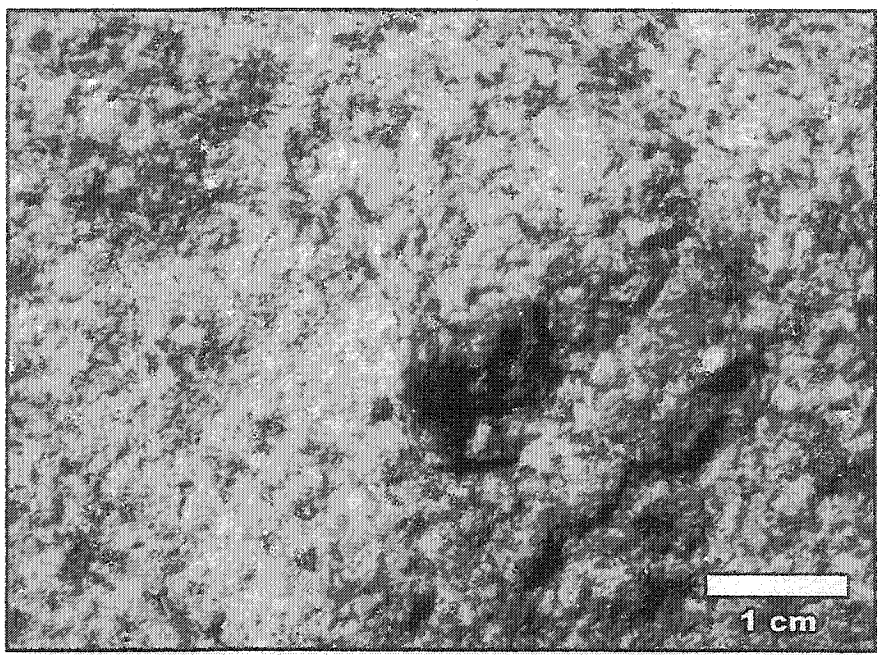

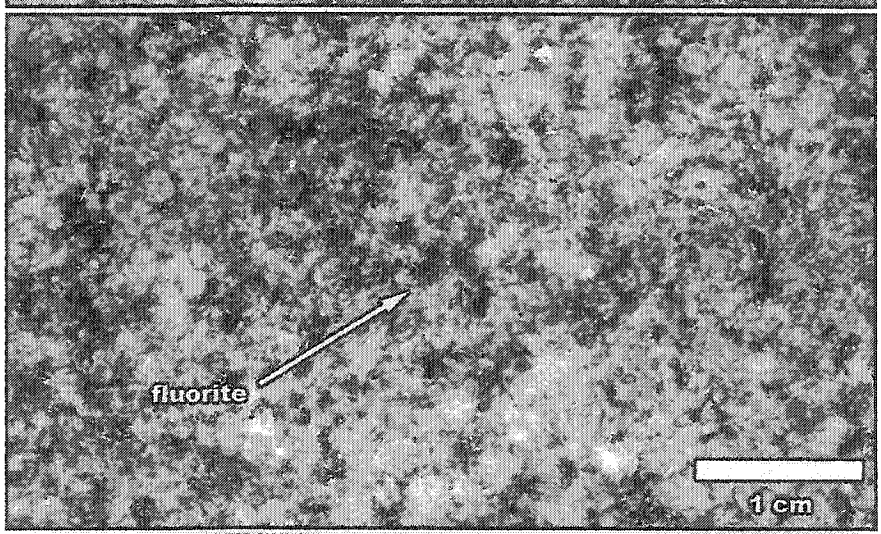

Figures 2.114 & 2.115
The hornblende quartz-monzonite rock. The rock is equigranular and contains a variable amount of quartz and magnesiohornblende. When porphyritic, the rock contains subhedral to euhedral phenocrysts of perthite and/or anhedral to subhedral phenocrysts of magnesiohornblende. Fluorite was identified in some samples.

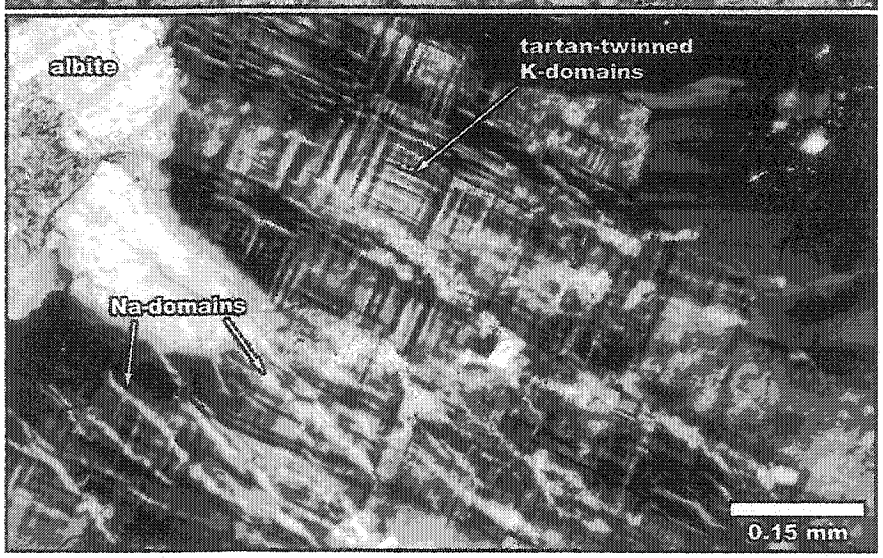

Figure 2.116 Vein perthite displaying tartan-twinned K-domains. Crossed polars.

(Figure 2.116). Twinning was usually not visible in the Na-domains. Perthite crystals commonly contain anhedral to subhedral albite inclusions displaying albite twinning (Figure 2.117). Perthite crystals are turbid and often contain patches of sericite alteration.

A minor amount of antiperthitic feldspar was identified (Figure 2.118). The antiperthite crystals are subhedral, 1 to 2 mm in size and contain 20 to 30 % K-domains. The K- and Na-domains respectively display good crosshatch and albite twinning (Figure 2.118).

In addition to its occurence in the perthite, albite also occurs as discrete anhedral to subhedral crystals varying in size from 0.5 to 2 mm. The crystals display good albite twinning and in some cases Carlsbad twinning. Albite crystals are frequently zoned. Zoned crystals have albite-twinned turbid cores and clear rims that do not display any visible twinning. Most albite crystals are highly turbid.

Amphibole is the most common ferromagnesian mineral in the Garrison intrusion (Table 2.11). Three amphibole species were encountered: magnesiohornblende, richterite and magnesioriebeckite. Magnesiohornblende crystals are subhedral to euhedral and 0.7 to 1 mm in size but partially altered phenocrysts can be up to 6 mm long. They display light green to olive green pleochroism and commonly contain small inclusions of apatite and magnetite (Figure 2.119). Euhedral crystals of magnesiohornblende are sometimes twinned (Figure 2.120). A few crystals of richterite and magnesioriebeckite were also identified using the microprobe (Figure 2.121). These amphiboles are anhedral and vary in size from 0.6 to 0.8 mm. They display light yellowish-green to light bluish-green pleochroic colors.

Pyroxene was identified in only one sample of the Garrison intrusion. It occurs as emerald green to light green pleochroic, 0.2 to 0.3 mm anhedral crystals of aegirine-augite (Figure 2.122). Some crystals contain minor small inclusions of apatite and turbid albite.

Magnetite and titanite are the most common accessory minerals present (Table 2.11). Both are ubiquitous and form small (0.2-0.4 mm) subhedral to euhedral crystals. Titanite crystals commonly display rhombic sections.

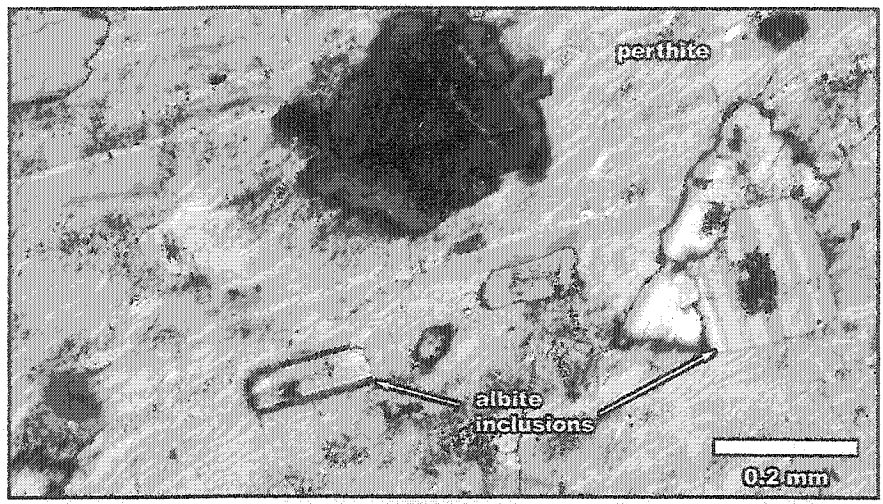

Figure 2.117 Perthite crystal containing albite inclusions. Albite twinning is visible in the inclusions. Crossed polars.

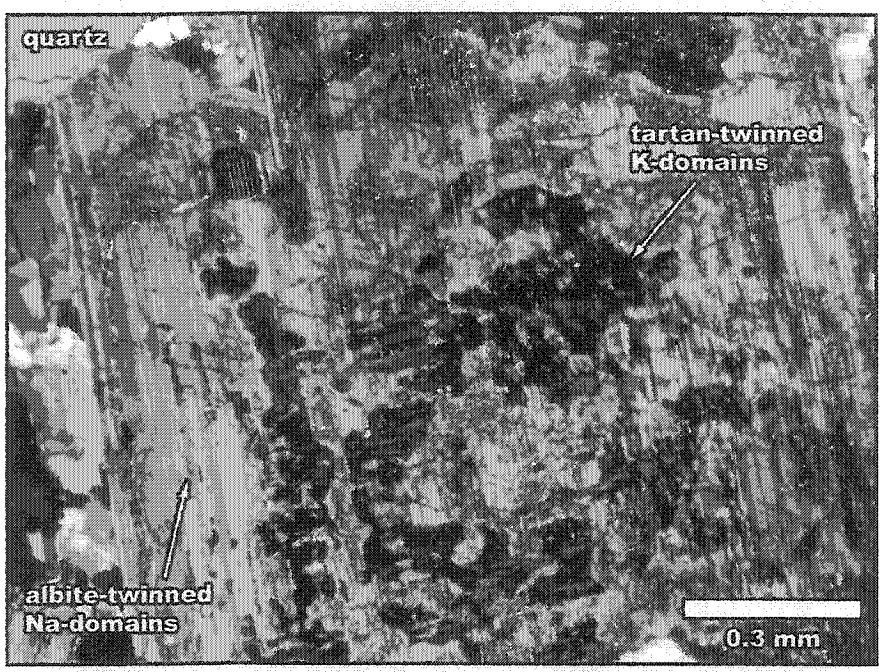

Figure 2.118 Antiperthite crystal containing albite-twinned Na-domains and tartan-twinned K-domains. Crossed polars.

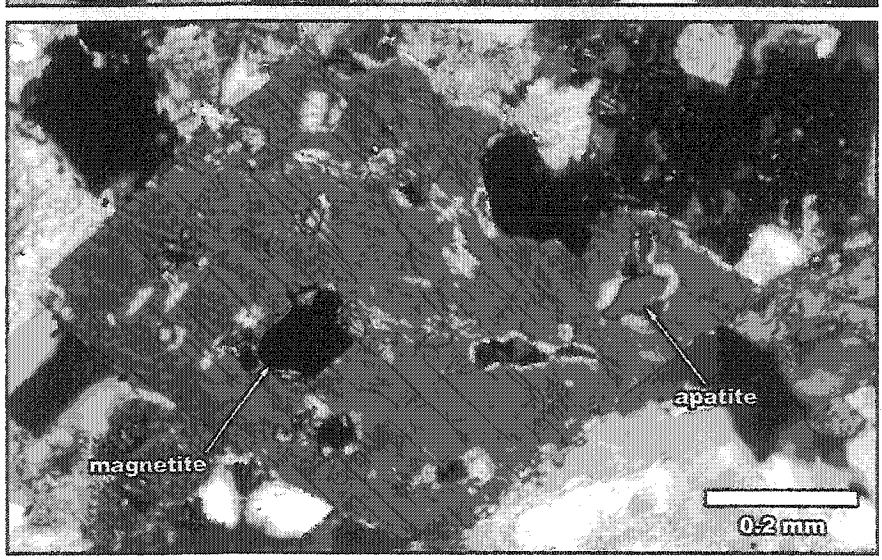

Figure 2.119 Euhedral crystal of magnesiohornblende containing magnetite and apatite inclusions. Crossed polars.

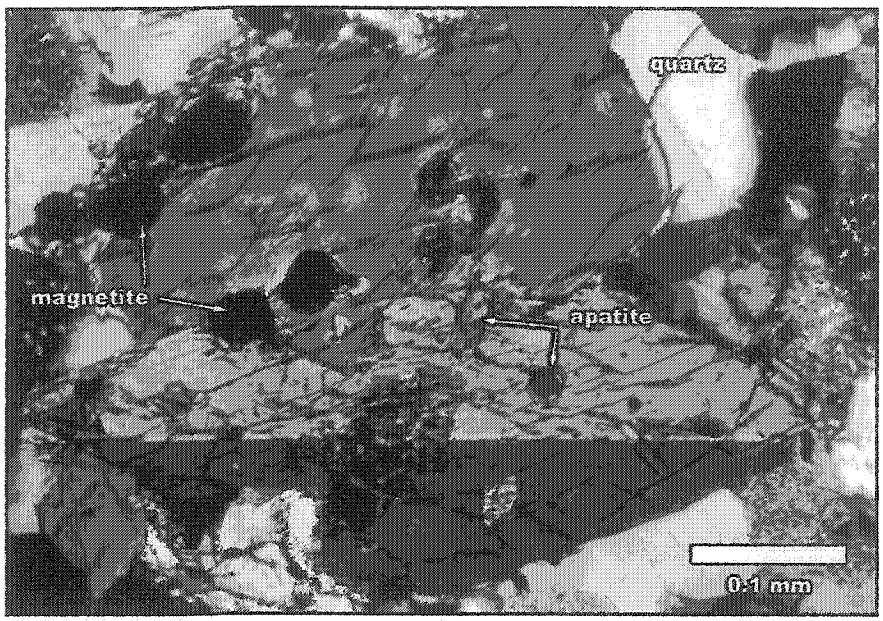

Figure 2.120 Twinned euhedral crystal of magnesiohornblende containing magnetite and apatite inclusions. Crossed polars.

Figure 2.121 Anhedral crystal of richterite. Rutile is visible along some cleavage planes. Parallel polars.

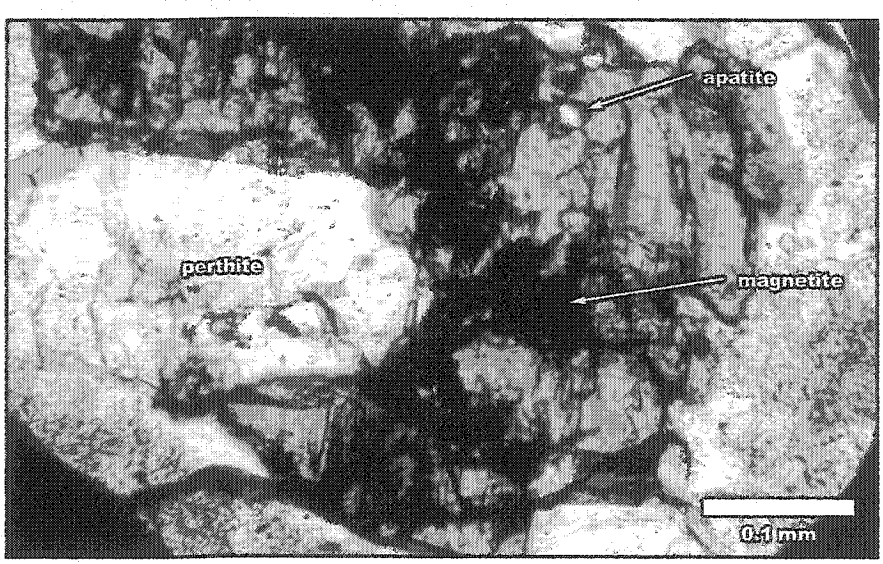

Figure 2.122 Anhedral crystal of aegirine-augite containing apatite and magnetite inclusions. Parallel polars.

VI. Ludgate intrusion

A. Alkali-feldspar quartz-syenite

The Ludgate intrusion is composed of coarse-grained alkali-feldspar quartz-syenite (hereinafter syenite) with large (1-3 cm) light gray to purplish-gray subhedral to euhedral tabular perthite phenocrysts. The color of the rock is variable and depends on the degree of hematization. In the least hematized samples the rock is purplish-gray whereas it is brick-red in the highly hematized ones (Figure 2.123 & 2.124). The rock is leucocratic, with a color index commonly less than 10 (Table 2.12). Large subhedral to euhedral crystals of black tourmaline are common near cataclastic fracture zones. The rock surrounding these zones is highly hematized, giving it a brick-red color. Primary (magmatic) flow alignment of perthite crystals producing a trachytic texture was observed near the fracture zone and in a nearby syenite dyke (Figure 2.124 & 2.125). The aligned tabular perthite are 1 to 3 cm long and are dark purplish-gray near the fracture zone and light gray to pinkish-gray in the dyke.

Perthite is the major component of the Ludgate syenite (Table 2.12). In the matrix, it occurs as anhedral to subhedral crystals varying in size from 1 to 3 mm. The large phenocrysts are subhedral to euhedral and 10 to 15 mm in size but can reach up to 3 cm. The smaller crystals are fresh whereas the large phenocrysts are commonly turbid. The Na- and K-domain distribution within the crystals is variable but Na-domains are usually dominant (45-75 %), therefore classifying these perthitic feldspars as antiperthite (Na>K). Exsolution lamellae are thin but elongated with aspect ratios in excess of 20:1, producing a texture

Mineral	Modal%
Perthite	70-75
Secondary albite	10-15
Quartz	5-10
Magnesioriebeckite	5
Aegirine-augite	tr.
Apatite	tr.
Magnetite	tr.
Pyrite	tr.

Table 2.12 Range of modal composition of the alkali-feldspar quartz-syenite unit.

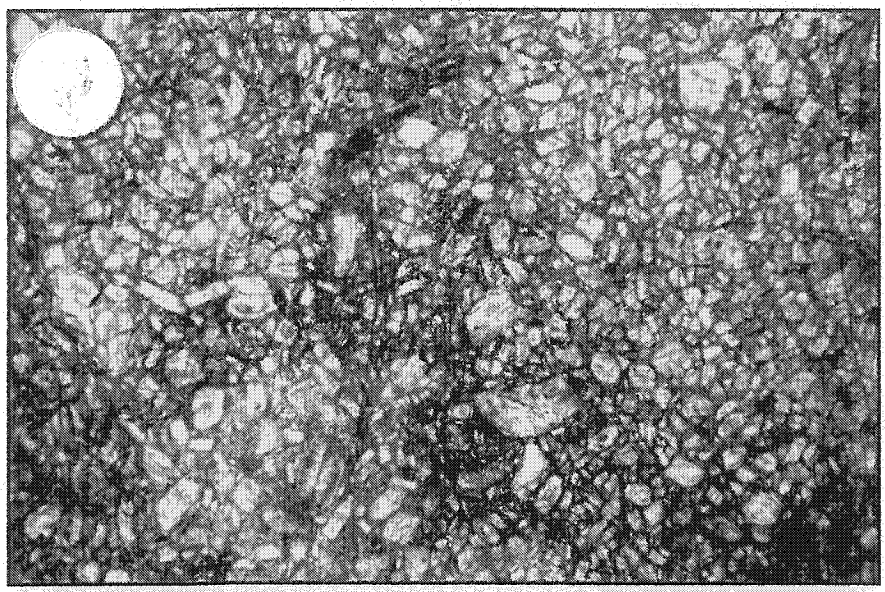

Figure 2.123 Hematized alkali-feldspar quartz-syenite rock. The rock contains large (1-3 cm) light gray to purplish-gray subhedral to euhedral tabular perthite phenocrysts. In the least hematized samples the rock is purplish-gray whereas it is brick-red in the highly hematized ones.

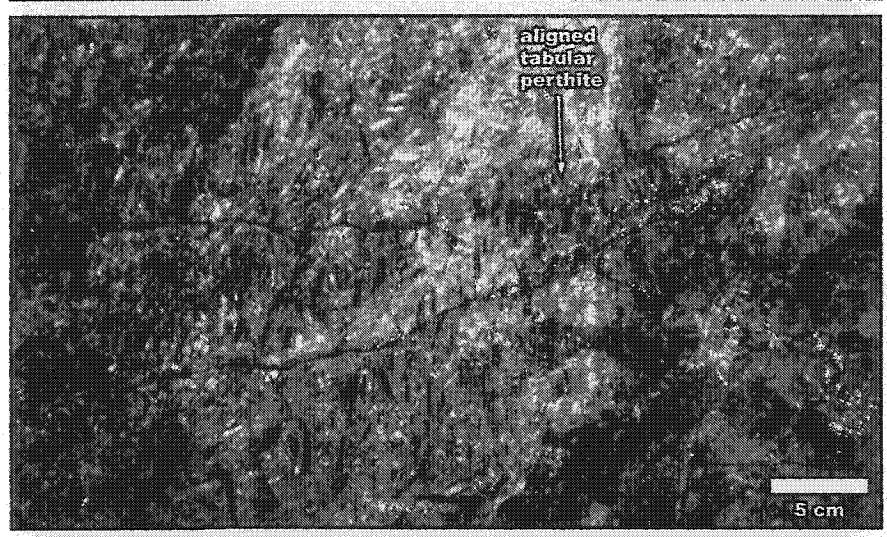

Figure 2.124 Highly hematized alkali-feldspar quartz-syenite rock containing aligned tabular dark purplish-gray perthite crystals.

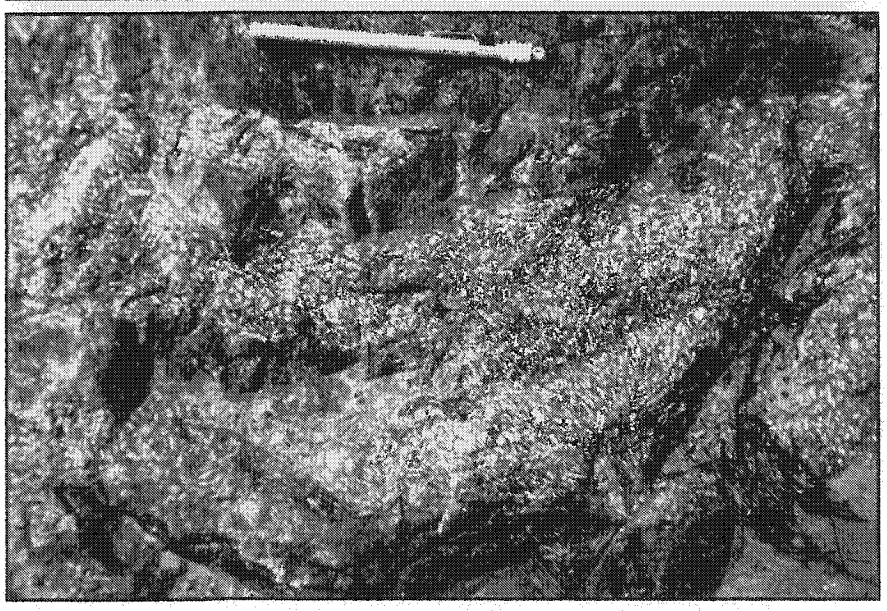

Figure 2.125 Hematized alkali-feldspar quartz-syenite dyke containing aligned tabular light gray perthite crystals.

closely resembling plate perthite. Patch perthite is also present. Apart for a few exceptions, twinning is absent from both Na- and K-domains. However, Carlsbad twinning is visible in some large phenocrysts. Figure 2.126 is an example of a Carlsbad-twinned crystal. On this particular crystal, which is most likely a cross section perpendicular to [001], the intersection of the twins is clearly defined by the opposite extinctions and the «reflection» of the exsolution lamellae. The irregular-shaped twin plane observed on Figure 2.126 may result from an interpenetrating Carlsbad twin.

Some perthite phenocrysts display a complex interplay of exsolution textures and compositional zoning. This is illustrated on Figure 2.127, where compositional zones and exsolution lamellae are perpendicular to one another in the lower left side of the image, and are oriented at ~60° to one another in the rest of the crystal. The zones are of various thickness that range between ~10 and 300 μm. Three broad zone compositions were identified: (1) pure albite, (2) antiperthite (Na>K) and (3) perthite (Na<K). Albite zones are located near the core and are thin (10-20 μm) relative to the other zones. They do not contain any exsolution lamellae. The antiperthite zones are the thickest (25-140 μm) and most abundant (~90 % of crystal). In general, they are composed of ~25 % thin elongated K-domains ranging in thickness from 3 to 6 μm and in length from 50 to 120 μm (Figure 2.127). However, the thin antiperthite zones separating the albite ones tend to have variable composition i.e. part of the zone is perthitic while the rest is antiperthitic (Figure 2.127). Upon closer inspection with the scanning electron microscope (SEM) these heterogeneous zones were shown to contain two distinct K-exsolution compositions (Figure 2.128a & 2.128b). Indeed, the energy spectra obtained on the EDS unit of the SEM revealed that certain K-exsolution lamellae are enriched in barium compared to the others. This compositional variation produces two different shades of gray on the back-scattered electron images, the lighter one corresponding to the Ba-enriched domains (Figure 2.129a & 2.129b).

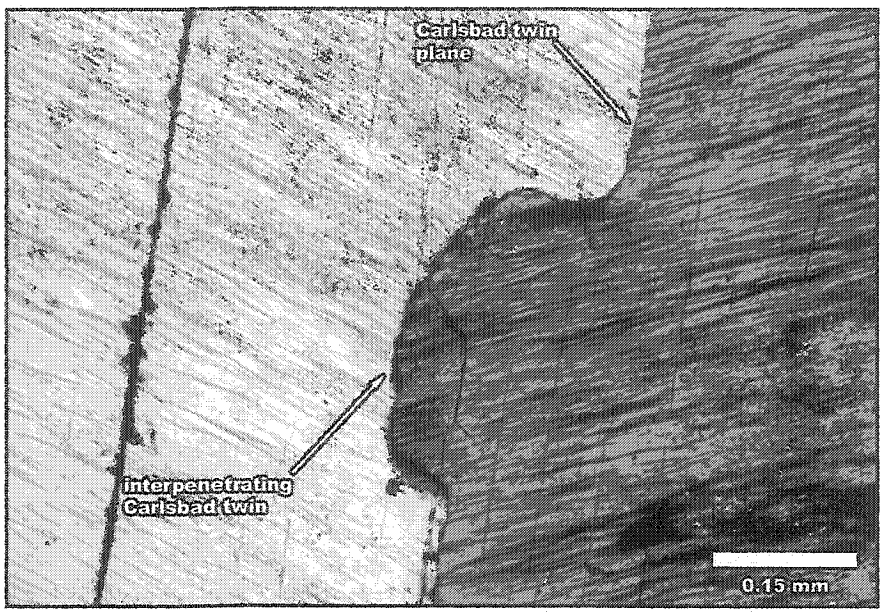

Figure 2.126 A perthite crystal displaying Carlsbad-twinning. The twin plane is clearly defined by the opposite extinctions and the «reflection» of the exsolution lamellae. The irregular-shaped twin plane is likely the result of an interpenetrating Carlsbad twin. Crossed polars.

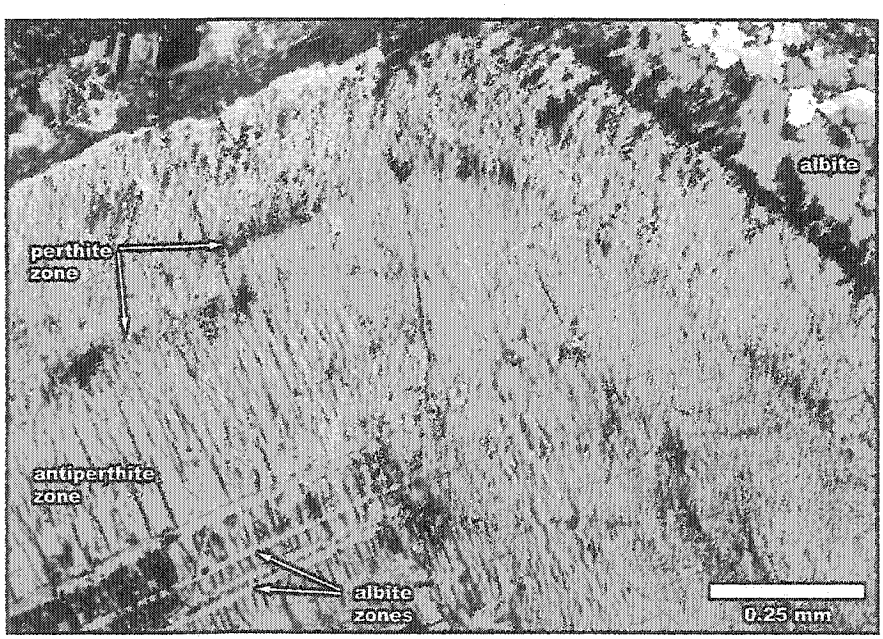

Figure 2.127 Perthite crystal displaying a complex interplay of exsolution textures and compositional zoning. See text for description. Crossed polars.

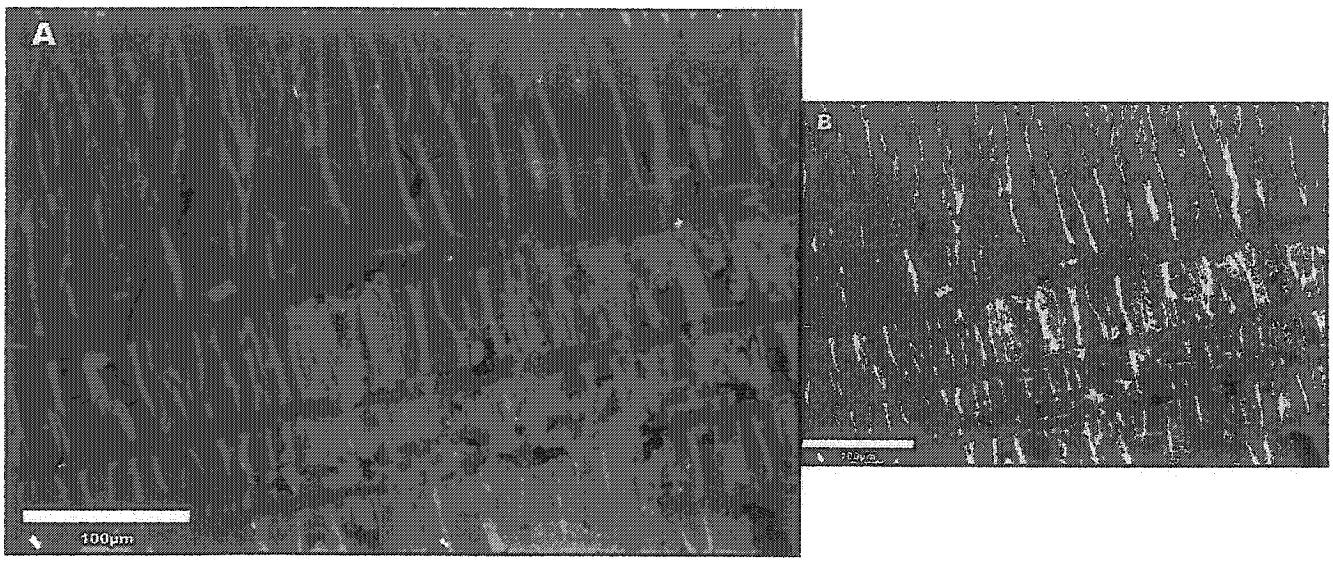

Figure 2.128a & b Back-scattered electron image (a) and corresponding false-color back-scattered electron image (b) of a zoned antiperthite crystal (same crystal as Figure 2.127). The albite zones and the two distinct K-rich exsolution domains are clearly visible on both images. See text for description. Red=albite; yellow=Ba-rich K-feldspar; blue=K-feldspar.

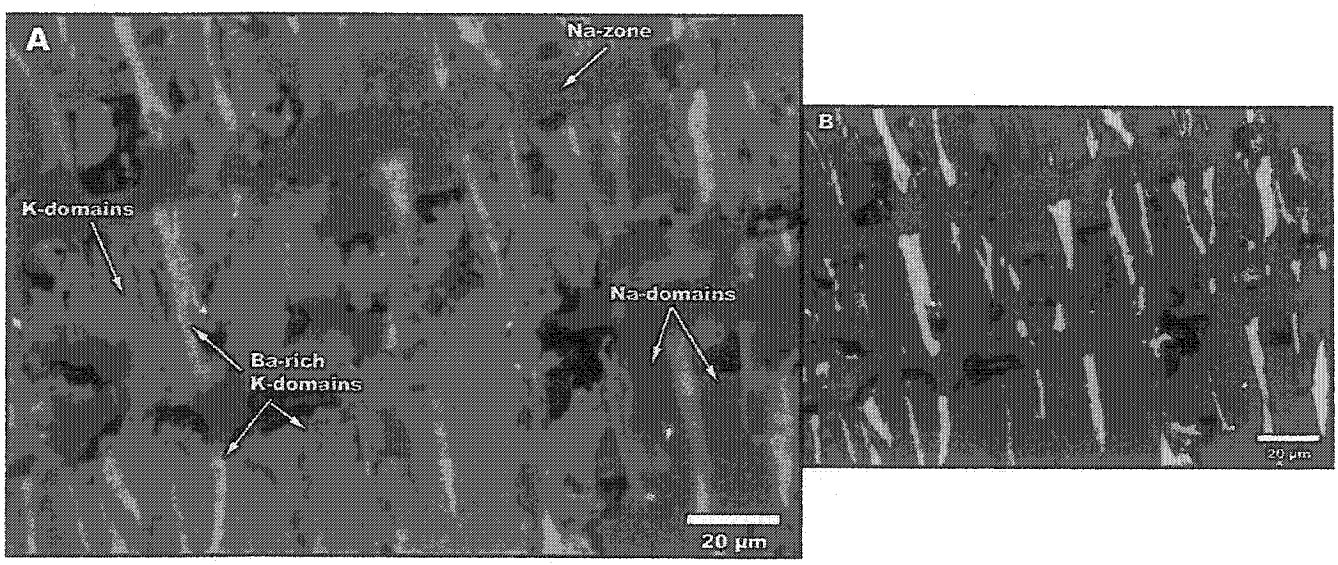

Figure 2.129a & b Back-scattered electron image (a) and corresponding false-color back-scattered electron image (b) of a zoned antiperthite crystal (close-up of Figure 2.128). The albite zones and the two distinct K-rich exsolution domains are clearly visible on both images. See text for description. Red=albite; green=Ba-rich K-feldspar; blue=K-feldspar.

The perthite zones are located near the rim (Figure 2.127) and are distinguished from the others by their high turbidity and different extinction angle.

Late albite is common in the Ludgate syenite (Table 2.12). It occurs as anhedral to subhedral crystals varying in size from 0.2 to 1 mm. The crystals are clear, fresh looking and interstitial or rimming the larger grains of perthite.

Sodic pyroxene and amphibole are not common in the Ludgate rocks (Table 2.12). Aegirine-augite occurs as small (0.2-0.4 mm) anhedral to subhedral grains (Figure 2.130). It normally displays yellowish-green to pale green to pale olive green pleochroism. Magnesioriebeckite crystals are generally anhedral, however a few crystals have euhedral shapes with acicular habit (Figure 2.131). Magnesioriebeckite crystals display light blue to light purplish-blue pleochroic colors.

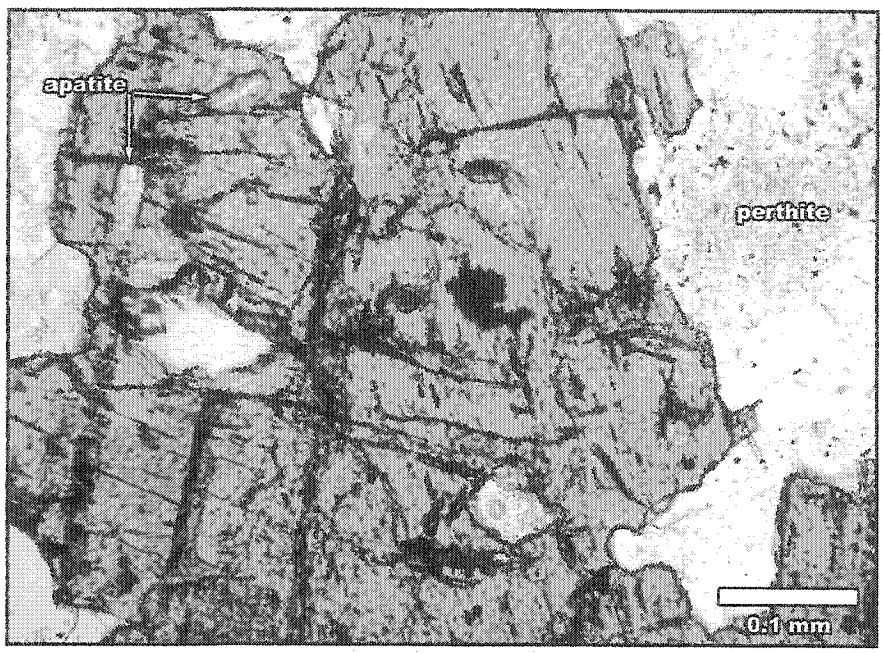

Figure 2.130 Anhedral crystal of aegirine-augite containing apatite inclusions. Parallel polars.

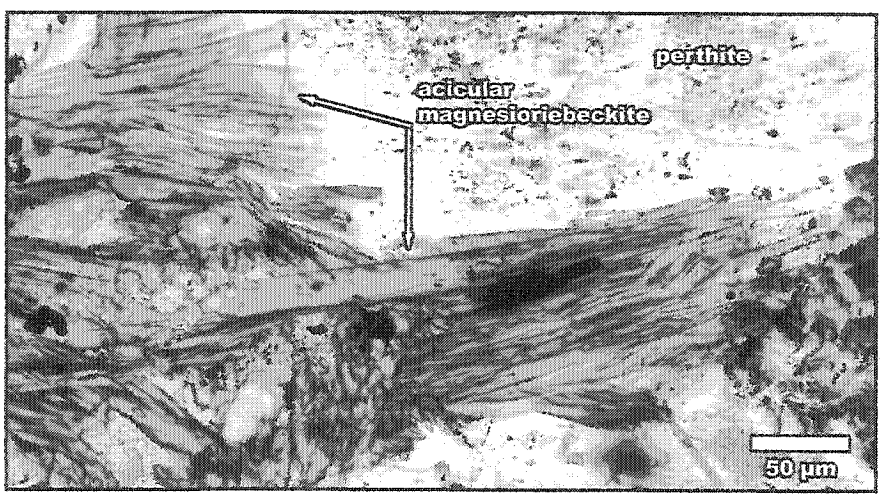

Figure 2.131 Acicular magnesio-riebeckite crystals. Parallel polars.

Chapter 3

Mineral chemistry

I. Analytical methods

All mineral analyses were carried out by wavelength-dispersive X-ray spectrometry on a Cameca electron microprobe at the Geoscience Laboratories, Ontario Geoservices Centre, Sudbury. Calibration and analyses were performed using a series of natural and synthetic standards. The acquired data was reduced using the PAP software package developed by Pouchou and Pichoir (1984). Operating conditions were set to 20kV and 10 to 20 nA using a beam diameter of 3 to 12 μm, the current and diameter dependent upon the mineral analysed. Since, for WDS analyses, alkali feldspars may be unstable for an electron beam narrower than 10 μm (Smith & Brown, 1974), a defocused beam with a diameter of 10-12 μm was used for all the feldspar analyses. Counting time varied between 10 to 20 seconds per element.

II. Pyroxene

A total of 25 pyroxene analyses were performed. All pyroxene formulae were calculated on the basis of 4 cations and 6 anions (Morimoto, 1989). Estimations of Fe^{2+}- and Fe^{3+}-contents were done by assuming ideal stoichiometry and electrostatic neutrality, i.e., a sufficient amount of FeO was converted to Fe_2O_3 in order to obtain the expected pyroxene stoichiometry. Although this method of ferrous/ferric iron estimation was proven statistically valid for calcic-clinopyroxenes or pyroxenes containing less than 20 percent of the jadeite component (Cawthorn & Collerson, 1974), the calculated ratios should still be accepted with caution since McGuire et al. (1989) have shown that calculated Fe^{2+}/Fe^{3+} ratios for pyroxene that crystallized under higher pressures are suspect.

Five representative pyroxene analyses are listed in Table 3.1. All the pyroxene analyses are plotted in the Q-J diagram of Morimoto (1989), on which the three main chemical components of pyroxenes are represented (Figure 3.1). Pyroxene analyses from the studied intrusions plot in both the pyroxene quadrilateral (Quad) and the Ca-Na fields of this diagram. All analyses from the Iris and Pangea intrusions roughly plot in the middle of the diopside field of the Quad diagram (Figure 3.2). Diopside from the Iris antiperthite syenite and monzodiorite rock have similar and constant Ca-contents with average wollastonite (Wo) component values of 47.08 % and 47.39 % respectively. Diopside from the antiperthite syenite is, however slightly enriched in the Ferrosilite (Fs) component (16.62-18.34 % Fs) compared to the ones from the monzodiorite (10.98-14.45 % Fs). In contrast, diopside from the Iris pyroxene-bearing hornblendite unit displays a wider range of compositions in both the Wo and Fs components. In this rock, the Wo content of the diopside varies from 46.93 to 48.90 % and the Fs component varies from 12.13 to 16.76 %. Furthermore, the Wo component increases with increasing Fs-content up to a composition of $Wo_{48.9}En_{37.3}Fs_{13.8}$, from where the Wo-content decreases with iron enrichment (Figure 3.2). Diopside from the pyroxene-bearing hornblendite and melasyenite units of the Pangea intrusion

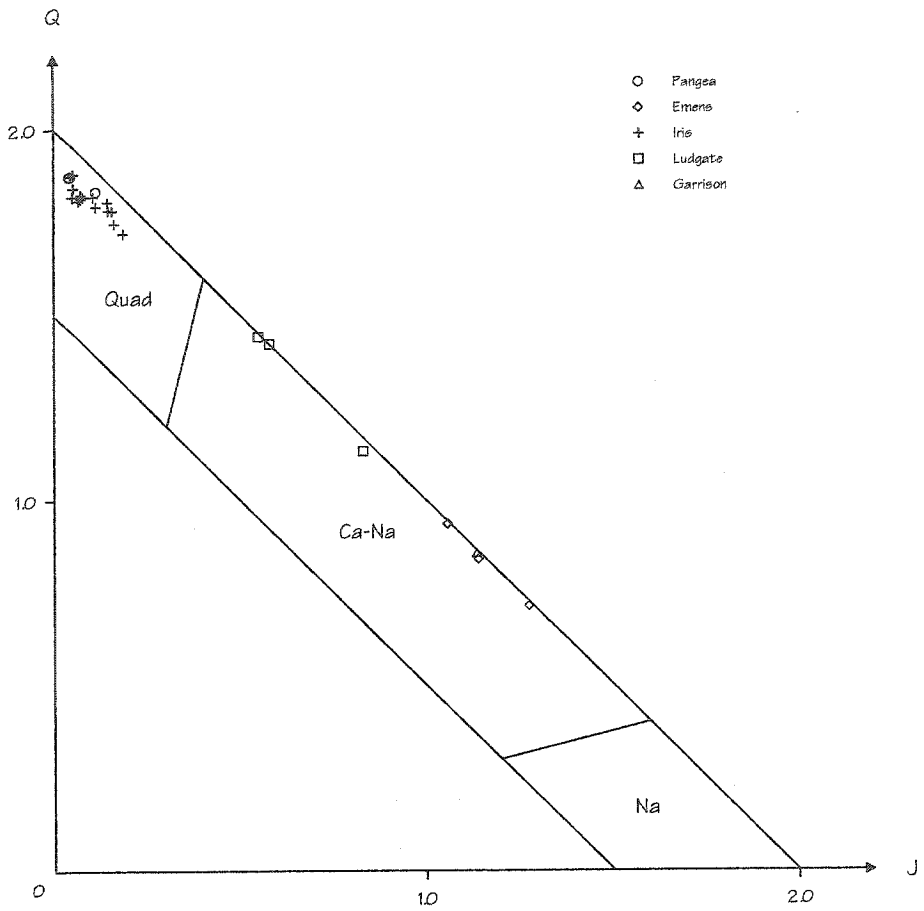

Figure 3.1 Q-J diagram for the pyroxenes (Morimoto, 1989), on which all pyroxene analyses are plotted.

have similar Wo-contents (48.1 and 48.3 % Wo respectively) but differ considerably in their Fs component composition (9.8 % and 19.1% Fs respectively).

Pyroxenes that fall in the Ca-Na field of the Q-J diagram are plotted on the Q-Jd-Ae diagram of Morimoto (1989)(Figure 3.3). Aegirine-augite has only been identified in the rocks from Emens, Ludgate and Garrison intrusions. Aegirine-augite crystals from the Emens intrusions are small and found in clusters of amphibole, chlorite and biotite. In contrast, aegirine-augite from the Ludgate and Garrison intrusions occur as anhedral to subhedral grains, ranging in size from 0.2 to 0.4 mm, that are relatively fresh (Figure 2.130). Unlike similar intrusions, especially the Lebel, Otto and Murdock Creek intrusions of the Kirkland Lake area (Rowins, 1990; Rowins et

Table 3.1 Representative microprobe analyses of pyroxene.

	1	2	3	4	5	6	7
	Pangea 26-11	Emens 45-31	Ludgate 91-11	Iris 69-11	Iris 125-11	Iris 126-12	Iris 129-32
SiO_2	51.28	53.11	52.51	50.68	51.35	49.85	50.46
TiO_2	0.54	0.04	0.09	0.51	0.35	0.74	0.74
Al_2O_3	2.08	1.35	0.38	2.69	3.06	4.13	3.61
Cr_2O_3	0.00	0.00	0.04	0.01	0.04	0.02	0.01
MgO	15.17	7.11	8.50	11.75	12.98	12.77	12.28
CaO	23.98	11.56	17.61	22.14	22.41	23.29	22.84
MnO	0.12	0.21	0.43	0.66	0.35	0.25	0.28
FeO	2.75	2.24	7.60	6.27	6.49	5.53	6.28
[a]Fe_2O_3	3.60	16.60	8.78	4.06	2.11	2.91	2.88
Na_2O	0.27	7.26	3.71	1.09	0.70	0.47	0.75
K_2O	0.01	0.03	0.03	0.00	0.00	0.01	0.00
Total	99.82	99.54	99.71	99.91	99.88	100.03	100.19
Chemical formulae calculated on the basis of 4 cations							
Si^{4+}	1.898	1.997	1.997	1.904	1.915	1.860	1.883
Al^{3+}	0.091	0.003	0.003	0.096	0.085	0.140	0.117
Fe^{3+}	0.011	0.000	0.000	0.000	0.000	0.000	0.000
Σ T	2.000	2.000	2.000	2.000	2.000	2.000	2.000
Al^{3+}	0.000	0.057	0.014	0.023	0.049	0.042	0.042
Fe^{3+}	0.089	0.470	0.251	0.115	0.059	0.082	0.081
Ti^{4+}	0.015	0.001	0.003	0.014	0.010	0.021	0.021
Cr^{3+}	0.000	0.000	0.001	0.000	0.001	0.001	0.000
Mg^{2+}	0.837	0.399	0.482	0.658	0.721	0.710	0.683
Fe^{2+}	0.059	0.070	0.242	0.190	0.160	0.144	0.173
Σ M1	1.000	0.997	0.993	1.000	1.000	1.000	1.000
Mg^{2+}	0.000	0.000	0.000	0.000	0.000	0.000	0.000
Fe^{2+}	0.026	0.000	0.000	0.007	0.043	0.029	0.023
Ca^{2+}	0.951	0.466	0.718	0.891	0.895	0.931	0.913
Na^{+}	0.019	0.529	0.274	0.079	0.051	0.034	0.054
Σ M2	0.996	0.995	0.992	0.977	0.989	0.994	0.990

1 Diopside from pyroxene-bearing hornblendite.
2 Aegirine-augite from melasyenite.
3 Aegirine-augite from alkali-feldspar quartz-syenite.
4 Diopside from antiperthite syenite.
5 Diopside from monzodiorite.
6 Diopside from pyroxene-bearing hornblendite.
[a] Estimated assuming ideal stoichiometry and electroneutrality.

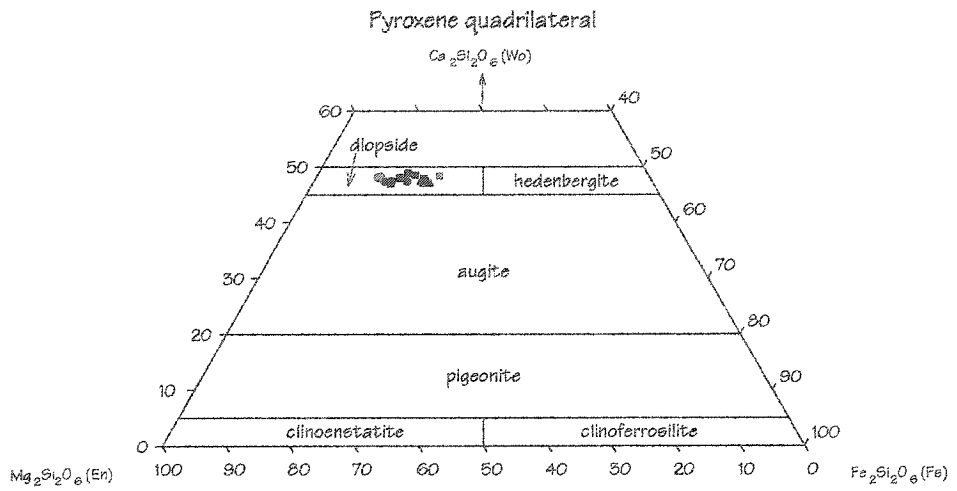

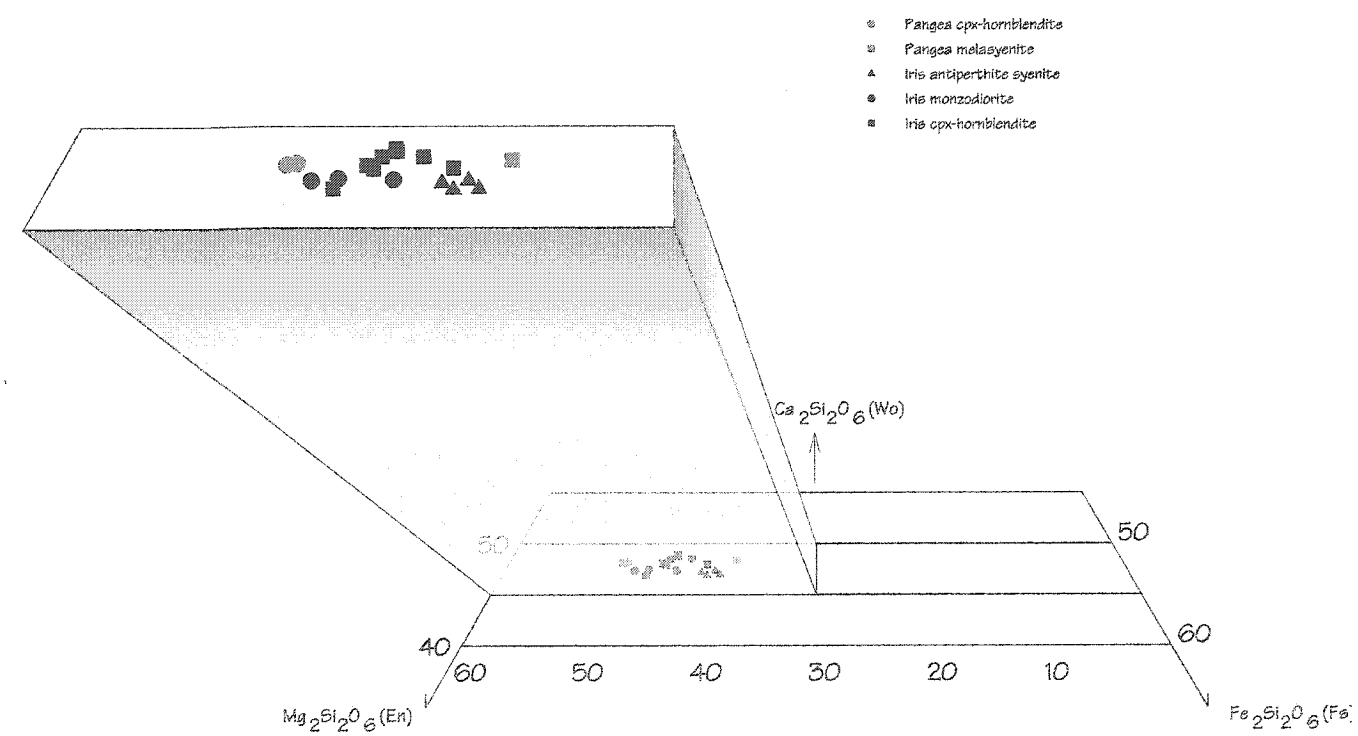

Figure 3.2 Pyroxene quadrilateral, on which all the calcic pyroxene are plotted. All pyroxene analysed from the Iris and Pangea intrusions are diopside.

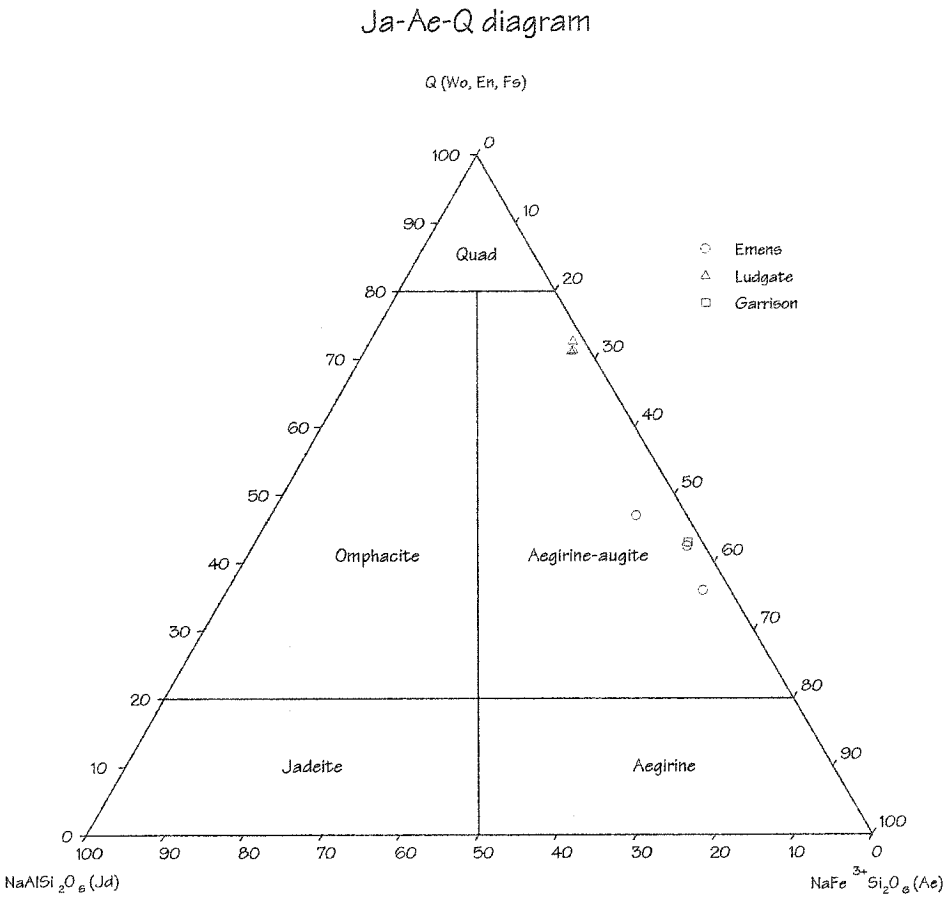

Figure 3.3 The jadeite-aegirine-quadrilateral ternary diagram for the classification of Ca-Na and Na pyroxenes (Morimoto, 1989), on which all the Ca-Na pyroxene analyses are plotted. Quad represents the Ca-Mg-Fe pyroxene area.

al., 1991, 1993; Levesque, 1994), aegirine-augite was only found as discrete crystals and was not observed rimming other pyroxenes. It should, however, be noted that no other species of pyroxene were identified at the Emens, Ludgate and Garrison intrusions. The aegirine-augite of these intrusions is interpreted to have formed late in the crystallization sequence from Na-rich fluids or by residual magma (Deer et al., 1996). The same fluids are also probably responsible for the crystallization of the Na-amphiboles, which are common in these rocks.

A. T-site

The Si^{4+}- and Al^{3+}-contents of diopside from the Iris and Pangea intrusions range from 1.841 to 1.943 atoms per formula unit (*apfu*) and 0.057 to 0.159 *apfu* respectively (Figure 3.4). Aluminium is usually sufficiently abundant to fill the T-site and have some excess in the octahedral M1-site. Only three analyses (2 from Pangea and 1 from Iris) did not have sufficient Al^{3+} to fill the T-site (Table 3.1). This deficiency was resolved by the allocation of a minor amount of Fe^{3+} in order to achieve an ideal T-site occupancy. Diopside with lower Si^{4+}-contents in the tetrahedral site (and higher Al^{3+}) are invariably found in the mafic rocks, while those with the highest Si^{4+}-contents (and lower Al^{3+}) are found in the more evolved rocks of each intrusion. These observations are in accordance with Kushiro (1960) who, although discussing about the

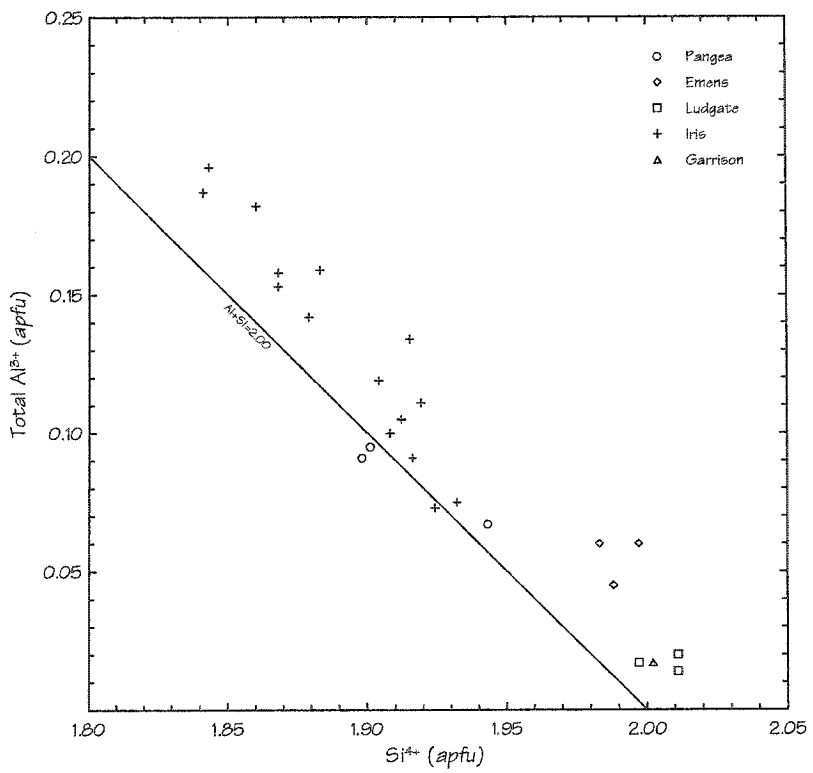

Figure 3.4 Total Al^{3+} as a function of Si^{4+}. Diopside with the lowest Si-content are found in the mafic units of the Iris intrusion.

role of Al and Ti in the T-site, concluded that during magmatic differentiation the proportion of Si^{4+} increases and that of Al^{3+} in the tetrahedral position decreases. Carmichael et al. (1970) and Gupta el al. (1973) later concluded that the activity of SiO_2 in a magma is the major factor controlling the amount of SiO_2 (and hence, Al_2O_3) that enters the precipitating pyroxene. Other factors that can influence the Al-content in pyroxene (and other ferromagnesian minerals) are temperature of crystallization, total pressure and oxygen fugacity (Leake, 1965; Helz, 1973; Neumann, 1976).

Aegirine-augite has higher and less variable Si^{4+}-contents (and lower Al^{3+}) compared to diopside (Si^{4+}: 1.983-2.011 *apfu*; Al^{3+}: 0-0.017 *apfu*). The high Si-content in the T-site indicates that most of the Al is present in the octahedral M1-site. Larsen (1976) had similar low tetrahedral Al values in her aegirine from the Ilímaussaq intrusion; she concluded that these low values were dependent, not on the lack of Al, (since Al was present in the M1 position, which is also the case here) but rather on the temperature of crystallization.

B. M-sites

Octahedral Al^{3+} is present in most of the analysed diopside M1-sites (apart for 3 analyses, where all the Al^{3+} was used to fill the T-site). In those that have $^{VI}Al^{3+}$, the content varies between 0.007 and 0.049 *apfu*. There is a minor correlation between the amount of Si^{4+} in the T-site and $^{VI}Al^{3+}$ (correl. = -0.50). Most of the Al^{3+} in aegirine-augite is in octahedral coordination since almost no Al^{3+} is present in the T-site, $^{VI}Al^{3+}$-contents vary between 0.014 and 0.057 *apfu*.

Ti^{4+}-contents in diopside are relatively low (0.005-0.021 *apfu*) considering the amount of Al present (c.f., Larsen, 1976; Levesque, 1994; Rowins, 1990; Rowins et al., 1991). A strong positive correlation exists between Ti^{4+} and total Al^{3+} (Figure 3.5), and, as expected, a strong negative

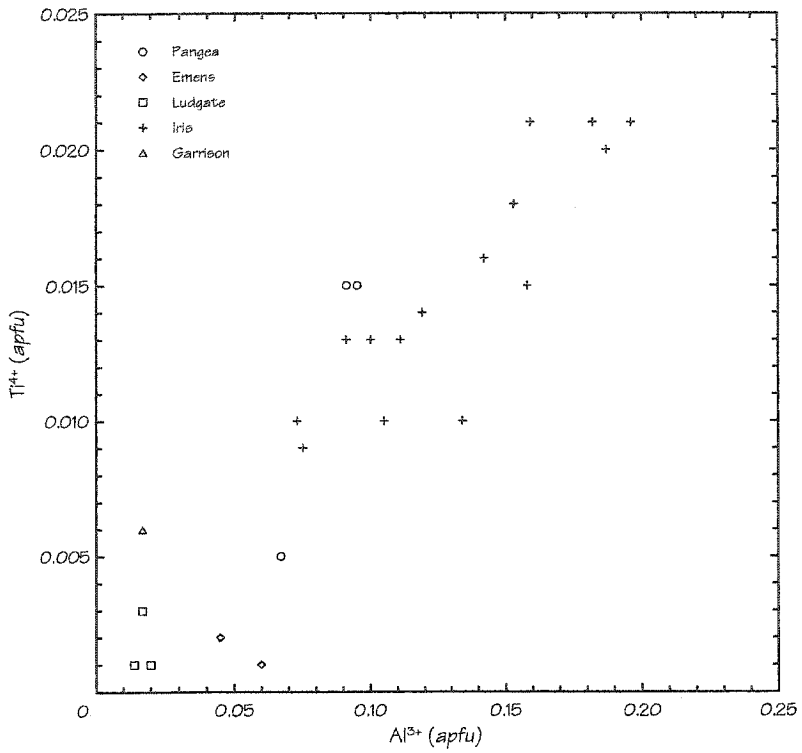

Figure 3.5 Ti^{4+} as a function of total Al^{3+}. The positive correlation between the two elements can be explained by the $Ti^{4+}Al^{3+}$ coupled substitution with $Si^{4+}Mg^{2+}$ or $Si^{4+}Fe^{2+}$.

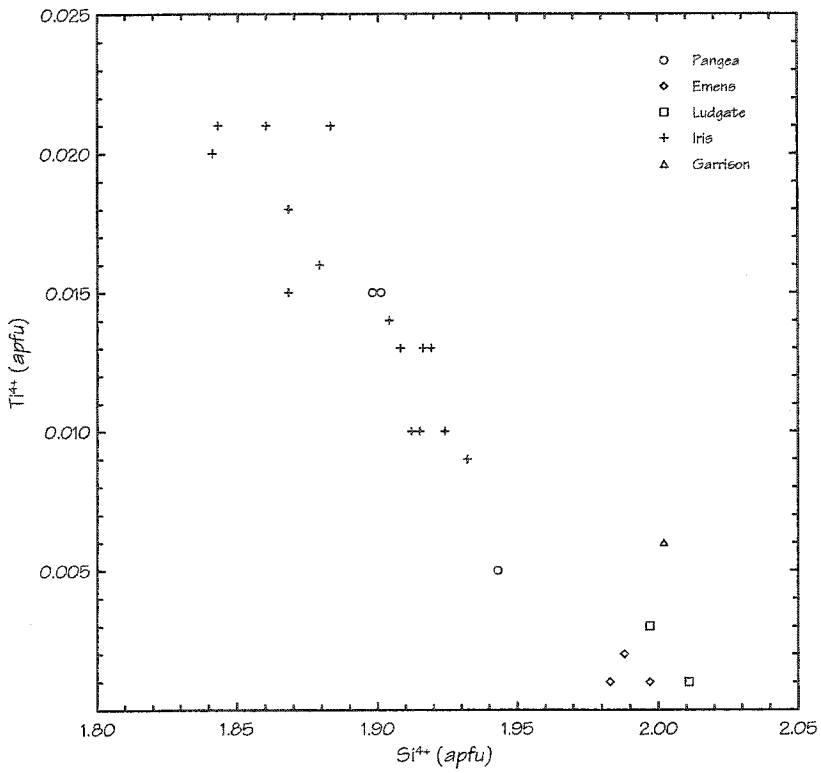

Figure 3.6 Ti^{4+} as a function of Si^{4+}. The negative correlation between the two elements can be explained by the $Ti^{4+}Al^{3+}$ coupled substitution with $Si^{4+}Mg^{2+}$ or $Si^{4+}Fe^{2+}$.

correlation is also present between Ti^{4+} and Si^{4+} (Figure 3.6). The two opposite correlations observed between Ti^{4+} and total Al^{3+}, and Ti^{4+} and Si^{4+}, can be explained by the $Ti^{4+}Al^{3+}$ coupled substitution with $Si^{4+}Mg^{2+}$ or $Si^{4+}Fe^{2+}$ (i.e., $^{VI}Ti^{4+} + 2\,^{IV}Al^{3+} = [^{VI}Mg^{2+}$ or $^{VI}Fe^{2+}] + 2\,^{IV}Si^{4+}$; Larson, 1976). Larsen (1976), while discussing $^{VI}Al^{3+}$ and the ratio $^{IV}Al^{3+}/Ti^{4+}$, concluded that the high ratios (2.19-6.13) she encountered in her iron-poor hedenbergite (ferrosalite) must be attributed to the presence of small amounts of Ca-Tschermak's component ($CaAl_2SiO_6$). This feature could also be the case here, since the $^{IV}Al^{3+}/Ti^{4+}$ ratios of the Iris and Pangea diopside (5.57-11.40) are considerably higher than those of Larsen (Figure 3.7). Numerous factors regulate the amount of Ti substitution in pyroxene, chief amongst them are the temperature and oxygen fugacity of the magma (Verhoogen, 1962), and the presence of early precipitating Ti-bearing minerals (Gibb, 1973; Tracy & Robinson, 1977). In this case, the latter is considered to be the more probable since titanite and magnetite are present in appreciable amounts, especially in the mafic rocks (Chapter 2).

Aegirine-augite shows a marked Ti-depletion (0.001-0.006 *apfu*). A plausible explanation for this depletion is, like in the case of the Iris and Pangea intrusions, the early precipitation of Ti-bearing minerals (previous paragraph), which act as a sink for Ti. Although no studied units from these intrusions were particularly enriched in magnetite or titanite (Chapter 2), the presence of such units is not excluded since, in all cases, the intrusions are poorly exposed or sampled via drill core.

$Fe/(Fe+Mg^{2+})$ ratios (where, $Fe=Fe^{2+}+Fe^{3+}$) of diopside from Iris and Pangea intrusions are low and display only small variations. In the case of Iris intrusion, the ratios vary between 0.204 and 0.331 while they vary between 0.181 and 0.356 at the Pangea intrusion (Figure 3.8). However, a small positive correlation exists between the $Fe/(Fe+Mg^{2+})$ ratio and Si-content (Figure 3.8). Assuming that the Si-content of pyroxene is an indication of the host-rock

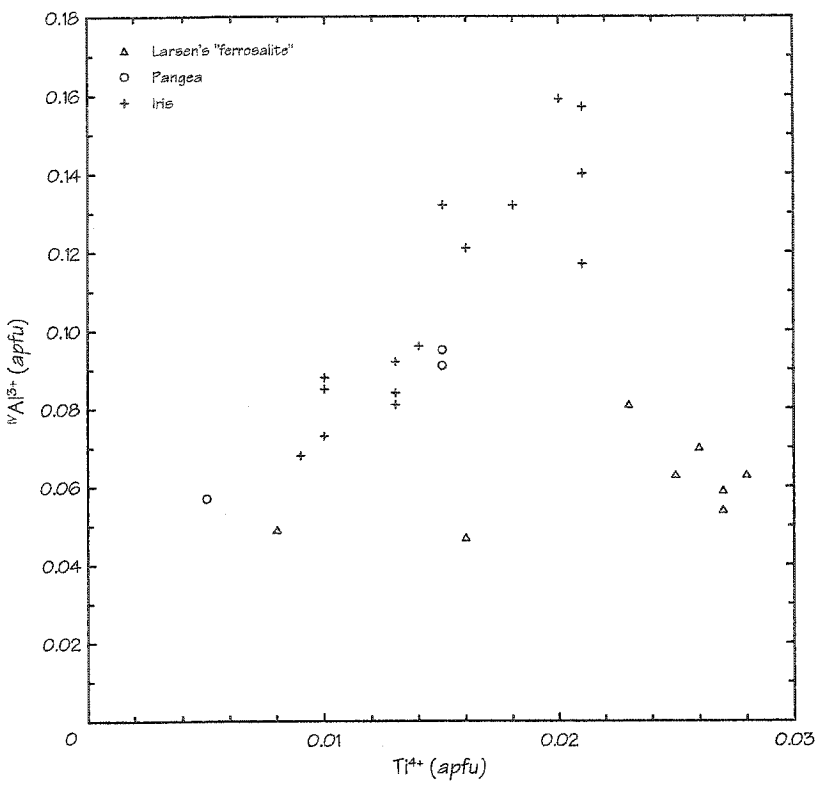

Figure 3.7 Ti^{4+} as a function of $^{IV}Al^{3+}$. The high $^{IV}Al^{3+}/Ti^{4+}$ ratios of diopside from Iris and Pangea intrusions most likely result from the presence of small amounts of the Ca-Tschermak's component ($CaAl_2SiO_6$).

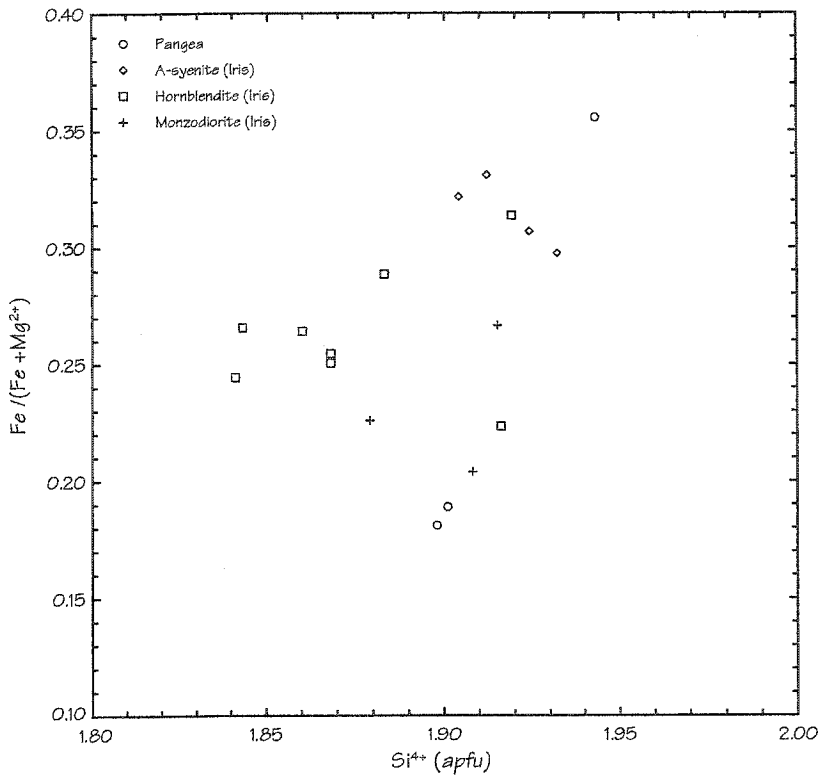

Figure 3.8 $Fe/(Fe+Mg^{2+})$ as a function of Si^{4+}. The weak positive correlation may indicate a minor Fe-enrichment trend with rock fractionation (see text).

differentiation (Kushiro, 1960; Carmichael et al., 1970 and Gupta et al., 1973), the correlation may suggests a minor Fe-enrichment with rock fractionation. This is also supported by minor but consistently higher values of $Fe/(Fe+Mg^{2+})$ for rims compared to cores of the Iris diopside crystals. $Fe/(Fe+Mg^{2+})$ ratios for the aegirine-augite of Emens, Garrison and Ludgate intrusions vary between 0.487 and 0.734 (Figure 3.8).

Numerous pyroxene compositional trends have been identified in alkaline intrusive complexes and volcanic rocks. Normally, during magmatic differentiation, pyroxene will evolve from magnesian compositions towards more Fe-rich compositions (LeBas, 1962). This type of pyroxene compositional trend is characterized by extensive substitution of Mg^{2+} by Fe^{2+} with minimum changes in the Wo-component. Clinopyroxenes that follow this crystallization trend will plot roughly parallel to the diopside-hedenbergite join of the pyroxene quadrilateral (hence, the name hedenbergite-enrichment trend). The hedenbergite-enrichment trend is observed in several alkaline intrusions and volcanic rocks, most notably in the Tristan de Cunha islands (Baker et al., 1964), Shonking Sag laccolith (Nash & Wilkinson, 1970), Shiant Isles (Gibb, 1973) and Klokken intrusion (Parsons, 1979).

Another pyroxene-enrichment trend is characterized by decreasing, or on occasion, constant $Fe/(Fe+Mg^{2+})$ throughout magmatic differentiation. This less common trend is similar to the hedenbergite-enrichment trend since it is also parallel to the diopside-hedenbergite join and Ca^{2+}-contents remain relatively stable. However, in contrast to the hedenbergite-enrichment trend, pyroxene that follows this crystallization trend will evolve towards more Mg-rich compositions. The Mg-enrichment trend is observed in intrusions where the magma was oxidized throughout its evolution. The high oxygen fugacity (fO_2) of the magma favors the oxidation of Fe^{2+} to Fe^{3+} leading to a Fe^{2+} deficiency in the remaining melt. Ferric iron is then preferentially incorporated into oxide phases, such as magnetite. Since, in pyroxene, Fe^{2+} and Mg^{2+} compete for the same site,

the Fe^{2+} deficiency in the melt leads to increased proportions of Mg^{2+} in the M-site. Magnesium-enrichment in pyroxene has been reported at Ben Nevis (Haslam, 1968), Finnmarka (Czamanske & Wones, 1973), Baie-des-Moutons (Lalonde & Martin, 1983), Murdock Creek (Rowins et al., 1991) and in the Kirkland Lake suite (Levesque, 1994).

Pyroxene in alkaline intrusions or volcanic rocks can also define an aegirine-enrichment trend. This trend is characterized by extensive substitution of $NaFe^{3+}$ for $CaFe^{2+}$ in the M-sites. Pyroxene crystallizing along the aegirine-enrichment trend will progressively get depleted in Ca, from diopside to the clinoferrosilite corner of the pyroxene quadrilateral. Aegirine-enrichment trends have been reported in numerous alkaline intrusions throughout the world: Shonking Sag laccolith (Nash & Wilkinson, 1970), the Itãpirapua complex (Gomes et al., 1970), the Ilímaussaq intrusion (Larsen, 1976), the Oslo rift (Neumann, 1976), the Coldwell complex (Mitchell & Platt, 1978), Clériсy pluton (Laflèche et al., 1991), the Little Murun complex (Mitchell & Vladykin, 1996), the Falcon Island pluton (Ayer, 1998) and Mont Saint-Hilaire (Piilonen et al., 1998).

To complicate the matter, it is not uncommon to find pyroxene that will follow two enrichment trends. This is the case for the South Qôroq Centre (Stephenson, 1972) and the Ilímaussaq intrusion (Larsen, 1976), both located in Southern Greenland. Pyroxene from both intrusions started crystallizing along the hedenbergite-enrichment trend and then departed from this trend to get progressively enriched in the aegirine component. In both cases, pyroxene evolved to almost pure aegirine. The inflection point, i.e. the point on the hedenbergite-enrichment trend where the $NaFe^{3+}$ substitution becomes more important than the $CaFe^{2+}$, can occur anywhere along the diopside-hedenbergite join. The location of the inflection point on the hedenbergite-enrichment trend depends on the interaction of numerous factors, the more important, which are the oxygen fugacity, temperature and Na/Ca ratio of the melt (Platt, 1996).

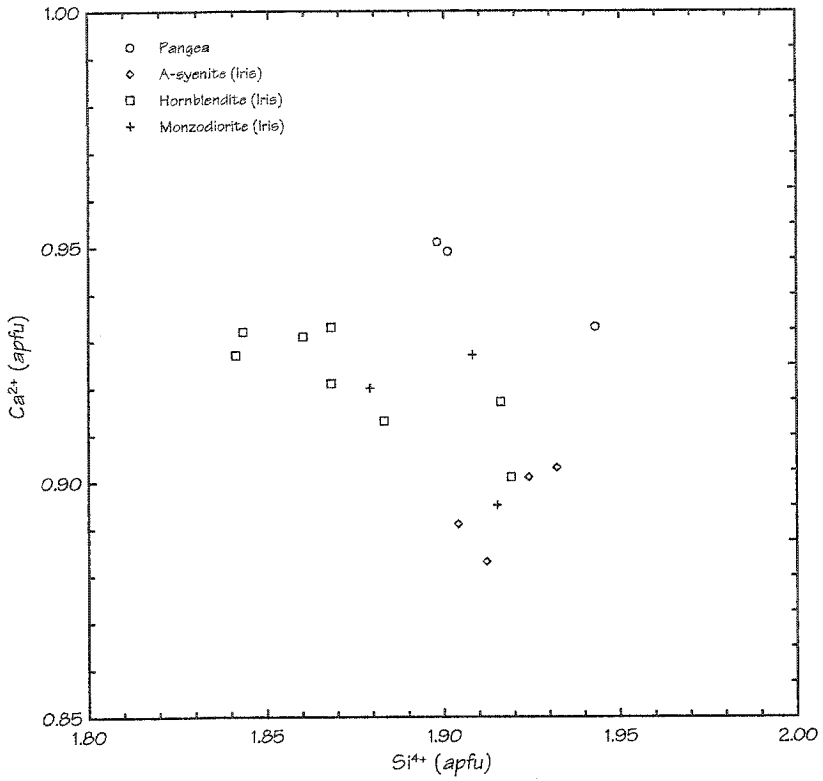

Figure 3.9 Ca^{2+} as a function of Si^{4+}. Diopside with the highest Ca-contents is found in the pyroxene-bearing hornblendite of Iris intrusion while those with the lowest contents are in antiperthite syenite.

Ca^{2+}-contents of diopside from the Iris and Pangea intrusions vary from 0.883 to 0.951 *apfu* with an average composition of 0.918 *apfu*. A trend of decreasing Ca^{2+} with increasing Si^{4+} is present in diopside from both intrusions (Figure 3.9). In the case of the Iris intrusion, diopside with the lowest Ca^{2+}-contents are found in the antiperthite syenite whereas diopside with the highest Ca^{2+}-contents are present in the more primitive (and nepheline normative; Chapter 4) pyroxene-bearing hornblendite rock. Similar negative correlations between Ca^{2+}-content and the degree of differentiation of the rock were reported by Smith & Lindsley (1971), Gibb (1973), Larsen (1976) and Rowins et al. (1991). This feature is related to the silica activity of the magma (Smith & Lindsley, 1971; Gibb, 1973) and not the alkalinity (Brown, 1967; Fodor et al., 1975; Larsen, 1976).

Aegirine-augite from the Emens, Garrison and Ludgate intrusions has variable Ca^{2+}-contents (0.358 to 0.718 *apfu*). In these pyroxenes, the sum Ca+Na approximates very closely to 1.0

(avg. = 0.998 *apfu*). This feature is common in alkali pyroxenes (Sabine, 1950; Tyler & King, 1967). Also, the amount of Ca is roughly equal to the sum of $Mg^{2+}+Fe^{2+}+Mn^{2+}$ present in the M1-site. This is an indication that these four cations are present as diopside, hedenbergite and johannsenite components (Larsen, 1976).

III. Amphibole

Amphibole is the dominant ferromagnesian mineral in the rocks of the Garrison, Iris, Ludgate and Pangea intrusions. It is the primary component of the Iris and Pangea pyroxene-bearing hornblendite units, and is also present in appreciable amounts in the Iris monzodiorite, Pangea melasyenite and Garrison hornblende quartz-monzonite units. Sodic-calcic and sodic amphiboles are also common in the alkali-feldspar syenite unit of the Ludgate intrusion.

A total of 25 amphibole analyses were performed. Amphibole formulae were calculated on the basis of 13 cations (i.e., 13 [Si^{4+}, Al^{3+}, Cr^{3+}, Ti^{4+}, Fe^{2+}, Fe^{3+}, Mg^{2+}, Mn^{2+}]) and assuming that (OH^-, Cl^-, F^-)=2. Assignments of cations and nomenclature of the amphiboles were done according to the current IMA recommendations (Figure 3.10; Leake et al., 1997). Estimations of Fe^{3+} were done by charge-balance considerations and solely for the purpose of nomenclature since it is most likely that these estimations do not reflect the true Fe^{3+}-contents (i.e., Cawthorn & Collerson, 1974; McGuire et al., 1989). Seven representative amphibole analyses from the five studied intrusions are given in Table 3.2.

The studied amphiboles have a wide range of compositions that spans from calcic to sodic-calcic to sodic amphiboles (Figure 3.10). On the basis of textural and chemical considerations, three amphibole varieties are defined: 1- Primary magmatic calcic amphiboles, 2- secondary calcic amphiboles that results from pyroxene alteration, 3- secondary sodic-calcic and sodic amphiboles that most likely crystallized from late Na-enriched deuteric fluids or residual magmas.

Primary magmatic calcic amphiboles were identified at the Iris, Garrison and Pangea intrusions. At the Iris intrusion, they vary in composition from pargasite to magnesiohastingsite while at the Pangea intrusion, they vary from magnesiohastingsite to hastingsite to tschermakite to ferrotschermakite. The amphiboles from Pangea intrusion have similar chemical compositions

Table 3.2 Representative microprobe analyses of amphibole.

	1	2	3	4	5	6	7
	Ludgate 088-32	Garrison 098-11	Garrison 101-11	Iris 125-41	Iris 129-41	Pangea 008-21	Pangea 009-31
SiO_2	55.62	48.04	56.49	39.47	39.92	55.83	42.76
TiO_2	0.08	0.92	0.09	2.65	2.46	0.05	2.44
Al_2O_3	0.41	6.22	0.39	12.33	13.40	0.51	9.49
Cr_2O_3	0.01	0.00	0.01	0.01	0.00	0.00	0.03
MgO	10.29	13.67	16.28	8.48	11.99	17.35	8.10
CaO	0.91	11.35	4.08	11.23	11.87	12.39	10.55
MnO	0.12	0.54	0.53	0.46	0.22	0.59	0.22
FeO	7.89	9.73	6.54	16.43	10.27	8.93	16.28
[a]Fe_2O_3	15.77	5.14	5.25	2.92	3.60	1.47	6.04
Na_2O	6.60	1.50	6.33	2.38	2.06	0.28	2.05
K_2O	0.09	0.69	1.34	1.87	1.76	0.07	0.88
F	0.14	0.49	1.76	0.10	0.15	0.13	0.09
Cl	0.03	0.00	0.00	0.11	0.04	0.00	0.04
[b]H_2O	2.00	1.82	1.27	1.88	1.92	2.05	1.94
O=F	-0.06	-0.21	-0.74	-0.04	-0.06	-0.05	-0.04
O=Cl	-0.01	0.00	0.00	-0.02	-0.01	0.00	-0.01
Total	99.90	99.90	99.62	100.26	99.58	99.59	100.85
Chemical formulae calculated on the basis of 13 (Si^{4+}, Ti^{4+}, Al^{3+}, Fe^{3+}, Cr^{3+}, Fe^{3+}, Mg^{2+}, Mn^{2+})							
Si^{4+}	8.027	7.025	8.055	6.038	5.971	7.940	6.447
Al^{3+}	0.000	0.975	0.000	1.962	2.029	0.060	1.553
Σ T	8.027	8.000	8.055	8.000	8.000	8.000	8.000
Al^{3+}	0.070	0.097	0.066	0.261	0.333	0.025	0.133
Ti^{4+}	0.009	0.101	0.010	0.305	0.277	0.005	0.277
Cr^{3+}	0.001	0.000	0.001	0.001	0.000	0.000	0.004
Fe^{3+}	1.713	0.565	0.563	0.336	0.405	0.157	0.685
Mg^{2+}	2.214	2.980	3.461	1.934	2.674	3.679	1.821
Fe^{2+}	0.952	1.190	0.780	2.102	1.284	1.062	2.052
Mn^{2+}	0.015	0.067	0.064	0.060	0.027	0.071	0.028
Σ C	4.974	5.000	4.945	4.999	5.000	4.999	5.000
Mn^{2+}	0.000	0.000	0.000	0.000	0.001	0.000	0.000
Ca^{2+}	0.141	1.778	0.623	1.841	1.902	1.888	1.704
Na^{+}	1.847	0.222	1.377	0.159	0.097	0.077	0.296
Σ B	1.988	2.000	2.000	2.000	2.000	1.965	2.000
Na^{+}	0.000	0.203	0.373	0.547	0.500	0.000	0.303
K^{+}	0.017	0.129	0.244	0.365	0.336	0.013	0.169
Σ A	0.017	0.332	0.617	0.912	0.836	0.013	0.472

1 Magnesioriebeckite from alkali-feldspar quartz-syenite.
2 Magnesiohornblende from hornblende quartz-monzonite.
3 Richterite from hornblende quartz-monzonite.
4 Hastingsite from monzodiorite.
5 Magnesiohastingsite from pyroxene-bearing hornblendite.
6 Actinolite from melasyenite.
7 Ferrotschermakite from pyroxene-bearing hornblendite.
[a] Estimated assuming ideal stoichiometry and electroneutrality.
[b] Estimated assuming (OH^-, Cl^-, F^-) = 2.

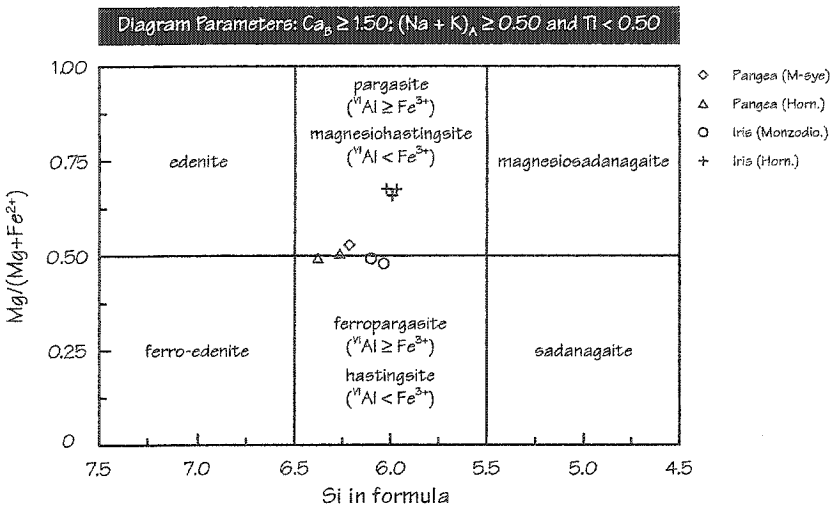

Figure 3.10a IMA classification of calcic amphiboles. Three species were identified: pargasite, magnesiohastingsite and hastingsite. M-sye: melasyenite, Horn.: pyroxene-bearing hornblendite, Monzodio.: monzodiorite.

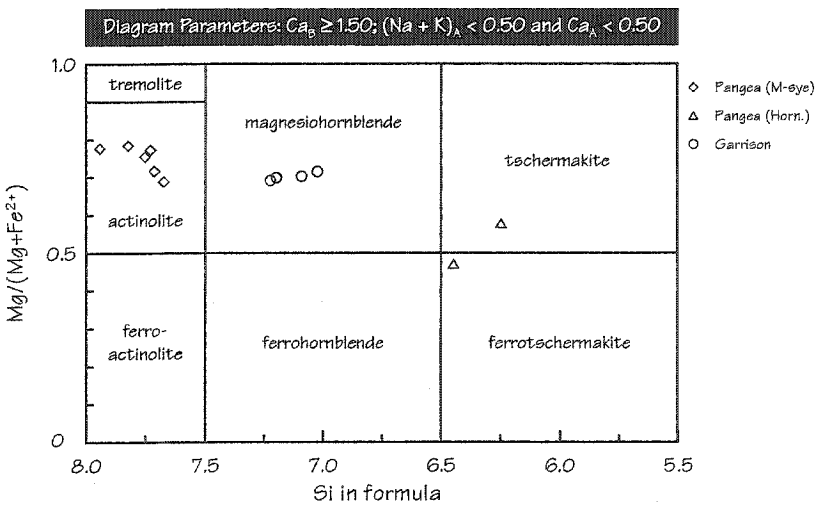

Figure 3.10b IMA classification of calcic amphiboles. Four species were identified: actinolite, magnesiohornblende, tschermakite and ferrotschermakite. M-sye: melasyenite, Horn.: pyroxene-bearing hornblendite.

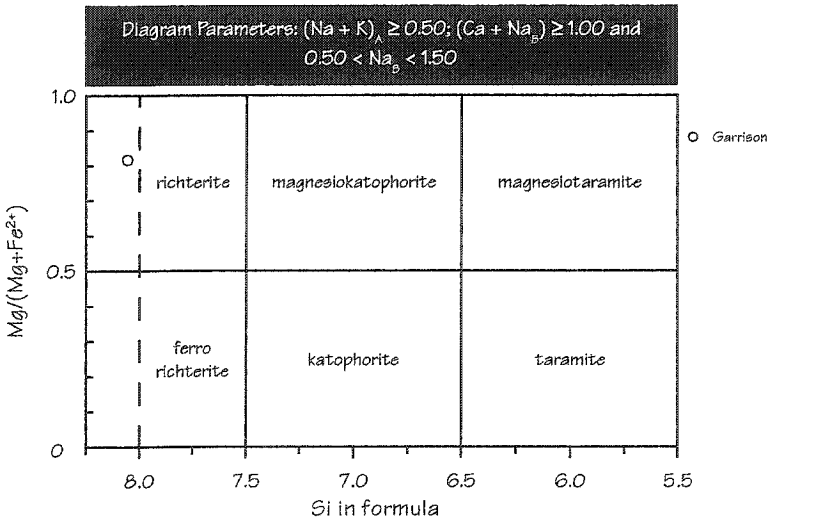

Figure 3.10c IMA classification of sodic-calcic amphiboles. One species was identified: richterite. However, this analysis plots slightly outside of the richterite field since it contains excess Si^{4+}.

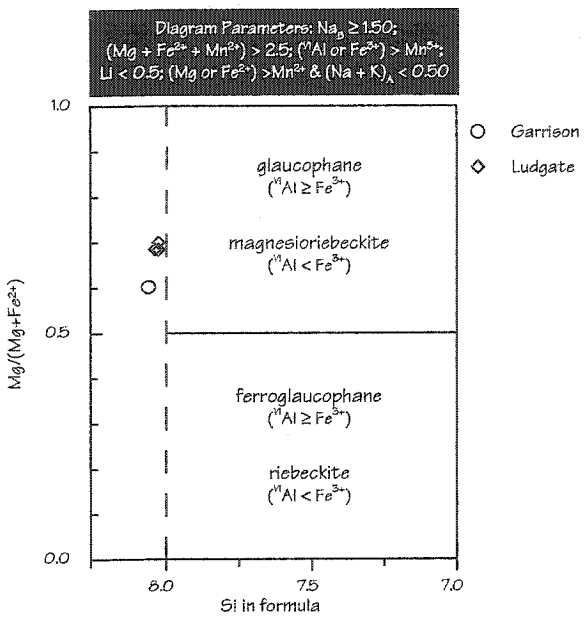

Figure 3.10d (*continued*) IMA classification of sodic amphiboles. One species was identified: magnesioriebeckite. However, this analysis plots slightly outside of the magnesioriebeckite field since it contains excess Si^{4+}.

apart for minor differences in $Mg/(Mg+Fe^{2+})$ and $(Na + K)_A$, which according to the current IMA classification, led to the four different amphibole species. Pargasite and magnesiohastingsite megacrysts from the pyroxene-bearing hornblendite unit of the Iris intrusion are sometimes zoned. Zoning consists in variations of the intensity and color of pleochroism between the core and the rim of the megacrysts. At the Garrison intrusion, the only primary magmatic amphibole identified was magnesiohornblende. It displays light green to olive green pleochroism and commonly contains apatite and magnetite inclusions.

Secondary deuteric amphibole is present in the Iris, Garrison, Ludgate and Pangea intrusions rocks. At the Iris and Pangea intrusions this amphibole is actinolite and is found partially or totally replacing euhedral crystals of diopside, and in clusters of various sizes. The Iris monzodiorite unit also contains hastingsite that commonly rims diopside crystals. Richterite and magnesioriebeckite were identified in the Garrison intrusion while only magnesioriebeckite was identified at the Ludgate intrusion.

$Fe/(Fe+Mg^{2+})$ ratios (where, $Fe=Fe^{2+}+Fe^{3+}$) in primary magmatic amphibole range from 0.35 to 0.60. The lowest ratios are found in magnesiohornblende from the Garrison intrusion while the highest ones are in ferrotschermakite from the Pangea intrusion (Figure 3.11). Amphibole from the Iris intrusion displays a marked increase in $Fe/(Fe+Mg^{2+})$ from an average ratio of 0.38 in the pyroxene-bearing hornblendite to 0.55 in the monzodiorite unit, without any significant changes in Si^{4+}. Although less striking, a similar trend of increasing $Fe/(Fe+Mg^{2+})$ ratios with rock fractionation is observed in pyroxene from the same intrusion. The highest $Fe/(Fe+Mg^{2+})$ ratio found in the Iris diopside (0.33) closely corresponds to the lowest ratio (0.36) observed in the amphiboles. Since petrographic evidence has clearly shown that pyroxene crystallized before the amphibole, this may suggest a continuous sequence of Fe-enrichment that spans throughout the pyroxene and amphibole crystallization. Amphibole from the pyroxene-bearing hornblendite unit of the Pangea intrusion displays an increase in $Fe/(Fe+Mg^{2+})$ ratios with increasing Si^{4+}. The ratios increase from 0.53 in tschermakite to 0.60 in ferrotschermakite. The ratios of magnesiohornblende from the Garrison intrusion remain relatively constant (0.35 to 0.37). Actinolite from the Pangea melasyenite unit displays a decrease in $Fe/(Fe+Mg^{2+})$ values from 0.37 to 0.25 with increasing Si^{4+}. The $Fe/(Fe+Mg^{2+})$ ratios of magnesioriebeckite from the Ludgate intrusion vary between 0.51 and 0.56 while the Si^{4+}-content remains constant.

Ca^{2+}-contents are similar in all the calcic-amphiboles with an average of 1.825 ± 0.039 *apfu* (Figure 3.12). Although the difference is minor, pargasite and magnesiohastingsite from the hornblendite unit of the Iris intrusion have higher Ca^{2+} values compared to hastingsite from the monzodiorite unit (avg. 1.896 and 1.849 *apfu* respectively). A similar trend of decreasing Ca^{2+} with rock fractionation was observed in diopside from the Iris intrusion.

Only sodic-calcic and sodic amphiboles from the Garrison and Ludgate intrusions show significant variations in their Ca^{2+} values. In the case of the Garrison intrusion, Ca^{2+} varies from

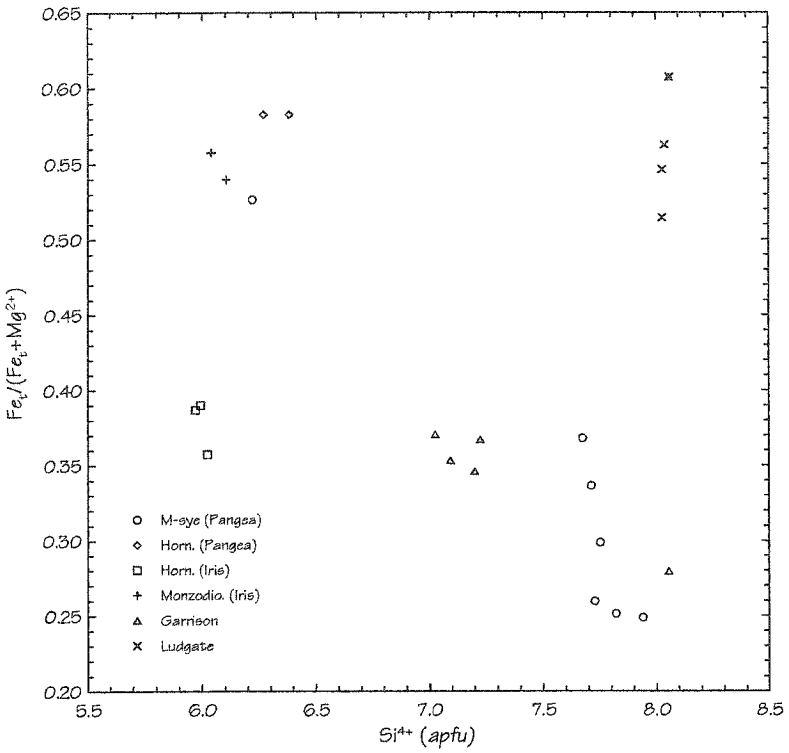

Figure 3.11 $Fe/(Fe+Mg^{2+})$ as a function of Si. Amphiboles have a wide range of $Fe/(Fe+Mg^{2+})$ values at given Si values.

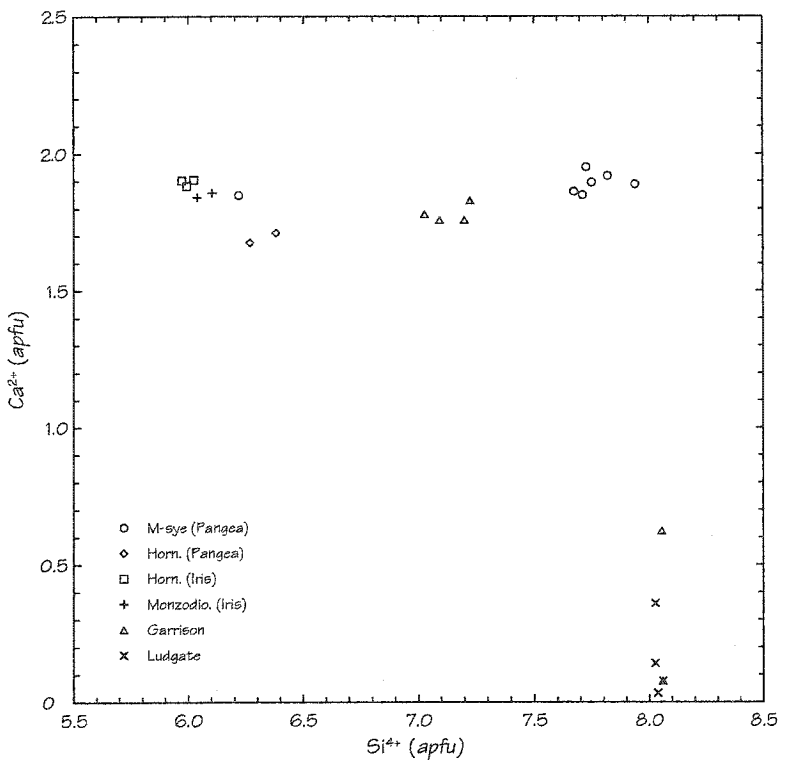

Figure 3.12 Ca^{2+} as a function of Si^{4+}. Ca^{2+} in calcic amphiboles remains relatively constant throughout the Si^{4+} spectrum while it is highly variable in the sodic-calcic and sodic amphiboles.

0.076 to 0.623 *apfu*, while the variation is from 0.033 to 0.359 *apfu* in magnesioriebeckite from the Ludgate intrusion.

In contrast with diopside from the Iris intrusion, there is no correlation between the Al^{3+} and Ti^{4+} in amphiboles of this intrusion. Al^{3+} values are higher in pargasite and magnesiohastingsite from the hornblendite unit (avg.: 2.359 *apfu*) than in the hastingsite of the monzodiorite unit (avg.: 2.160 *apfu*). Ti^{4+} is however enriched in hastingsite (avg.: 0.301 *apfu*) compared to pargasite and magnesiohastingsite (avg.: 0.272 *apfu*). Amphiboles of the pyroxene-bearing hornblendite unit from Pangea intrusion have similar Ti^{4+} values (avg.: 0.291 *apfu*) compared to those from the Iris intrusion, but contain less Al^{3+} (avg.: 1.814 *apfu*). The Ti^{4+}-content of amphiboles from the pyroxene-bearing hornblendite units of Pangea and Iris intrusions are consistently higher than the ones from similar rocks of the Kirkland Lake area (c.f. Rowins et al., 1991; Levesque, 1994). Ti^{4+} and Al^{3+} values are much lower in magnesiohornblende from the Garrison intrusion (avg.: 0.094 and 0.964 *apfu* respectively). A negligible amount of Ti^{4+} is present in actinolite from the Pangea melasyenite unit. This is also the case for the Na-rich amphiboles of the Garrison and Pangea intrusions.

Na^{+} values decrease with increasing Si^{4+} in all the calcic amphiboles apart for the amphiboles of the Iris intrusion where they display a minor increase (Figure 3.13). Na-content of magnesioriebeckite from the Ludgate intrusion varies from 1.676 *apfu* to an almost complete A-site occupancy (1.990 *apfu*). Potassium values are highest in amphibole from the Iris intrusion. Hastingsite from the monzodiorite has an average K^{+}-content of 0.364 *apfu* while magnesiohastingsite and pargasite from the pyroxene-bearing hornblendite unit have an average content of 0.324 *apfu*. Magnesiohornblende and richterite from the Garrison intrusion are enriched in fluorine (0.393 and 0.794 *apfu* respectively) compared to amphiboles from the other intrusions.

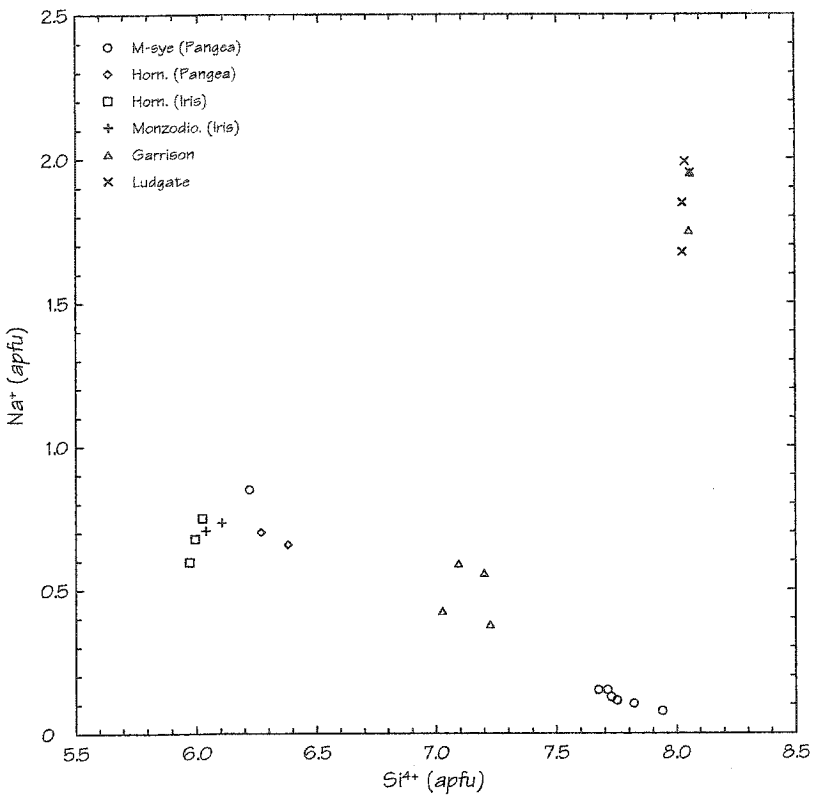

Figure 3.13 Na^{+} as a function of Si^{4+}. A negative correlation exists between the two elements.

IV. Mica

Mica is present in appreciable amounts in the alkali-feldspar porphyritic biotite-syenite from Emens intrusion and in some melasyenite and pyroxene-bearing hornblendite samples from the Pangea intrusion. No mica was identified at Garrison and Ludgate intrusions, and only one sample from Iris intrusion contained trace amounts. A total of 18 mica analyses were performed. All mica formulae are calculated on the basis of 12 anions [10 oxygen + 2 (OH^-, Cl^-, F^-)]. Classification and site assignments for the micas were done according to current IMA recommendations (Rieder et al., 1998). Iron is only reported as Fe^{2+} since Fe^{3+} estimations in micas are notoriously inaccurate (Lalonde, personnal communication, 2001).

Five representative mica analyses are given in Table 3.3. All mica analyses are plotted on the annite-siderophyllite-eastonite-phlogopite quadrilateral, on which the horizontal line located at $Fe/(Fe+Mg^{2+}) = 0.50$ (where Fe is the total iron reported as FeO) represents the boundary between annite and phlogopite (Figure 3.14). Most analyses, apart from four analyses described below, are phlogopite in the sense of the IMA (i.e., $Fe/(Fe+Mg^{2+}) < 0.50$). Of the four exceptions, two mica analyses from the Emens intrusion clearly plot in the annite field (i.e., $Fe/(Fe+Mg^{2+}) = 0.613$ and 0.510) while the two others, one from the Iris intrusion and one from the Pangea intrusion, plot in the annite field but very close to the boundary with phlogopite (i.e., $Fe/(Fe+Mg^{2+}) = 0.500$ and 0.502). These two analyses could probably be classified as phlogopite if the analytical errors would be taken into account. Notwithstanding the presence of some annite, all micas will collectively be referred to as phlogopite. Furthermore, since most of the mica analyses are from the Emens intrusion, the following chemical descriptions are based on observations made from the micas of that intrusion, except if the mica from the other intrusions behaves so differently that it warrants discussion.

Table 3.3 Representative microprobe analyses of mica.

	1	2	3	4	5
	Pangea 015-11	Iris 069-32	Emens 084-21	Emens 178-31	Emens 161-21
SiO_2	36.26	35.39	37.57	37.18	35.86
TiO_2	2.94	3.04	1.48	1.57	2.20
Al_2O_3	14.94	14.97	14.17	16.77	17.15
Cr_2O_3	0.00	0.00	0.13	0.03	0.03
MgO	11.40	11.56	16.10	12.10	11.23
CaO	0.01	0.06	0.00	0.03	0.00
MnO	0.20	0.98	0.49	0.64	0.76
FeO	20.44	20.36	15.75	17.30	18.35
Na_2O	0.06	0.08	0.02	0.00	0.02
K_2O	9.93	9.35	10.23	10.40	10.19
F	0.27	0.22	0.29	0.33	0.00
Cl	0.02	0.01	0.00	0.00	0.00
H_2O^a	3.79	3.79	3.86	3.83	3.94
O=F	-0.11	-0.09	-0.12	-0.14	0.00
O=Cl	0.00	0.00	0.00	0.00	0.00
Total	100.14	99.72	99.97	100.04	99.73
Chemical formulae calculated on the basis of 12 anions [10 O + 2 (OH^-, F^-, Cl^-)]					
Si^{4+}	2.770	2.722	2.817	2.799	2.727
Al^{3+}	1.230	1.278	1.183	1.201	1.273
Σ T	4.000	4.000	4.000	4.000	4.000
Al^{3+}	0.115	0.079	0.069	0.287	0.264
Ti^{4+}	0.169	0.176	0.083	0.089	0.126
Cr^{3+}	0.000	0.000	0.008	0.002	0.002
Mn^{2+}	0.013	0.064	0.031	0.041	0.049
Fe^{3+}	1.306	1.310	0.988	1.089	1.167
Mg^{2+}	1.298	1.326	1.800	1.358	1.273
Σ M	2.901	2.955	2.979	2.866	2.881
Ca^{2+}	0.001	0.005	0.000	0.002	0.000
K^+	0.968	0.917	0.979	0.999	0.989
Na^+	0.009	0.012	0.003	0.000	0.003
Σ I	0.978	0.934	0.982	1.001	0.992
Fe/(Fe+Mg)	0.502	0.497	0.354	0.445	0.478

1 Annite from titanite-rich melasyenite.
2 Phlogopite from antiperthite syenite.
3 Phlogopite from alkali-feldspar porphyritic biotite-syenite.
4 Phlogopite from alkali-feldspar porphyritic biotite-syenite.
5 Phlogopite from alkali-feldspar syenite.
[a] Estimated assuming (OH^-, Cl^-, F^-) = 2.

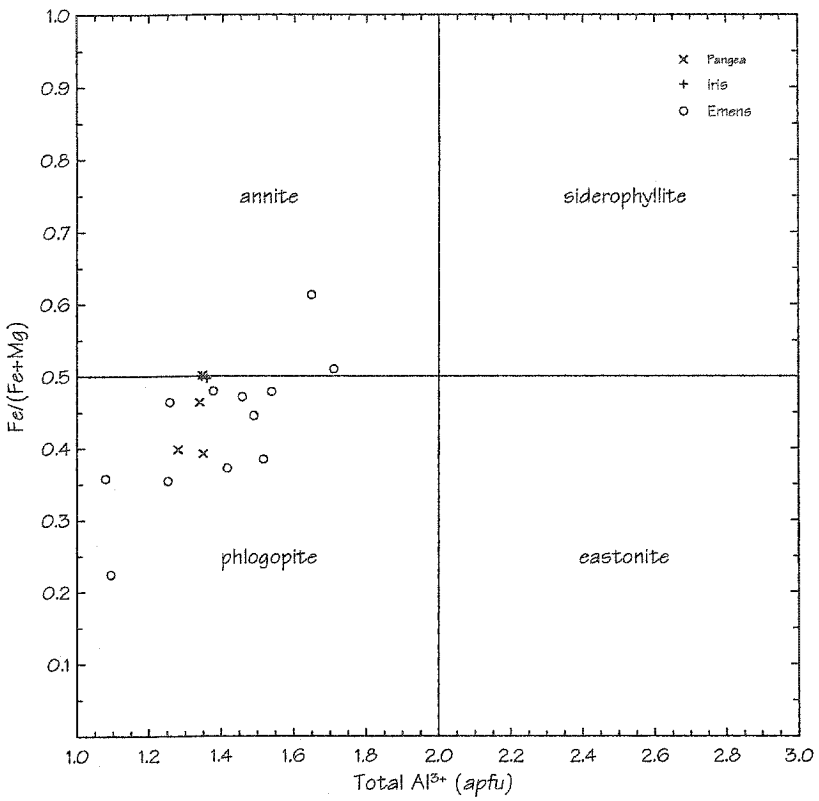

Figure 3.14 The annite-siderophyllite-eastonite-phlogopite quadrilateral used to classify the micas. Most mica analyses plot in the phlogopite field of the diagram.

All analysed phlogopite crystals have octahedral-site occupancies ranging from 2.809 to 2.985 and contain 87.3 to 100 % monovalent interlayer cations, which satisfies the conditions of classification for trioctahedral and true micas. (Rieder et al., 1998).

Si^{4+} values in phlogopite vary from 2.648 to 3.006 *apfu* while those of Al^{3+} vary between 1.079 and 1.709 *apfu* (Figure 3.15). Concentrations of both elements are negatively correlated. Similar correlations are common since Al^{3+}-content in mica is influenced by the silica activity of the host magma (Czamanske & Wones, 1973; Thompson, 1974). Other factors controlling the amount of Al^{3+} in mica are temperature, total pressure (Czamanske & Wones, 1973; De Albuquerque, 1973; Thompson, 1974) and the peraluminosity of the host magma (Lalonde & Bernard, 1993). In all cases, Al^{3+} is present in sufficient quantity to fill the tetrahedral site and appear in the octahedral site. Octahedral Al^{3+} ($^{VI}Al^{3+}$) values vary from 0.049 *apfu*, in a sample from the Pangea intrusion, to 0.398 *apfu*. The amount of $^{VI}Al^{3+}$ in biotite depends mostly on the Al activity of the magma,

or on the Al activity relative to Si activity of the magma (De Albuquerque, 1973). This appears to be the case at the Emens intrusion since $^{VI}Al^{3+}$ in phlogopite is positively correlated with the ratio $Al_2O_3/(Al_2O_3+SiO_2)$ of the corresponding host-rock (Figure 3.16).

Ti^{4+}-content in phlogopite from the Emens intrusion is moderate, values range from 0.013 to 0.132 *apfu*. Phlogopite from the Iris and Pangea intrusions have higher Ti^{4+} values, which range from 0.048 to 0.220 *apfu*. Ti^{4+} values are correlated with those of $^{IV}Al^{3+}$ (Figure 3.17). This correlation occurs because the substitution of Al^{3+} for Si^{4+} in the tetrahedral site facilitates the entry of Ti^{4+} in the octahedral site (De Albuquerque 1973). Temperature and fO_2 of the magma are also important factors regulating the Ti^{4+}-content in mica (De Albuquerque, 1973).

$Fe/(Fe+Mg^{2+})$ ratios of phlogopite vary between 0.225 and 0.613. However, 90 % of the ratios fall between 0.354 and 0.510. The ratios slightly increase with increasing total Al^{3+} (Figure 3.14). A similar trend of increasing $Fe/(Fe+Mg^{2+})$ ratios is observed in Figure 3.18 where the $Fe/(Fe+Mg^{2+})$ ratios of phlogopite are plotted against the host-rock Fractionation Index (F.I. = normative wt% Qtz+Ab+Or+Ne+Lc+Ns). Similar positive correlations were reported at the Shonkin Sag (Nash & Wilkinson, 1973) and the Falcon Island (Ayer, 1998). The authors attributed this behaviour to a progressive fO_2 decrease during magmatic differentiation. Mica from other intrusions, such as Ben Nevis (Haslam, 1968), Finnmarka (Czamanske & Wones, 1973), Baie-des-Moutons (Lalonde & Martin, 1983), Murdock Creek (Rowins et al., 1991) and Kirkland Lake suite (Levesque, 1994) display constant or decreasing values of $Fe/(Fe+Mg^{2+})$ with fractionation, which is interpreted to result from constant or increasing magmatic oxidation.

Mn^{2+} values range between 0.013 to 0.064 *apfu* and are positively correlated with the host-rock fractionation index (Figure 3.19). Similar positive correlations were reported in both oxidized (Czamanske & Wones, 1973; Parsons, 1979; Rowins et al., 1991) and reduced intrusions (Ague

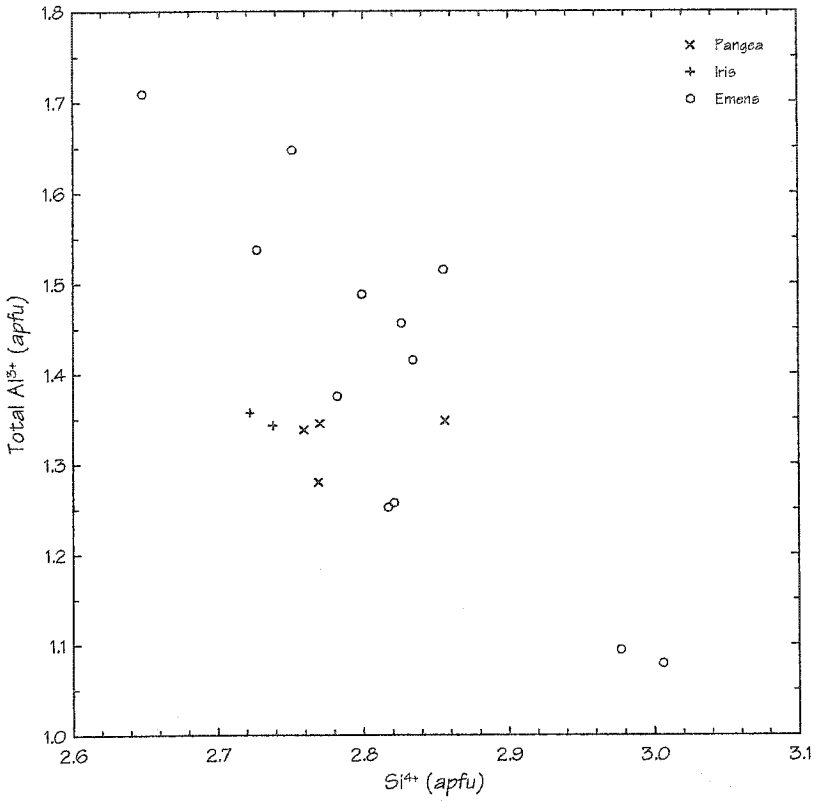

Figure 3.15 Total Al^{3+} as a function of Si^{4+}. The elements are correlated because Al^{3+}-content in mica is influenced by the SiO_2 activity of the host magma.

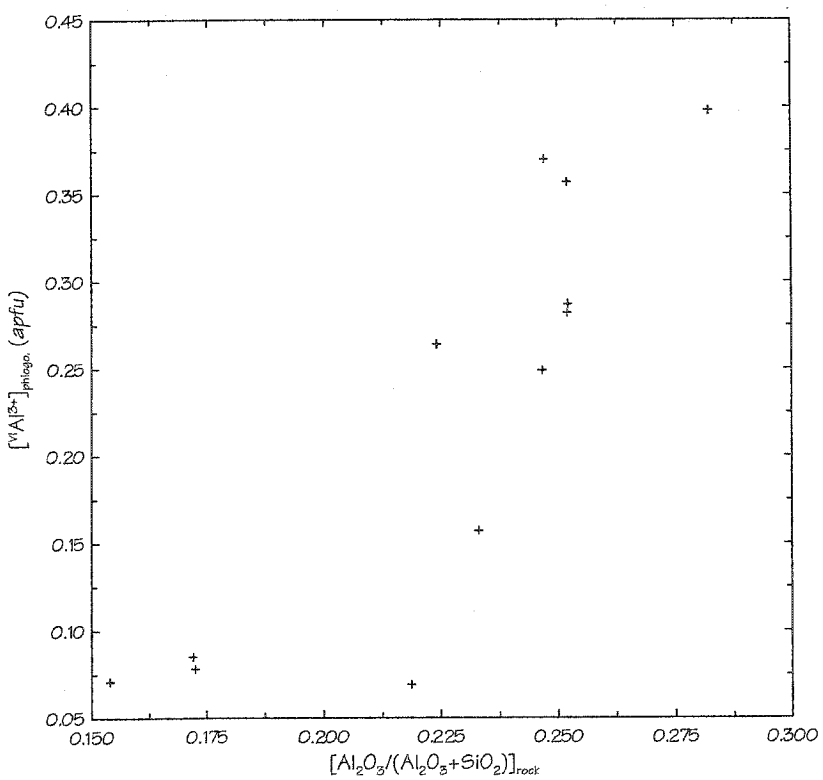

Figure 3.16 $^{VI}Al^{3+}$ as a function of $Al_2O_3/(Al_2O_3+SiO_2)$. The positive correlation suggests that $^{VI}Al^{3+}$-content in biotite depends mostly on the Al-content of the rock.

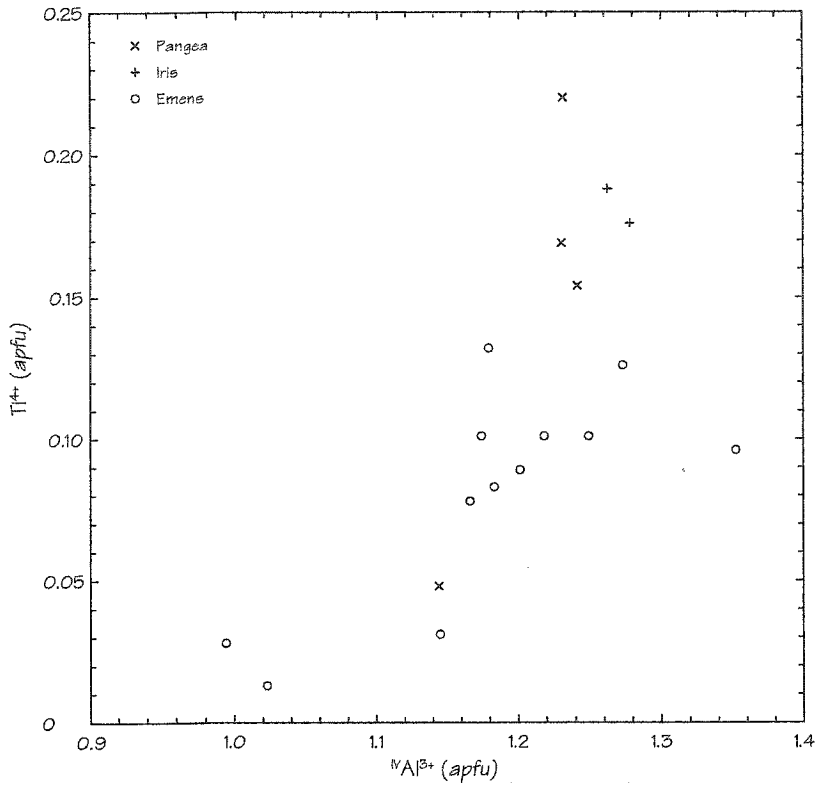

Figure 3.17 Ti^{4+} as a function of $^{IV}Al^{3+}$. A positive correlation exists because the substitution of Al^{3+} for Si^{4+} facilitates the entry of Ti^{4+} in the octahedral site.

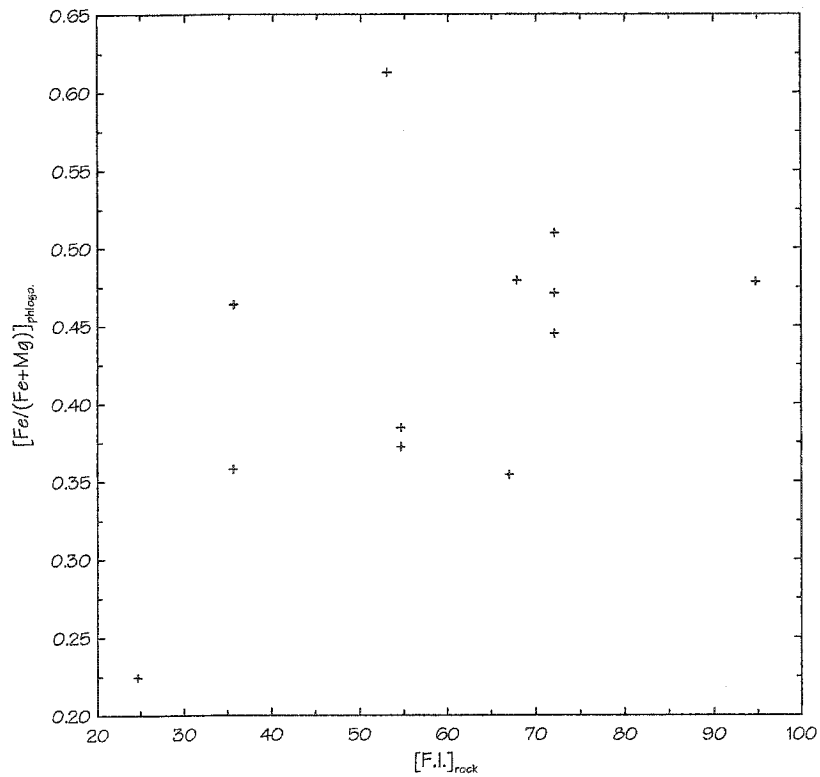

Figure 3.18 Fe/(Fe+Mg) in phlogopite from Emens intrusion as a function of host-rock Fractionation Index (see text). The very poor positive correlation can be attributed to a progressive decrease of fO_2 during magmatic differenciation.

& Brimhall, 1988; Ayer, 1998). Harrison (1990) speculated that the Mn-enrichment trend he encountered in mica from the Cairngorm pluton, probably results from the absence of any significant amount of pyroxene or amphibole fractionation during the early stages of magmatic evolution.

F^- and Cl^- values vary from 0.000 to 0.162 *apfu* and 0.000 to 0.003 *apfu* respectively. Most phlogopite crystals analyzed have undetectable Cl concentrations. F-values are negatively correlated with the fractionation index (Figure 3.20). Jiang et al. (1994) found that halogen content is related to the Mg/Fe ratio of mica. He suggested that F is preferentially incorporated into micas with high Mg/Fe ratios, whereas Cl tends to be enriched in those with lower Mg/Fe ratios. This behaviour is commonly refered to as the Mg-F avoidance rule. However, in the cases of Emens intrusion, no correlation between the F-content and Mg/Fe ratio exists.

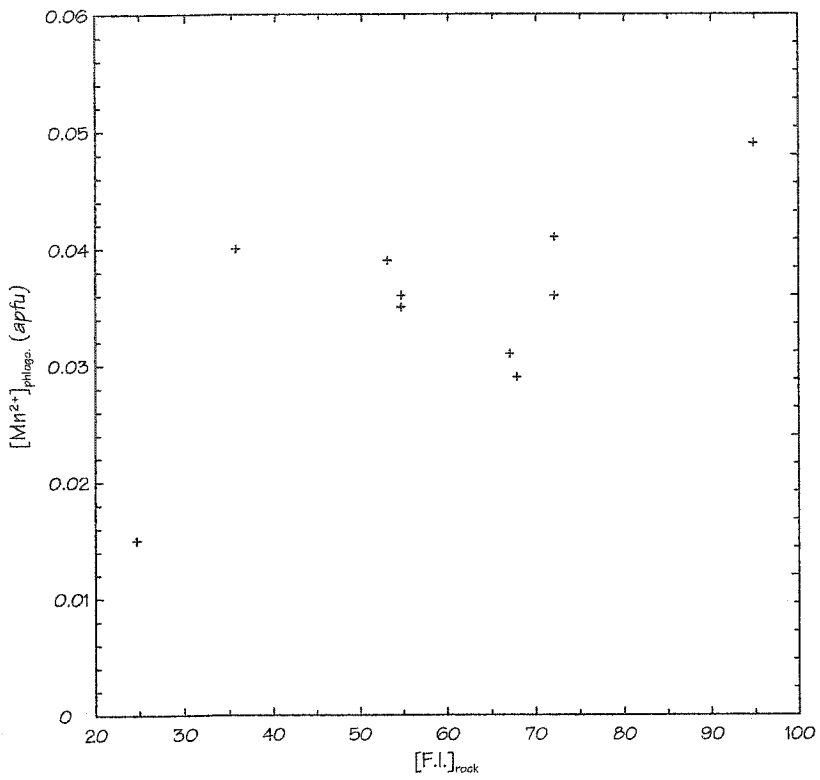

Figure 3.19 Mn^{2+} in phlogopite from Emens intrusion as a function of host-rock Fractionation Index (see text). The positive correlation may result from the absence of any significant amount of pyroxene or amphibole fractionation during the early stages of magmatic evolution.

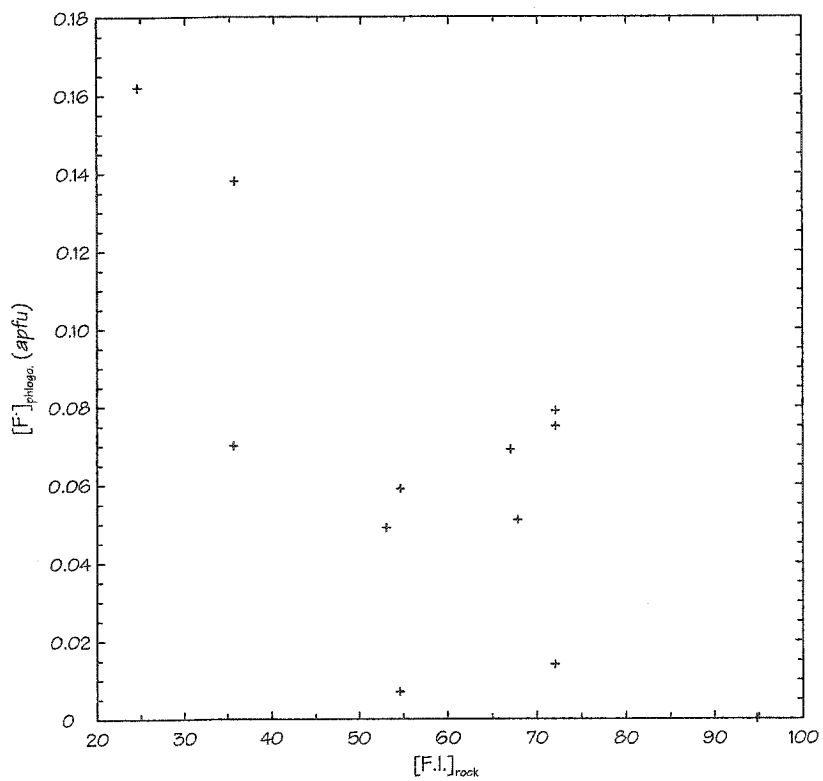

Figure 3.20 F^- in phlogopite from Emens intrusion as a function of host-rock Fractionation Index (see text).

V. Feldspar

A number of feldspar microprobe analyses were done on samples from the Iris, Garrison and Ludgate intrusions in order to establish the bulk composition of some microperthite crystals. Microperthite selected for analyses were clear, fresh looking and contained μm-scale homogeneously distributed exsolution domains (Figure 2.32). A defocused beam with a diameter of 10 to 12 μm was used during the analyses in order to have an average composition of several domains. An average of five analyses were performed on each grain with the location of each analysis randomly selected within the grain. Feldspar formulas are calculated on the basis of 8 oxygen. Average microperthite compositions (and the 95% confidence interval on the average) are given in Table 3.4. It should be noted that since only four or five analyses were performed on each grain the confidence intervals are usually high. Therefore, the average compositions reported in Table 3.4 should be taken as rough estimations of the true microperthite composition. All feldspar analyses are plotted on the Na-K-Ca ternary diagram in terms of their mole % end-member compositions (Figure 3.21).

The composition of microperthite from the Ludgate intrusion varies from $Ab_{63.8}Or_{36.2}An_0$ to $Ab_{72.0}Or_{27.8}An_{0.1}$ while the average microperthite compositions from Garrison and Iris intrusions are $Ab_{34.0}Or_{64.8}An_{1.1}$ and $Ab_{50.2}Or_{49.1}An_{0.7}$ respectively. In all cases, values of the anorthite component are negligible apart for the microperthite crystal from Garrison intrusion, which contains 1.1 mole % An.

Si^{4+}- and Al^{3+}-contents are usually close to the ideal alkali feldspar composition (i.e., 3:1). Si^{4+} values range from 2.986 to 3.012 *apfu* in microperthite from the Ludgate intrusion while the values range from 2.982 to 2.999 *apfu* in the one from Iris intrusion.

Table 3.4 Representative microprobe analyses of microperthite.

	1	2	3	4
	Ludgate 88-2 (n=4)	Ludgate 91-4 (n=5)	Garrison 101-3 (n=5)	Iris 108-2 (n=5)
SiO_2	67.08±0.79[a]	66.55±1.26	64.45±0.56	66.16±0.78
TiO_2	0.00	0.01±0.01	0.01±0.01	0.11±0.28
Al_2O_3	18.57±0.14	18.72±0.25	18.74±0.24	18.57±0.19
CaO	0.01±0.01	0.03±0.05	0.23±0.11	0.15±0.11
FeO	0.33±0.03	0.25±0.07	0.15±0.02	0.28±0.06
SrO	0.04±0.10	0.12±0.08	0.24±0.04	0.03±0.06
BaO	0.113±0.11	0.17±0.15	0.89±0.20	0.08±0.05
Na_2O	7.49±1.22	8.47±2.65	3.85±1.65	5.86±0.91
K_2O	6.44±2.05	4.93±3.66	11.13±2.41	8.71±1.43
Total	100.06	99.25	99.68	99.97
Chemical formulae calculated on the basis of 8 oxygen				
Si^{4+}	3.003±0.010	2.992±0.006	2.968±0.007	2.990±0.012
Al^{3+}	0.980±0.004	0.992±0.007	1.017±0.007	0.989±0.006
ΣT	3.983	3.984	3.985	3.979
Ti^{4+}	0.000	0.000	0.000	0.004±0.010
Fe^{2+}	0.013±0.002	0.009±0.002	0.006±0.001	0.011±0.002
Sr^{2+}	0.001±0.002	0.003±0.002	0.007±0.001	0.001±0.002
Ba^{2+}	0.002±0.002	0.003±0.003	0.016±0.004	0.001±0.001
Ca^{2+}	0.000	0.001±0.002	0.012±0.005	0.007±0.006
Na^+	0.650±0.101	0.737±0.220	0.343±0.144	0.513±0.076
K^+	0.368±0.120	0.285±0.216	0.654±0.156	0.503±0.087
ΣA	1.034	1.038	1.038	1.040
Mol.% end-member				
Ab	63.7	71.8	33.5	50.1
Or	36.1	27.8	63.8	49.1
An	0.0	0.1	1.1	0.7
Cs[b]	0.2	0.3	1.6	0.1

1 Film microperthite from alkali-feldspar quartz-syenite.
2 Film microperthite from alkali-feldspar quartz-syenite.
3 Film microperthite from hornblende quartz-monzonite.
4 Film microperthite from alkali-feldspar quartz-syenite.

[a] All uncertainties are calculated using the 95% confidence interval on the average composition.

[b] Celsian ($BaAl_2Si_2O_8$)

Na^+-content is highest in microperthite from Ludgate intrusion with values ranging from 0.470 to 0.933 *apfu* while K^+ values are highest in feldspar from Garrison intrusion with values ranging from 0.461 to 0.738 *apfu*.

Microperthite from Garrison intrusion is enriched in Ba^{2+} and Sr^{2+} compared to the ones from the other intrusions. Ba^{2+} values range from 0.011 to 0.020 *apfu* while those of Sr^{2+} range from 0.006 to 0.009 *apfu*. In comparison, microperthite from the Ludgate intrusion has much lower values with average Ba^{2+}- and Sr^{2+}-contents of 0.002 ± 0.002 *apfu* and 0.001 ± 0.002 *apfu* respectively. The higher Ba^{2+} values in the Garrison intrusion microperthite crystal is most likely related to the fact that this crystal has a higher Or-content compared to all the others. Indeed, Icenhower & London (1996) have shown that, in peraluminous systems, the incorporation of Ba into alkali feldspar is a linear function of the orthoclase content. In contrast, the amount of Sr entering alkali-feldspar does not appear to be affected by variations in albite and orthoclase content (Icenhower & London, 1996).

One analysis from the Iris intrusion contains a high Ti^{4+} value of 0.018 *apfu*. This probably reflects the presence of minute inclusions of a Ti-bearing mineral such as rutile or hematite. Hematite is the most likely candidate since one hematite grain analysed in the same sample contained 1.11 wt% TiO_2 (see oxide section).

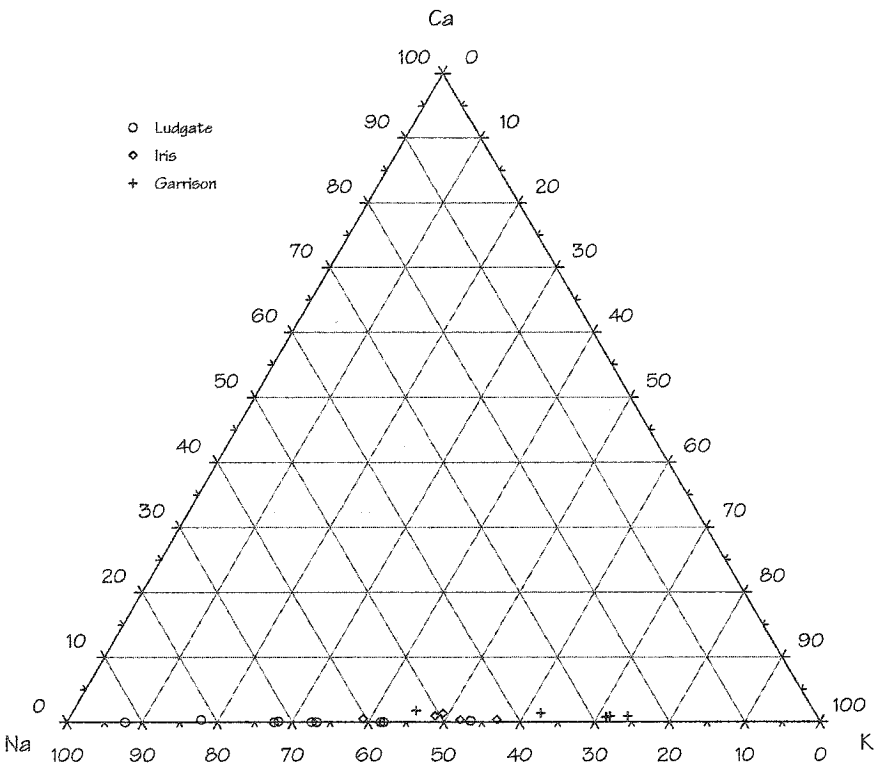

Figure 3.21 The composition of all microperthite analyses in terms of their mole % end-member.

VI. Garnet

Garnet is a common accessory mineral in the rocks from the Emens intrusion and was also identified in one sample from the Pangea intrusion.

Garnet formulas are calculated on the basis of 12 anions and 8 cations. Ferric and ferrous Iron-contents are estimated assuming ideal stoichiometry. Most analysed garnets crystals from Emens intrusion are titanian-andradite whereas the ones from Pangea intrusion are grossular-titanian-andradite. Furthermore, since most garnet crystals have TiO_2-contents that are within the range of compositions of melanite i.e. between 1 and 5 wt % (Deer et al., 1962), they can collectively be referred to as melanite. Five representative garnet analyses are listed in Table 3.5. Cations were assigned to structural sites following the scheme of Deer et al. (1996).

In general, garnet crystals from Pangea intrusion are enriched in grossular ($Ca_3Al_2Si_3O_{12}$) compared to the ones from Emens intrusion. The average grossular content of melanite from Emens intrusion is 11.45 % while it is 18.0 % at the Pangea intrusion. Melanite from both intrusions has similar Ti^{4+}-contents. Ti^{4+} values range from 0.165 to 0.218 *apfu* in garnet from Pangea intrusion and from 0.063 to 0.231 *apfu* in garnet from Emens intrusion. In thin section, melanite containing the higher values of Ti^{4+} is usually dark brown whereas the ones that have less TiO_2 are light brown. Vanadium values are elevated in melanite from both intrusions. The values range from 0.011 to 0.028 *apfu* in garnet from Pangea intrusion while they range from 0.013 to 0.028 *apfu* in the ones from Emens intrusion. A minor amount of Zr^{4+} and Y^{3+} are also present in melanite from both intrusions.

Titanian-andradite and melanite are common in alkaline rocks (Deer et al., 1996) and more precisely in alkaline silica-undersaturated potassic to ultrapotassic rocks (Mitchell, 1996). In fact, titanian-andradite is a characteristic mineral of the malignite-borolanite group of potassic

Table 3.5 Representative microprobe analyses of melanite.

	1	2	3	4	5
	Pangea 041-31	Emens 045-21	Emens 083-31	Emens 086-11	Emens 164-41
SiO_2	35.30	33.91	34.75	35.30	35.31
TiO_2	2.62	3.63	3.21	2.22	2.02
Nb_2O_5	0.06	0.00	0.00	0.08	0.00
ZrO_2	0.12	0.28	0.15	0.00	0.09
Al_2O_3	6.31	2.39	2.31	3.83	2.83
Cr_2O_3	0.03	0.01	0.00	0.00	0.01
MgO	0.24	0.26	0.13	0.02	0.08
V_2O_5	0.20	0.31	0.50	0.25	0.40
Y_2O_3	0.09	0.00	0.01	0.03	0.00
CaO	32.17	32.19	32.32	33.29	32.73
MnO	0.60	0.32	0.45	0.55	0.66
[a]FeO	4.04	2.44	3.22	1.45	1.98
[a]Fe_2O_3	17.47	23.27	21.78	22.38	23.26
Na_2O	0.02	0.09	0.05	0.03	0.04
K_2O	0.00	0.01	0.00	0.00	0.00
Total	99.30	99.11	98.88	99.43	99.41
Chemical formulae calculated on the basis of 12 anions and 8 cations					
Si^{4+}	2.948	2.871	2.939	2.944	2.961
Al^{3+}	0.052	0.129	0.061	0.056	0.039
Σ Z	3.000	3.000	3.000	3.000	3.000
Al^{3+}	0.569	0.109	0.169	0.320	0.241
Ti^{4+}	0.165	0.231	0.204	0.139	0.127
Fe^{3+}	1.098	1.482	1.386	1.405	1.468
Nb^{5+}	0.002	0.000	0.000	0.003	0.000
Zr^{4+}	0.005	0.011	0.006	0.000	0.004
Cr^{3+}	0.002	0.001	0.000	0.000	0.001
V^{5+}	0.011	0.017	0.028	0.013	0.022
Y^{3+}	0.004	0.000	0.000	0.001	0.000
Σ Y	1.856	1.852	1.793	1.881	1.863
Ca^{2+}	2.789	2.920	2.929	2.975	2.941
Mn^{2+}	0.042	0.023	0.032	0.039	0.047
Mg^{2+}	0.030	0.033	0.016	0.002	0.010
Fe^{2+}	0.282	0.173	0.228	0.101	0.139
Na^{+}	0.003	0.015	0.009	0.004	0.006
K^{+}	0.000	0.001	0.000	0.000	0.000
Σ X	3.146	3.165	3.214	3.121	3.233
Mol. % End-members					
Prp	1.0	1.1	0.5	0.1	0.3
Adr[b]	68.9	92.7	90.4	82.8	86.8
Alm	9.0	5.5	7.1	3.4	4.4
Uv[c]	0.1	0.1	0.0	0.0	0.1
Sps	1.3	0.7	1.0	1.3	1.5
Grs	19.8	0.0	1.0	12.6	6.9

1 Melanite from garnet-rich melasyenite.
2 Melanite from melasyenite.
3 Melanite from alkali-feldspar porphyritic biotite-syenite.
4 Melanite from melasyenite.
5 Melanite from alkali-feldspar porphyritic biotite-syenite.
[a] Estimated assuming ideal stoichiometry.
[b] Andradite component includes Ti^{4+}.
[c] Uvarovite [$Ca_3Cr_2(SiO_4)_3$]

plutonic complexes (Mitchell, 1996). Examples of this group include the Kruger complex, British Columbia (Campbell, 1939), intrusions in the Kobuk-Selawik Lowlands, Alaska (Miller, 1972), the Borralan complex, Scotland (Woolley, 1973) and the Poohbah Lake complex, Ontario (Mitchell & Platt, 1979). In some cases, like the Granite Mountain pluton (Miller, 1972) in the Kobuk-Selawik Lowlands, andradrite is extremely abundant. In this pluton, the garnet syenite unit contains from 6 to 25 % andradite.

VII. Other accessory silicates

Representative analyses of chlorite, epidote and titanite are listed in Tables 3.6, 3.7 & 3.8 respectively. Chlorite formulas are calculated on the basis of 18 (O, F, Cl) while the epidote formulas are based on 13 (O, F, Cl). Only one titanite analysis was performed. The formula is calculated on the basis of 5 oxygen. In the case of epidote and chlorite, H_2O-content was estimated assuming ideal site occupancy. No Fe^{3+} estimations were performed.

Although no compositional boundary is given in Deer et al. (1996) for the nomenclature of the clinozoisite-epidote solid solution, the high FeO-content (10.26-15.16 wt%) in the analysed crystals suggests that they are epidote and not clinozoisite. Chlorite is enriched in Mg^{2+} (2.57-2.90 *apfu*) compared to Fe^{2+} (1.72-1.91 *apfu*) and can therefore be classified as clinochlore.

Table 3.6 Representative analyses of chlorite.

	1	2	3
	Pangea 050-12	Emens 161-11	Emens 161-22
SiO_2	27.34	27.12	27.14
TiO_2	0.01	0.00	0.02
Al_2O_3	20.05	20.35	20.15
Cr_2O_3	0.02	0.00	0.00
MgO	18.98	16.56	16.81
CaO	0.05	0.06	0.03
MnO	1.34	1.30	2.01
FeO	20.07	21.91	21.51
Na_2O	0.00	0.00	0.00
K_2O	0.03	0.00	0.13
F	0.00	0.03	0.16
Cl	0.02	0.00	0.00
[a]H_2O	11.68	11.50	11.47
O=F	0.00	-0.01	-0.07
O=Cl	0.00	0.00	0.00
Total	99.59	98.82	99.37
Chemical formulae calculated on the basis of 18 (O, F, Cl)			
Si^{4+}	2.805	2.825	2.819
Ti^{4+}	0.001	0.000	0.002
Al^{3+}	2.424	2.498	2.466
Cr^{3+}	0.001	0.000	0.000
Mg^{2+}	2.903	2.572	2.603
Ca^{2+}	0.006	0.007	0.003
Mn^{2+}	0.117	0.115	0.177
Fe^{2+}	1.722	1.909	1.868
Na^+	0.000	0.000	0.000
K^+	0.004	0.000	0.018
F^-	0.000	0.011	0.052
Cl^-	0.003	0.000	0.000
OH^-	7.997	7.989	7.948

1 Chlorite from alkali-feldspar syenite.
2 Chlorite from alkali-feldspar syenite.
3 Chlorite from alkali-feldspar syenite.
[a] Estimated assuming (OH^-, Cl^-, F^-) = 8.

Table 3.7 Representative analyses of epidote.

	1	2	3	4
	Pangea 008-11	Pangea 015-21	Pangea 020-11	Pangea 026-21
SiO_2	37.25	38.19	36.96	36.69
TiO_2	0.11	0.13	0.07	0.03
Al_2O_3	22.24	26.42	22.40	22.23
Cr_2O_3	0.01	0.00	0.02	0.00
MgO	0.02	0.04	0.04	0.01
CaO	21.65	22.92	21.70	22.52
MnO	0.28	0.12	0.33	0.09
FeO	15.16	10.26	14.51	14.77
Na_2O	0.00	0.00	0.00	0.00
K_2O	0.00	0.01	0.00	0.00
F	0.06	0.06	0.00	0.10
Cl	0.01	0.00	0.05	0.00
[a]H_2O	1.77	1.85	1.78	1.74
O=F	-0.02	-0.02	0.00	-0.04
O=Cl	0.00	0.00	-0.01	0.00
Total	98.53	99.97	97.85	98.14
Chemical formulae calculated on the baais of 13 (O, F, Cl)				
Si^{4+}	3.101	3.049	3.093	3.072
Ti^{4+}	0.007	0.008	0.004	0.002
Al^{3+}	2.182	2.486	2.209	2.194
Cr^{3+}	0.001	0.000	0.002	0.000
Mg^{2+}	0.003	0.004	0.005	0.001
Ca^{2+}	1.931	1.960	1.946	2.020
Mn^{2+}	0.020	0.008	0.023	0.006
Fe^{2+}	1.056	0.685	1.015	1.034
Na^+	0.000	0.000	0.000	0.000
K^+	0.000	0.001	0.000	0.001
F^-	0.015	0.015	0.000	0.026
Cl^-	0.001	0.001	0.008	0.000
OH^-	0.984	0.984	0.992	0.974

1 Epidote from melasyenite.
2 Epidote from melasyenite.
3 Epidote from melasyenite.
4 Epidote from pyroxene-bearing hornblendite.
[a] Estimated assuming (OH^-, Cl^-, F^-) = 1.

VIII. Oxides

A few analyses of hematite, ilmenite and magnetite were performed. Fe^{3+} values were estimated by assuming ideal stoichiometry and electrostatic neutrality. Hematite and ilmenite formulas are calculated on the basis of 2 cations and 3 oxygen whereas magnetite formulas are based on 3 cations and 4 oxygen. All oxide analyses are listed in Table 3.9.

Hematite from the Iris intrusion is almost pure. Estimated Fe_2O_3 values range between 97.04 and 99.34 wt%. However, one analysis has higher concentrations of TiO_2 and FeO, (i.e., 1.11 and 1.44 wt% respectively) which is most likely the result of minute exsolved ilmenite domains. Vanadium is elevated in both hematite analyses with values ranging from 0.26 to 0.36 wt%. Cr^{3+}, Mg^{2+}, Mn^{2+} and Ni^{2+} were detected but only in trace amounts (total = 0.05 wt%).

Magnetite is also almost pure with estimated $FeO+Fe_2O_3$-contents ranging between 99.40 and 99.49 wt%. TiO_2 and V_2O_5 values are higher in magnetite from Pangea intrusion with 0.65 and 0.41 wt% respectively compared to the ones from Iris intrusion with 0.11 and 0.19 wt% respectively. All other elements (i.e., Si, Nb, Al, Cr, Mg, Ni and Zn) are present in trace amounts (total = 0.27 wt%).

One coarse ilmenite exsolution lamella in a magnetite crystal from the pyroxene-bearing hornblendite unit was analysed. The only striking characteristic is the elevated Mn^{2+}-content of 3.55 wt%, corresponding to 0.076 *apfu*.

Table 3.8 Single analysis of titanite.

	1
	Emens 043-32
SiO_2	29.68
TiO_2	36.44
Nb_2O_5	0.05
ZrO_2	0.30
Al_2O_3	1.17
Cr_2O_3	0.02
V_2O_5	0.11
Y_2O_3	0.00
CaO	27.66
MgO	0.00
MnO	0.02
FeO	1.48
Na_2O	0.00
K_2O	0.00
Total	96.93
Based on 5 oxygen	
Si^{4+}	1.005
Ti^{4+}	0.928
Nb^{5+}	0.001
Zr^{4+}	0.005
Al^{3+}	0.047
Cr^{3+}	0.000
V^{5+}	0.002
Y^{3+}	0.000
Ca^{2+}	1.003
Mg^{2+}	0.000
Mn^{2+}	0.001
Fe^{2+}	0.042
Na^{+}	0.000
K^{+}	0.000

1 Titanite from alkali-feldspar porphyritic biotite-syenite.

Table 3.9 Analyses of hematite, magnetite and ilmenite.

	1	2	3	4	5
	Iris 108-11	Iris 129-23	Pangea 009-41	Pangea 009-42	Iris 129-22
SiO_2	0.08	0.03	0.07	0.07	0.08
TiO_2	1.11	0.22	50.48	0.65	0.11
Nb_2O_5	0.00	0.05	0.04	0.05	0.00
Al_2O_3	0.00	0.00	0.00	0.00	0.00
Cr_2O_3	0.03	0.03	0.01	0.11	0.03
V_2O_5	0.26	0.36	0.06	0.41	0.19
MgO	0.02	0.02	0.08	0.04	0.02
MnO	0.00	0.02	3.55	0.00	0.06
FeO	1.44	0.79	41.82	32.64	31.37
$^{a}Fe_2O_3$	97.04	99.34	3.61	66.85	68.03
NiO	0.02	0.01	0.00	0.00	0.02
ZnO	0.00	0.00	0.06	0.00	0.02
Total	100.00	100.87	99.79	100.83	99.92
Based on:	2 cations and 3 oxygen			3 cations and 4 oxygen	
Si^{4+}	0.002	0.001	0.002	0.003	0.003
Ti^{4+}	0.022	0.004	0.961	0.019	0.003
Nb^{5+}	0.000	0.001	0.000	0.001	0.000
Cr^{3+}	0.001	0.001	0.000	0.003	0.001
V^{5+}	0.005	0.006	0.001	0.010	0.005
Mg^{2+}	0.001	0.001	0.003	0.002	0.001
Mn^{2+}	0.000	0.000	0.076	0.000	0.002
Fe^{2+}	0.032	0.017	0.886	1.042	1.011
Fe^{3+}	1.937	1.969	0.069	1.920	1.973
Ni^{2+}	0.000	0.000	0.000	0.000	0.001
Zn^{2+}	0.000	0.000	0.001	0.000	0.001

1 Hematite from alkali-feldspar quartz-syenite.
2 Hematite from pyroxene-bearing hornblendite.
3 Ilmenite from pyroxene-bearing hornblendite.
4 Magnetite from pyroxene-bearing hornblendite.
5 Magnetite from pyroxene-bearing hornblendite.
[a] Estimated assuming ideal stoichiometry and electroneutrality.

Chapter 4

Whole-rock chemistry

I. Introduction

THE principal objectives of this chapter are two-fold; first, to characterize the whole-rock major element and trace element geochemistry of the individual intrusions and the suite as a whole and, second, to use this geochemical information to gain insights into the petrogenesis of these rocks. In order to achieve these goals, over 90 whole-rock geochemical analyses were performed on a suite of samples that included representatives of all the major units from each intrusion. Since most of the fieldwork (mapping and core logging) was done on the Iris, Pangea and Emens intrusions, the abundance of samples (and hence analyses) from these intrusions greatly outnumbers those from the Ludgate and Garrison intrusions. It should be noted that only one outcrop of the Ludgate intrusion was sampled and that only one day was spent in the field on the Garrison intrusion. Consequently, emphasis is placed on those three (i.e., Iris, Pangea and Emens) intrusions where a wealth of information is available.

II. Analytical methods

A. Sample preparation

In order to get an accurate account of the primary geochemical characteristics of the studied intrusions, only those samples that were not altered (when possible) or veined were chosen for geochemical analyses. For the samples that were collected in the field (as opposed to drill core), all weathering was removed using a diamond blade. Samples were then crushed to particles ranging in size from 3 to 10 mm in a conventional jaw crusher. The jaw crusher was thoroughly cleaned between each crushing to minimize contamination. The crushed samples were then sent to the Geoscience Laboratories of the Ontario Geoservices Centre in Sudbury where they were pulverized to a fine powder (~90 μm) in a 99.8 % pure Al_2O_3 planetary ball mill. The appropriate amount of powder was then fused with lithium metaborate and lithium carbonate to produce glass disks suitable for X-ray fluorescence spectrometry (XRF) analyses. Splits of the powders were prepared for ICP-MS analyses (Inductively-coupled plasma mass spectrometry) by acid digestions using the closed beaker method. The use of a closed beaker allows the acid to reflux, thereby allowing a continuous exposure of the sample to the acid over long periods of time, ensuring total digestion of all solids (Geoscience Laboratories, 2002). This method is favoured for the determination of high field strength (HFSE) and rare earth elements (REE).

B. Instrumentation

All major and trace elements were determined by a combination of X-ray fluorescence spectrometry (XRF), inductively coupled plasma mass spectrometry (ICP-MS) and inductively-coupled plasma atomic emission spectrometry (ICP-AES), and titrimetry at the Geoscience Laboratories, Ontario Geoservices Centre, Sudbury. A subset of 29 samples were also analysed for rare earth elements by ICP-MS at the same facility. Table 4.1 summarizes the analytical methods

Table 4.1 Analytical methods used and detection limits for each element analysed.

Oxide	Method	Detection limit
Al_2O_3	XRF	0.01
CaO	XRF	0.01
Fe_2O_3(t)	XRF	0.01
FeO	Titration	0.06
K_2O	XRF	0.01
MgO	XRF	0.01
MnO	XRF	0.01
Na_2O	XRF	0.01
P_2O_5	XRF	0.01
SiO_2	XRF	0.01
TiO_2	XRF	0.01
LOI	Furnace	0.05
CO_2	IRS	0.03
S	IRS	0.01

XRF	X-Ray Fluorescence
IRS	Infrared Spectroscopy
ICP-MS	Inductively Coupled Plasma-Mass Spectroscopy
ICP-AES	Inductively Coupled Plasma-Atomic Emission Spectroscopy

Element	Method	Detection Limit LL(ppm)	UL(ppm)
Ba	ICP-MS	5.0	3500
Be	ICP-AES	3.0	
Ce	ICP-MS	0.01	2500
Cs	ICP-MS	0.01	250
Cr	ICP-MS	1.0	500
Co	ICP-AES	1.0	3500
Cu	ICP-AES	2.0	1000
Dy	ICP-MS	0.01	800
Er	ICP-MS	0.01	300
Eu	ICP-MS	0.01	300
Gd	ICP-MS	0.01	700
Ga	ICP-MS	1.0	900
Hf	ICP-MS	0.01	900
Ho	ICP-MS	0.01	200
La	ICP-MS	0.01	250
Pb	ICP-MS	0.01	7000
Lu	ICP-MS	0.01	250
Mo	ICP-AES	8.0	
Nd	ICP-MS	0.01	2000
Ni	ICP-AES	5.0	
Nb	ICP-MS	0.02	300
Pr	ICP-MS	0.01	250
Rb	ICP-MS	1.0	400
Sm	ICP-MS	0.01	1800
Sc	ICP-AES	1.0	
Sr	ICP-MS	0.01	3000
Sr	ICP-AES	1.0	
Ta	ICP-MS	0.01	350
Tb	ICP-MS	0.01	200
Th	ICP-MS	0.02	500
Tm	ICP-MS	0.01	200
Sn	ICP-MS	3.0	1000
W	ICP-AES	35.0	
U	ICP-MS	0.02	500
V	ICP-AES	5.0	
Yb	ICP-MS	0.01	300
Y	ICP-MS	0.05	800
Zn	ICP-AES	2.0	
Zr	ICP-MS	1.0	2000
Au	ICP-AES	5 ppb	
Pt	ICP-AES	8 ppb	
Pd	ICP-AES	8 ppb	

and the detection limits for each of the elements analysed. The loss on ignition (LOI) values were calculated after the disks were heated 1 hour at 1000°C in a furnace. Values of CO_2 and S were determined by infrared spectroscopy (IRS). The Geoscience Laboratories certified that all analyses met their quality control standards, which in the case of ICP-MS and WD-XRF, are results with precision and accuracy better than ± 5 % when a particular element concentration is 10 times the limit of quantification (Personnal communication, Schweyer 2002). The limit of quantification (LOQ) is the concentration of an analyte, which can be reliably detected with statistical reproducibility. The LOQ is quantified as a signal 10 times the standard deviation of the background (Taylor, 1987).

III. Major and compatible trace elements

A. General classification

Analyses of major and trace elements of representative samples from each intrusion are listed in Table 4.2. A complete listing of all the data is found in Appendix 1. All five intrusions are alkaline following the classification of Miyashiro (1978), i.e most samples have Na_2O+K_2O values higher than the defined boundary with only a few samples from the Iris intrusion plotting in the subalkaline field (Figure 4.1). The Emens and Pangea intrusions are enriched in K_2O compared to the Iris, Garrison and Ludgate intrusions. Most of their samples plot within the potassic ($K_2O/Na_2O > 1$; LeBas et al., 1986) and ultrapotassic fields ($K_2O/Na_2O > 2$; Foley et al., 1987) on the K_2O-Na_2O diagram (Figure 4.2). It should be noted that, although numerous samples plot in the ultrapotassic field, only five of these are ultrapotassic *sensu stricto* since the definition of ultrapotassic rocks of Foley et al. (1987) requires other parameters such as: $K_2O > 3$ wt% and $MgO > 3$ wt%.

The Iris and Ludgate intrusions are Na-rich compared to the other intrusions. Most syenite samples from the Iris intrusion plot within the sodic field ($Na_2O - 4 > K_2O$; LeBas et al., 1986) whereas the mafic rocks of that intrusion, which contain considerably less Na_2O and K_2O, plot in the «transitional» field of the Na_2O versus K_2O diagram (Figure 4.2). Accordingly, the syenite units can be referred to as sodic. Similarly, the two samples from the Ludgate intrusion either plot within, or very close to, the sodic field while samples from the Garrison intrusion cluster in the «transitional» field.

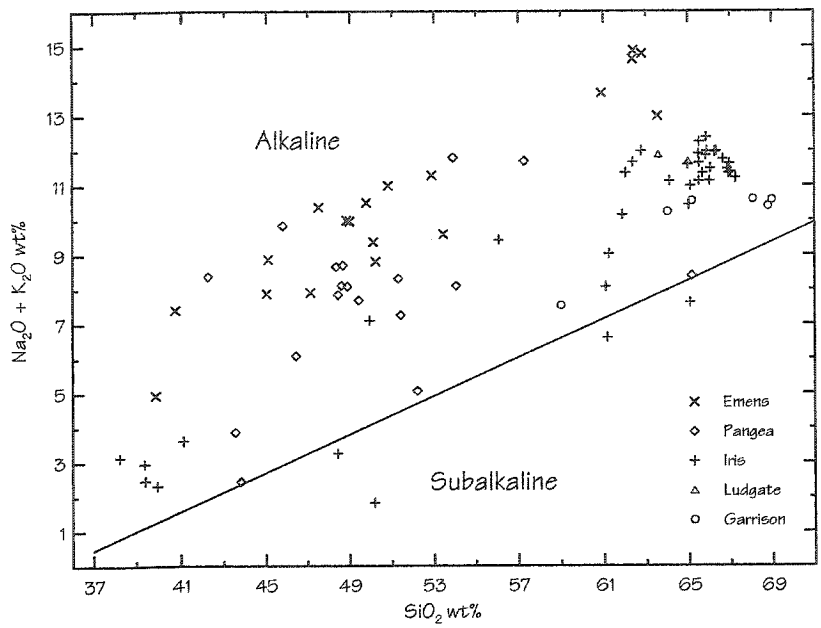

Figure 4.1 $K_2O + Na_2O$ as a function of SiO_2. The five studied intrusions are alkaline in the sense of Miyashiro (1978). Only a few samples from Iris intrusion plot in the subalkaline field.

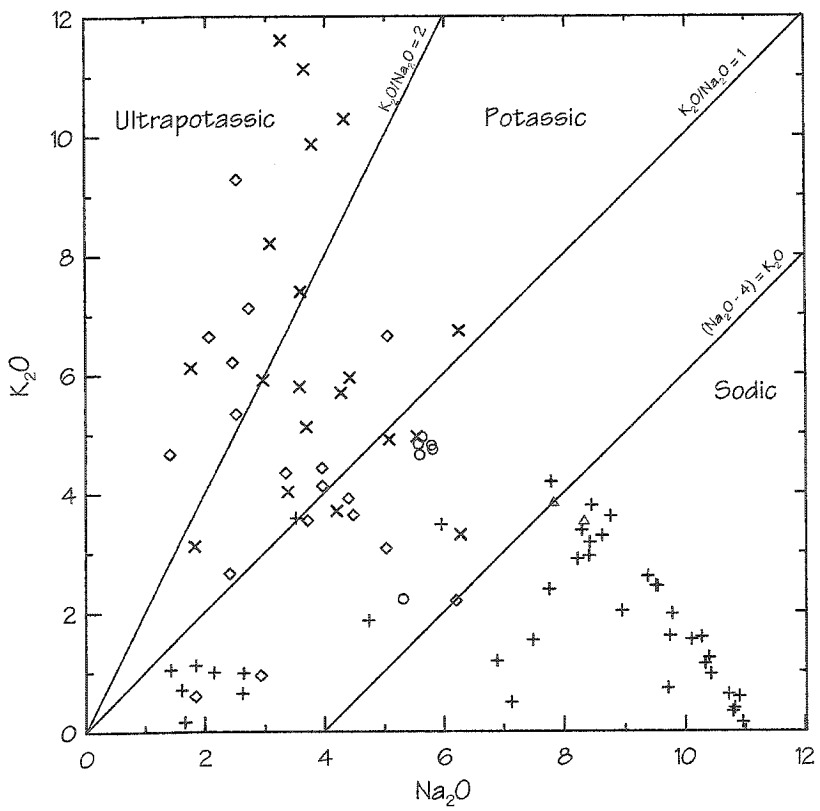

Figure 4.2 K_2O (wt%) as a function of Na_2O (wt%). Most samples from the Iris and Ludgate intrusions plot in the sodic field whereas samples from Emens and Pangea intrusions plot in the potassic and ultrapotassic fields. Potassic and sodic boundaries are from LeBas et al. (1986) and the ultrapotassic boundary is from Foley et al. (1987). Symbols are as in previous Figure.

Table 4.2 Major and trace elements analyses of representative rocks from the studied intrusions.

	Emens intrusion						Pangea intrusion					
Unit	B-Sye	B-Sye	B-Sye	B-Sye	M-Sye	Sye	Hbdt	M-Sye	M-Sye	M-Sye	M-Sye	Sye
Sample	084	157	177	178	080	165	019	035	180	186	191	193
SiO_2	52.88	50.21	47.50	49.78	45.02	60.88	43.54	46.42	48.88	51.28	52.20	57.26
TiO_2	0.87	0.64	0.87	0.76	0.60	0.18	2.17	1.39	1.25	1.18	0.71	0.37
Al_2O_3	14.80	13.92	16.58	16.78	9.69	17.40	14.01	9.52	15.31	15.61	15.00	17.71
Fe_2O_3	3.34	6.57	2.27	2.84	3.07	1.02	7.04	3.82	6.13	4.88	1.83	0.99
FeO	2.64	1.52	4.01	2.87	4.84	1.22	9.92	5.81	3.72	4.14	5.99	2.45
MnO	0.13	0.16	0.15	0.16	0.13	0.06	0.23	0.18	0.19	0.20	0.18	0.10
MgO	4.77	4.13	2.49	2.26	16.67	1.60	6.05	9.44	3.41	3.07	6.65	0.87
CaO	5.43	10.08	6.72	5.90	7.81	1.77	9.94	11.40	7.68	7.01	9.63	3.59
Na_2O	3.08	3.69	4.42	5.54	1.76	3.78	2.93	1.41	3.96	4.40	2.41	5.05
K_2O	8.20	5.11	5.94	4.95	6.11	9.86	0.94	4.66	4.12	3.91	2.65	6.64
BaO	0.22	0.33	0.20	0.20	0.06	0.17	0.02	0.20	0.17	0.23	0.05	0.15
SrO	0.22	0.40	0.37	0.28	0.05	0.20	0.06	0.14	0.17	0.23	0.04	0.20
P_2O_5	0.53	0.61	0.40	0.35	0.29	0.11	0.18	0.79	0.58	0.41	0.06	0.16
[a]CO_2	0.24	0.11	5.15	4.06	0.71	0.54	0.88	2.57	1.25	1.2	0.37	2.07
[a]S	0.12	0.24	0.31	0.15	0.01	0.09	0.34	0.03	0.22	0.52	*n.d.*	0.02
[b]LOI	1.13	0.79	5.66	5.03	1.77	1.26	2.01	3.71	2.88	1.74	1.86	3.18
Total	98.24	98.16	97.58	97.70	97.87	99.51	99.04	98.89	98.45	98.29	99.26	98.72
Be (ppm)	*n.d.*	*n.d.*	5	7	*n.d.*	*n.d.*	3	*n.d.*	4	5	*n.d.*	6
Co	29	24	18	19	54	7	60	55	26	30	41	7
Cu	59	95	87	156	15	192	150	64	159	127	11	59
Mo	15	20	10	*n.d.*	16	11	*n.d.*	*n.d.*	9	9	8	9
Ni	49	42	28	25	429	26	123	61	30	39	89	9
Sc	11	14	9	8	23	4	33	33	13	13	30	2
V	146	252	216	181	192	55	374	252	314	261	236	106
W	*n.d.*	*n.d.*	*n.d.*	*n.d.*	*n.d.*	69	*n.d.*	*n.d.*	*n.d.*	*n.d.*	*n.d.*	*n.d.*
Zn	163	105	160	143	117	65	193	174	139	157	69	120
Ba	1926	2960	1770	1819	514	1496	164	1774	1482	2064	436	1346
Cr	161	89	27	25	>500	35	157	156	19	63	188	2
Ga	22.90	16.48	23.18	22.00	15.16	21.26	20.18	18.23	25.35	24.16	16.92	33.20
Pb	9.76	10.22	18.22	17.78	5.19	32.88	5.73	7.80	22.09	19.75	2.67	60.35
Sn	*n.d.*	*n.d.*	*n.d.*	*n.d.*	*n.d.*	*n.d.*	*n.d.*	*n.d.*	*n.d.*	*n.d.*	*n.d.*	*n.d.*
Rb	182.63	109.30	140.02	131.14	236.62	157.12	26.75	141.40	62.98	55.94	103.71	136.05
Sr	1935.8	2811.4	2989.3	2443.6	466.6	1889.3	630.3	1340.6	1702.2	1946	451.1	1934.6
Nb	7.61	5.46	12.50	11.76	3.77	1.76	7.17	8.38	13.11	14.20	2.19	31.86
Cs	3.46	1.85	5.82	2.70	-	-	1.82	-	1.54	1.14	-	1.24
Hf	3.59	3.95	5.57	5.00	-	-	2.60	-	8.67	8.57	-	9.94
Ta	0.27	0.29	0.65	0.52	0.18	0.07	0.40	0.38	0.68	0.77	0.13	0.75
Th	8.00	7.09	11.93	11.57	5.19	2.3	2.17	6.52	16.54	15.5	0.50	38.10
U	1.67	1.03	1.93	2.93	-	-	0.70	-	3.74	3.76	-	9.20
Y	24.98	29.32	42.48	36.74	12.93	5.97	32.94	27.39	48.69	49.25	16.07	34.16
Zr	127.83	120.89	175.43	171.42	75.13	69.54	92.35	124.63	299.08	287.44	54.58	431.09

continued

B-Sye Alkali-feldspar porphyritic biotite-syenite
M-Sye Melasyenite
Sye Alkali-feldspar syenite
Hbdt Pyroxene-bearing hornblendite
n.d. Not detected

\- Not analysed
[a] Not included in totals
[b] Loss on ignition at 1000° C

Table 4.2 Major and trace elements analyses of representative rocks from the studied intrusions. *(continued)*

	Iris intrusion										
Unit	A-Sye	A-Sye	MD	MD	Hbdt	Hbdt	P-Sye	P-Sye	Q-Sye	Q-Sye	Q-Sye
Sample	118	153	125	133	129	154	116	121	107	113	117
SiO_2	62.36	62.77	49.93	48.42	41.09	39.35	64.96	65.09	65.87	66.96	66.64
TiO_2	0.29	0.25	1.11	2.83	1.72	1.88	0.26	0.25	0.14	0.13	0.05
Al_2O_3	18.18	18.02	15.29	12.78	9.55	9.70	17.86	17.42	18.59	18.36	18.03
Fe_2O_3	1.85	1.36	5.77	6.13	10.59	10.20	1.40	1.39	1.26	1.04	0.97
FeO	0.80	0.81	5.32	8.44	8.17	8.97	0.60	0.62	0.32	0.24	0.23
MnO	0.03	0.04	0.20	0.30	0.32	0.28	0.04	0.05	0.02	0.01	*n.d.*
MgO	0.48	0.40	4.76	4.94	8.54	9.81	0.42	0.43	0.22	0.12	0.11
CaO	1.58	1.55	7.86	9.85	12.70	13.47	1.01	1.22	0.36	0.17	0.13
Na_2O	8.29	7.79	3.51	2.62	2.64	1.85	8.42	8.95	9.54	10.39	9.78
K_2O	3.37	4.19	3.58	0.64	0.98	1.11	3.17	2.02	2.43	1.23	1.97
BaO	0.12	0.10	0.10	0.04	0.04	0.05	0.12	0.12	0.12	0.12	0.11
SrO	0.11	0.08	0.12	0.03	0.06	0.08	0.08	0.07	0.07	0.06	0.05
P_2O_5	0.06	0.05	0.50	0.30	1.33	0.68	0.07	0.07	0.03	0.02	0.01
[a]CO_2	0.77	0.87	0.10	0.29	0.45	0.16	0.42	0.70	0.10	0.09	0.10
[a]S	0.01	0.01	0.01	0.22	0.01	0.01	0.02	0.06	0.02	0.06	0.13
[b]LOI	1.32	1.44	1.36	1.67	1.36	1.01	1.07	1.35	0.55	0.53	0.70
Total	98.84	98.85	99.41	98.99	99.09	98.44	99.48	99.05	99.52	99.38	98.78
Be (ppm)	*n.d.*	*n.d.*	3	4	4	4	*n.d.*	*n.d.*	*n.d.*	*n.d.*	*n.d.*
Co	*n.d.*	*n.d.*	36	52	59	65	*n.d.*	*n.d.*	*n.d.*	*n.d.*	*n.d.*
Cu	n.d.	7	135	87	7	24	8	9	9	6	7
Mo	15	*n.d.*	10	*n.d.*	*n.d.*	*n.d.*	14	15	17	14	16
Ni	7	*n.d.*	30	78	49	63	5	6	5	*n.d.*	*n.d.*
Sc	2	2	25	36	42	52	2	2	*n.d.*	*n.d.*	*n.d.*
V	50	47	288	500	468	522	33	39	26	22	11
W	*n.d.*	*n.d.*	*n.d.*	*n.d.*	*n.d.*	*n.d.*	*n.d.*	*n.d.*	*n.d.*	*n.d.*	*n.d.*
Zn	33	33	144	198	205	188	31	31	18	11	12
Ba	1061	930	930	345	407	463	1065	1095	1072	1097	958
Cr	3	*n.d.*	12	66	7	56	7	4	*n.d.*	*n.d.*	*n.d.*
Ga	18.12	22.01	22.23	20.25	22.45	21.19	20.99	21.06	23.11	22.91	22.34
Pb	14.17	17.24	11.35	6.99	5.69	3.73	12.84	6.32	12.00	4.43	6.97
Sn	*n.d.*	*n.d.*	*n.d.*	*n.d.*	*n.d.*	*n.d.*	*n.d.*	*n.d.*	*n.d.*	*n.d.*	*n.d.*
Rb	38.31	76.07	102.30	14.32	15.48	17.10	34.02	21.61	28.94	13.78	22.75
Sr	961	653.6	1043.7	258.8	630.4	718.5	662.4	574.1	622.6	529.8	390.7
Nb	5.94	6.40	7.71	4.57	8.53	5.21	6.50	6.68	4.59	3.67	1.92
Cs	0.25	0.35	0.83	-	0.11	0.10	0.13	0.13	0.14	0.14	0.13
Hf	1.71	4.21	4.96	-	5.58	3.91	1.79	2.54	2.96	3.03	2.12
Ta	0.70	0.30	0.40	0.28	0.36	0.24	0.30	0.30	0.16	0.15	0.05
Th	2.78	7.92	7.87	0.45	5.06	2.46	2.44	4.26	5.59	8.17	4.60
U	0.85	2.18	1.96	-	1.17	0.60	0.81	1.63	2.02	1.93	2.39
Y	13.19	17.09	38.73	40.36	63.09	43.88	14.32	13.24	8.92	6.30	4.63
Zr	61.74	210.74	166.32	89.59	157.70	108.60	61.39	95.23	117.70	94.74	92.17

continued

A-Sye Antiperthite syenite
MD Monzodiorite
Hbdt Pyroxene-bearing hornblendite
P-Sye Alkali-feldspar porphyritic syenite
Q-Sye Alkali-feldspar quartz-syenite

n.d. Not detected
\- Not analysed
[a] Not included in totals
[b] Loss on ignition at 1000° C

Table 4.2 Major and trace elements analyses of representative rocks from the studied intrusions. *(continued)*

	Garrison intrusion						Ludgate intrusion	
Unit	HQM	HQM	HQM	HQM	HQM	HQM	Q-Sye	Q-Sye
Sample	097	098	099	100	101	102	088	091
SiO_2	65.16	64.01	59.00	68.80	68.98	68.08	64.98	63.58
TiO_2	0.28	0.34	0.65	0.19	0.22	0.21	0.20	0.25
Al_2O_3	16.04	16.61	16.27	15.25	15.15	16.00	16.60	16.53
Fe_2O_3	1.66	1.63	3.77	1.12	1.29	1.15	1.34	1.51
FeO	1.11	1.36	2.62	0.45	0.53	0.62	0.31	0.48
MnO	0.05	0.05	0.14	0.03	0.03	0.03	0.03	0.05
MgO	1.12	1.24	2.11	0.57	0.68	0.74	0.57	1.03
CaO	1.72	2.54	5.57	1.21	1.26	1.29	1.37	2.06
Na_2O	5.81	5.59	5.31	5.57	5.63	5.79	7.83	8.33
K_2O	4.73	4.64	2.22	4.82	4.94	4.80	3.85	3.54
BaO	0.13	0.21	0.08	0.11	0.12	0.13	0.13	0.12
SrO	0.15	0.19	0.10	0.11	0.12	0.13	0.11	0.09
P_2O_5	0.17	0.18	0.26	0.08	0.11	0.12	0.08	0.09
[a]CO_2	n.d.	0.04	0.29	*n.d.*	0.04	*n.d.*	0.78	0.71
[a]S	0.020	*n.d.*	0.08	*n.d.*	*n.d.*	*n.d.*	0.08	0.05
[b]LOI	0.52	0.38	1.05	0.44	0.41	0.49	1.32	1.13
Total	98.65	98.97	99.15	98.75	99.47	99.58	98.72	98.79
Be (ppm)	4	*n.d.*	*n.d.*	*n.d.*	4	4	*n.d.*	3
Co	5	7	16	*n.d.*	*n.d.*	*n.d.*	*n.d.*	*n.d.*
Cu	7	9	15	*n.d.*	5	15	11	14
Mo	18	14	13	15	15	15	16	16
Ni	16	16	17	7	9	12	11	16
Sc	4	4	11	2	2	3	2	3
V	50	48	137	27	33	31	42	68
W	*n.d.*	*n.d.*	*n.d.*	*n.d.*	*n.d.*	*n.d.*	*n.d.*	*n.d.*
Zn	75	57	76	45	54	49	35	61
Ba	1173	1856	758	1015	1045	1130	1204	1070
Cr	30	49	11	9	12	11	20	24
Ga	21.26	20.78	21.68	19.45	20.02	20.58	25.34	25.23
Pb	115.25	22.76	5.67	33.75	34.76	32.06	16.17	13.73
Sn	*n.d.*	*n.d.*	*n.d.*	3.4	*n.d.*	*n.d.*	*n.d.*	*n.d.*
Rb	131.25	119.83	38.24	117.18	147.92	153.60	66.10	64.53
Sr	1252.7	1579.3	815.5	966.6	991.8	1127.3	894.2	778.9
Nb	10.13	9.60	9.35	6.63	8.41	8.61	6.79	6.08
Cs	2.40	1.39	-	-	-	2.39	0.48	0.47
Hf	6.53	5.72	-	-	-	5.18	3.51	1.54
Ta	0.63	0.60	0.54	0.42	0.52	0.53	0.34	0.23
Th	11.30	5.80	7.83	6.67	10.69	11.07	5.48	1.58
U	2.08	1.53	-	-	-	1.88	1.49	0.63
Y	13.46	15.12	44.10	6.31	7.75	9.53	9.18	8.58
Zr	234.48	216.78	187.95	146.00	165.51	180.82	114.79	43.36

HQM Hornblende quartz-monzonite
Q-Sye Alkali-feldspar quartz-syenite
n.d. Not detected
\- Not analysed
[a] Not included in totals
[b] Loss on ignition at 1000° C

B. CIPW-normative mineralogy

Although the CIPW norm is primarily a tool to compare fine-grained rocks where the modal mineralogy is not easily identifiable, it can still be used in coarse-grained plutonic rocks to identify certain chemical characteristics. Since CIPW norm calculations assign elements to minerals following a strict set of rules, the resulting normative mineralogy does not usually reflect the true mineral composition of the rock. For example, at the Emens intrusion, nepheline, leucite and olivine are present in the norm but are not identified in the mode.

A characteristic feature of the Emens and Pangea intrusions, that is not observed in other intrusions, is their degree of SiO_2-undersaturation. This is best observed on the Total Alkali vs. Silica (TAS) diagram (LeBas et al., 1986; Figure 4.3). The rocks that plot in the fields above the bold line are usually nepheline and/or leucite normative whereas those below are usually SiO_2-saturated or -oversaturated (quartz normative). Although the diagram was originally developed to classify volcanic rocks, it is still a useful tool to differentiate plutonic rocks. The Emens and Pangea intrusions both have most of their analyses (>85 %) plotting in the SiO_2-undersaturated fields (from foidite to phonolite) of the TAS diagram whereas the Iris and Ludgate intrusions both have the bulk of their analyses (>85 %) plotting in the SiO_2-saturated to -oversaturated portion (from basalt to trachyte) of the diagram.

In more detail, all rocks from the Emens intrusion are SiO_2-undersatured and contain between 1.5 to 12 wt% normative nepheline and 0.5 to 7 wt% olivine (Table 4.3). Furthermore, two samples are both nepheline and leucite normative. Rocks from the Pangea intrusion are mostly SiO_2-undersaturated to -saturated. The SiO_2-undersaturated rocks contain 0.3 to 2.9 wt% nepheline while those that are SiO_2-saturated contain no nepheline and quartz but have 0.7 to 11 wt% and 0.3 to 20.8 wt% normative olivine and hypersthene respectively. Rocks from the Emens

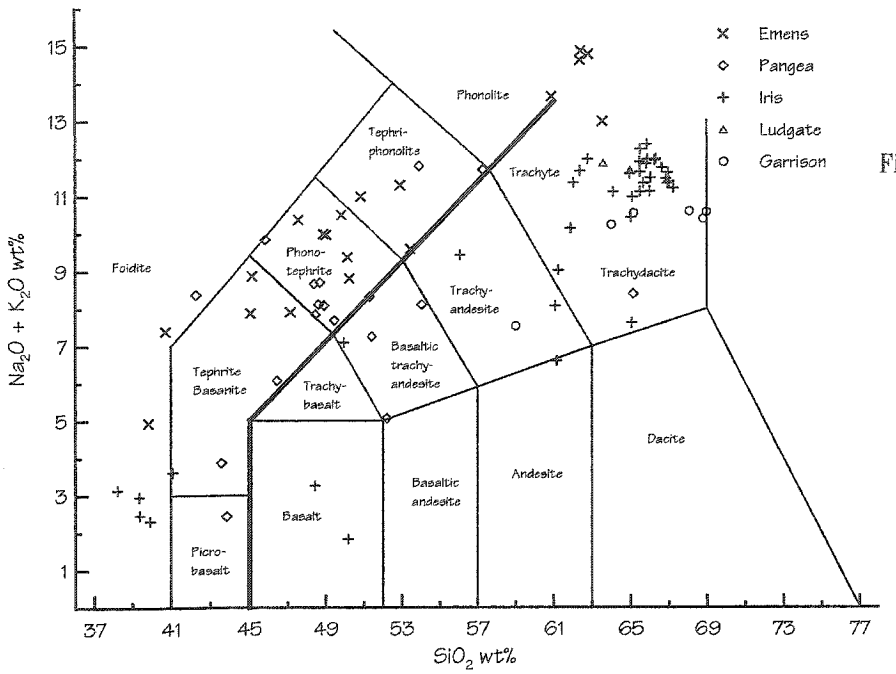

Figure 4.3 Total Alkali vs. Silica diagram (TAS) of LeBas et al. (1986). Most samples from Emens and Pangea intrusions plot in the SiO_2-undersaturated portion of the diagram (above the bold line) whereas most samples from Iris, Ludgate and Garrison intrusions plot in the SiO_2-oversaturated portion.

Table 4.3 CIPW-normative mineralogy in wt% of representative samples from all five intrusions.

	Emens intrusion						Pangea intrusion					
Unit	B-Sye	B-Sye	B-Sye	B-Sye	M-Sye	Sye	Hbdt	M-Sye	M-Sye	M-Sye	M-Sye	Sye
Sample	084	157	177	178	080	165	019	035	180	186	191	193
Quartz	0.00	0.00	0.00	0.00	0.00	0.00	0.00	0.00	0.00	0.00	0.00	0.00
Leucite	0.00	0.00	0.00	0.00	21.86	0.00	0.00	0.00	0.00	0.00	0.00	0.00
Nepheline	8.92	9.61	4.24	4.84	8.07	2.33	0.00	0.00	2.73	1.40	0.00	0.60
Aegirine	0.00	0.00	0.00	0.00	0.00	0.00	0.00	0.00	0.00	0.00	0.00	0.00
NaMeta.	0.00	0.00	0.00	0.00	0.00	0.00	0.00	0.00	0.00	0.00	0.00	0.00
Olivine	3.93	0.00	7.23	5.46	25.02	2.83	11.62	12.71	2.30	3.31	0.94	4.03
Corundum	0.00	0.00	2.88	1.83	0.00	0.00	0.00	0.00	0.00	0.00	0.00	0.87
Hypersthene	0.00	0.00	0.00	0.00	0.00	0.00	0.31	0.20	0.00	0.00	14.97	0.00
Orthoclase	48.47	30.20	35.11	29.26	8.23	58.28	5.56	27.54	24.35	23.11	15.66	39.25
Albite	9.59	13.49	29.56	37.94	0.00	27.67	24.79	11.93	28.46	34.65	20.39	41.62
Anorthite	2.34	6.33	0.00	1.32	0.50	1.39	22.30	5.89	11.84	11.30	22.29	3.68
Diopside	15.39	22.19	0.00	0.00	25.15	2.61	16.51	23.29	11.35	10.53	18.45	0.00
Wollastonite	0.00	4.38	0.00	0.00	0.00	0.00	0.00	0.00	0.00	0.00	0.00	0.00
Magnetite	4.84	3.56	3.29	4.12	4.45	1.48	10.21	5.54	8.89	7.07	2.65	1.44
Hematite	0.00	4.11	0.00	0.00	0.00	0.00	0.00	0.00	0.00	0.00	0.00	0.00
Ilmenite	1.65	1.21	1.65	1.44	1.14	0.34	4.12	2.64	2.37	2.24	1.35	0.70
Apatite	1.26	1.44	0.95	0.83	0.69	0.26	0.43	1.87	1.37	0.97	0.14	0.38
Calcite	0.55	0.25	11.05	9.23	1.61	1.23	2.00	5.84	2.84	2.73	0.84	4.71

continued

B-Sye Alkali-feldspar porphyritic biotite-syenite
M-Sye Melasyenite
Sye Alkali-feldspar syenite
Hbdt Pyroxene-bearing hornblendite

Table 4.3 *(Continued)*

	Iris intrusion										
Unit	A-Sye	A-Sye	MD	MD	Hbdt	Hbdt	P-Sye	P-Sye	Q-Sye	Q-Sye	Q-Sye
Sample	118	153	125	133	129	154	116	121	107	113	117
Quartz	0.00	0.02	0.00	6.17	0.00	0.00	2.47	4.16	0.39	1.68	2.28
Leucite	0.00	0.00	0.00	0.00	0.00	0.00	0.00	0.00	0.00	0.00	0.00
Nepheline	0.25	0.00	1.86	0.00	3.77	6.74	0.00	0.00	0.00	0.00	0.00
Aegirine	0.00	0.00	0.00	0.00	0.00	0.00	0.00	0.00	0.00	0.27	0.85
NaMeta.	0.00	0.00	0.00	0.00	0.00	0.00	0.00	0.00	0.00	0.00	0.00
Olivine	0.80	0.00	5.65	0.00	7.27	8.82	0.00	0.00	0.00	0.00	0.00
Corundum	0.00	0.00	0.00	0.00	0.00	0.00	0.00	0.08	0.00	0.00	0.00
Hypersthene	0.00	1.01	0.00	9.25	0.00	0.00	0.93	1.07	0.47	0.25	0.25
Orthoclase	19.92	24.77	21.16	3.78	5.79	6.56	18.74	11.94	14.36	7.27	11.64
Albite	69.67	65.91	26.26	22.17	15.37	3.20	71.24	75.72	80.72	87.60	81.78
Anorthite	2.45	1.83	15.40	21.23	11.32	14.89	1.58	1.17	0.74	0.00	0.00
Diopside	0.10	0.02	15.75	19.33	31.83	36.95	0.24	0.00	0.17	0.11	0.00
Wollastonite	0.00	0.00	0.00	0.00	0.00	0.00	0.00	0.00	0.00	0.00	0.00
Magnetite	1.84	1.97	8.36	8.89	15.35	14.79	1.31	1.44	0.69	0.43	0.60
Hematite	0.58	0.00	0.00	0.00	0.00	0.00	0.50	0.40	0.78	0.65	0.27
Ilmenite	0.55	0.47	2.11	5.37	3.27	3.57	0.49	0.47	0.27	0.25	0.09
Apatite	0.14	0.12	1.18	0.71	3.15	1.61	0.17	0.17	0.07	0.05	0.02
Calcite	1.75	1.98	0.23	0.66	1.02	0.36	0.96	1.59	0.23	0.20	0.21

	Garrison intrusion						Ludgate intrusion	
Unit	HQM	HQM	HQM	HQM	HQM	HQM	Q-Sye	Q-Sye
Sample	097	098	099	100	101	102	088	091
Quartz	9.05	7.75	7.84	15.41	14.85	12.96	4.09	0.00
Leucite	0.00	0.00	0.00	0.00	0.00	0.00	0.00	0.00
Nepheline	0.00	0.00	0.00	0.00	0.00	0.00	0.00	0.00
Aegirine	0.00	0.00	0.00	0.00	0.00	0.00	2.02	4.37
NaMeta.	0.00	0.00	0.00	0.00	0.00	0.00	0.00	0.05
Olivine	0.00	0.00	0.00	0.00	0.00	0.00	0.00	0.18
Corundum	0.00	0.00	0.00	0.00	0.00	0.00	0.00	0.00
Hypersthene	1.72	2.02	2.37	0.30	0.32	1.08	0.93	0.93
Orthoclase	27.96	27.42	13.12	28.49	29.20	28.37	22.76	20.92
Albite	49.16	47.30	44.93	47.13	47.63	48.99	63.96	65.32
Anorthite	3.72	6.53	14.01	2.38	1.48	3.50	0.00	0.00
Diopside	2.91	3.69	7.99	2.41	2.96	1.65	1.05	4.09
Wollastonite	0.00	0.00	0.00	0.00	0.00	0.00	0.00	0.00
Magnetite	2.41	2.36	5.47	1.00	1.17	1.49	0.52	0.00
Hematite	0.00	0.00	0.00	0.43	0.48	0.12	0.29	0.00
Ilmenite	0.53	0.65	1.23	0.36	0.42	0.40	0.38	0.47
Apatite	0.40	0.43	0.62	0.19	0.26	0.28	0.19	0.21
Calcite	0.00	0.09	0.66	0.00	0.09	0.00	1.77	1.61

P-Sye	Alkali-feldspar porphyritic syenite	HQM	Hornblende quartz-monzonite
Q-Sye	Alkali-feldspar quartz-syenite	MD	Monzodiorite
Sye	Alkali-feldspar syenite	Hbdt	Pyroxene-bearing hornblendite
A-Sye	Antiperthite syenite		

and Pangea intrusions are all magnetite and ilmenite normative and, less frequently, hematite normative.

The Iris intrusion is composed mostly of SiO_2-oversaturated rocks except for the pyroxene-bearing hornblendite and monzodiorite units, which are SiO_2-undersaturated, and which contain 0.4 to 6.7 wt% normative nepheline and 5.5 to 13.5 wt% normative olivine. Both units have high normative magnetite and ilmenite values that range from 6.5 to 16.7 wt% and 1.9 to 5.4 wt%, respectively. The alkali-feldspar quartz-syenite (AF Qz-syenite) and alkali-feldspar porphyritic syenite (AFP syenite) units are slightly SiO_2-oversaturated with normative quartz values ranging from 0.4 to 4.7 wt%. They all contain a minor amount of normative hypersthene and/or aegirine with values ranging from 0.1 to 2.6 wt% and 0.1 to 1.5 wt%, respectively. The highly leucocratic AF Qz-syenite from the Ludgate intrusion is SiO_2-saturated to -oversaturated. Normative aegirine is abundant (2.0 wt% and 4.4 wt%) and one sample contains a minor amount (0.05 wt%) of Na-metasilicate (Na_2SiO_3). The Garrison intrusion is composed of SiO_2-oversaturated rocks that contain higher values of normative quartz (7.8-15.4 wt%) compared to all the other intrusions. All samples are hypersthene-normative with values ranging from 0.3 to 2.0 wt%.

C. Peraluminosity and peralkalinity

The Emens and Pangea intrusions are metaluminous with A/CNK (Table 4.4) and agpaitic index (AI) values (Table 4.4) ranging from 0.12 to 0.90 and 0.30 to 0.99, respectively. Only one sample from the Emens intrusion is peralkaline (AI = 1.17). However, the alkali-feldspar syenite unit has high AI values (0.97 to 0.99) that are very close the metaluminous-peralkaline limit. The AF Qz-syenite and AFP syenite units of the Iris intrusion are peralkaline (AI = 1.00-1.02) while the pyroxene-bearing hornblendite and monzodiorite are metaluminous (A/CNK = 0.09-0.40 & AI = 0.39-0.63). Rocks from the Ludgate intrusion are peralkaline with AI values between 1.03

and 1.06, which is consistent with the presence of minor amounts of Na-rich aegirine-augite and magnesioriebeckite in the mode. The Garrison intrusion is metaluminous with an average AI and A/CNK value of 0.92 and 0.78, respectively.

Index	Formula
AI	Mol. $(Na_2O+K_2O)/Al_2O_3$
A/CNK	Mol. $Al_2O_3/(CaO+Na_2O+K_2O)$
Peraluminous	A/CNK > 1
Metaluminous	A/CNK < 1 and AI <1
Peralkaline	AI >1

Table 4.4 Formulas used to calculate the agpaitic index (AI) and the peraluminosity index (A/CNK). Also present are the equations defining the boundary of peraluminous, metaluminous and peralkaline rocks.

D. Major and compatible trace elements variations

The SiO_2-content is used in this study as a qualitative fractionation index since samples from all intrusions span a wide range of SiO_2-compositions, from hornblendite (~39-42 wt%) to melasyenite and biotite-syenite (~42-54 wt%) to syenite (~60-67 wt%). Similarly, MgO-content is used qualitatively as a mafic fractionation index in order to assess the compatible trace elements (CTE: Co, Ni, Sc, V, Cr) trends. Vanadium is discussed in this section because it behaves as a compatible element due to the early crystallization of magnetite.

The Emens, Pangea and Iris intrusions show typical geochemical characteristics of fractionation with concentrations of MgO, Fe_2O_3, FeO, CaO, MnO, TiO_2 and the CTE that are negatively correlated with SiO_2 while Al_2O_3 and the alkalies are positively correlated with SiO_2. The Emens and Pangea intrusions have significant scatter in the major element contents but have good correlations with respect to MgO and the CTE. The well-correlated trends observed between SiO_2 and the

major elements, and MgO with the CTE of the Iris intrusion are evidence that all units from this intrusion are related and probably originated from a common source that underwent crystal fractionation. The end-result of this crystal fractionation is interpreted to be the extremely Na-rich, CaO-, MgO-, FeO- and CTE-poor AF Qz-syenite. In the case of the Emens and Pangea intrusions, a similar conclusion, based solely on the major element variations, is not possible because of the significant scatter that exists in most of the data. This scatter is most likely the result of mobilization during low temperature alteration. However, it is clear that fractional crystallization of ferromagnesian minerals did play a role in the differentiation of these intrusions since, as a whole, the rocks have progressively lower concentrations of oxides compatible in the major ferromagnesian phases (CaO, MgO, FeO, etc.), and the CTE. The CTE trends are more coherent than those of the major elements. This probably reflects the fact that CTE are generally considered to be relatively immobile during alteration and low-grade metamorphism (Leybourne et al., 1997).

1. Iris intrusion

MgO, Fe_2O_3 and CaO values are highest in the pyroxene-bearing hornblendite (hereinafter hornblendite) and display a progressive decrease down to the AF Qz-syenite unit, where they are considerably lower compared to the latter (Figure 4.4a-c). TiO_2 and FeO define negative trends against SiO_2 (Figure 4.4d&f) whereas Na_2O and Al_2O_3 define good positive correlations (Figure 4.4g&i). The K_2O values are scattered and do not define any trend (Figure 4.4h). The hornblendite unit, which has abundant apatite, is P_2O_5-rich compared to all the other units. The $Fe^{3+}/(Fe^{3+}+Fe^{2+})$ ratios rapidly increase in the AF Qz-syenite, which is evidence that the rocks were affected by late oxidation (Figure 4.4j). Fe_2O_3 and TiO_2 are negatively correlated in the hornblendite and positively correlated in the felsic rocks (Figure 4.4e).

In general, the major element trends of the Iris intrusion are remarkably similar to the ones reported in comparable alkaline syenitic rocks of the Kirkland Lake region (c.f., Rowins, 1990; Levesque, 1994). In the case of the Murdock Creek intrusion, Rowins (1990) attributed the almost linear covariation of most major elements with SiO_2 to the continuous removal of clinopyroxene from the magma. At the Iris intrusion, the removal of pyroxene along with apatite and titanite is also interpreted to be the early mechanism of fractionation. However, as the magma got progressively SiO_2- and H_2O-enriched, amphibole may also have influenced fractionation of the major elements. In igneous rocks, amphibole usually starts crystallizing at about 55 wt% SiO_2 (Jakes & White, 1972; Anderson, 1980) and at H_2O-contents above 4 wt% (Czamanske & Wones, 1973; Noyes et al., 1983).

The compatible trace elements (CTE), Ni, Sc, V and Co correlate positively with MgO (Figure 4.4k-n), a feature commonly attributed to fractionation dominated by olivine and/or pyroxene (e.g., Ablay et al., 1998; Rogers et al., 1998). No correlation exists between the MgO- and Cr-contents in the rocks from Iris intrusion. The CTE concentrations are highest, as expected, in the hornblendite unit, and are lowest in the AF quartz-syenite unit. Vanadium values are usually higher compared to the other CTE (Figure 4.4k). The low CTE concentrations in the syenites is the evidence supporting that these rocks are highly fractionated. Similarly the hornblendite, although containing between 8.5 to 10.4 wt% MgO has low CTE concentrations (especially Ni and Cr). These low values are not characteristic of so-called "primary mantle melts" (Frey et al., 1978; Rhodes, 1981; Rock, 1987). Usually primary mantle melts are characterized Ni-contents over 500 ppm, Cr-contents over 1000 ppm and SiO_2-contents not greatly exceeding 50 wt%. This is illustrated on Figure 4.4l, where all the hornblendite samples (and those of other units) plot below the Ni-values of primary mantle melts (Hart & Davies, 1978; Rogers et al., 1998). However, these criteria may not apply for rocks that originate from modified or enriched mantle sources, such as potassic and ultrapotassic rocks (Foley et al., 1987).

2. Emens and Pangea intrusions

The major element trends of the Emens and Pangea intrusions are not as well defined as those from the Iris intrusions. As previously discussed, it is likely that the major element chemistry was disturbed by alteration and therefore may not be as reliable as the «immobile» trace elements for genetic interpretations.

At the Emens intrusion, K_2O values are positively correlated with those of SiO_2 whereas a similar trend is not visible at the Pangea intrusion (Figure 4.4h). At the Pangea intrusion, Na_2O values are positively correlated with those of SiO_2 while, at the Emens intrusion, the correlation is less defined (Figure 4.4g). In both cases, Al_2O_3 increases with fractionation, although the Pangea trend is less defined (Figure 4.4i). Concentrations of the oxides compatible in the major ferromagnesian minerals i.e. MgO, CaO and FeO are highest, as expected, in the more mafic rocks of each intrusion. In both cases, MgO, CaO and FeO define broad negative trends against SiO_2, which is consistent with fractionation of ferromagnesian minerals (Figure 4.4a,c,f). In general, Fe_2O_3 values decrease with fractionation while the $Fe^{3+}/(Fe^{3+}+Fe^{2+})$ ratios are highly variable (Figure 4.4b,j). Fe_2O_3 and TiO_2 values define broad negative trends with those of SiO_2 (Figure 4.4e).

Co, Ni, Sc and V define positive trends against MgO, although in the case of the Pangea intrusion, the trend with V is less defined (Figure 4.4k-n). Positive correlations between the CTE and MgO are usually indicative of fractionation dominated by olivine and/or pyroxene (e.g., Ablay et al., 1998; Rogers et al., 1998). No correlation exists between Cr and MgO in the Emens and Pangea intrusion rocks. The CTE abundances are similar in both intrusions and are highest in the mafic rocks. Compatible trace elements values of Emens and Pangea intrusions are generally higher than those from Iris intrusion. One melasyenite sample is considerably enriched in MgO (16.7 wt %), Ni (429 ppm) and Cr (> 500 ppm) compared to the other samples.

3. Garrison and Ludgate intrusions

All samples from the Garrison intrusion have similar major elements abundances, apart for one amphibole-rich sample, which is enriched in FeO, Fe_2O_3 and MgO compared to the others. The Na_2O concentrations remain relatively constant with values ranging from 5.31 to 5.81 wt%. K_2O is less abundant than Na_2O with values ranging from 2.22 to 4.94 wt%. Elements compatible with major ferromagnesian minerals, i.e. Mg, Ca and Fe^{2+}, are all negatively correlated with SiO_2, although the variations are usually minimal (Table 4.2).

In the case of the Ludgate Qz-syenite, the leucocratic nature of the rock is reflected in the high SiO_2- and Al_2O_3-contents, and low MgO, FeO and Fe_2O_3 values (Table 4.2). The average SiO_2-content is 64.3 wt% while the one of Al_2O_3 is 16.6 wt%. Na_2O concentrations (avg.: 8.08 wt%) are more than two times higher than K_2O (avg.: 3.70 wt%). Average FeO- and MgO-contents are less than 1 wt% while the average Fe_2O_3-content is 1.43 wt %.

Rocks from Garrison and Ludgate intrusions have low concentrations of compatible trace elements with Ni and Cr contents less than 17 ppm and 49 ppm respectively. This is also the case for V (<137ppm), Sc (<11ppm) and Co (<16ppm). These extremely low CTE concentrations is the evidence suggesting that the rocks from Garrison and Ludgate intrusions are highly fractionated.

Figure 4.4 (next 5 pages) Major oxides (wt%) and compatible trace elements (ppm) diagrams displaying the compositional variability of the rocks from the five studied intrusions. Note that the major element trends for Emens and Pangea intrusions commonly display significant scatter. The "mantle melt" boundary of Figure 4.4l is from Rogers et al. (1998).

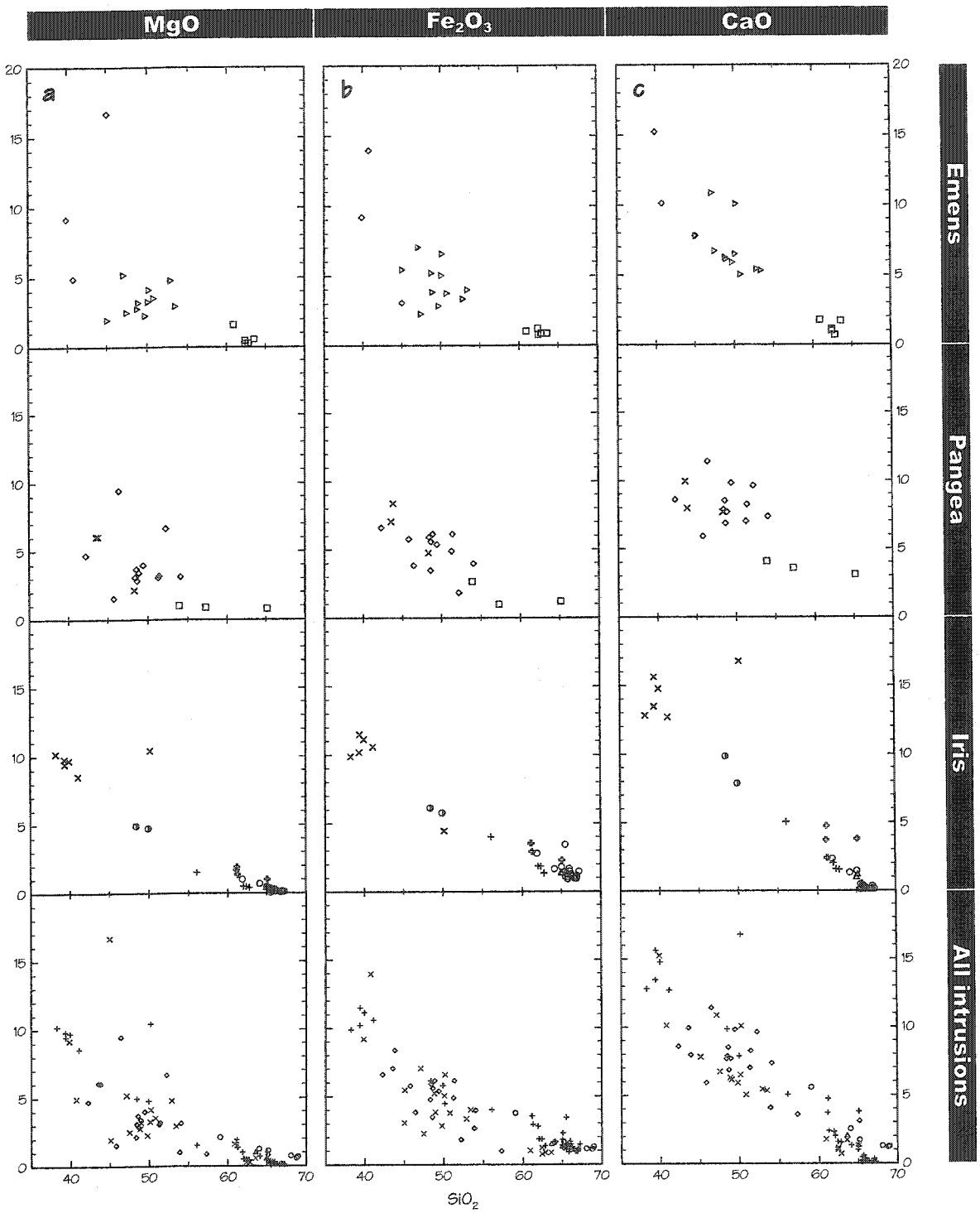
MgO
Fe2O3
CaO
a
b
c
Emens
Pangea
Iris
All intrusions
SiO2
Legend for Emens, Pangea and Iris graphs
AF syenite
AFP biotite-syenite
AFP syenite
AF Qz-syenite
Antiperthite-syenite
Cpx-hornblendite
Melasyenite
Monzodiorite
Monzonite
Legend for the all intrusions graph
Garrison
Emens
Pangea
Iris
Ludgate

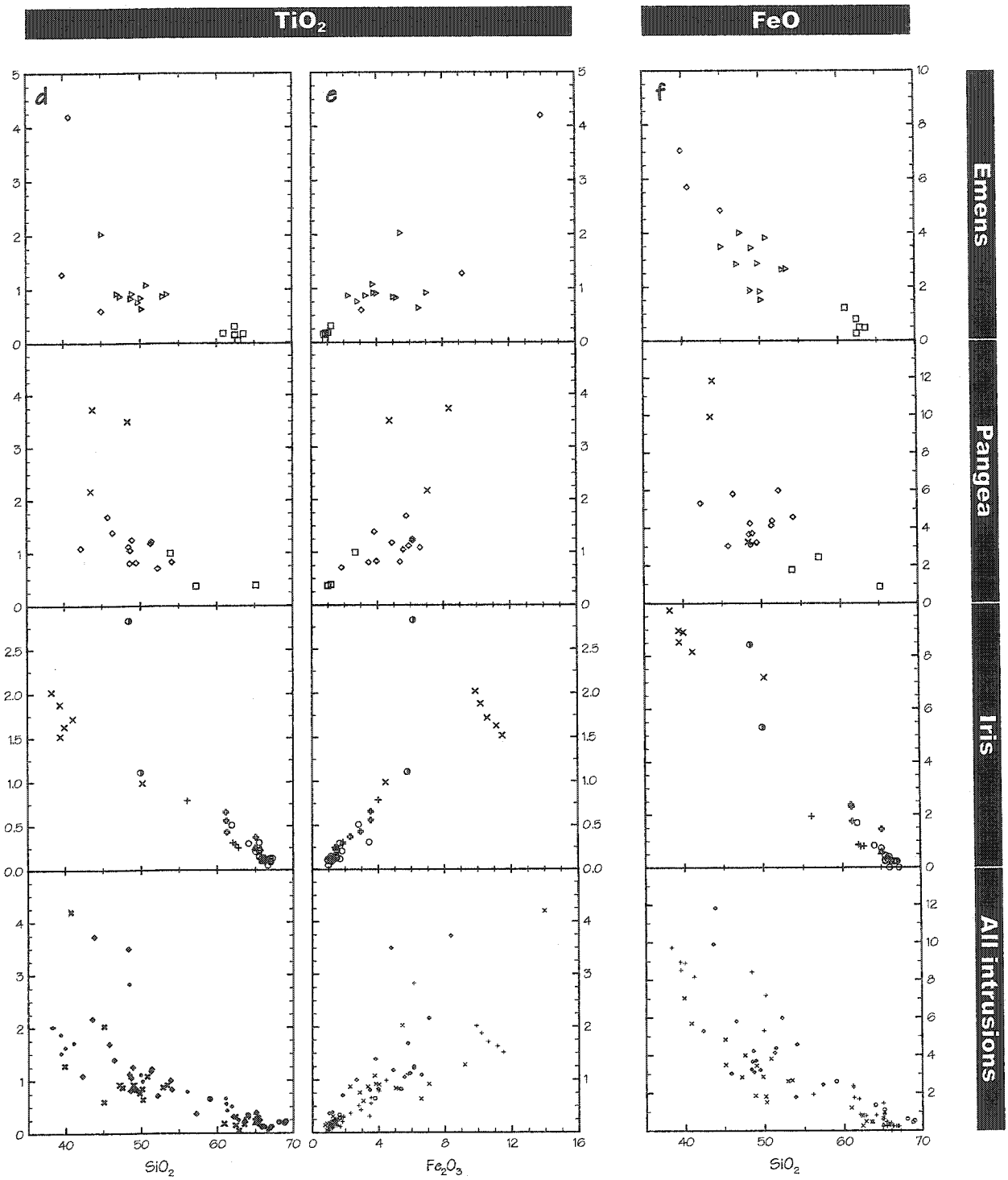

Legend for Emens, Pangea and Iris graphs

- AF syenite
- AFP biotite-syenite
- AFP syenite
- AF Qz-syenite
- Antiperthite-syenite
- Cpx-hornblendite
- Melasyenite
- Monzodiorite
- Monzonite

Legend for the all intrusions graph

- Garrison
- Emens
- Pangea
- Iris
- Ludgate

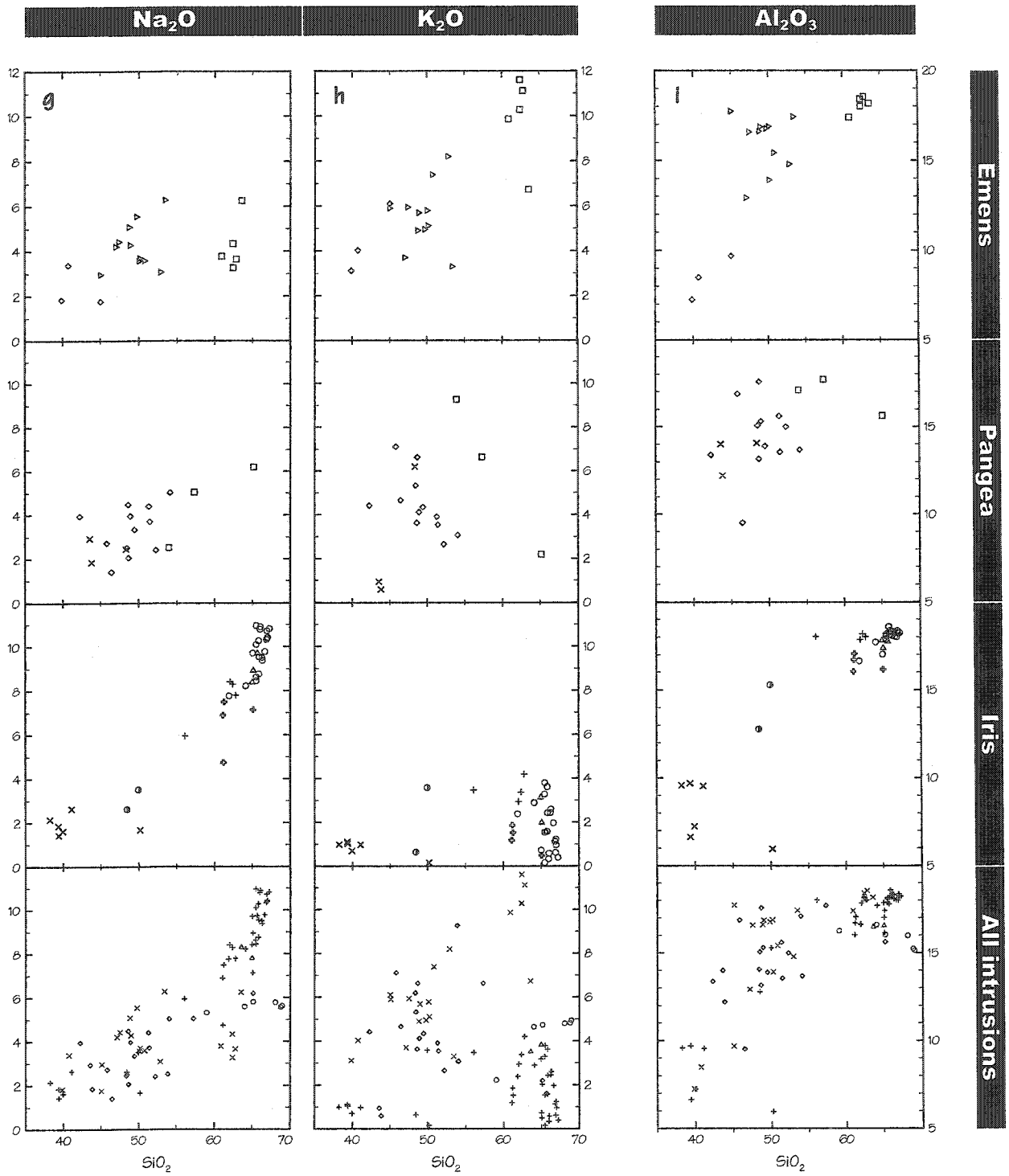

Legend for Emene, Pangea and Iris graphs

- AF syenite
- AFP biotite-syenite
- AFP syenite
- AF Qz-syenite
- Antiperthite-syenite
- Cpx-hornblendite
- Melasyenite
- Monzodiorite
- Monzonite

Legend for the all intrusions graph

- Garrison
- Emene
- Pangea
- Iris
- Ludgate

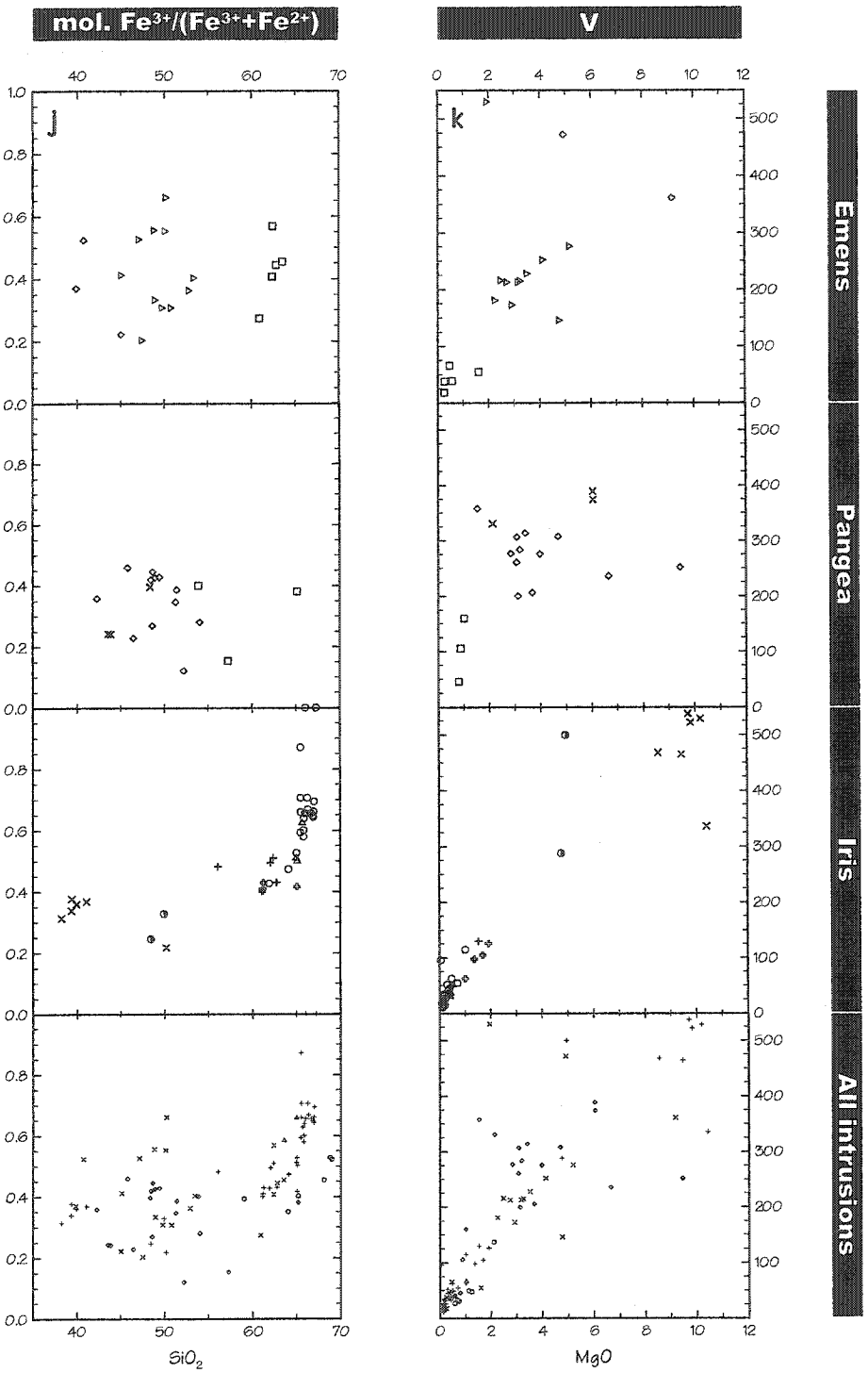
mol. Fe3+/(Fe3++Fe2+)
V
J
K
Emens
Pangea
Iris
All intrusions
SiO2
MgO
Legend for Emens, Pangea and Iris graphs
AF syenite
AFP biotite-syenite
AFP syenite
AF Qz-syenite
Antiperthite-syenite
Cpx-hornblendite
Melasyenite
Monzodiorite
Monzonite
Legend for the all intrusions graph
Garrison
Emens
Pangea
Iris
Ludgate

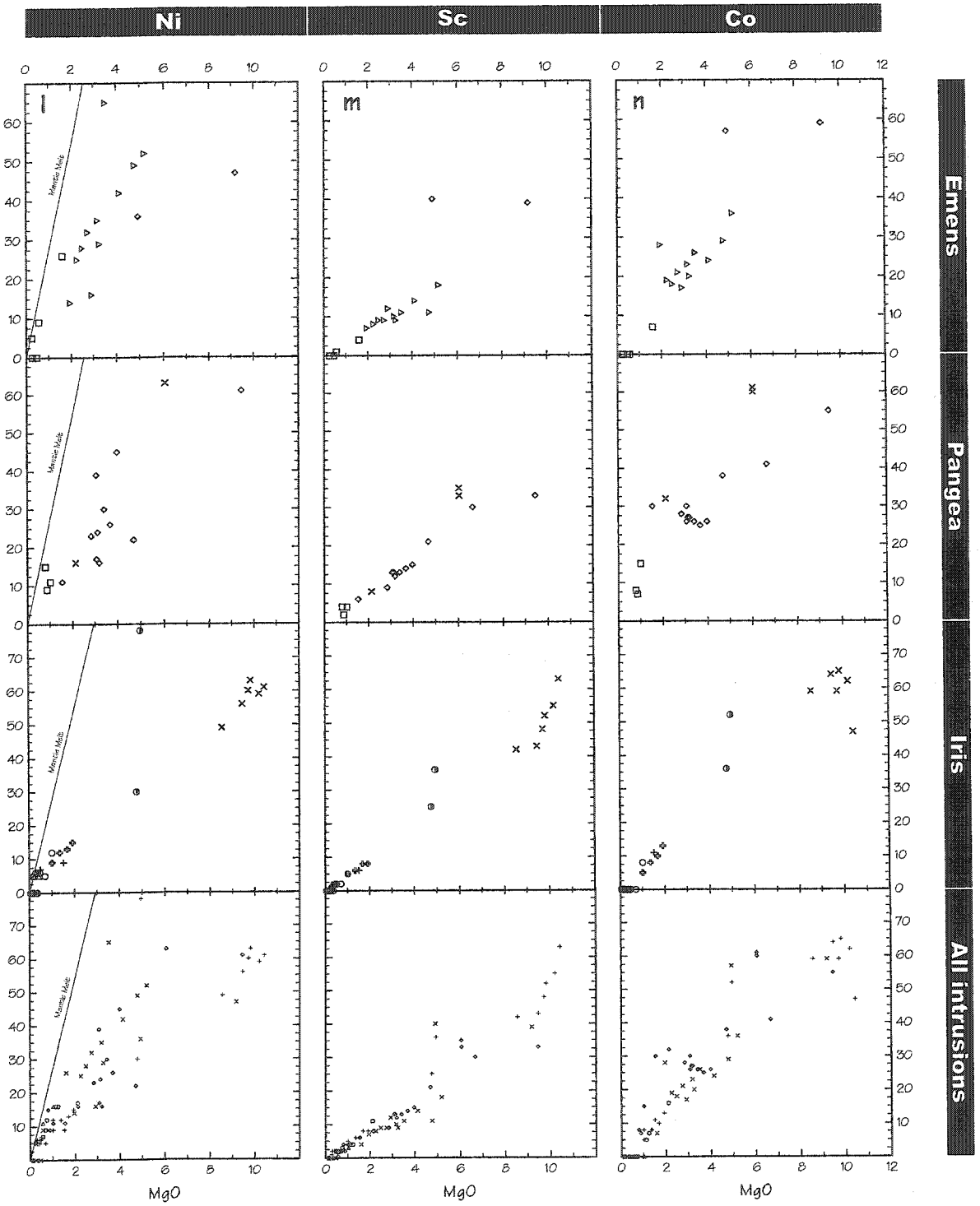

Legend for Emens, Pangea and Iris graphs

- AF syenite
- AFP biotite-syenite
- AFP syenite
- AF Qz-syenite
- Antiperthite-syenite
- Cpx-hornblendite
- Melasyenite
- Monzodiorite
- Monzonite

Legend for the all intrusions graph

- Garrison
- Emens
- Pangea
- Iris
- Ludgate

IV. Incompatible trace elements

A. Iris intrusion

Concentrations of the common incompatible trace elements (ITE) of all the studied intrusions are illustrated on Figure 4.5a-d, where they are normalized against their respective primitive mantle values (Table 4.5; McDonough & Sun, 1995). Rare earth elements (REE) will be discussed in the next section.

	Chondrite	Primitive mantle
P	1080	90
K	550	240
Ti	440	1205
Rb	2.30	0.600
Sr	7.25	19.9
Y	1.57	4.3
Zr	3.82	10.5
Nb	0.240	0.658
Cs	0.190	0.021
Ba	2.410	6.600
La	0.237	0.648
Ce	0.613	1.675
Pr	0.0928	0.254
Nd	0.457	1.250
Sm	0.148	0.406
Eu	0.0563	0.154
Gd	0.199	0.544
Tb	0.0361	0.099
Dy	0.246	0.674
Ho	0.0546	0.149
Er	0.160	0.438
Tm	0.0247	0.068
Yb	0.161	0.441
Lu	0.0246	0.0675
Hf	0.103	0.283
Ta	0.0136	0.037
Th	0.029	0.0795
U	0.0074	0.0203

Table 4.5 Chondrite and primitive mantle values (in ppm) used for normalization. Values are from McDonough & Sun (1995).

In general, primitive mantle normalized incompatible trace element $(ITE)_{pm}$ patterns of the Iris intrusion are characterized by variable negative anomalies (relative to adjacent elements) of Nb, Ta, P and Ti. Although the intensities of the negative anomalies vary between rock units, the general shapes of the $(ITE)_{pm}$ patterns are remarkably similar for all units of the intrusion. Only P, Ti and the light rare earth elements (LREE) display marked depletions in the more differentiated units. Such depletions are consistent with apatite and titanite fractionation. Minor differences are also present. Zirconium defines small negative anomalies in the hornblendite unit while it defines positive anomalies in the AF Qz-syenite unit. In contrast, Sr does not define any major anomalies in the hornblendite while large positive anomalies are

present in the AF Qz-syenite. Notwithstanding the effect of crystal fractionation, the similarity between the patterns of the Iris intrusion units, especially the negative anomalies defined by most high field strength elements (HFSE: Ti, Y, Nb, Ta, Zr, Hf), support the hypothesis that the units are genetically related and most likely evolved from the same parental magma.

Of particular interest is the behavior of the HFSE because these elements are commonly used to infer the tectonic settings that prevailed during magma genesis (Perfit et al., 1980; Pearce, 1983; Macdonald et al., 1985; Thompson & Fowler, 1986; Foley et al., 1987; Wheller et al., 1987; Stolz et al., 1988; Muller & Groves, 2000). Titanium oxide concentrations significantly decrease from ~1.7 wt% ($[Ti]_{pm}$ = ~8) in the hornblendite to ~0.2 wt% ($[Ti]_{pm}$ = ~1) in the AF Qz-syenite, a feature attributed to the early fractionation of titanite. This sharp Ti-decrease in the syenites amplifies the already existing negative Ti anomalies on the $(ITE)_{pm}$ diagram (Figure 4.5a). Zirconium is more abundant in the felsic rocks with an average content of 144 ppm ($[Zr]_{pm}$ = ~14) compared to 111 ppm ($[Zr]_{pm}$ = ~11) in the mafic rocks (Figure 4.6a). Zirconium and Hf are positively correlated (Figure 4.6b), a feature attributed to zircon accumulation. The Zr/Y ratio remains relatively constant at ~2.5 in the mafic rocks while it rapidly increases in the felsic rocks, from ~4.0 in the antiperthite syenite to ~28 in the AF Qz-syenite (Figure 4.6c). This sharp increase is attributed to the strong partitioning of Y in apatite and titanite (Nash, 1972; Green, 1981). Nb and Ta concentrations slightly decrease from average values of 4.9 ppm and 0.2 ppm respectively in the mafic rocks and 4.5 ppm and 0.2 ppm respectively in the AF Qz-syenite. The behavior of Nb and Ta is especially helpful in determining if titanite fractionation occurred during the magma evolution (Eby et al., 1998). Green (1995) noted that in alkaline suites, Nb/Ta ratios tend to fall into two groups. The first is characterized by consistent Nb/Ta ratios that are similar to chondritic (Nb/Ta = 17.65) or primitive mantle values (Nb/Ta = 17.78) whereas the second group has highly variable Nb/Ta ratios that are significantly higher than mantle values. At the Iris intrusion, Nb and Ta are positively correlated (Figure 4.6d) and the ratios fall within the

second group with Nb/Ta ratios between 7 and 38, and with an average ratio of ~22. Green and Pearson (1987) reported that titanite, rutile and ilmenite have partition coefficients significantly greater than unity for both elements and that rutile and titanite favor Ta with respect to Nb. Fractionation of these two minerals would result in an increase in the Nb/Ta ratio of the melt. Furthermore, they calculated the effect of fractionation of these minerals on the Nb/Ta ratio of the magma, and concluded that a ratio increase in the order of 20% may occur by fractional crystallization. Thus, in the case of the Iris intrusion, titanite fractionation could be responsible for the variable and high Nb/Ta ratios, and the increasingly pronounced negative Ti anomalies in the felsic rocks. It should be noted that all units of the Iris intrusion have very low Nb and Ta concentrations, which is inferred to indicate highly fractionated liquids. These low contents indicate that titanite fractionation occurred early in the crystallization sequence. Evidence of titanite fractionation is corroborated by the peculiar U-shaped REE patterns of the syenitic units, which is attributed to titanite and apatite fractionation (this chapter, next section).

Large ion lithophile elements (LILE: K, Rb, Sr, Cs and Ba) do not produce any coherent trends against SiO_2. However, Sr, Rb and Cs values are well correlated with those of K_2O (Figure 4.6g,h) while Ba does not define any trend (Figure 4.6f). The lack of any correlation with SiO_2 is most likely due to the mobility of these elements during low temperature alteration (Clague and Frey, 1982). Barium and rubidium are more abundant in the syenitic units where they substitute K in alkali-feldspar. However, Rb-contents are highly variable in the AF Qz-syenite unit. Barium concentrations are highest in the syenites with an average of 950 ppm ($[Ba]_{pm} = \sim 144$) whereas the average content of the mafic rocks is 424 ppm ($[Ba]_{pm} = \sim 64$). Rubidium is considerably less abundant with values ranging between 1.13 ppm and 102.3 ppm ($[Rb]_{pm} = \sim 2\text{-}171$) and with an average content of 25.7 ppm. The K/Rb ratio varies between 371 and 828 in the hornblendite

Figure 4.5a Primitive mantle normalized incompatible trace element patterns of samples from Iris intrusion. Normalizing factors are from McDonough & Sun (1995) and are listed in Table 4.5.

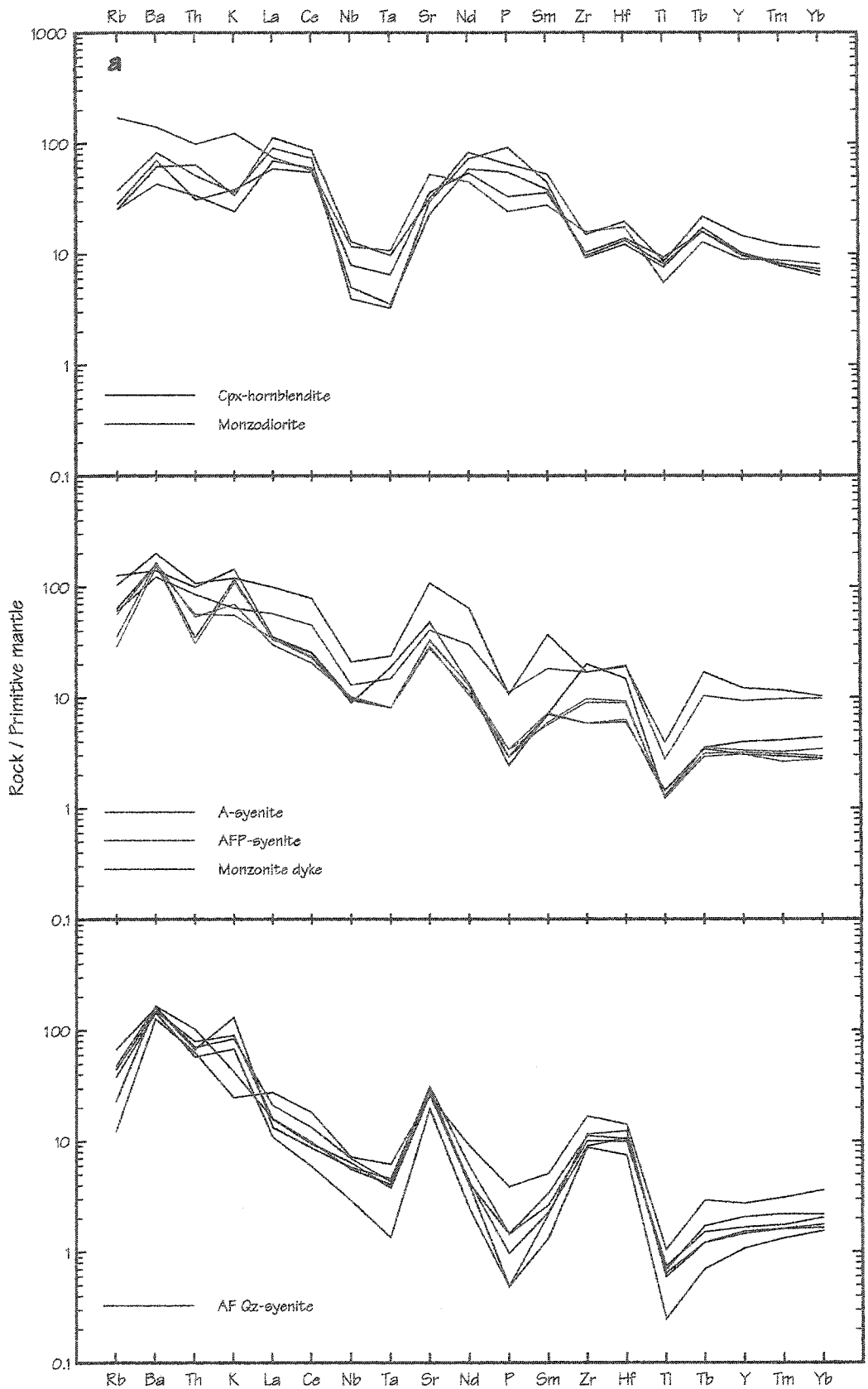
Rb Ba Th K La Ce Nb Ta Sr Nd P Sm Zr Hf Ti Tb Y Tm Yb
a
1000
100
10
1
0.1
Cpx-hornblendite
Monzodiorite
A-syenite
AFP-syenite
Monzonite dyke
AF Qz-syenite
Rock / Primitive mantle

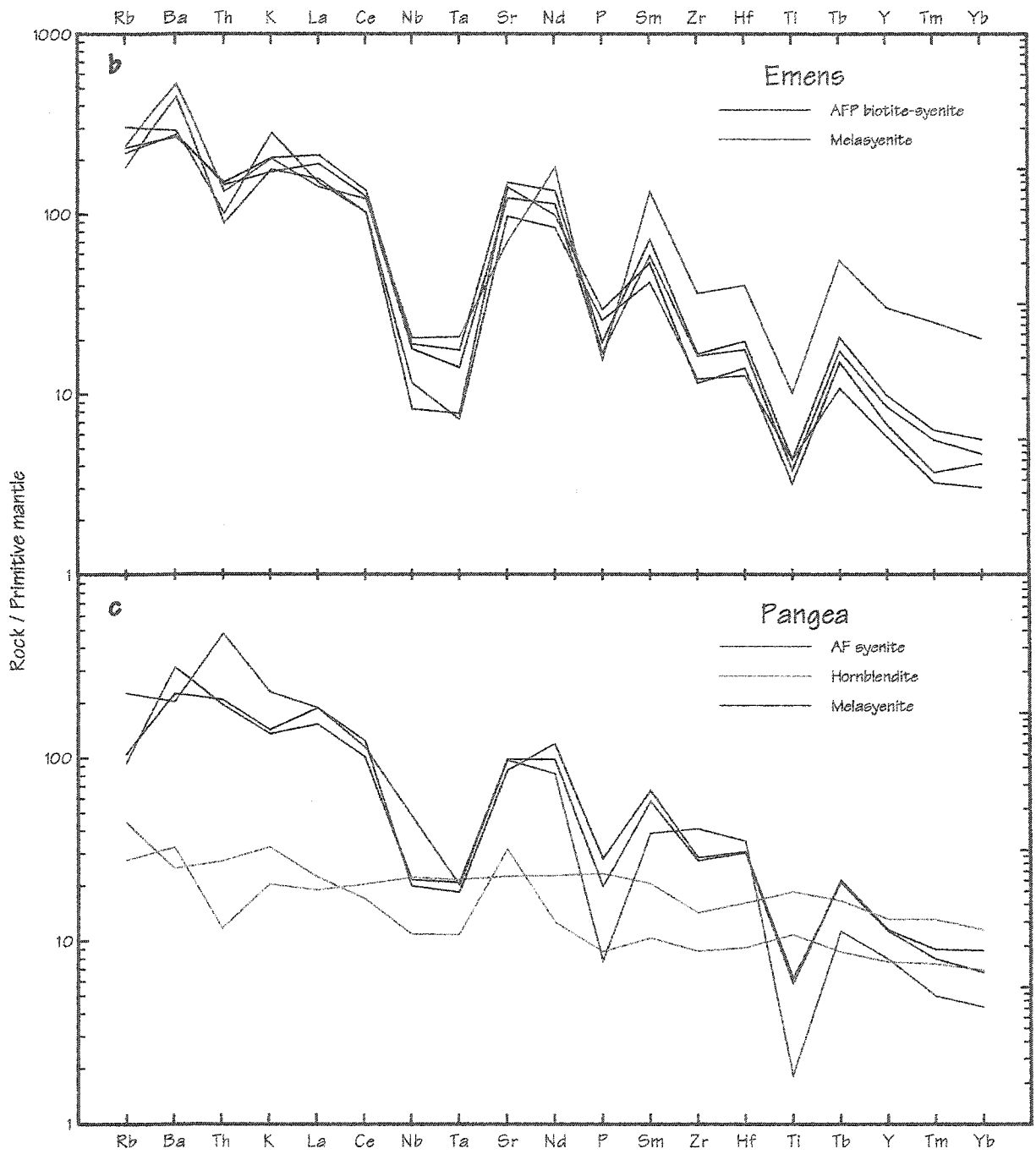

Figure 4.5b & c Primitive mantle normalized incompatible trace element patterns of samples from Emens and Pangea intrusions. Normalizing factors are from McDonough & Sun (1995) and are listed in Table 4.5.

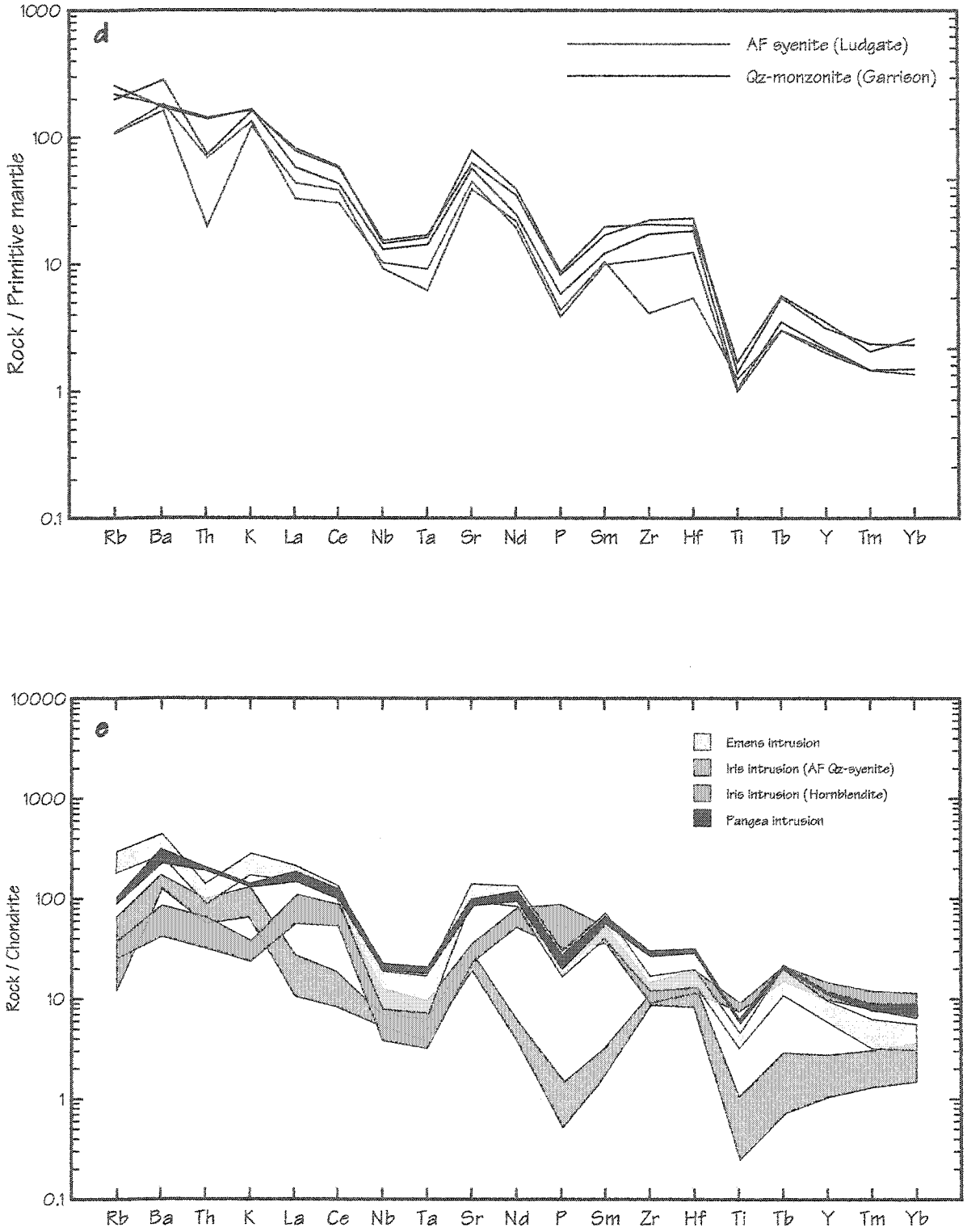

Figure 4.5d & e Primitive mantle normalized incompatible trace element patterns of samples from Garrison and Ludgate intrusions. Figure 4.5e is a composite diagram displaying the fields of patterns from Iris, Emens and Pangea intrusions. Normalizing factors are from McDonough & Sun (1995) and are listed in Table 4.5.

whereas it varies between 502 and 1102 in the syenites (Figure 4.6e). The highest K/Rb ratios are found in the highly fractionated AF Qz-syenite unit, which is opposite to the expected behavior of the K/Rb ratio during magmatic differentiation (Shaw, 1968). In general, the K/Rb ratio of an evolving magma decreases because of an increase in the abundance of biotite in the more differentiated rocks. However, since the rocks of the Iris intrusion contain no biotite (except for one sample with trace amount), the K/Rb ratio was probably influenced by other factors. Of particular interest are the low and variable concentrations of Rb within individual units and the lack of any correlation with SiO_2, which is also the case with all other LILE. This may be interpreted to result from LILE mobilization during low temperature alteration (Clague & Frey, 1982).

Strontium-contents are highest in the antiperthite syenite unit with an average content of 1062 ppm ($[Sr]_{pm} = \sim 53$). The monzodiorite, AFP syenite and monzonite dykes have similar Sr-contents with average concentrations of 552 ppm, 520 ppm and 519 ppm respectively. The hornblendite and AF Qz-syenite contain an average Sr-content of ~400 ppm. In the case of the hornblendite unit, most of the Sr is probably located in apatite, substituting for Ca (Edgar, 1989) whereas in the AF Qz-syenite, Sr is most likely substituting for K in alkali-feldspar.

All major LILE ratios, i.e. K/Sr, K/Ba, Rb/Sr, Rb/Ba and Ba/Sr, do not define any trends when plotted against SiO_2. In general, the ratios remain relatively constant in the mafic rocks and are highly variable in the syenitic units. The extreme variability of the ratios in the syenitic units is consistent with the heterogeneous distribution of the LILEs within these units, which is presumably the result of mobilization during alteration.

Figure 4.6 (next 3 pages) Incompatible trace element diagrams displaying the compositional variability of rocks from the five studied intrusions.

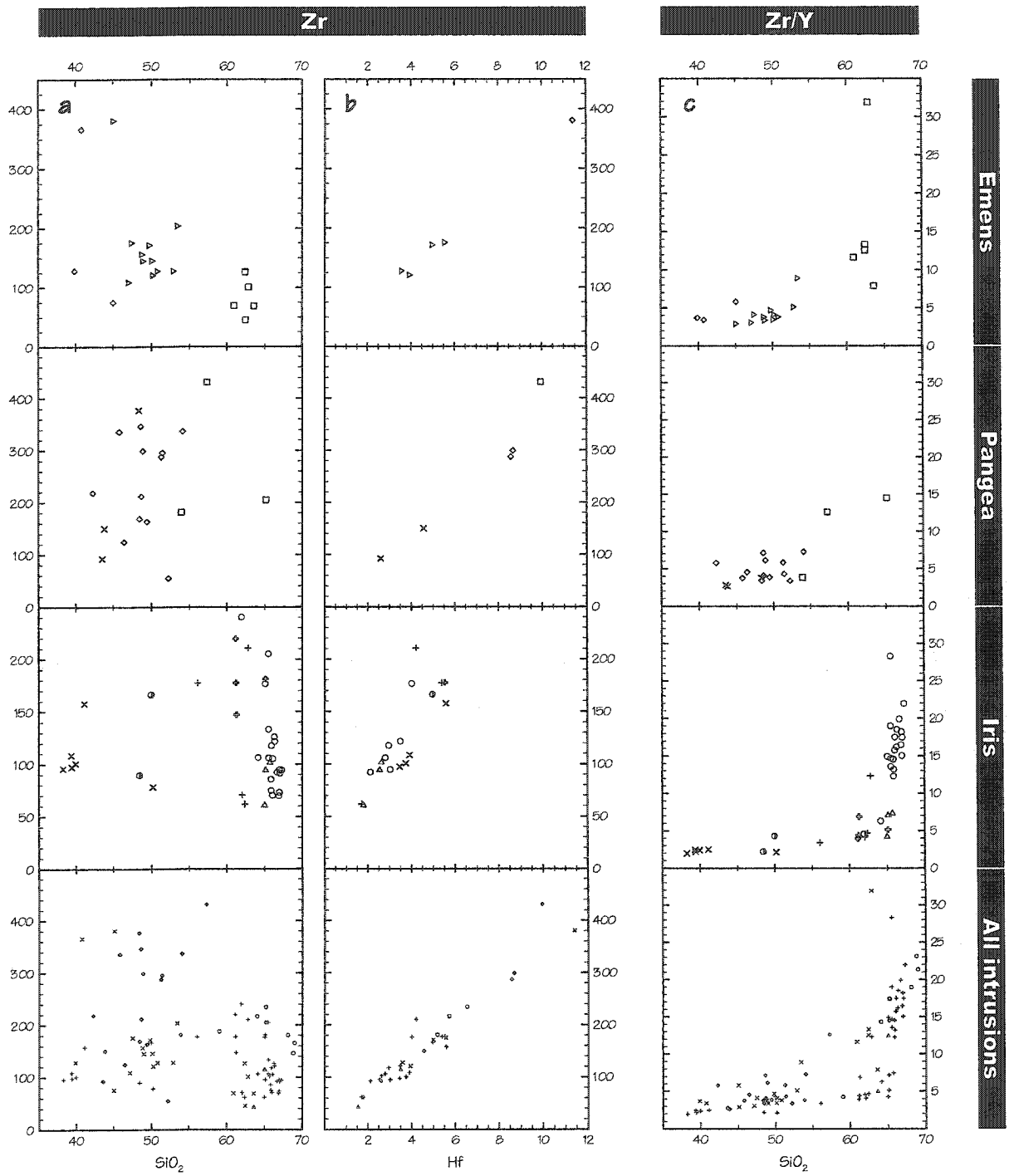

Legend for Emens, Pangea and Iris graphs

- AF syenite
- AFP biotite-syenite
- AFP syenite
- AF Qz-syenite
- Antiperthite-syenite
- Cpx-hornblendite
- Melasyenite
- Monzodiorite
- Monzonite

Legend for the all intrusions graph

- Garrison
- Emene
- Pangea
- Iris
- Ludgate

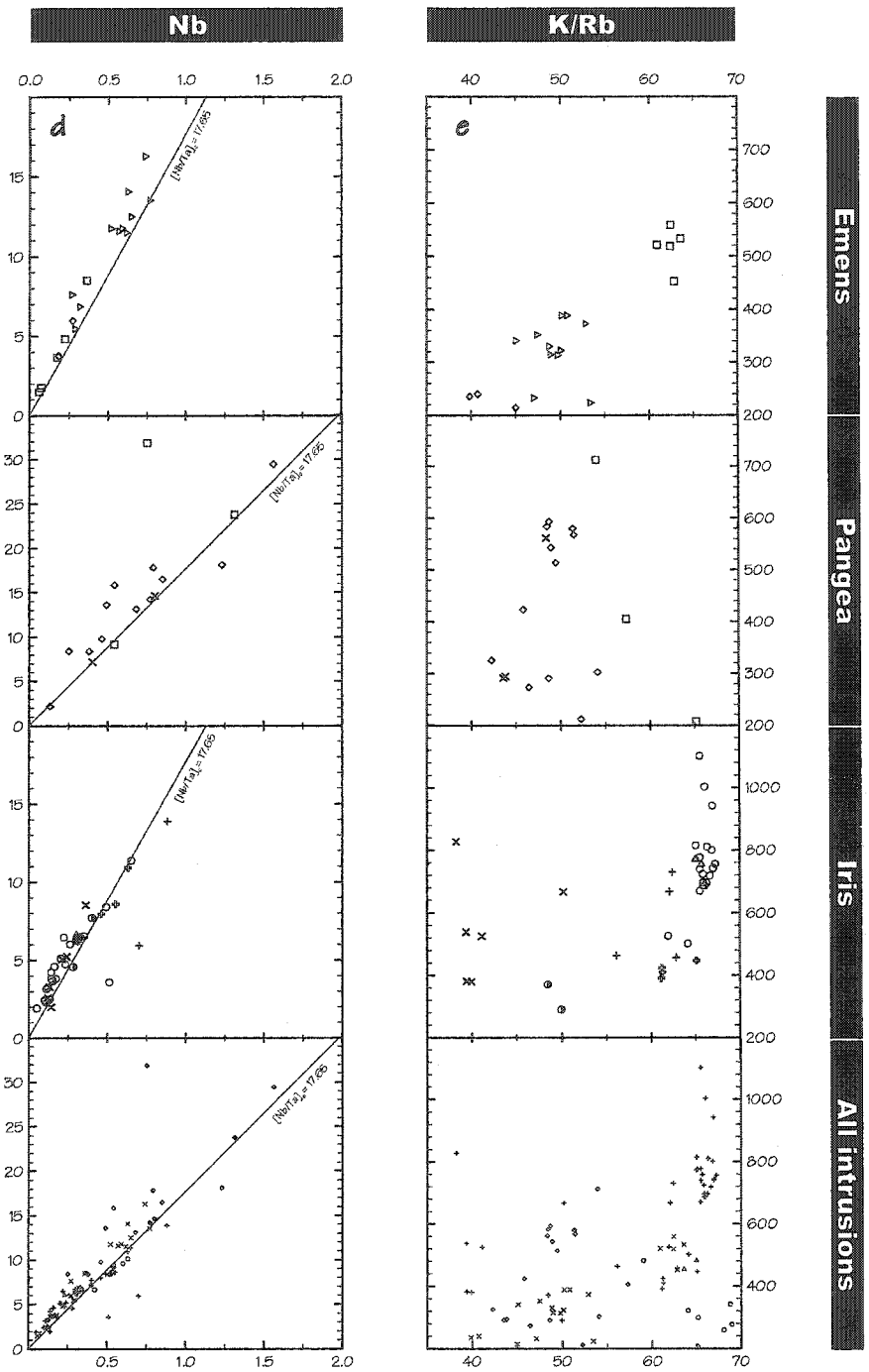

Legend for Emeis, Pangea and Iris graphs

- AF syenite
- AFP biotite-syenite
- AFP syenite
- AF Qz-syenite
- Antiperthite-syenite
- Cpx-hornblendite
- Melasyenite
- Monzodiorite
- Monzonite

Legend for the all intrusions graph

- Garrison
- Emeis
- Pangea
- Iris
- Ludgate

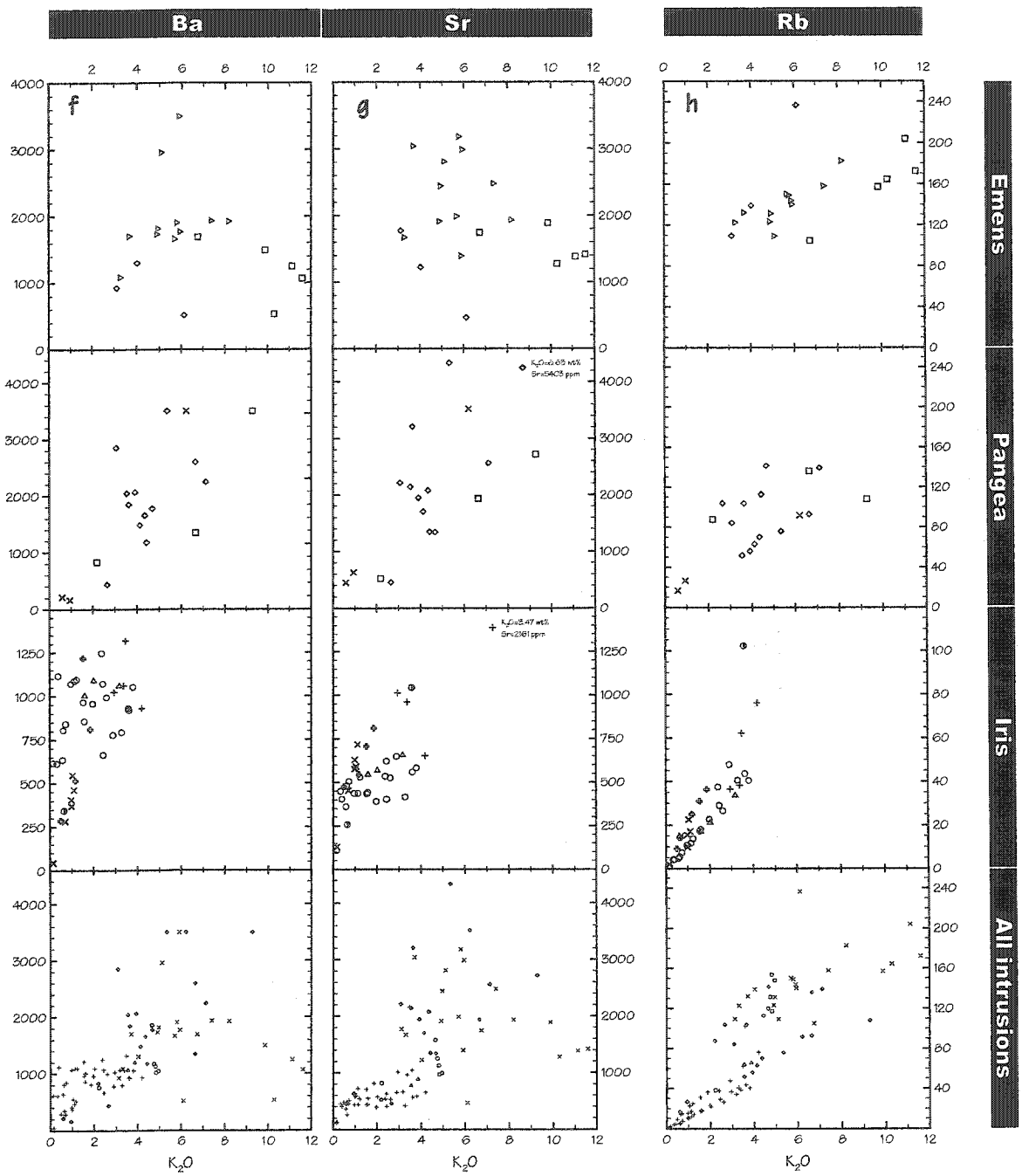

Legend for Emens, Pangea and Iris graphs

- AF syenite
- AFP biotite-syenite
- AFP syenite
- AF Qz-syenite
- Antiperthite-syenite
- Cpx-hornblendite
- Melasyenite
- Monzodiorite
- Monzonite

Legend for the all intrusions graph

- Garrison
- Emens
- Pangea
- Iris
- Ludgate

Thorium concentrations are much higher than the primitive mantle. The highest values are found in the more differentiated AF Qz-syenite unit where the average concentration is 5.43 ppm ($[Th]_{pm}$ =~68; excluding one anomalous value of 43.5 ppm) while the hornblendite unit contains an average of 2.89 ppm ($[Th]_{pm}$ =~36). Similarly, uranium values are highest in the AF Qz-syenite with an average of 2.16 ppm ($[U]_{pm}$ =~106) and lowest in the mafic rocks with 0.88 ppm ($[U]_{pm}$ =~43). The relative enrichment of Th and U in the felsic rocks compared to the mafic ones is consistent with the geochemical behavior of the two elements, which because of their high incompatibility in common rock forming minerals, usually remain in the melt. In contrast, Th/U ratios are highest in the mafic rocks (avg. = 4.03) whereas the lowest ratios are found in the AF Qz-syenite (avg. = 2.80). This produces a broad trend of decreasing Th/U ratio with increasing U-content. Negative correlations between Th/U ratios and U-content can be interpreted to result from the mobilization of U by a fluid phase (Eby et al., 1998).

B. Emens and Pangea intrusions

With the exception of the hornblendite, the Emens and Pangea intrusion rocks have very similar $(ITE)_{pm}$ patterns (Figure 4.5b&c). The AFP biotite-syenite and melasyenite units of the Emens intrusion and the melasyenite and AF syenite units from the Pangea intrusion are characterized by strong negative Nb, Ta, P and Ti anomalies. Only the hornblendite unit from the Pangea intrusion has considerably different characteristics. The two $(ITE)_{pm}$ patterns from the hornblendite unit are quite different. One pattern, although considerably depleted, roughly parallels the ones of AF syenite and melasyenite; the other, similarly depleted, shows a relatively flat pattern from La onwards. In contrast with the melasyenite and AF syenite units, the hornblendite unit does not display any major negative Nb, Ta, P and Ti anomalies; instead, small positive Ti anomalies are observed. Comparison of the $(ITE)_{pm}$ patterns for the Emens and Pangea intrusions and the hornblendite of the Iris intrusion shows that they have surprisingly

similar overall patterns (Figure 4.5e). However, Emens and Pangea intrusions display greater absolute enrichments in LILE, LREE and Th while they have similar or lower contents of MREE, HREE and most HFSE compared to the hornblendite of Iris intrusion (Figure 4.5e).

In both the Emens and Pangea intrusions, HFSE values are highest in the less evolved units of each intrusion and lowest in their respective AF syenite units. In the case of the Emens intrusion, the higher concentrations in the mafic rocks compared to the felsic ones is probably related, in part, to the presence of HFSE-rich magmatic andradite. Andradite is also present in the more evolved rocks but contains considerably less HFSE compared to andradite from the more primitive rocks.

At the Emens intrusion, TiO_2 values range from 0.05 to 4.20 wt% ($[Ti]_{pm}$= ~0.25-21) and average 0.86 wt% ($[Ti]_{pm}$= ~12) in the AFP biotite-syenite while, at the Pangea intrusion, they range from 0.37 to 3.73 wt% ($[Ti]_{pm}$= ~5-51) and average 1.10 wt% ($[Ti]_{pm}$= ~4) in the melasyenite unit. In contrast with the Iris intrusion, Zr defines a broad negative trend against SiO_2 (Figure 4.6a). Zirconium-contents are highest in the melasyenite unit of the Emens and Pangea intrusions with an average of 238 ppm ($[Zr]_{pm}$= ~23) and 272 ppm ($[Zr]_{pm}$= ~26), respectively. The Emens and Pangea intrusions display a limited range of Zr/Hf ratios from 30.6 to 35.6 and 32.9 to 43.4, respectively (Figure 4.6b), compared to the significant variations found at the Iris intrusion (Zr/Hf = 26.9-50.1). However, the average ratio is similar in the three intrusions (avg. Zr/Hf = 33-36). Green (1995) reported similar ranges of Zr/Hf ratios (38-52) for other alkaline suites while Rowins (1990) reported a notably higher average ratio (avg. Zr/Hf = 45) in the shoshonitic Murdock Creek intrusion; an intrusion displaying numerous geochemical similarities with the Emens and Pangea intrusions. Increasing Zr/Nb within the Pangea melasyenite unit (i.e., 10.3-26.0) may result from titanite fractionation (Wolff, 1984). A similar increase is not present at the Emens intrusion. Like the Iris intrusion, the Zr/Y

ratio remains relatively constant at ~4.2 in both intrusions and rapidly increases in the more differentiated AF syenite units (Figure 4.6c). At the Emens intrusion, Nb concentrations decrease from an average of 10.9 ppm ($[Nb]_{pm}$ = ~17) in AFP biotite-syenite to 4.05 ppm ($[Nb]_{pm}$ = ~6) in the AF syenite whereas, at the Pangea intrusion, the average content increases from 17.9 ppm ($[Nb]_{pm}$ = ~27) in the melasyenite to 21.6 ppm ($[Nb]_{pm}$ = ~33) in the AF syenite. In both cases, Ta values decrease with rock fractionation. Niobium and Tantalum are positively correlated in both intrusions and both have variable Nb/Ta ratios consistent with the second group of alkaline suites described by Green (1995). The Nb/Ta ratio varies between 17.6 and 28.2 at the Emens intrusion while it varies between 13.3 and 42.5 at the Pangea intrusion (Figure 4.6d). The average Nb/Ta ratios of the Emens and Pangea intrusions are almost identical to the one from Iris (Nb/Ta = 21.6) with 21.6 and 21.7 respectively. The extensive range of Nb/Ta ratios and the high average ratios encountered in the rocks from the Emens and Pangea intrusions are consistent with titanite fractionation. Furthermore, although Nb and Ta concentrations are slightly higher than those of Iris intrusion, rocks from both intrusions are still Nb- and Ta-poor, which is evidence that the rocks are fractionated.

Most LILE do not define any coherent trends against SiO_2. Only Rb defines a rough positive trend against SiO_2 in the rocks from the Pangea intrusion while, at the Emens intrusion, Rb remains relatively constant throughout the SiO_2 spectrum. However, in the case of the Pangea intrusion, Ba, Sr and Rb define positive correlations with K_2O whereas, at the Emens intrusion, only Rb is positively correlated (Figure 4.6f-h). At the Emens intrusion, the average Rb-content in the AFP biotite-syenite is 140 ppm ($[Rb]_{pm}$ = ~234) while the average is 162 ppm ($[Rb]_{pm}$ = ~270) in the AF syenite unit. At the Pangea intrusion, Rb concentrations are lower than those from the Emens intrusion but display a systematic increase from an average content of 45.0 ppm ($[Rb]_{pm}$ = ~75) in the hornblendite to 111 ppm ($[Rb]_{pm}$ = ~184) in the AF syenite. Strontium and barium concentrations are highest in the Emens AFP biotite-syenite unit with an average

of 2342 ppm ($[Sr]_{pm}$= ~118) and 2001 ppm ($[Ba]_{pm}$= ~303) respectively while, in the Pangea melasyenite unit, the average Sr and Ba contents are 2358 ppm ($[Sr]_{pm}$= ~118) and 1973 ppm ($[Ba]_{pm}$= ~299), respectively. Concentrations of Ba, Sr and Rb are considerably higher than those of the Iris intrusion. In the case of the Emens intrusion, the higher Ba and Rb concentrations relative to the rocks from the Iris intrusion can be explained by the presence of numerous minute barite crystals disseminated throughout the rock and by the presence of a considerable amount of phlogopite, which are both absent from the Iris intrusion rocks. The high Sr-contents are not as easily explained. K-feldspar probably hosts an appreciable amount of the observed Sr (and Ba). For example, K-feldspar from the Kirkland Lake intrusive complex has a considerable celsian ($BaAl_2Si_2O_8$) and slawsonite ($SrAl_2Si_2O_8$) component. In these rocks, K-feldspar containing up to 3.01 wt% BaO and 2.88 wt% SrO have been reported (Hattori, 1989). However, it is doubtful that only K-feldspar is responsible for the high Sr-contents of the rock. Another possibility lies with barite. Most barite is relatively pure $BaSO_4$, although small amounts of Sr may be present as there is a complete solid solution series with celestite (Nesse, 1991). Hattori (1989) found barite-celestite intergrowths in Archean plutons of the Kirkland Lake intrusive complex, which have an almost identical mode of occurrence as the barite in Emens intrusion (Chapter 3). It is therefore possible that barite and/or barite-celestite intergrowths are responsible for the high Sr-content of the Emens and Pangea intrusions.

The K/Rb ratios of the Emens and Pangea intrusions are positively correlated with SiO_2-contents, although the trend for Pangea intrusion is less defined (Figure 4.6e). At the Emens intrusion, the highest K/Rb ratios are found in the AF syenite while the lowest values are in the melasyenite unit. Similarly, at the Pangea intrusion, the highest K/Rb ratios are in the AF syenite while the lowest are in the hornblendite. A similar trend of increasing K/Rb ratios with differentiation is present at the Iris intrusion. Although significant scatter exists, the K/Sr,

K/Ba, Rb/Ba and Ba/Sr ratios remain relatively constant throughout the SiO_2 spectrum of both intrusions.

Thorium and uranium concentrations in the Emens and Pangea intrusion are higher than those of the Iris intrusion. This can be explained by the presence of a minor amount of allanite, which can accommodate a significant amount of U and Th in its structure. In the case of the Emens intrusion, Th-contents decrease slightly with increasing fractionation. Indeed, concentrations are higher in the melasyenite and AFP biotite-syenite units with an average content of 9.8 ppm ($[Th]_{pm}$= ~123) compared to the 4.4 ppm ($[Th]_{pm}$= ~55) in the AF syenite unit. In contrast, Th-contents of the Pangea intrusion consistently increases from an average of 5.5 ppm ($[Th]_{pm}$= ~69) in the hornblendite to 20.4 ppm ($[Th]_{pm}$= ~257) in the AF syenite. Uranium appears to behave in the same manner in both intrusions. Uranium values decrease from 3.95 ppm ($[U]_{pm}$= ~195) in the Emens melasyenite to 1.03 ppm ($[U]_{pm}$= ~51) in the AFP biotite-syenite whereas the values increase from 0.70 ppm ($[U]_{pm}$= ~34) in the Pangea hornblendite to 9.2 ppm ($[U]_{pm}$= ~453) in the AF syenite. Unfortunately, since only a few samples were analyzed for U, the U trends are less significant than the ones for Th. In both cases, the Th/U ratios increase with increasing silica contents. Th/U ratios of the Emens intrusion range from 2.7 to 6.9 while they range from 3.1 to 4.4 at the Pangea intrusion.

C. Garrison and Ludgate intrusions

The Garrison and Ludgate intrusions share several geochemical characteristics as the Iris, Emens and Pangea intrusions. Indeed, their $(ITE)_{pm}$ patterns display negative Nb, Ta, P and Ti anomalies (Figure 4.5d). However, the Ludgate intrusion is slightly depleted in all ITE compared to the Garrison intrusion. Although LILE- and HFSE-contents (apart for Ti and Y) are similar to

those from the Emens intrusion, Ti, Y and the REE (especially the HREE) absolute contents are more characteristic of the Iris intrusion.

In the case of the Garrison intrusion, TiO_2 and Y define a negative linear trend against SiO_2 whereas Nb, Ta and Zr values increase with silica-contents up to ~65 wt% SiO_2 and then rapidly decrease to their minimum. Titanium oxide and Y are positively correlated indicating that the Y distribution in the rocks from Garrison intrusion is greatly influenced by the titanite content (Figure 4.7i). Zirconium values vary between 146 and 235 ppm ($[Zr]_{pm}$= ~14-22) while Y-contents vary between 6.3 and 44.1 ppm ($[Y]_{pm}$= ~1-10). The Ludgate intrusion AF Qz-syenite has average Zr- and Y-contents of 79.1 and 8.9 ppm, respectively ($[Zr]_{pm}$= ~8; $[Y]_{pm}$= ~2). At the Garrison intrusion, Zr/Y ratios are positively correlated with SiO_2-contents with values ranging from 4.3 to 23.1 (Figure 4.7e). The Zr/Y increase is evidence of titanite and/or apatite fractionation since Y is strongly partitioned in both minerals (Nash, 1972; Green, 1981). The average Zr/Hf ratio of the Garrison intrusion is similar to those from the Emens, Iris and Pangea intrusions. The ratios are relatively constant with values ranging from 34.9 to 37.9 and averaging 36.2. These values are within the range of average Zr/Hf ratios observed in the other three intrusions (i.e., Zr/Hf =33-36). Similarly, Nb and Ta values are positively correlated (Figure 4.7h). Comparable correlations are present at the Emens, Iris and Pangea intrusions and are attributed to titanite fractionation (Green & Pearson, 1987). The Nb/Ta ratios of the Garrison intrusion do not display any significant variations. These values are consistent with the first group of alkaline suites identified by Green (1995), which are characterized by consistent Nb/Ta ratios that are similar to chondritic (Nb/Ta = 17.65) or primitive mantle values (Nb/Ta = 17.78). Since only two geochemical analyses of the Ludgate intrusion are available, it is difficult to accurately classify the intrusion into the first or second group of alkaline suites. However, based on the two ratios available (20.0 & 26.4), it appears that the Ludgate intrusion belongs, like the Emens, Iris and Pangea intrusions, to the second group of alkaline suites.

Rubidium, strontium and barium are all correlated with SiO_2. Rubidium values increases with increasing SiO_2 (Figure 4.7f) whereas Sr and Ba values are negatively correlated with those of SiO_2, although these trends are less defined. Rubidium values range from 38.2 to 154 ppm ($[Rb]_{pm}$= ~64-256) while Sr values range from 816 to 1579 ppm ($[Sr]_{pm}$= ~41-79). Barium concentrations are similar to those for Sr with concentrations ranging from 758 to 1856 ppm ($[Ba]_{pm}$= ~115-281). The K/Rb ratios are negatively correlated with SiO_2 (Figure 4.7g), which is consistent with Shaw's (1968) predictions for the behavior of the K/Rb ratios during magmatic differentiation. The decrease of Sr and Ba contents with increasing SiO_2, coupled with increases in the K/Sr (21.6-41.4), K/Ba (20.8-39.4), Rb/Sr (0.05-0.15) and Rb/Ba (0.05-0.14) may suggest the involvement of K-feldspar crystallization in the fractionation process (Figure 4.7a-d; Laflèche et al., 1991). The Ludgate syenite is enriched in Ba compared to Sr with average contents of 1137 ppm ($[Ba]_{pm}$= ~172) and 788 ppm ($[Sr]_{pm}$= ~40), respectively. The average Rb-content of the Ludgate AF Qz-syenite (65.3 ppm) is higher than the one observed in the comparable AF quartz-syenite unit of the Iris intrusion (20.8 ppm).

Thorium-contents are not correlated with that of SiO_2. Thorium values vary between 5.8 and 11.3 ppm ($[Th]_{pm}$= ~73-142) at the Garrison intrusion while the average content is 3.5 ppm ($[Th]_{pm}$= ~44) at the Ludgate intrusion. Th/U ratios of the Garrison (3.8-5.9) and Ludgate (2.5-3.7) intrusions fall within the range of ratios observed at the other intrusions.

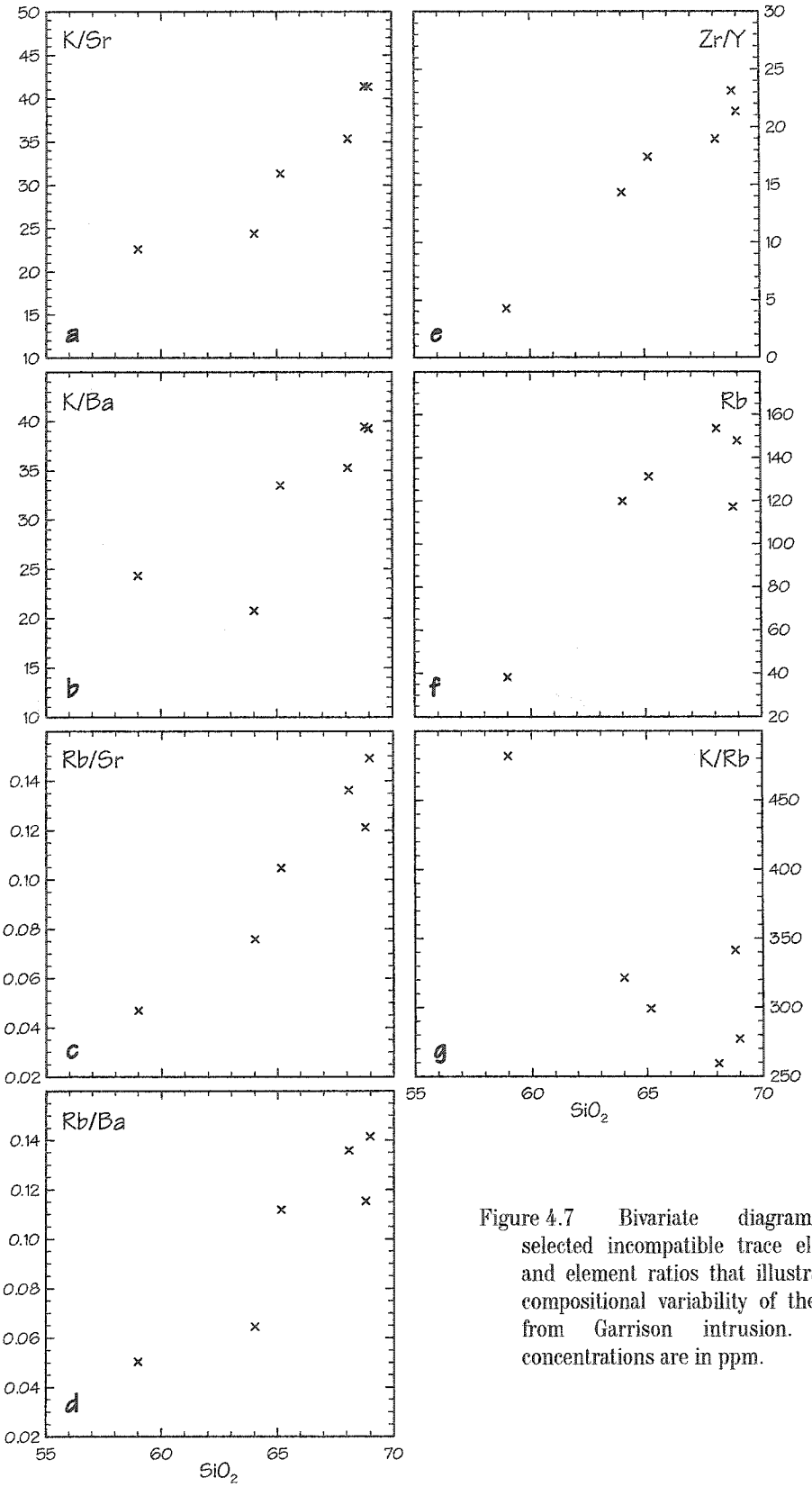

Figure 4.7 Bivariate diagrams of selected incompatible trace elements and element ratios that illustrate the compositional variability of the rocks from Garrison intrusion. All concentrations are in ppm.

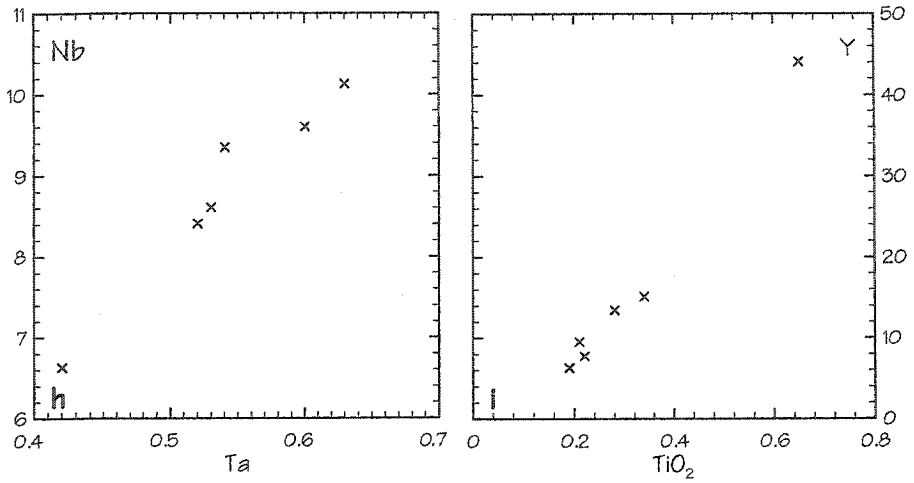

Figure 4.7 (*continued*) Bivariate diagrams of selected incompatible trace elements and element ratios that illustrate the compositional variability of the rocks from Garrison intrusion.

V. Rare earth elements

A. Iris intrusion

Rare earth elements (REE) concentrations of representative samples of the different intrusions are listed in Table 4.6. Chondrite-normalized REE ($[REE]_c$) patterns of the Iris intrusion rocks are illustrated in Figure 4.8. Normalizing values are taken from McDonough & Sun (1995) and are given in Table 4.5.

The most prominent characteristic of the syenite units from the Iris intrusion is the pronounced concave-up or U-shaped patterns. The samples are divided in three groups based on their abundances and REE patterns. The mafic units, i.e. hornblendite and monzodiorite, have high ΣREE-contents and display «typical» fractionated patterns (i.e., LREE>MREE>HREE). The second group, comprised of the alkali-feldspar porphyritic syenite (AFP syenite) and antiperthite-syenite (A-syenite), is the «transitional» group. It contains lower ΣREE than the mafic rocks and displays flat HREE patterns (i.e., LREE>MREE ≅ HREE). The third group, comprised of the alkali-feldspar quartz-syenite (AF Qz-syenite), contains much lower ΣREE compared to the other two groups and has a peculiar concave-up or U-shaped pattern (i.e., LREE>MREE<HREE). The details of each group are discussed below.

The $(REE)_c$ patterns of the hornblendite and monzodiorite show moderate LREE enrichment with $[La]_c$ ranging from 161 to 309 while $[Lu]_c$ ranges from 19.1 to 34.6 (Figure 4.8). $[La/Yb]_c$ values range from 9.24 to 14.0. The LREE patterns are relatively flat with $[La/Sm]_c$ values ranging from 1.64 to 2.69. Small negative Ce anomalies ($[Ce/Ce^*]_c = [Ce]_c/([La]_c+[Pr]_c)/2$) of 0.83 to 0.91 are characteristic of the mafic rocks. $[Gd/Lu]_c$ ranges from 1.78 to 3.50 with small negative Eu anomalies of 0.80 to 0.85 ($[Eu/Eu^*]_c = \{[Eu]_c/([Sm]_c+[Gd]_c)/2\}$). The HREE are relatively flat with $[Dy/Lu]_c$ between 1.20 and 1.98. Patterns for the A-syenite and AFP syenite

Table 4.6 Representative analyses of rare earth elements of samples from the studied intrusions. Concentrations are in parts per million (ppm).

	Emens		Pangea			Garrison	Ludgate
Unit	M-sye	B-sye	Hbdt	M-sye	Sye	HQM	Q-Sye
Sample	043	178	019	180	193	097	088
La	91.84	123.40	14.49	121.76	122.22	50.31	21.18
Ce	204.31	210.15	28.50	208.29	192.50	96.05	51.13
Pr	47.47	37.62	3.84	37.69	29.97	12.76	6.90
Nd	227.83	142.70	15.84	149.68	102.58	43.75	24.30
Sm	54.39	23.93	4.22	27.11	15.71	6.92	4.04
Eu	16.19	6.40	1.60	6.92	4.10	1.83	1.10
Gd	38.25	14.53	4.77	17.48	9.29	3.96	2.53
Tb	5.49	1.72	0.86	2.07	1.12	0.54	0.30
Dy	28.84	9.40	5.14	11.61	6.88	2.86	1.80
Ho	5.22	1.33	1.24	1.74	1.04	0.45	0.29
Er	13.63	3.95	3.37	4.91	3.14	1.39	0.82
Tm	1.71	0.38	0.51	0.54	0.34	0.16	0.09
Yb	9.01	2.06	3.04	2.97	1.92	1.02	0.60
Lu	1.30	0.33	0.50	0.50	0.30	0.17	0.10

	Iris						
Unit	MD	Hbdt	Hbdt	A-Sye	P-Sye	Q-Sye	Q-Sye
Sample	125	068	154	118	116	104	108
La	48.43	58.50	38.22	21.62	21.95	17.87	10.23
Ce	95.89	122.59	91.52	42.52	39.30	30.63	15.89
Pr	14.03	20.93	15.33	5.12	4.64	3.38	1.68
Nd	56.05	90.20	67.40	16.72	15.90	11.40	5.07
Sm	11.23	17.99	14.52	2.88	2.93	2.08	0.89
Eu	2.87	4.24	3.63	0.76	0.80	0.58	0.27
Gd	8.78	13.30	11.54	2.29	2.25	1.67	0.77
Tb	1.27	1.72	1.56	0.34	0.35	0.29	0.12
Dy	7.31	9.32	9.00	2.06	2.21	1.75	0.80
Ho	1.42	1.64	1.66	0.44	0.46	0.39	0.19
Er	4.12	4.42	4.45	1.31	1.39	1.23	0.59
Tm	0.60	0.53	0.56	0.20	0.22	0.21	0.11
Yb	3.56	2.83	3.05	1.24	1.52	1.59	0.73
Lu	0.61	0.47	0.54	0.19	0.26	0.31	0.13

B-Sye	Alkali-feldspar porphyritic biotite-syenite	A-Sye	Antiperthite syenite
M-Sye	Melasyenite	MD	Monzodiorite
Sye	Alkali-feldspar syenite	P-Sye	Alkali-feldspar porphyritic syenite
Hbdt	Pyroxene-bearing hornblendite	Q-Sye	Alkali-feldspar quartz-syenite
HQM	Hornblende quartz-monzonite		

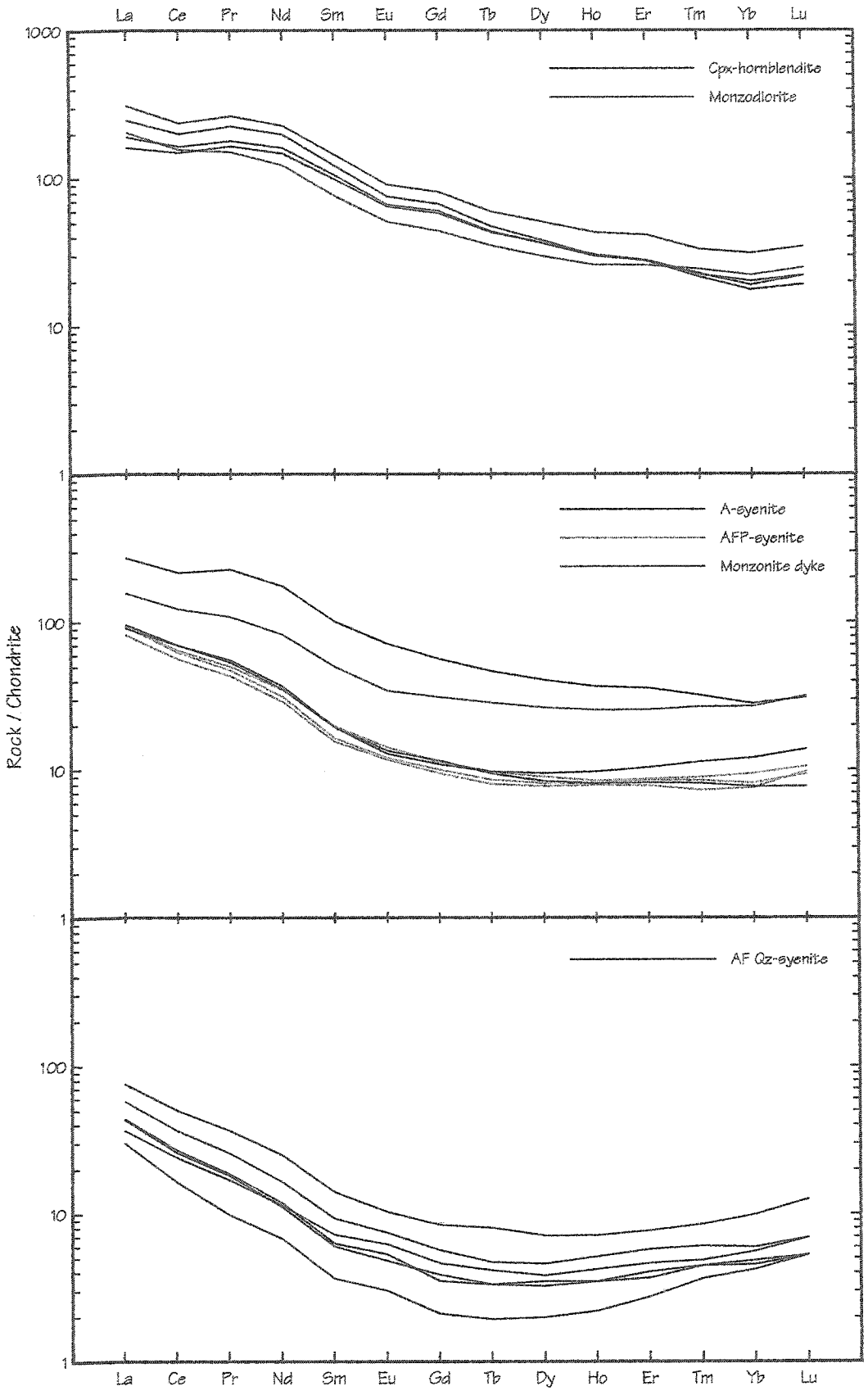

Figure 4.8 Chondrite-normalized rare earth element diagrams of rocks from the Iris intrusion. Normalizing factors are listed in Table 4.5.

are similar to those of the mafic rocks but lack any significant negative Ce anomalies and have flat HREE patterns. $[La/Yb]_c$ ranges from 7.97 to 11.8, $[La/Sm]_c$ from 4.68 to 5.73, $[Dy/Lu]_c$ from 0.69 to 1.08, $[La]_c$ from 81.9 to 96.0 and $[Lu]_c$ from 7.72 to 13.8. It should be noted that one A-syenite sample is pyroxene-rich which is not typical of the unit, therefore, its REE abundances are not accounted in the previous description (Figure 4.8). Patterns for the AF Qz-syenite are significantly different compared to the other units in that they are concave-up or U-shaped, i.e. the HREE>MREE. They have considerably lower absolute abundances with $[La]_c$ ranging from 29.9 to 75.4 and $[Lu]_c$ ranging from 5.28 to 12.6. The patterns have steeper LREE ends compared to the others with $[La/Sm]_c$ ratios that range from 5.04 to 8.19 and have relatively flat MREE patterns with $[Gd/Dy]_c$ = 1.04 to 1.24. The HREE end increases from Dy to Lu with $[Dy/Lu]_c$ ranging from 0.38 to 0.66. Small positive Eu anomalies ($[Eu/Eu^*]_c$= 0.92-1.09) are apparent in the more REE-depleted samples. The lack of any significant negative Eu anomalies in the rocks of Iris intrusion is an indication that plagioclase did not participate in the fractionation of the intrusion or that fO_2 remained high throughout the fractionation history (Weill & Drake, 1973; Drake, 1975; Drake & Weill, 1975).

1. REE behavior in the Iris intrusion rocks

The Iris intrusion is characterized by higher REE contents in rocks with lower SiO_2-contents (Figure 4.9). In fact, two trends are observed. The first, present in the hornblendite unit consists in a sharp increase in the ΣREE with only a minor increase in SiO_2-contents (39.4-41.1 wt%) while the second consists of a sharp decrease in the ΣREE with increasing SiO_2-contents. This suggests the involvement of two processes in the distribution of the REE: (1) accumulation of REE-rich phases, especially LREE-rich, in the hornblendite unit and (2) fractionation of REE-bearing minerals such as apatite and titanite resulting in a REE-depletion of the melt. This is consistent with the mineralogy of the hornblendite unit, which is composed of a significant amount of euhedral apatite and titanite crystals. Apatite favors LREE relative to the MREE

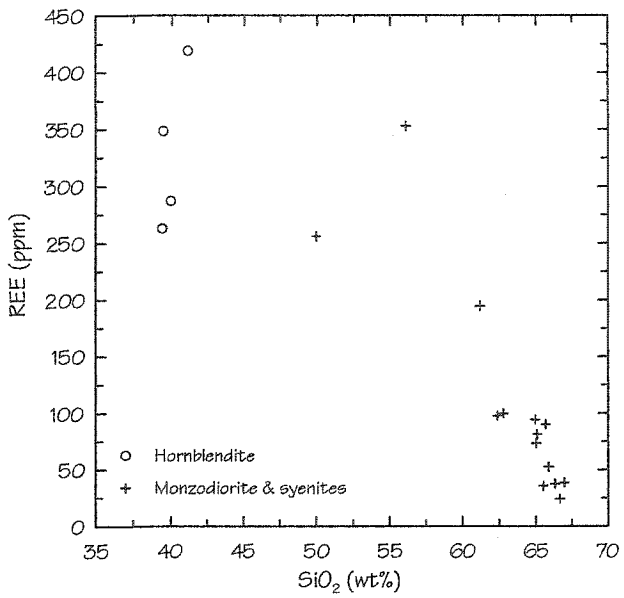

Figure 4.9 ΣREE as a function of SiO_2. The ΣREE increases with SiO_2 in the Iris intrusion hornblendite unit while it rapidly decreases in the monzodiorite and syenites.

and HREE (Wörner et al., 1983; Lemarchand et al., 1987), resulting in an LREE-enrichment in the apatite-bearing rocks and consequently, an LREE-depletion in the rocks that crystallized from the remaining magma. In order to assess which minerals played key roles in the REE fractionation history of the Iris intrusion, it is useful to evaluate REE fractionation trends (also called mineral vectors) on bivariate REE graphs using the fractional crystallization equation (i.e., $C_{li}/C_{oi} = F^{(Di-1)}$, where C_{li} = concentration in the melt, C_{oi} = initial concentration, F = fraction of melt remaining and Di = bulk distribution coefficient) given by Neumann et al. (1954) in conjunction with published mineral-melt distribution coefficients (Table 4.7). Most partition coefficients are given in: Arth (1976), Mahood & Hildreth (1983), Lemarchand et al. (1987), Chen et al. (1990), Singer et al. (1992) and Hart & Dunn (1993). It should be noted that for simplicity, all distribution coefficients were assumed constant throughout fractionation. However, in reality the distribution coefficients are influenced by numerous factors such as pressure, temperature and mineral composition (Wood & Blundy, 2001). This is especially the case for diopside where the REE distribution coefficients are also highly dependant on the ^{IV}Al-content of the pyroxene (Wood & Blundy, 2001). The vectors correspond to the expected compositional path of a magma

when the mineral is crystallized. The lengths of the mineral vectors are proportional to the partition coefficients of the elements in that mineral and to the extent of fractional crystallization, i.e. the percent amount of the mineral that was removed from the magma. Fractionation vectors of phenocrysts found in the hornblendite unit (i.e., apatite, diopside, hornblende and titanite) are illustrated in Figures 4.11a-f.

	Diopside	Apatite	Titanite	Amphibole	Feldspar
La	0.05	25.00	35.00	1.00	0.11
Ce	0.09	34.70	53.00	1.50	0.10
Pr[a]	0.14	44.50	70.50	2.90	0.09
Nd	0.19	54.30	88.00	4.30	0.09
Sm	0.29	59.00	90.00	7.80	0.05
Eu	0.33	30.40	101.00	5.10	2.20
Gd	0.44[a]	56.30	102.00	10.00	0.04
Tb	0.56[a]	53.50[a]	91.50[a]	11.50[a]	0.02
Dy	0.44	50.70	81.00	13.00	0.02
Ho[a]	0.41	46.35	70.00	12.50	0.12
Er	0.39	42.00	59.00	12.00	0.20[a]
Tm[a]	0.41	32.95	48.00	10.20	0.11
Yb	0.43	23.90	37.00	8.40	0.02
Lu	0.43	20.20	27.00	5.50	0.01

Table 4.7 Mineral/melt distribution coefficients used to calculate mineral vectors and the fractional crystallization model (next paragraph). [a] Estimated from two adjacent elements. References are cited in the text.

Based on the REE variation diagrams and mineral vectors, it is clear that two different mineral assemblages are responsible for the observed REE compositional variation (Figure 4.10a-f). This is especially visible when $[La/Sm]_c$ is plotted against $[Ce]_c$ (Figure 4.10f). On this graph, the hornblendite unit defines a trend that is almost perpendicular to the one defined by the other units. The slope of the hornblendite trend is similar to the direction of the diopside mineral vector, which indicates that diopside fractionation may be, in part, responsible for the hornblendite trend. In contrast, the trend defined by the monzodiorite, A-syenite, AFP syenite and AF Qz-syenite units is more characteristic of a magma fractionating apatite and/or titanite.

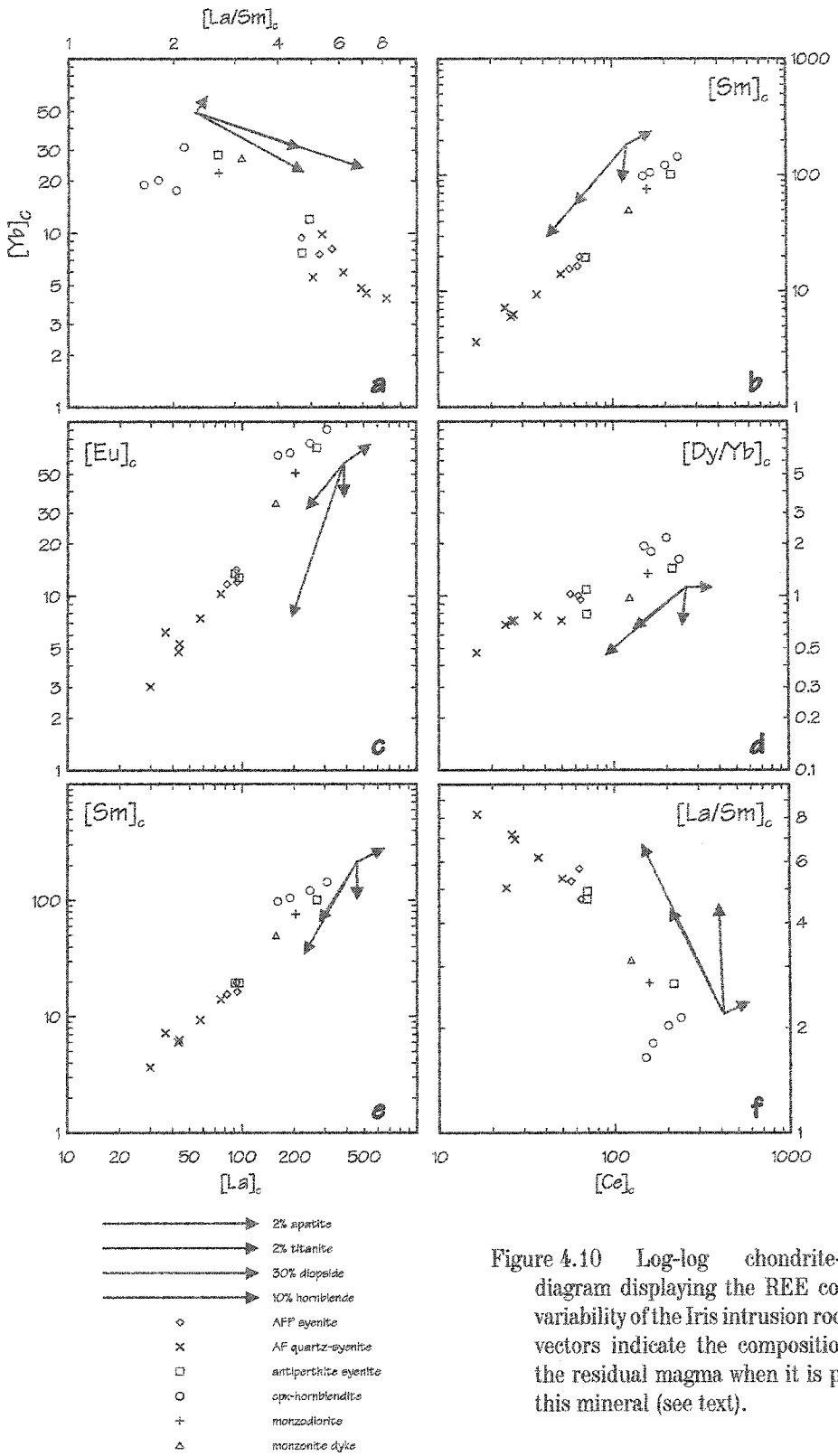

Figure 4.10 Log-log chondrite-normalized diagram displaying the REE compositional variability of the Iris intrusion rocks. Mineral vectors indicate the compositional path of the residual magma when it is precipitating this mineral (see text).

Similar conclusions can be drawn from most of the other graphs of Figure 4.10. A strong positive correlation between Ce and P_2O_5 and, Ce and TiO_2 further supports the evidence that apatite and titanite were influential during the REE fractionation of the Iris intrusion. Furthermore, because titanite has a strong preference for the MREE (Wörner et al., 1983; Green & Pearson, 1983), titanite fractionation may have produced the U-shaped $[REE]_c$ patterns observed for the AF Qz-syenite unit. U-shaped patterns are unusual but have been reported in nepheline syenite dykes from Mont-Royal in the Monteregian Hills, Canada (Eby, 1984), in the Ulindi nepheline syenite intrusion from the North Nyasa alkaline province of Malawi (Eby et al., 1998) and in peralkaline granites of the Oslo Rift in Norway (Neumann et al., 1977). Eby et al. (1998) concluded that titanite fractionation, along with the addition of HREE by hydrothermal fluids, were the likely causes for the U-shaped patterns in the Ulindi nepheline syenite. In the case of the Iris intrusion, some evidence also suggest that the HREE patterns were disturbed by hydrothermal fluids. There is a broad trend of decreasing Th/U ratio with increasing U-content (previous section), which can be interpreted to result from the mobilization of U by a hydrothermal fluid phase. Since carbonate complexes of the HREE and U are known to be stable under alkaline and oxidizing conditions (Langmuir, 1978), the hydrothermal fluids that affected the U distribution may have also influenced the HREE. Further proof is visible on the HREE end of the $[REE]_c$ diagrams (Figure 4.8), where patterns commonly cross. This cannot be explained by simple fractional crystallization but is consistent with the addition of HREE by hydrothermal fluids. However, on the other hand, the crossing patterns may simply result from analytical errors.

2. Fractional crystallization model

It has been shown in the previous paragraph (i.e. REE variation diagram and mineral vectors) that apatite, diopside and titanite are the minerals that were likely the most influential during fractional crystallization of the Iris intrusion. Although mineral vectors are useful in determining

which mineral or mineral assemblage affected the crystallization history, they cannot explain the overall variations of the $[REE]_c$ patterns or the extent of fractional crystallization. In order to assess if this assemblage could be the cause of the U-shaped patterns present in the syenites, a simple model based on the fractional crystallization equation of Neumann et al. (1954) was used. Mineral/melt distribution coefficients used to calculate the bulk distribution coefficient for each REE are listed in Table 4.7. The REE distribution coefficients were assumed constant throughout crystallization (see previous section). The hornblendite sample containing the lowest SiO_2-content is used as the starting composition. Figure 4.11 shows the incremental effect on the REE content of a melt and accumulating assemblage produced by crystallizing an assemblage composed of 7.8 % apatite, 10.4 % diopside, 65.3 % alkali-feldspar, 13.1 % hornblende and 3.4 % titanite. The addition of alkali-feldspar in the fractionating assemblage is consistent with the observed mineralogy of the AFP-syenite and also significantly lowers the bulk REE distribution coefficients resulting in smoother patterns. At 2 % fractionation (i.e., F=0.98), the calculated melt closely matches the observed REE composition of the monzodiorite (Figure 4.11a). Similarly, the composition of the accumulating assemblage (the one fractionating in the other model) falls within the compositional field of the hornblendite unit (Figure 4.11b). The discrepancy observed in the LREE and HREE ends of the patterns (i.e. both are higher in the monzodiorite compared to hornblendite) probably reflects analytical errors or the modification of the patterns by a secondary mechanism (previous paragraph). The area outlined by the 15 % and 20 % fractionation lines (i.e., F=0.85 and 0.80, respectively) is roughly similar to the compositional field of A-syenite and AFP syenite (Figure 4.11c) whereas the corresponding accumulated assemblage has MREE-contents over the hornblendite field (Figure 4.11d). Continued fractionation of this assemblage to 25 % (F=0.75) and 30 % (F=0.70) has the effect of significantly depleting the MREE relative to the LREE and HREE producing U-shaped

Figure 4.11 (next page) Fractional crystallization model displaying the incremental effect on the REE content of a melt and accumulating assemblage produced by crystallizing an assemblage of 7.8% apatite, 10.4% diopside, 65.3 % alkali-feldspar, 13.1% hornblende and 3.4% titanite.

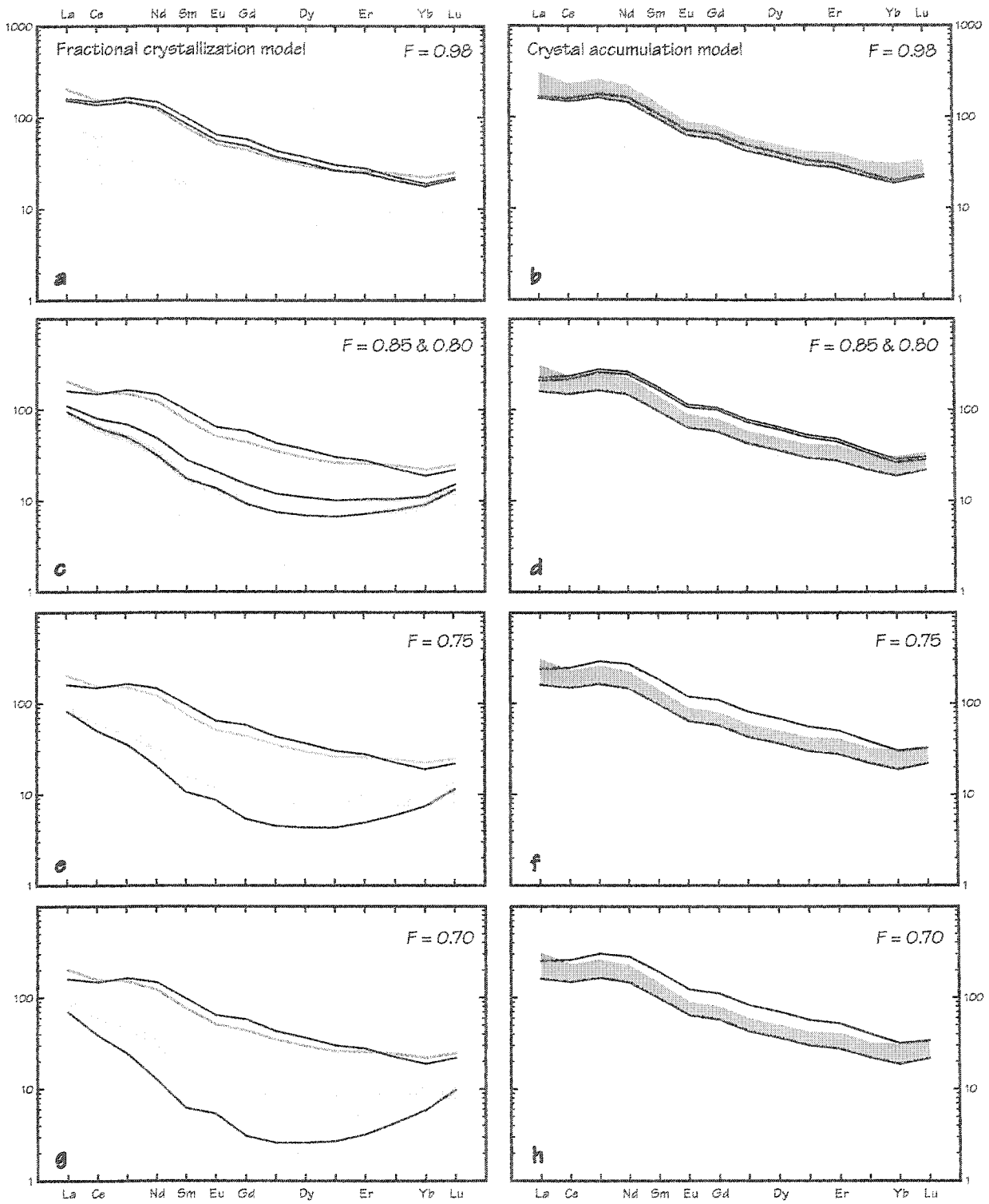
La Ce Nd Sm Eu Gd Dy Er Yb Lu
1000
100
10
1
Fractional crystallization model
F = 0.98
a
Crystal accumulation model
F = 0.98
b
F = 0.85 & 0.80
c
F = 0.85 & 0.80
d
F = 0.75
e
F = 0.75
f
F = 0.70
g
F = 0.70
h
A-syenite & AFP syenite field (n=5)
AF Qz-syenite field (n=6)
Cpx-hornblendite field (n=4)
Monzodiorite field (n=1)
Original composition
Calculated model based on the fractionation or accumulation of:
65.3% alkali-feldspar
7.8% apatite
10.4% diopside
13.1% hornblende
3.4% titanite

patterns that correlated well with those of the AF Qz-syenite unit (Figures 4.12e&g). However, the modelled LREE and HREE patterns are somewhat steeper compared to the actual ones. On the other hand, at this level of fractionation, the patterns of the accumulating assemblage are higher (enriched) compared to the field defined by the hornblendite (Figures 4.12f&h).

In conclusion, the crystal fractionation history of the Iris intrusion can successfully be modeled using the REE-contents of the rocks. Two mechanisms were influential during the REE distribution: (1) crystal fractionation and (2) crystal accumulation. The crystal fractionation of an assemblage containing apatite, diopside, alkali-feldspar, hornblende and titanite can adequately explain the evolution of the monzodiorite, antiperthite syenite, alkali-feldspar syenite and alkali feldspar Qz-syenite units. The U-shaped $[REE]_c$ patterns of the most fractionated units result from apatite, titanite and, to a lesser extent, amphibole fractionation. Amphibole also favors the MREE relative to the other REE. The crystal accumulation model adequately explains the increase of ΣREE with increasing SiO_2 in the hornblendite unit. At low values of fractionation, the modelled composition of the accumulating phase is within the field of hornblendite compositions. However, as the modeled accumulation progresses the calculated composition leaves the hornblendite field but remains parallel to it.

B. Emens and Pangea intrusions

The Emens AFP biotite-syenite and the Pangea melasyenite have remarkably similar $[REE]_c$ patterns (Figure 4.12). The patterns are characterized by strong $[LREE]_c$ enrichments relative to $[HREE]_c$ ($[La]_c$= 408-583, $[La/Yb]_c$= 17.3-49.1), significant negative Ce anomalies ($[Ce/Ce^*]_c$= 0.70-0.78), minor positive Er anomalies ($[Er/Er^*]_c$= 1.04-1.25), no negative Eu anomalies and flattening of the HREE ($[Tm/Lu]_c$= 0.89-1.15). The absence of negative Eu anomalies, is evidence of the non-involvement of plagioclase during fractionation or is an indication that fO_2 remained high throughout the crystallization history (Weill & Drake, 1973; Drake, 1975; Drake & Weill, 1975). The negative Ce and positive Er anomalies are not as easily explained. It is likely that these result from analytical uncertainties. The Emens melasyenite displays similar LREE characteristics but has higher MREE and HREE concentrations compared to the AFP biotite-syenite ($[Gd]_c$= 192; $[Lu]_c$= 52.9), which produces an overall less fractionated pattern ($[La/Yb]_c$= 6.92) (Figure 4.12a). The Pangea AF syenite unit pattern is similar to the ones from the melasyenite unit but has lower MREE- and HREE-contents relative to the latter ($[Gd]_c$= 46.7; $[Lu]_c$= 12.2). As with the $[ITE]_{pm}$ patterns, the $[REE]_c$ patterns of the hornblendite unit are noticeably different compared to any other units (Figure 4.12b). The patterns do not display any significant LREE-enrichment resulting in an almost flat-line distribution of the $[REE]_c$ ($[La/Yb]_c$= 1.64-3.24; $[Gd/Lu]_c$= 1.18-1.24). The REE distribution in this unit is enigmatic. The fact that the patterns cross the ones of the melasyenite and AF syenite units at the HREE end suggest that these units cannot be related by fractional crystallization. One mechanism that could explain this behavior is partial melting. For example, if we consider an assemblage composed of 20 % amphibole, 30 % plagioclase and 50 % garnet that has the same REE pattern as the hornblendite. A 1 % partial melt of this assemblage would produce a melt that has a remarkably similar composition as the melasyenite. Furthermore, the modeled pattern crosses at the HREE

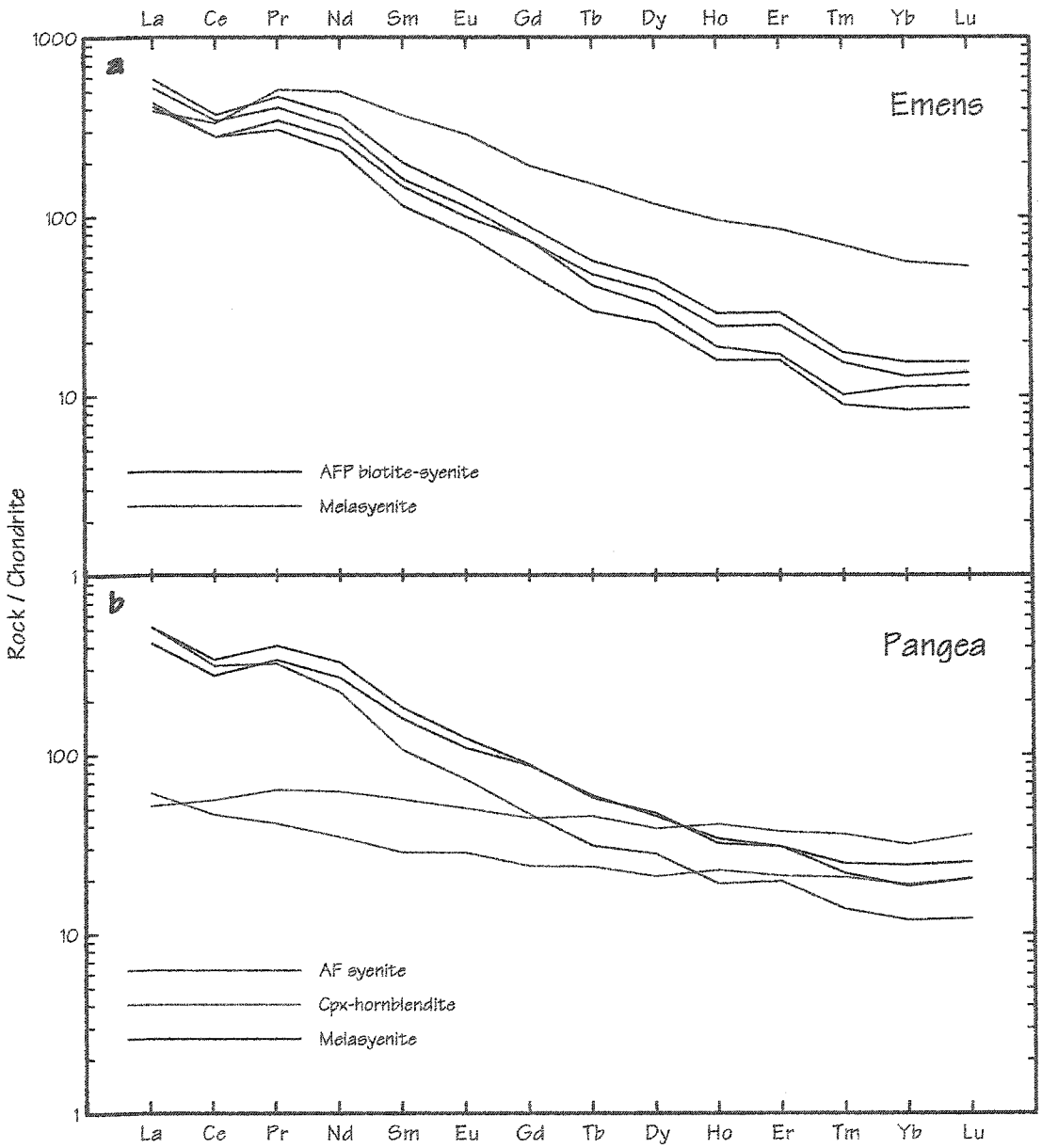

Figure 4.12 Chondrite-normalized rare earth element diagrams of rocks from the Emens and Pangea intrusions. Normalizing factors are listed in Table 4.5.

end of the diagram (Figure 4.13). Although such an assemblage is unlikely, it demonstrates that the Pangea hornblendite and melasyenite could be related by partial melting.

In comparison with the Iris hornblendite unit ($[La]_c$= 161-309; $[Lu]_c$= 19.1-34.6; $[La/Yb]_c$= 9.24-14.0), the main units of Emens and Pangea intrusions have steeper $[REE]_c$ patterns, have higher LREE-contents and have similar or lower HREE abundances (Figure 4.14). The higher LREE concentrations in these rocks compared to the Iris intrusion are attributed to the presence of a minor amount of allanite (Chapter 2). The presence of this mineral in the AFP biotite-syenite is an indication that original melt was highly REE-enriched (Hattori et al., 1996).

C. Garrison and Ludgate intrusions

The Garrison hornblende-monzonite and the Ludgate AF Qz-syenite have very similar $[REE]_c$ patterns although the Ludgate syenite has lower REE-contents relative to the Garrison monzonite (Figure 4.15). The Garrison patterns are characterized by strong $[LREE]_c$ enrichments relative to $[HREE]_c$ ($[La]_c$= 158-223; $[Lu]_c$= 4.88-6.91; $[La/Yb]_c$= 31.48-38.56), minor negative and positive Ce and Er anomalies respectively ($[Ce/Ce^*]_c$= 0.85-0.91; $[Er/Er^*]_c$= 1.18). No samples have significant negative Eu anomalies, which suggest that plagioclase fractionation did not occur.

In the Ludgate syenite, $[La]_c$ ranges from 89.4 to 119.6, $[Lu]_c$ from 3.66 to 4.07 and $[La/Yb]_c$ from 24.0 to 29.2. No significant negative Eu anomalies are present while minor negative and positive Ce and Er anomalies respectively are present.

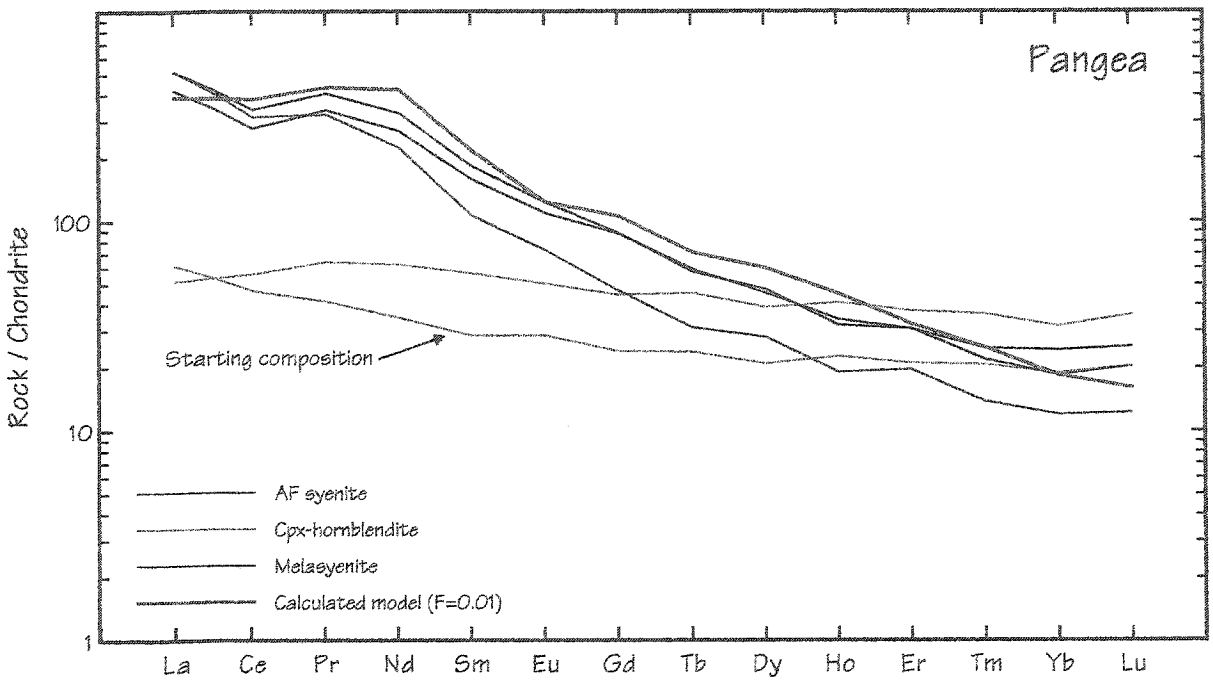

Figure 4.13 Calculated chondrite-normalized pattern resulting from a 1% partial melt of a mineral assemblage having a REE composition similar to the hornblendite rock (see text).

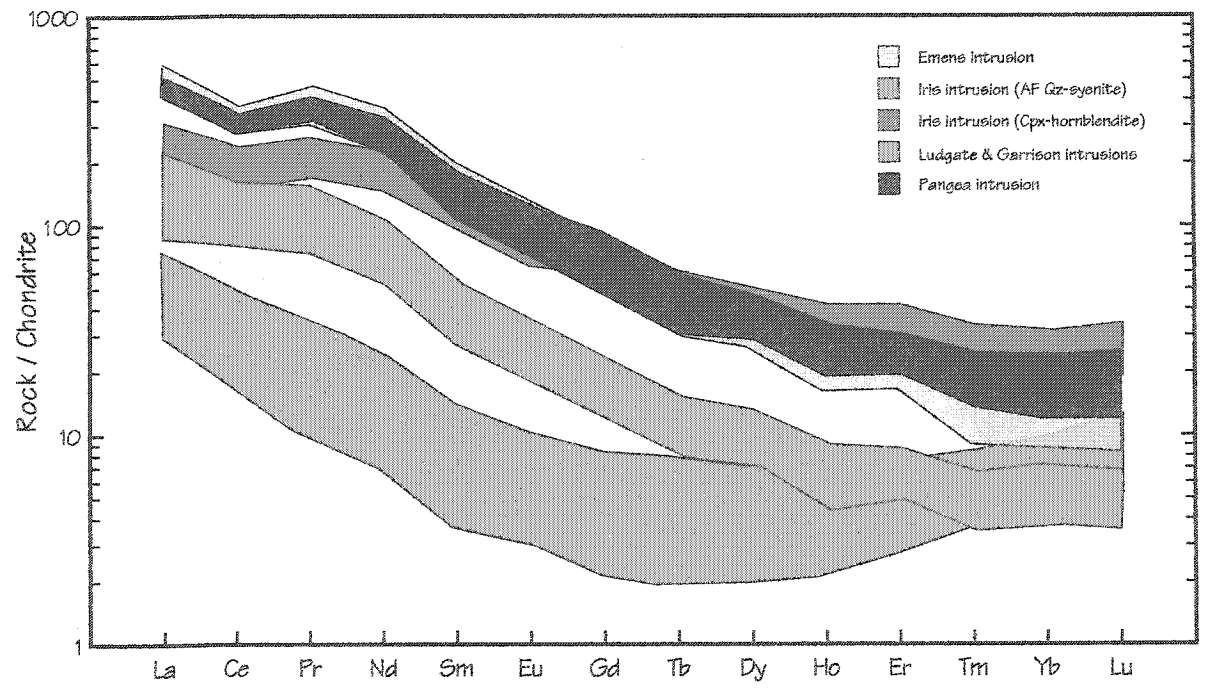

Figure 4.14 Composite diagram displaying the chondrite-normalized REE patterns of the major units from the five intrusions. Normalizing factors are from McDonough & Sun (1995) and are listed in Table 4.5.

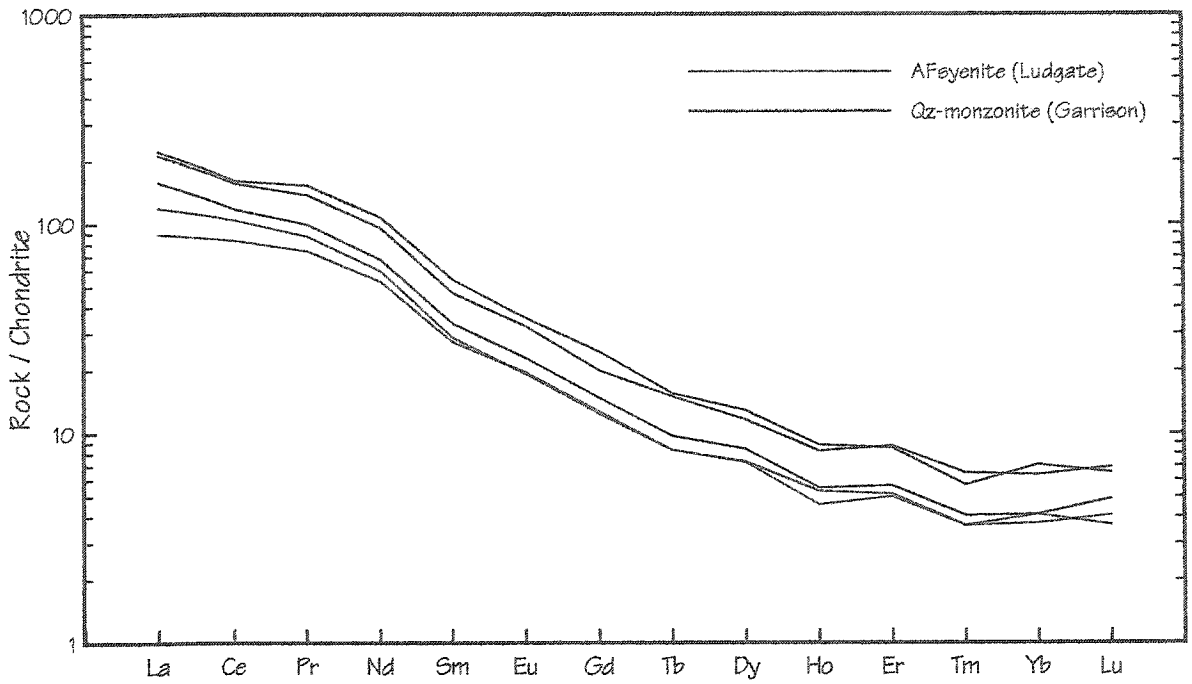

Figure 4.15 Chondrite-normalized rare earth element diagrams of rocks from the Garrison and Ludgate intrusions. Normalizing factors are listed in Table 4.5.

Chapter 5

Discussion and petrogenesis

THE main goals of this chapter is to integrate the salient characteristics of the Matheson suite presented in the previous chapters and use this information to compare the present suite with rocks from other well-known localities, i.e. Kirkland Lake and Roman province. The subject of contrasting alkali-contents and SiO_2-saturation properties is addressed, and comparison is given with other intrusions displaying the same properties. The petrogenesis of the Matheson suite is discussed in light of these comparisons.

Alkaline magmatism along the Porcupine-Destor fault zone (PDFZ) near Matheson (hereinafter Matheson suite) is characterized by significant variations in terms of rock types, silica saturation and alkali-contents (Chapter 4). However, in spite of the obvious dissimilarities, two magmatic series were identified: 1) a silica undersaturated potassic series comprised of the Emens and Pangea intrusions, and 2) a silica oversaturated sodic series comprised of the Iris, Ludgate and Garrison intrusions. Members of the potassic series are located north of the PDFZ (Figure 1.1). The Pangea intrusion is located north of the Arrow fault whereas the Emens intrusion is to the south of the fault. Members of the sodic series are located on both sides of the PDFZ but are all south of the Arrow fault (Figure 1.1). All intrusions have sub-rounded outlines apart for the Pangea intrusion, which is thin and elongated. Interestingly, the Pangea intrusion is the only intrusion of the suite that is located north of the Arrow fault (Figure 1.1) and which also displays an elongated morphology, suggesting that the Pangea intrusion was intruded when the PDFZ was still active (i.e., Cameron, 1990).

Although the rocks from the Emens and Pangea intrusions (potassic series) are quite different mineralogically and texturally (Chapter 2), they do nevertheless share numerous common geochemical properties. Indeed, both intrusions are composed of rocks that are potassic and SiO_2-undersaturated to -saturated on the basis of normative mineralogy. It should be noted that both intrusions also contain some ultrapotassic rocks in the sense of Foley et al. (1987).

They are also characterized by elevated large ion lithophile element contents with respect to high field strength element contents and fractionated rare earth element patterns with no negative Eu anomalies (Chapter 4).

Similarly, members of the sodic series display several contrasting textural and mineralogical characteristic but again share comparable geochemical traits amongst themselves. For example, the Garrison intrusion is composed of medium-grained slightly porphyritic subsolvus hornblende quartz-monzonite whereas the Iris and Ludgate intrusions are mostly composed of coarse-grained highly leucocratic hypersolvus alkali-feldspar quartz-syenite. Despite this, all three intrusions are silica oversaturated on the basis of modal and normative mineralogy and have $Na_2O/K_2O>1$. However, one member of the sodic series, i.e the Iris intrusion, contains undersaturated mafic units that are genetically related to oversaturated sodic felsic units (Chapter 4). The genetic association between undersaturated and oversaturated rocks and its significance will be discussed below. Members of the sodic series are characterized by moderate large ion lithophile element contents relative to the high field strength element contents and with fractionated rare earth element patterns with no negative Eu anomalies.

In spite of these obvious distinctions, members of both series share several traits, which tend to suggest a close genetic relationship. Indeed, a close spatial association of the intrusions along the PDFZ, coupled with almost identical trace element compositions is evidence that they are consanguineous. This type of association was also recognized in the Kirkland Lake area where volcanic and intrusive rocks that are intimately associated with the Kirkland Lake-Larder Lake fault (KLF) display several common characteristics with the Matheson suite.

In the Kirkland Lake area, the Timiskaming Assemblage (2687-2675 Ma; Ayer et al., 2002) forms a narrow corridor parallel to the KLF. It consists predominantly of polymictic conglomerate

and sandstone deposited in subaerial alluvial-fan, fluvial and deltaic environments (Mueller et al., 1994; Born, 1995). The conglomerates are intercalated with a minor amount of shoshonitic volcanic rocks. The conglomerates and volcanic rocks are intruded by numerous alkalic to subalkalic intrusions, some forming large composite syenitic and granitic intrusions (Hattori et al., 1996). Well-known examples of the composite intrusions are the Otto stock (Lovell, 1972; Smith & Sutcliffe, 1988; Ben Othman et al., 1990; Sutcliffe et al., 1990), the Murdock Creek intrusion (Rowins et al., 1989, 1991, 1993; Rowins, 1990; Wilkinson et al., 1999) and the Lebel stock (Levesque, 1994.; Cruden & Launeau, 1994; Wilkinson et al., 1999). The Otto stock was dated at 2680 ± 1 Ma by Corfu et al. (1989) and at 2679 ± 1 Ma by Corfu & Noble (1992), the Lebel stock at 2673 ± 2 Ma (Wilkinson et al., 1999) and Murdock Creek intrusion 2672 ± 2 Ma (Wilkinson et al., 1999). The Otto, Murdock Creek intrusions are two intrusions, amongst others located in the Kirkland Lake area that display several comparable characteristics with the members of the Matheson suite.

The most obvious similarity between the two regions is the close spatial association of all the Timiskaming-age intrusions with the major structure of the region i.e. the KLF in the case of Kirkland Lake area and the PDFZ in the present case. On the same note, both regions have numerous gold deposits that are localized principally along these two faults (Corfu et al., 1991). The style of intrusion emplacement is also variable depending on the location with respect to the faults. Indeed, this is clearly visible in the Kirkland Lake region, where the intrusions located within KLF zone are thin and elongated whereas those south of the KLF have large sub-rounded outlines. A similar change in intrusion morphology, although less dramatic, is present along the Arrow fault, a splay of the PDFZ near Matheson. Cameron (1990) explained the orientation and morphology of the Kirkland Lake intrusive bodies by passive intrusion into fractures while the KLF was undergoing extension.

The absolute ages of the intrusions of both regions are surprisingly similar. The age of the Garrison intrusion which was determined by U-Pb geochronology to be 2678 ± 2 Ma (Marmont & Corfu, 1989), is analytically indistinguishable to the Otto stock (2679 ±1 Ma; Corfu & Noble, 1992). In fact, other alkalic plutons such as the Winnie Lake stock and Watabeag batholith all yield similar ages of 2680-2676 Ma (Frarey & Krogh, 1986; Corfu et al., 1991).

In addition to a similar geological setting and age, the Matheson and Kirkland Lake suites also share comparable petrography and geochemistry. The Kirkland Lake intrusive suite is characterized, like in present case, by significant variations in terms of SiO_2-saturation and alkali ratios of the rocks (this study, Corfu et al., 1991). Indeed, some intrusions are mostly composed of quartz-bearing or quartz-normative syenite and granite whereas others are mostly composed of nepheline-normative and/or leucite-normative melasyenite and syenite (Levesque, 1994). For example, the Otto intrusion is mostly composed of sodic SiO_2-oversaturated rocks (Sutcliffe et al., 1990) and the Murdock Creek intrusion is composed of potassic to ultrapotassic SiO_2-undersaturated rocks (Rowins et al., 1993). The general geochemical characteristics of these two intrusions are strikingly similar to those of the Matheson suite. In addition to these similarities, rocks from the Matheson and Kirkland Lake suites share key trace element characteristics, which likely indicates that they originated from the same petrogenetic processes. Rocks from both suites are characterized by moderate to high large ion lithophile element contents (with Ba and Sr values that commonly reach over 2000 ppm) and low high field strength element contents. The high field strength element depletions produce the characteristic Nb-Ta-Ti troughs that are visible on primitive mantle-normalized incompatible trace elements ($[ITE]_{pm}$) diagrams (Figure 5.1). It is clear from Figure 5.1 that rocks from both regions share similar trace element characteristics. Rare earth element patterns of both suites are also almost identical. The rocks are characterized by fractionated REE patterns that lack any significant negative Eu anomalies (this study; Rowins et al., 1993; Levesque, 1994).

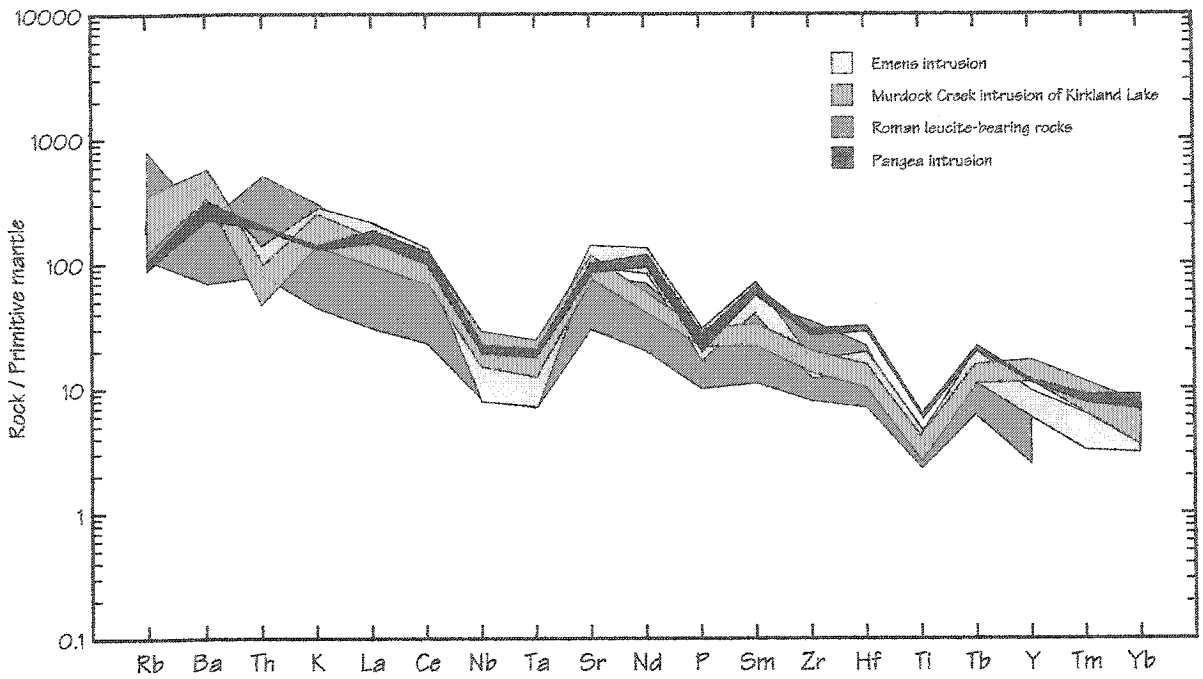

Figure 5.1 Composite primitive mantle-normalized incompatible trace element diagram displaying the similarities between the patterns of the potassic series of the Matheson suite with those of the Murdock Creek intrusions of Kirkland Lake (data from Rowins, 1990) and the Roman province leucite-bearing rocks (Data from Conticelli et al., 2002).

The fact that intrusions from the Kirkland Lake and Matheson suite are:

1. spatially associated to a major fault,

2. have similar absolute ages,

3. have closely associated sodic SiO_2-oversaturated and potassic to ultrapotassic SiO_2 undersaturated rocks,

4. have similar $[ITE]_{pm}$ patterns that are characterized by negative Nb-Ta-Ti anomalies,

5. have similar $[REE]_c$ patterns characterized by light rare earth elements enrichment relative to the heavy rare earth elements and no Eu anomalies

is not fortuitous and indicates that the two suites were formed by similar petrogenetic processes. It is now well established that the parental mafic melts responsible for alkaline rocks along the KLF and PDFZ are mantle-derived (Basu et al., 1984; Ben Othman et al., 1990; Hattori & Hart, 1990; Sutcliffe et al., 1990; Corfu et al., 1991; Rowins et al., 1993, Hattori et al., 1996; Kerrich & Ludden, 2000). For example, Hattori et al. (1996) have shown through isotopic evidence that the parental magmas of the Murdock Creek intrusion and several lamprophyre dykes of the Kirkland Lake area were derived from a depleted mantle, which was metasomatically enriched shortly before melting. The geochemical traits that characterize the rocks from both regions, i.e. the prominent negative Nb-Ta-Ti anomalies and high large ion lithophile and light rare earth elements concentration, are directly related to subduction processes (Hattori et al., 1996). These geochemical signatures are also typical of younger shoshonitic and ultrapotassic volcanic rocks that were formed in subduction-related setting such as the Roman province of Italy.

To this point, the discussion was mainly centred on comparing the potassic and sodic rocks of the Matheson suite to those of the Kirkland Lake suite. However, potassic and ultrapotassic rocks of Emens and Pangea intrusions also share several geochemical characteristics with those of the Roman province of Italy (Holm et al., 1982; Peccerillo, 1985, 1990, 1998, 1999; Rogers et al., 1985; Beccaluva et al., 1991; Di Battistini et al., 2001; Conticelli et al., 2002).

In general, rocks from the Matheson suite and Roman province are metaluminous and are characterized by elevated Al_2O_3-contents with moderate to low agpaitic index values (this study, Shaw, 1996). These characteristics are in contrast with other ultrapotassic and potassic rocks such as those from Leucite Hills and Toro-Ankole, which usually have lower Al_2O_3-contents and have higher agpaitic index values (Foley et al., 1987). Barton (1979) devised a classification in which the potassic rocks are divided into three types; i.e. Roman province-, Leucite Hills- and Toro-Ankola-types. This classification is based on silica content and agpaitic index of the rocks.

Interestingly, based on this classification, most potassic rocks from Emens and Pangea intrusions are classified as Roman province-type (Figure 5.2). Similarities between the Roman province and Matheson suite are not restricted to major elements but also extend to trace elements. This is best illustrated on Figures 5.1 where it is clear that rocks from both regions share several key trace element characteristics. Indeed, they are characterized by variable amounts of highly incompatible trace elements and by marked depletion in the abundance of high field strength elements with respect to large ion lithophile elements (this study; Peccerillo, 1985; Roger et al., 1985). These depletions translate into intense negative anomalies, especially at the Nb, Ta and Ti positions, on $[ITE]_{PM}$ diagrams. A similar geochemical signature is observed in the closely associated calc-alkaline rocks of the active Eolian arc, south of the Roman province (Barberi et al., 1974). The similarities with the active arc led many authors to suggest that the rocks of

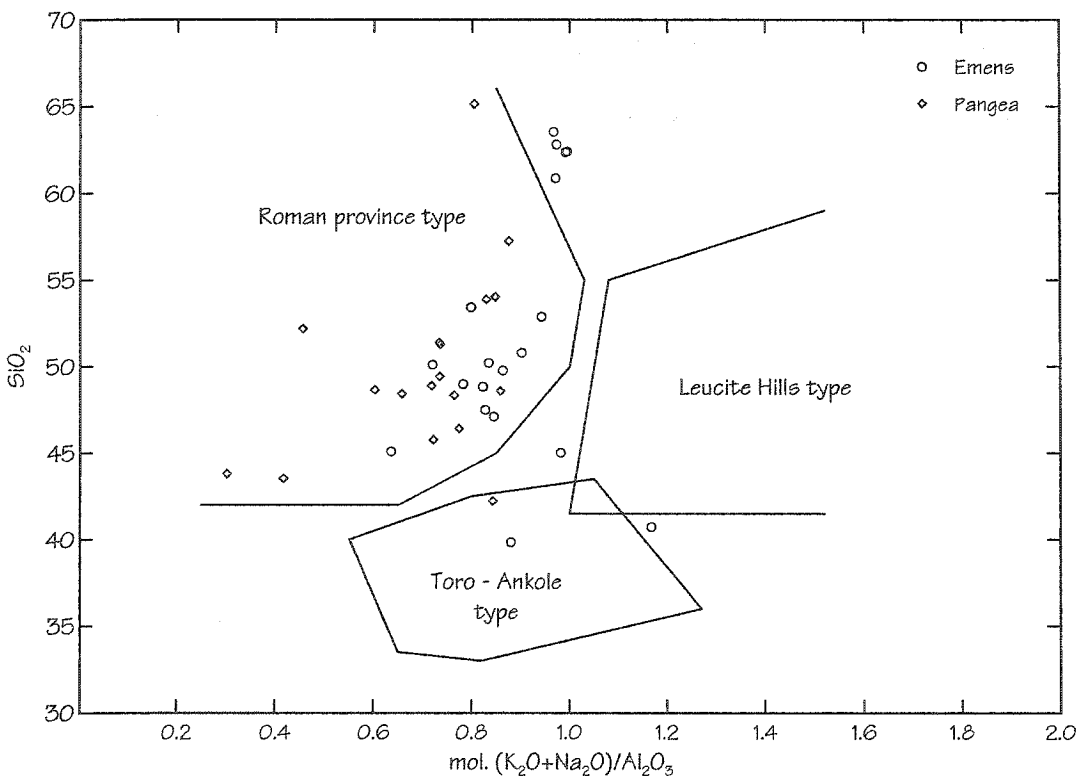

Figure 5.2 Classification of potassic rocks according to Barton (1979). Potassic rocks of Emens and Pangea intrusions mostly plot in the Roman province-type potassic rocks field.

the Roman province may also be subduction-related (Holm et al., 1982; Rogers et al., 1985; Peccerillo, 1985, 1998; Beccaluva et al., 1991; Conticelli & Peccerilo, 1992; Conticelli et al., 2002). This logic was also extended to the Timiskaming potassic rocks (Cooke & Moorhouse, 1969; Ujike, 1985; Ben Othman et al., 1990; Ayer et al., 1999), which include the Kirkland Lake and Matheson suites. However, Shaw (1996) notes that, considering the metamorphosed and altered character of the Timiskaming group, direct comparison with younger potassic rocks (i.e., Roman province, Eolian arc) may be misleading.

Several models have been proposed for the petrogenesis of the Roman province potassic and ultrapotassic rocks (e.g., Cundari, 1979, 1980; Edgar, 1980; Holm & Munksgaard, 1982; Peccerillo, 1985; Rogers et al., 1985; Ellam et al., 1989; Foley, 1992; Melluso et al., 1996) and for other regions of the world displaying similar petrological suites - rocks (e.g., Indonesia, Philippine and Superior province). The reader is referred to Shaw (1996) for a thorough review of the models; also, the following is inspired by part of that review.

To explain the formation and geochemical characteristics of the Roman province, Peccerrillo (1990, 1992) proposed a multistage model involving subduction-related processes. In this model, a subducted slab, composed of upper crustal and sedimentary rocks, is melted in the mantle. This produces acidic rocks with an isotopic signature similar to the source, except that HFSE are retained in residual phases (Foley & Wheller, 1990). The acidic melts rise in the mantle and metasomatize it. After collision and end of subduction, modification of the mantle geotherm induces melting of the metasomatized mantle. This produces strongly undersaturated ultrapotassic melts at deep levels, and saturated to oversaturated potassic melts at shallow levels. The last stage involves rifting, which favors melting and produces a conduit for large volumes of potassic magma.

One of the major problems in addressing the petrogenesis of the Matheson suite is the necessity to explain the occurrence of genetically related SiO_2-undersaturated and SiO_2-oversaturated rocks. Indeed, these associations have puzzled petrologists for many years. Experimental investigations in petrogeny's residua system (SiO_2-$KAlSiO_4$-$NaAlSiO_4$ system; Bowen, 1937) indicate that such associations are highly improbable. In this system, fractionating melts cannot cross the low-pressure thermal divide defined by the albite-orthoclase join. Therefore, in a closed system environment, a melt will fractionate either towards the granite minimum producing oversaturated rocks, or toward the phonolite minimum producing undersaturated rocks, but not both. However, in spite of these constraints, genetically related oversaturated and undersaturated rocks and intrusions are relatively common. For example, Thirwall and Burnard (1990) have studied the association of shoshonitic oversaturated and undersaturated syenites in the Borralan pluton in NW Scotland. There, strongly undersaturated mafic syenites are intimately associated with quartz-syenites. The oversaturated and undersaturated units of the complex display continuous major and trace elements chemical variations consistent with a common lineage (Thirwall & Burnard, 1990 and references therein). Isotopic data confirmed that both undersaturated and oversaturated rocks had the same parental magma but that the oversaturated syenites displayed evidence of crustal contamination. They concluded that the rocks of the Borralan complex were probably derived by extensive fractional crystallization of mantle-derived parental magmas, with minor crustal assimilation required to produce the most fractionated oversaturated syenites. Fowler and Henney (1996) reached a similar conclusion in their study of the mixed Caledonian appinite magmas. They demonstrated that undersaturated lamprophyric magmas could be driven, by the crystallization and removal of various minerals, to silica-saturated syenitic and granitic compositions, and this, with only a minor crustal input. This is of particular interest, since several workers have recently proposed that the parental magmas for the Murdock Creek (Rowins et al., 1993), Otto (Sutcliffe et al., 1990) intrusions may have had hornblenditic compositions, which is similar in mineralogy and geochemistry to calc-alkaline lamprophyres (Rock, 1991).

In the case of the Abu Khrug alkaline complex of eastern Egypt (Landoll et al., 1994 and references therein), the cogenetic nature of undersaturated and oversaturated syenites was explained through a crustal contamination mechanism. Indeed, the quartz syenites of the Abu Khrug complex have a distinct Nd crustal component while a similar signature is absent in the nepheline syenites. To the authors this indicated that the quartz syenites have formed by simultaneous assimilation and fractional crystallization (AFC) of a critically undersaturated magma, whereas the nepheline syenites evolved from such magma without being affected by contamination. Similarly, isotopic studies of undersaturated and oversaturated rocks of Mount Brome, Québec have established that they are related through AFC processes (Foland et al., 1993).

Other mechanisms have also been proposed to explain the genetic relationship between undersaturated and oversaturated rocks. For example, Henderson et al. (1989) attributed the occurrence of cogenetic quartz- and nepheline-syenite in the Red Hill alkaline complex in New Hampshire to a completely different mechanism. Indeed, they proposed that fractional crystallization of alkali-rich amphiboles from a critically undersaturated magma in the lower levels of the magma chamber led to the development of oversaturated magma. However, they also acknowledge the presence of some crustal contamination. Eby (1985) proposed that oversaturated and undersaturated rocks of Mount Brome were not genetically related but were derived from the injection of different magma batches that were formed from different sources at different depths.

It is difficult to pinpoint the exact mechanism which led to the association of both undersaturated and oversaturated rocks in the Matheson suite. The main difficulty lies in the fact that the undersaturated rocks of the suite are potassic and in a few cases ultrapotassic whereas the oversaturated rocks are extremely sodic. It is hard to fathom an AFC scheme that could link these two extremes. Also, to complicate the matter, Foland et al. (1993) clearly states that the transition

is only in one direction, namely oversaturated suites develop from initially undersaturated melts via crustal input. In this case it implies that, if an AFC model is to be used, the oversaturated sodic rocks must be derived from the undersaturated potassic rocks. One possible AFC scheme is the crystal fractionation K-bearing minerals such as leucite, biotite and K-feldspar while simultaneously assimilating Na-rich crust. The resulting melt would be depleted in potassium while progressively enriched in sodium. However, there is evidence that militates against this model. The most convincing is related to the presence of an undersaturated pyroxene-bearing hornblendite unit at the Iris intrusion. Indeed, this unit is Na_2O-rich ($Na_2O/K_2O>1$) and is the likely source of the oversaturated Na-rich Qz-syenites of the Iris intrusion (this study, Chapter 4). An AFC model, as described above, cannot explain this occurrence since significant fractionation and assimilation would likely be needed to drive a residual melt to sodic compositions. Therefore, under this scheme, sodic mafic rocks like the hornblendite are unlikely. However a model similar to the one proposed by Fowler and Henney (1996) for their appinite-syenite-granite association could explain the genetic relationship between the undersaturated pyroxene-bearing hornblendite and quartz-syenite units at the Iris intrusion. Indeed, this model advocates that, with only minor crustal input, 50 % fractionation of an assemblage composed of biotite, pyroxene, titanite and apatite will drive monzodiorite (appinite) to syenite, from where 60 % fractionation of K-feldspar, plagioclase, amphibole, apatite, titanite and magnetite will produce granite. This fractionating mineral assemblage is similar to the one proposed for the model discussed in Chapter 4, although biotite and plagioclase are absent in the latter.

The problem of contrasting alkali contents in the rocks of the Matheson suite is one that would be more effectively addressed using an isotopic approach. Indeed, on the premise that the sodic and potassic suites are cogenetic, which they probably are in light of almost identical trace element characteristics, several mechanisms can produce this association. However, these

can be broadly grouped into two categories : 1) characteristics of the sources and 2) secondary postmagmatic event.

Several possibilities can be explored in order to explain the genetic association of potassic and sodic rocks in the Matheson suite. For example, McNeil and Kerrich (1986) proposed that the close spatial association between extremely sodic trondhjemite and potassic lamprophyres at the Canadian Arrow deposit close to Matheson could be explained in terms of different source areas. Indeed, they suggested that the sodic trondhjemite originated from the partial melting of mafic granulite at the base of the crust whereas alkalic magmas such as the potassic lamprophyres originated from the mantle. The PDFZ then served as a conduit by both magmas resulting in a close spatial association between lamprophyre and trondhjemite. However, it is unlikely that a comparable mechanism can be used to explain the contrasting alkali contents of the Matheson suite since several geochemical features of the suite are not compatible with this model. The most compelling is the similar fractionated REE patterns without negative Eu anomalies of the rocks from the Na- and K-series. Furthermore, the primitive mantle-normalized trace element patterns have similar shapes with characteristic negative Nb-Ta-Ti anomalies. It is unlikely that a crustal melt would have the same REE and ITE characteristics as a mantle derived one.

McNeil and Kerrich (1986) also suggest that the extreme Na_2O-enrichment of the Canadian Arrow trondhjemite is also related to secondary spilitization reactions in the presence of thermal seawater. They proposed that extensive reactions with marine water occurred during the emplacement of the trondhjemite intrusion into a submarine volcanic sequence. This induced the conversion of plagioclase to albite producing enrichment in sodium. This enrichment can be in the order of 3 to 4 wt% (King & Kerrick, 1987).

Albitization is a characteristic of the rocks from Iris, Ludgate and Garrison intrusions. Indeed, there is a wealth of evidence suggesting that these rocks were influenced by late- to postmagmatic Na-rich fluids. For example, the occurrence of late Na-amphibole and Na-pyroxene in the rocks of Ludgate and Garrison intrusions supports this interpretation (Chapter 2). In addition, perthite crystals from these intrusions and Iris also bear the mark of intense albitization. This is evident in the Iris syenites where most perthite crystals are rimmed by a layer of clear albite (Figure 2.47, 2.51, 2.59 & 2.127). Furthermore, fractures in perthite crystals and the areas in the crystals adjacent to these fractures are commonly completely filled or replaced by albite (Figure 2.33). Albite-filled fractures are also visible in hand sample (Figures 2.5 & 2.8). Replacement of K-feldspar by albite is also likely responsible for the presence of abundant antiperthite crystals in the sodic syenites. Indeed, most antiperthite crystals have patchy textures defined by irregular shaped K-domains (Figures 2.31, 2.56, 2.57, 2.59, 2.118). This texture is likely the consequence of an almost complete albitization of perthite crystals, which leaves only small zones of K-rich perthite yielding an overall antiperthitic composition. The extremely turbid nature of most feldspar crystals is also considered evidence that the rocks were affected by late hydrous fluids. In the case of Iris intrusion, geochemical evidence also supports these petrographic observations. The pronounced variations in the contents of large ion lithophile elements and their ratios, coupled with incoherent trends with respect to SiO_2 indicates that these rocks were influenced by a late or postmagmatic event. The behavior of other elements also supports this interpretation. A broad negative correlation exists between the Th/U ratio and U-contents in the syenites, which indicates that U was mobilized by hydrothermal fluids (Chapter 4). Similarly, the occurrence of unusual U-shaped rare earth element patterns (Figure 4.8) in the Iris intrusion syenites may in part result from the addition of heavy rare earth elements by hydrothermal fluids (Chapter 4). That the rocks of Iris intrusion were affected by a postmagmatic event is indisputable; that they were enriched in sodium is a fact; however, it is difficult to ascertain if secondary Na-enrichment alone is responsible for such sodium enrichment. However, the possibility that

extensive albitization of Iris, Ludgate, and to a lesser degree Garrison intrusion, is responsible for the high Na-contents may shed some light on the difficulty of deriving a suite of cogenetic intrusions displaying such an extreme variation in alkali-contents. If this is the case, the Iris, Ludgate and Garrison intrusions were derived from the same magmatic source as the Emens and Pangea intrusions. The contrasting silica-saturation characteristics between the two suites could therefore be reasonably explained through assimilation fractional crystallization processes.

There is also the possibility that the contrasting alkali-contents of the Matheson suite are a characteristic of the mantle source. To reinforce this argument, Hattori et al. (1996) write that "at least two distinct metasomatized mantle sources in late Archean are suggested beneath the southern Abitibi belt from two distinct lamprophyres: Na-rich spessartite lamprophyres (Legault and Hattori, 1994) and high K-minette lamprophyre dykes". Since it is now well established that syenites can be derived from the fractionation of lamprophyres (Fowler & Henney, 1996), it is possible that the potassic and sodic rocks of the Matheson suite are derived from these two distinct sources. Following this line of reasoning, the contrasting silica saturation properties of the sodic and potassic rocks may be explained in terms of the depth that the partial melting occurred. Indeed, melts produced at deep levels are expected to be highly SiO_2-undersaturated whereas the ones produced at shallower levels are likely to be SiO_2-saturated to -oversaturated (Peccerillo, 1990, 1992). The contrasting characteristics of the mantle sources can best be explained if they were variably metasomatized by fluids derived by partial melting or dehydration of a subducted slab (e.g., Kerrich & Ludden, 2000). Since metasomatism and melt generation all occured within a common tectonic framework and event, both potassic and sodic melts can thus be regarded as cogenetic.

Conclusions and recommendations for future work

I. Conclusions
II. Recommendations for future work

I. Conclusions

THE conjuncture of major crustal faults, syenitic intrusions and gold mineralization is a characteristic of the Abitibi greenstone belt. Although this type of occurrence has long been recognized in the Matheson area, it did not receive as much attention as in the Kirkland Lake region. This research addresses the syenitic intrusive component of the association in the Matheson area. Here are the main conclusions:

1. A suite of five syenitic intrusions was sampled. Several petrographic units were identified in each intrusion. The Iris intrusion contains three distinct syenitic units and two mafic units whereas only alkali-feldspar quartz-syenite and hornblende quartz-monzonite were identified at Ludgate and Garrison intrusions, respectively. Three rock types were identified at the Pangea intrusion while only alkali-feldspar porphyritic biotite-syenite was found in the Emens intrusion drill core.

2. The Emens, Pangea, Ludgate and Iris intrusions have hypersolvus feldspar assemblages whereas the Garrison intrusion displays a subsolvus feldspar assemblage.

3. The occurrence of late- to postmagmatic aegirine-augite and Na-amphibole at Garrison, Emens, Ludgate and Pangea intrusions, and the presence of clear albite rims, in addition to evidence of extensive K-feldspar/perthite replacement by albite suggests that all the studied intrusions were variably affected by late Na-rich fluids. This is especially the case of Ludgate and Iris intrusions where most antiperthite crystals display signs of extensive albitization.

4. The occurrence of minerals such as melanite, bastnasite, allanite and barite in the rocks of Emens intrusion is considered evidence that these rocks are alkaline and that the parent magma was LILE- and REE-enriched.

5. The following mineral paragenesis is suggested based on mineral inclusion data: apatite, magnetite and titanite were early precipitating phases while diopside, feldspar, amphibole and phlogopite respectively, appeared later in the paragenetic sequence.

6. Two magmatic series were identified based on SiO_2-saturation properties and alkali-contents: the first, comprised of Iris, Ludgate and Garrison intrusions, is characterized by SiO_2-oversaturated sodic rocks; and the second, comprised of Emens and Pangea intrusions, is characterized by SiO_2-undersaturated to -saturated potassic rocks. Several samples from these intrusions are also classified as ultrapotassic.

7. Emens and Pangea intrusions have elevated LILE-contents whereas the others have moderate LILE-contents.

8. All intrusions have prominent negative Nb-Ta-Ti anomalies on primitive mantle-normalized diagrams and all intrusions have similar fractionated chondrite-normalized REE patterns without negative Eu anomalies.

9. Rare earth element fractionation trends indicate that apatite, titanite and diopside fractionation is responsible for the REE compositional variability observed in the rocks of Iris intrusion.

10. Rare earth element modelling suggests that the pyroxene-bearing hornblendite and syenite units of Iris intrusion are cogenetic and are related through fractional crystallization. The unusual U-shaped REE patterns of the syenites are the result of this fractionation. However, since experimental investigations in the petrogeny's residua system demonstrate that SiO_2-undersaturated and -oversaturated rocks cannot be related through simple fractional crystallization, an open system process must be considered. This may include crustal contamination combined with fractional crystallization or simply a postmagmatic silica addition by an alteration event.

11. Pronounced variations in the contents of large ion lithophile elements and their ratios in the Iris intrusion rocks, coupled with incoherent trends with respect to SiO_2-contents indicate that the rocks were modified by a late or postmagmatic event. Other geochemical evidence such as a negative correlation between the Th/U ratio and U-contents, and the occurrence of unusual U-shaped rare earth element patterns in the syenites may also in part be related to late fluid action.

12. Rocks from the Matheson suite have several characteristics in common with the Murdock Creek intrusion of Kirkland Lake and the leucite-bearing rocks of the Roman province. In particular, Emens and Pangea intrusions (i.e. the potassic series) have almost identical trace elements patterns as the Murdock Creek intrusions, and have pronounced negative Nb-Ta-Ti anomalies, which are characteristic of the Roman province rocks.

13. The numerous similarities of the Matheson suite and Kirkland Lake suites indicate that the two suites were formed through similar petrogenetic processes. Geochemical traits such as elevated large ion lithophile and light rare earth elements, and prominent negative Nb-Ta-Ti

anomalies were acquired from the mantle source and are directly related to subduction processes (Hattori et al., 1996).

14. A dilemma still exists as to the origin of the contrasting alkali-contents in the rocks from the Matheson suite. The potassic nature of Emens and Pangea intrusions is clearly a characteristic of their mantle source. The sodic nature of Iris, Ludgate and Garrison intrusions is likely a consequence of extensive albitization during late- or postmagmatic events. Evidence for this is outlined in paragraphs 3 and 11 of this section. The high Na-contents of these rocks could also be a characteristic of the source. Hattori et al. (1996) indicate that two distinct mantle sources were present beneath the southern Abitibi belt in the late Archean: a K-rich source and a Na-rich source. Fractional crystallization of a melt from the Na-rich source may have lead to the observed Na-enrichment in the sodic series. A combination of both processes is also possible.

II. Recommendations for future work

An isotopic study of rocks from the sodic and potassic series should give better constraints on the petrogenetic processes that lead to the formation of both series. Nd isotope data should help identify if the two suites were formed from the same or different mantle reservoirs. Similarly, Nd isotope data could shed some light on the problem of contrasting silica-saturation properties of the rocks by identifying if significant crustal contamination is present in the SiO_2-oversaturated rocks. A stable isotope study of feldspar (especially antiperthite) and quartz, coupled with a fluid inclusion investigation of the sodic quartz-syenites would determine if these minerals have a magmatic signature or are the result of hydrothermal alteration and, if this is the case, constrain the nature and origin of these hydrothermal fluids.

References

Ablay, G. J., Carroll, M. R., Palmer, M. R., Mart, J. & Sparks, R. S. J. (1998). Basanite-Phonolite Lineages of the Teide-Pico Viejo Volcanic Complex, Tenerife, Canary Islands. *Journal of Petrology*, vol. 39, 905-936.

Ague, J. J., & Brimhall, G. H. (1988). Regional variations in bulk chemistry, mineralogy, and the compositions of mafic and accessory minerals in the batholiths of California. *Geological Society of America Bulletin*, vol. 100, 891-911.

Anderson, A. T. (1980). Significance of hornblende in calc-alkaline andesites and basalts. *American Mineralogist*, vol. 65, 837-851.

Anderson, O. (1928). The genesis of some types of feldspar from granite pegmatites. *Norsk Geologisk Tidskrifft*, vol. 10, 116-207.

Arth, J. G. (1976). Behavior of trace elements during magmatic processes - a summary of theoretical models and their applications. *Journal of Research of the U. S. Geological Survey*, vol. 4, 41-47.

Ayer, J. A. (1998). The mafic minerals of the Falcon Island ultrapotassic pluton, Lake of the Woods, Ontario: Progressive reduction during fractionation. *Canadian Mineralogist*, vol. 36, 49-66.

Ayer, J. A., Trowell, N. F., Madon, Z., Kamo, S., Kwok, Y. Y. & Amelin, Y. (1999). Compilation of the Abitibi greenstone belt in the Timmins-Kirkland Lake area: revisions to stratigraphy and new geochronological results. In: *Summary of field work and other activities 1999, Ontario Geological Survey, Open File Report* 6000, 4-1 to 4-14.

Ayer, J. A., Amelin, Y., Corfu, F., Kamo Z., Ketchum, J., Kwok, Y. Y. & Trowell, N. (2002). Evolution of the Abitibi greenstone belt based on U-Pb geochronology: autochthonous volcanic construction followed by plutonism, regional deformation and sedimentation. *Precambrian Research*, vol. 115, 63-95.

Baker, P. E., Gass, I. G., Harris, P. G. & Lemaitre R. W. (1964). The volcanological report of the Royal Society expedition to Tristan de Cunha, 1962. *Philosophical Transactions of the Royal Society of London*, vol. 256A, 439-575.

Barberi, F., Innocenti, F., Ferrara, G., Keller J. & Villari L. (1974). Evolution of Eolian arc volcanism (Southern Tyrrhenian Sea). *Earth and Planetary Science Letters*, vol. 21, 269-276.

Barton, M. (1979). A comparative study of some minerals occurring in the potassium-rich alkaline rocks of Leucite Hills, Wyoming, the Vico Volcano, Western Italy and Toro-Ankole region, Uganda. *Neues Jahrbuch Mineralogie Monatshefte*, vol. 137, 113-134.

Basu, A. R., Goodwin, A. N. & Tatsumoto, M. (1984). Sm-Nd study of Archean alkalic rocks from the Superior province of the Canadian Shield. *Earth and Planetary Science Letters*, vol. 70, 40-46.

Beccaluva, L., Di Girolamo, P. & Serri, G. (1991). Petrogenesis and tectonic setting of the Roman Volcanic Province, Italy. *Lithos*, vol. 26, 191-221.

Bennett, G., Dressler, B. O. & Robertson, J. A. (1991). The Huronian Supergroup and associated intrusive rocks. In: *Geology of Ontario, Ontario Geological Survey, Special Volume 4*, Part 1, 549-591.

Ben Othman, D., Arndt, N. T., White, W. M. & Jochum, K. P. (1990). Geochemistry and age of Timiskaming alkali volcanics and the Otto syenite stock, Abitibi, Ontario. *Canadian Journal of Earth Sciences*, vol. 27, 1304-1311.

Berger, B. R., & Amelin, Y. (1999). Geological Investigations along Highway 101, Guibord, Michaud and Garrison Townships. In: *Summary of Field work and other Activities 1998, Ontario Geological Survey, Miscellaneous Paper* 169, p. 25-32.

Bleeker, W. & Parrish, R. R. (1996). Stratigraphy and U-Pb zircon geochronology of Kidd Creek: implications for the formation of giant volcanogenic massive sulphide deposits and tectonic history of the Abitibi greenstone belt. *Canadian Journal of Earth Sciences*, vol. 33, 1213-1231.

Born, P. (1995). A sedimentary basin analysis of the Abitibi greenstone belt in the Timmins area, northern Ontario, Canada. Unpublished Ph.D. thesis, Carleton University, Ottawa, 489p.

Bowen, N. L. (1937). Recent high temperature research on silicates and its significance in igneous petrology. *American Journal of Science*, vol. 33, 1-21.

Brown, G. M. (1967). Mineralogy of basaltic rocks. In: *Basalts*, 103-162.

Calvert, A. J. & Ludden, J. N. (1999). Archean continental assembly in the southeastern Superior Province of Canada. *Tectonics*, vol. 18, 412-429.

Cameron, E. M. C. (1988). Archean gold relation to granulite formation and redox zoning in the crust, *Geology*, vol. 16, 109-112.

Cameron, E. M. C. (1990). Alkaline magmatism at Kirkland Lake, Ontario: Product of strike-slip orogenesis. In: *Geological Survey of Canada, Current Reasearch Paper* 90-1C, Part C, 261-269.

Cameron, E. M. C. (1993).Precambrian gold: perspectives from the top and bottom of shear zones, *Canadian Mineralogist*, vol. 31, 917-944.

Cameron, E. M. C. & Hattori, K. (1987). Archean gold mineralization and oxidized hydrothermal fluids, *Economic Geology*, vol. 82, 1177-1191.

Campbell, C. D. (1939). The Kruger alkaline syenites of British Columbia. *American Journal of Science*, vol. 237, 527-549.

Card, K. D. (1979). Regional geological synthesis, Central Superior Province. *Geological Survey of Canada, Paper* 79-1A, 87-90.

Card, K. D. (1990). A review of the Superior Province of the Canadian Shield, a product of Archean accretion. *Precambrian Research*, vol. 48, 99-156.

Carmichael, I. S. E., Nicholls, J. & Smith, A. L. (1970). Silica activity in igneous rocks. *American Mineralogist*, vol. 55, 246-263.

Cawthorn, R. G. & Collerson, K. D. (1974). The recalculation of pyroxene end-member parameters and the estimation of ferrous and ferric iron content from electron microprobe analyses. *American Mineralogist*, vol. 59, 1203-1208.

Chen, C.-Y., Frey, F. A. & Garcia, M. O. (1990). Evolution of alkalic lavas at Haleakala Volcano, east Maui, Hawaii. *Contribution to Mineralogy and Petrology*, vol. 105, 197-218.

Clague, D. A. & Frey F. A. (1982). Petrology and trace element geochemistry of the Honolulu volcanics, Oahu: Implications for the oceanic mantle below Hawaii. *Journal of Petrology*, vol. 23, 447-504.

Colvine, A. C., Fyon, J. A., Heather, K. B., Marmont, S., Smith, P. M. & Troop, D. G. (1988). Archean lode gold deposits in Ontario. *Ontario Geological Survey, Miscellaneous Paper* 139, 136 pp.

Conticelli, S., D'Antonio, M., Pinarelli, L. & Civetta, L. (2002). Source contamination and mantle heterogeneity in the genesis of Italian potassic and ultrapotassic volcanic rocks: Sr-Nd-Pb isotope data from Roman Province and southern Tuscany. *Mineralogy and Petrology*, vol. 74, 189-222.

Conticelli, S. & Peccerillo, A. (1992). Petrology and geochemistry of potassic and ultrapotassic volcanism in central Italy: petrogenesis and inferences on the evolution of the mantle sources. *Lithos*, vol. 28, 221-240.

Cooke, D. L. & Moorhouse, W. W. (1969). Timiskaming volcanism in the Kirkland Lake area, Canada. *Canadian Journal of Earth Sciences*, vol. 6, 117-132.

Corfu, F. (1993). The evolution of the southern Abitibi greenstone belt in light of precise U-Pb geochronology. *Economic Geology*, vol. 88, 1323-1340.

Corfu, F., Jackson, S. L. & Sutcliffe, R. H. (1991). U-Pb ages and tectonic significance of late alkalic magmatism and nonmarine sedimentation: Timiskaming Group, southern Abitibi belt, Ontario. *Canadian Journal of Earth Sciences*, vol. 28, 489-503.

Corfu, F., Krogh, T. E., Kwok, Y. Y. & Jensen, L. S. (1989). U-Pb zircon geochronology in the southwestern Abitibi greenstone belt, Superior Province. *Canadian Journal of Earth Sciences*, vol. 26, 1747-1763.

Corfu, F. & Noble, S. R. (1992). Genesis of the southern Abitibi greenstone belt, Superior Province, Canada: evidence from zircon Hf isotope analyses using a single filament technique. *Geochimica et Cosmochimica Acta*, vol. 56, 2081-2097.

Cundari, A. (1979). Petrogenesis of leucite-bearing lavas in the Roman Volcanic Region, Italy. *Contributions to Mineralogy and Petrology*, vol. 76, 9-21.

Cundari, A. (1980). Role of subduction in the genesis of leucite-bearing rocks: Facts or fashion? *Contributions to Mineralogy and Petrology*, vol. 73, 432-434.

Cruden, A. R. & Launeau, P. (1994). Structure, magnetic fabric and emplacement of the Archean Lebel stock, SW Abitibi greenstone belt. *Journal of Structural Geology*, vol. 16, 677-691.

Czamanske, G. K. & Wones, D. R. (1973). Oxidation during magmatic differentiation, Finmarka Complex, Oslo area, Norway: Part 2. The mafic silicates. *Journal of Petrology*, vol. 14, 349-380.

De Albuquerque, C. R. A. (1973). Geochemistry of biotites from granite rocks, northern Portugal. *Geochimica et Cosmochimica Acta*, vol. 37, 1779-1802.

Deer, W. A., Howie, R. A. & Zussman, J. (1962). *Rock-Forming Minerals: Ortho- and ring silicates,* vol. 1, Wiley & Sons, New York.

Deer, W. A., Howie, R. A. & Zussman, J. (1996). *An Introduction to the Rock-Forming Minerals*, second edition. Addison-Wesley Publishing Company, 720pp.

Di Battistini, G., Montanini, A., Vernia, L., Venturelli, G. & Tonarini, S. (2001). Petrology of melilite-bearing rocks from the Montefiascone volcanic complex (Roman magmatic province): new insights into the ultrapotassic volcanism of central Italy. *Lithos*, vol. 59, 1-24.

Dimroth, E., Imreh, L., Goulet, N. & Rocheleau, M. (1983a). Evolution of the southcentral segment of the Abitibi Belt, Québec: Part 2. Tectonic evolution and geomechanical model. *Canadian Journal of Earth Sciences*, vol. 20, 1355-1373.

Dimroth, E., Imreh, L., Goulet, N. & Rocheleau, M. (1983b). Evolution of the south-central segment of the Archean Abitibi belt, Québec: Part 3. Plutonic and metamorphic evolution and geotectonic model. *Canadian Journal of Earth Sciences*, vol. 20, 1374-1388.

Drake, M. J. (1975). The oxidation state of europium as an indicator of oxygen fugacity. *Geochimica et Cosmochimica Acta*, vol. 39, 55-64.

Drake, M. J. & Weill, D. F. (1975). Partition of Sr, Ba, Ca, Y, Eu^{2+}, Eu^{3+}, and other REE between plagioclase feldspar and magmatic liquid: an experimental study. *Geochimica et Cosmochimica Acta*, vol. 39, 689-712.

Duuring, P., Hagemann, S. G. & Groves, D. I. (2000). Structural setting, hydrothermal alteration, and gold mineralization at the Archaean syenite-hosted Jupiter deposit, Yilgarn Craton, Western Australia. *Mineralium deposita*, vol. 35, 402-421.

Easton, R. M. (1992). The Grenville and the Proterozoic history of central and southern Ontario. In: *Geology of Ontario, Ontario Geological Survey, Special Volume* 4, Part 2, 714-904.

Eby, G. N. (1984). Monteregian Hills I. Petrography, major and trace element geochemistry, and strontium isotopic chemistry of the western intrusions: Mounts Royal, St Bruno, and Johnson. *Journal of Petrology*, vol. 25, 421–452.

Eby, G. N. (1985). Monteregian Hills II. Petrography, major and trace element geochemistry, and strontium isotopic chemistry of the eastern intrusions: Mounts Shefford, Brome, and Megantic. *Journal of Petrology*, vol. 26, 418-448.

Eby, G. N., Woolley, A. R., Din, V. & Platt, G. (1998). Geochemistry and petrogenesis of nepheline syenites: Kasungu-Chipala, Ilomba, and Ulindi nepheline syenites intrusions, north Nyasa alkaline province, Malawi. *Journal of Petrology*, vol. 39, 1405-1424.

Edgar, A. D. (1980). Role of subduction in the genesis of leucite-bearing rocks: Discussion. *Contributions to Mineralogy and Petrology*, vol. 73, 429-431.

Edgar, A. D. (1989). Barium- and strontium-enriched apatite in lamproites from west Kimberly, western Australia. *American Mineralogist*, vol. 74, 889-895.

Edgar, A. D., Sutcliffe, R. H., Collison, M. S., Clegg, M. & Barron, K. (1991). Mineralogy, petrology and geochemistry of alkaline metavolcanic rocks and their relationship to gold mineralization in the Kirkland Lake area. In: *Abstracts, Ontario Mines and Minerals Symposium*, 30.

Ellam, R. M., Hawkesworth, C. J., Menzies, M. A. & Rogers, N. W. (1989). The volcanism of southern Italy: Role of subduction and the relationship between potassic and sodic alkaline magmatism. *Journal of Geophysical Research*, vol. 94, 4589-4601.

Fang, H. R. & Zhang, L. H. (1995). A genetic relationship between the Macassa gold deposit and the Kirkland Lake syenite composite stock, north-eastern Ontario, Canada. In: *Program with abstracts, Geological Association of Canada; Mineralogical Association of Canada; Canadian Geophysical Union, Joint Annual Meeting*, vol. 20, 43p.

Fodor, R. V., Keil, K. & Bunch, T. E. (1975). Contributions to the mineral chemistry of Hawaiian rocks: Part 4. Pyroxenes in rocks from Haleakala and West Maui volcanoes, Maui, Hawaii. *Contributions to Mineralogy and Petrology*, vol. 50, 173-195.

Foland, K. A., Landoll, J. D., Henderson, C. M. B. & Jiangfeng, C. (1993). Formation of cogenetic quartz and nepheline syenites. *Geochimica et Cosmochimica Acta*, vol. 57, 697-704.

Foley, S. F. (1992). Vein-plus-wall-rock melting mechanisms in the lithosphere and the origin of potassic alkaline magmas. *Lithos*, vol. 28, 435-454.

Foley, S. F., Venturelli, G., Green, D. H. & Toscani, L. (1987). The ultrapotassic rocks: characteristics, classification and constraints for petrogenetic models. *Earth Science Reviews*, vol. 24, 81-134.

Foley, S. F. & Wheller, G. E. (1990). Parallels in the origin of the geochemical signatures of island arc volcanics and continental potassic rocks: The role of residual titanates. *Chemical Geology*, vol. 85, 1-18.

Fowler, A. D., Berger, B., Shore, M., Jones, M. I., & Ropchan, J. (2002). Supercooled rocks: development and significance of varioles, spherulites, dendrites and spinifex in Archean volcanic rocks, Abitibi Greenstone belt, Canada. *Precambrian Research*, vol. 115, 311-328.

Fowler, M. B. & Henney, P. J. (1996). Mixed Caledonian appinite magmas: implications for lamprophyre fractionation and high Ba-Sr granite genesis. *Contributions to mineralogy and Petrology*, vol. 126, 199-215.

Frarey, M. J. & Krogh, T. E. (1986). U-Pb zircon ages of late internal plutons of the Abitibi and eastern Wawa Subprovinces, Ontario and Québec. In: *Geological Survey of Canada, Current Research Paper* 86-1A, Part A, 43-48.

Frey, F. A., Chappell, B. W. & Roy, S. D. (1978). Fractionation of rare-earth elements in the Tuolumne intrusive series, Sierra Nevada Batholith, California. *Geology*, vol. 6, 239-242.

Fyon, J. A., Troop, D. G., Marmont, S. & MacDonald, A. J. (1989). Introduction of gold into Archean crust, Superior province, Ontario-Coupling between mantle-initiated magmatism and lower crustal thermal maturation. *Economic Geology Monograph* 6, 479-490.

Geoscience Laboratories (2002). *Schedule of fees and services*, vol. 1, Issue 3, 25pp.

Gibb, F. C. F. (1973). The zoned clinopyroxene of the Shiant Isles sill, Scotland. *Journal of Petrology*, vol. 14, 203-230.

Goldich, S. & Kinser, J. (1939). Perthite from Tory Hill, Ontario. *American Mineralogist*, vol. 24, 407-427.

Gomes, C. B., Moro, S. L. & Dutra, C. V. (1970). Pyroxenes from the alkaline rocks of Itapirapuã, San Paulo, Brazil. *American Mineralogist*, vol. 55, 224-230.

Goodwin, A. M. (1977). Archean volcanism in the Superior Province, Canadian Shield. *Geological Association of Canada, Special Paper* 16, 205-241.

Goodwin, A. M. & Ridler, R. (1970). The Abitibi orogenic belt. In: *Symposium on Basins and Geosynclines of the Canadian Shield. Geological Survey of Canada, Paper* 70-40, 1-30.

Green, A. G., Milkereit, B., Mayrand, I. J., Mayrand, L. J., Lunden, J. N., Hubert, C., Jackson, S. L., Sutcliffe, R. H., West, G. F., Verpealst, P. & Simard, A. (1990). Deep structure of an Archean greenstone terrane. *Nature*, vol. 344, 327-330.

Green, T. H. (1981). Experimental evidence for the role of accessory phases in magma genesis. *Journal of Volcanology and Geothermal Research*, vol. 10, 405-422.

Green, T. H. (1995). Significance of Nb/Ta as an indicator of geochemical processes in the crust-mantle system. *Chemical Geology*, vol. 120, 347-359.

Green, T. H. & Pearson, N. J. (1983). Effect of pressure on rare earth element partition coefficients in common magmas. *Nature*, vol. 305, 414–416.

Green, T. H. & Pearson, N. J. (1987). An experimental study of Nb and Ta partitioning between Ti-rich minerals and silicate liquids at high pressure and temperatures. *Geochimica et Cosmochimica Acta*, vol. 51, 55-62.

Gupta, A. K., Onuma, K., Yagi, K. & Lidiak, E. G. (1973). Effect of silica concentration on the diopsidic pyroxenes in the system diopside-$CaTiAl_2O_6$-SiO_2. *Contributions to Mineralogy and Petrology*, vol. 41, 333-344.

Hamilton, J. V. (1986). The structural and stratigraphic setting of gold mineralization in the vicinity of Larder Lake, south-central Abitibi greenstone belt, northeastern Ontario. *Unpublish M.Sc. thesis*, Queen's University, Kingston, Ontario.

Harrison, T. N. (1990). Chemical variation in micas from the Cairngorm pluton, Scotland. *Mineralogical Magazine*, vol. 54, 355-366.

Hart, S. R. & Davies, K. E. (1978). Nickel partitioning between olivine and silicate melt. *Earth and Planetary Science Letters*, vol. 40, 203-219.

Hart, S. R. & Dunn, T. (1993). Experimental cpx/melt partitioning of 24 trace elements. *Contributions to Mineralogy and Petrology*, vol. 113, 1-8.

Haslam, H. W. (1968). The crystallization of intermediate and acid magmas at Ben Nevis, Scotland. *Journal of Petrology*, vol. 9, 84-104.

Hattori, K. (1989). Barite-celestine intergrowths in Archaean plutons: The product of an oxidizing hydrothermal activity related to alkaline intrusions. *American Mineralogist*, vol. 74, 1272-1279.

Hattori, K. (1993). Diverse metal sources of Archean gold deposits: evidence from in situ lead-isotope analysis of individual grains of galena and altaite in the Ross and Kirkland Lake deposits, Abitibi Greenstone belt, Canada. *Contributions to Mineralogy and Petrology*. vol. 113, 185-195.

Hattori, K. & Hart, S. R. (1990). Fast recycling model inferred from isotope and trace element study of pyroxenes and feldspars in Timiskaming-type alkaline rocks, southern Abitibi greenstone belt. *Extented Abstract Volume,* 3rd International Archean Symposium, Perth, 267-269.

Hattori, K., Hart, S. R. & Shimizu, N. (1996). Melt and source mantle compositions in the late Archean: A study of Sr- and Nd-isotope and trace elements in clinopyroxenes from shoshonitic alkalinc rocks. *Geochimica et Cosmochimica Acta*, vol. 60, 4551-4562.

Hawke, D. R. (1993). Report on the 1988 exploration program Iris joint venture project NTS 32D/5. *Assessment file KL-3170*, Ministry of Northern Development and Mines of Ontario, Residant Geologist Office, Kirkland Lake, Ontario.

Heather, K. B. (1998). New insights on the stratigraphy and structural geology of the southwestern Abitibi greenstone belt: Implications for tectonic evolution and setting of mineral deposits in the Superior Province. In: *The first age of giant ore formation: stratigraphy, tectonics and mineralization in the Late Archean and Early Proterozoic*; Papers presented at the Prospectors and Developers Association of Canada Annual Convention, Toronto, 63-101.

Heather, K. B., Shore, G. T. & van Breemen, O. (1996). Geological investigations in the Swayze greenstone belt, southern Superior Province, Ontario: a final update. In: *Geological Survey of Canada, Current Research Paper* 1996-1C, 125-136.

Helz, R. T. (1973). Phase relations of basalts in the melting range at $P(H_2O) = 5$ kbars as a function of oxygen fugacity. *Journal of Petrology*, vol. 14, 249-302.

Henderson, C. M. B., Pendlebury, K. & Foland, K. A. (1989). Mineralogy and petrology of the Red Hill alkaline igneous complex, New Hampshire, USA. *Journal of Petrology*, vol. 30, 627-666.

Hodgson, C. J. (1983). Preliminary report on the Timmins-Kirkland Lake area gold deposits file. *Ontario Geological Survey, Open File Report* 5467, 434 pp.

Hodgson, C. J. (1986). Abitibi greenstone belt, Ontario, Canada. *Transactions of the Institution of Mining and Metallurgy*, vol. 95, B183-194.

Hodgson, C. J. & Hamilton, J. V. (1989). Gold mineralization in the Abitibi greenstone belt: End stage result of Archean collisional tectonics?. *Economic Geology Monograph* 6, 86-100.

Hodgson, C. J., Hamilton, J. V. & Piroshco, D. W. (1990). Structural setting of gold deposits and the tectonic evolution of the Timmins-Kirkland Lake area, southwestern Abitibi greenstone belt. In: *Gold and base-metal mineralization in the Abitibi Subprovince, Canada, with emphasis on the Québec segment.* Short Course Notes, The University of Western Australia, Department of Geology, Publication No. 24, 101-120.

Hoffman, P. F. (1989). Precambrian geology and tectonic history of North America. In: *The Geology of North America - An overview: Boulder, Colorado, Geological Society of America, The Decade of North American Geology,* vol. A, 447-512.

Holm, P. M., Lou, S. & Nielsen, A. (1982). The geochemistry and petrogenesis of the Vulsinian district, Roman province, central Italy. *Contributions to Mineralogy and Petrology*, vol. 80, 367-378.

Holm, P. M. & Munksgaard, N. C. (1982). Evidence for mantle metasomatism: an oxygen and strontium isotope study of the Vulsinian District, Central Italy. *Earth and Planetary Science letters*, vol. 60, 376-388.

Hyde, R. S. (1980). Sedimentary facies in the Archean Timiskaming Group and their tectonic implications, Abitibi greenstone belt, northeastern Ontario, Canada. *Precambrian Research*, vol. 12, 161-195.

Icenhower, J. P. & London, D. (1996). Experimental partitioning of Rb, Cs, Sr, and Ba between alkali feldspar and peraluminous melt. *American Mineralogist*, vol. 81, 719-734.

Jackson, S. L., Sutcliffe, R. H., Ludden, J. N., Hubert, C., Green, A.G., Milkereit, B., Mayrand, L., West, G. F. & Verpealst, P. (1990). Southern Abitibi greenstone belt: Archean crustal structure from seismic reflection profiles. *Geology*, vol. 18, 1086-1090.

Jackson, S. L. & Fyon, J. A. (1991). The western Abitibi Subprovince in Ontario. In: *Geology of Ontario, Ontario Geological Survey, Special Volume* 4, Part 1, 405-482.

Jackson, S. L., Fyon, J. A. & Corfu, F. (1994). Review of Archean supracrustal assemblages of the southern Abitibi greenstone belt in Ontario, Canada: products of microplate interaction within a large-scale plate-tectonic setting. *Precambrian Research*, vol. 65, 183-205.

Jakes, P. & White, A. J. R. (1972). Hornblende from calc-alkaline volcanic rocks of island arcs and continental margins. *American Mineralogist*, vol. 57, 887-902.

Jensen, L. S. & Langford, F. F. (1985). Geology and petrogenesis of the Archean Abitibi belt in the Kirkland Lake area, Ontario. *Ontario Geological Survey, Miscellaneous Paper* 123, 130 pp.

Jiang, S.-Y., Palmer, M. R., Xue, C.-J. & Li, Y.-H. (1994). Halogen-rich scapolite-biotite rocks from the Tongmugou Pb-Zn deposit, Qinling, northwestern China: implications for the ore-forming processes. *Mineralogical Magazine*, vol. 58, 543-552.

Jolly, W. T. (1978). Metamorphic history of the Archean Abitibi belt. In: *Metamorphism in the Canadian Shield. Geological Survey of Canada, Paper* 78-10, 63-78.

Jolly, W. T. (1980). Development and degradation of Archean lavas, Abitibi area, Canada, in light of major element geochemistry. *Journal of Petrology*, vol. 21, 323-363.

Kerrich, R. (1989). Archean gold: Relation to granulite formation or felsic intrusions? *Geology*, vol. 17, 1011-1015.

Kerrich, R. & Ludden, J. (2000). The role of fluids during formation and evolution of the southern Superior Province lithosphere: an overview. *Canadian Journal of Earth Sciences*, vol. 37, 135-164.

King, R. W. & Kerrich, R. (1987). Fluorapatite fenitization and gold enrichment in sheeted trondhjemites within the Destor-Porcupine fault zone, Taylor Township, Ontario. *Canadian Journal of Earth Sciences*, vol. 24, 479-502.

Klein, C. & Hurlbut, C. S. (1993). *Manual of Mineralogy*, 21st edition. John Wiley & Sons Inc., 681pp.

Kushiro, I. (1960). Si-Al relation in clinopyroxenes from igneous rocks. *American Journal of Science*, vol. 258, 548-554.

Laflèche, M. R., Dupuy, C. & Dostal, J. (1991). Archean orogenic ultrapotassic magmatism: an example from the southern Abitibi greenstone belt. *Precambrian Research*, vol. 52, 71-96.

Lalonde, A. E. & Martin, R. F. (1983). The Baie-des-Moutons syenitic complex, La Tabatière, Québec: Part 2. The ferromagnesian minerals. *Canadian Mineralogist*, vol. 21, 81-91.

Lalonde, A. E. & Bernard, P. (1993). Composition and color of biotite granites: Two useful properties in the characterization of plutonic suites from the Hepburn internal zone of Wopmay Orogen, Northwest Territories. *Canadian Mineralogist*, vol. 31, 203-217.

Landoll, J. D., Foland, K. A. & Henderson, C. M. B. (1994). Nd isotopes demonstrate the role of contamination in the formation of coexisting quartz and nepheline syenites at the Abu Khrug complex, Egypt. *Contributions to Mineralogy and Petrology*, vol. 117, 305-329.

Langmuir, D. (1978). Uranium solution-mineral equilibria at low temperatures with applications to sedimentary ore deposits. *Geochimica et Cosmochimica Acta*, vol. 42, 547–560.

Larsen, L. M. (1976). Clinopyroxenes and coexisting mafic minerals from the alkaline Ilímaussaq intrusion, South Greenland. *Journal of Petrology*, vol. 17, 258-290.

LeBas, M. J. (1962). The role of aluminium in igneous clinopyroxenes with relation to their parentage. *American Journal of Science*, vol. 260, 267-288.

LeBas, M. J., LeMaitre, R. W., Streckeisen, A. & Zanettin, B. (1986). A chemical classification of volcanic rocks based on the total alkali-silica diagram. *Journal of Petrology*, vol. 27, 745-750.

Leake, B. E. (1965). The relationship between tetrahedral aluminium in natural calciferous and subcalciferous amphiboles. *American Mineralogist*, vol. 50, 843-851.

Leake, B. E., Woolley, A. R., Arps, C. E. S., Birch, W. D., Gilbert, M. C., Grice, J. D., Hawthorne, F. C., Kato, A., Kisch, H. J., Krivovivhev, V. G., Linthout, K., Laird, J., Mandarino, J. A., Maresch, W. V., Nickel, E. H., Rock, N. M. S., Schumacher, J. C., Smith, D. C., Stephenson, N. C. N., Ungaretti, L., Whittaker, E. J. W. & Youzhi, G. (1997). Nomenclature of amphiboles: report of the subcommittee on amphiboles of the International Mineralogical Association, Commission on New Minerals and Mineral Names. *Canadian Mineralogist*, vol. 35, 219-246.

Legault, M. I. & Hattori, K. (1994). Provenance of igneous clasts in conglomerates of the Archean Timiskaming Group, Kirkland Lake area, Abitibi greenstone belt, Canada. *Canadian Journal of Earth Sciences*, vol. 31, 1749-1762.

Lemarchand, F., Villemant, B. & Calas, G. (1987). Trace element distribution coefficients in alkaline series. *Geochimica and Cosmochimica Acta*, vol. 51, 1071-1081.

Levesque, G. (1994). Duality of magmatism at Kirkland Lake, Ontario, Canada. *Unpublish M.Sc. thesis*, University of Ottawa, Ottawa, Ontario.

Levesque, G. & Hattori, K. (1989). Late Archean alkaline intrusive complex hosting the Kirkland Lake gold camp. In: *Program with abstracts, Geological Association of Canada*. vol. 14, A81.

Leybourne, M. I., van Wagoner, N. A. & Ayres, L. D. (1997). Chemical stratigraphy and petrogenesis of the early Proterozoic Amisk Lake volcanic sequence, Flin Flon-Snow Lake greenstone belt, Canada. *Journal of petrology*, vol. 38, 1541-1564.

Lovell, H. L. (1972). Geology of the Eby and Otto area, district of Timiskaming, *Ontario. Ontario Department of Mines and Northern Affairs, Geological Report 99*, 34pp.

Ludden, J., Hubert, C. & Gariepy, C. (1986). The tectonic evolution of the Abitibi greenstone belt of Canada. *Geological Magazine*, vol. 123, 153-166.

Luinstra, B. (2002). Geology, structure and gold mineralization within the Porcupine-Destor deformation zone, Harker-Holloway gold camp, southwestern Abitibi greenstrone belt, Canada. Unpublished Ph.D. thesis, University of Ottawa, Ottawa.

Luinstra, B. & Benn, K. (1999). Structural geology of the Holloway Township gold camp, Abitibi greenstone belt, northeastern Ontario. In: *Summary of field work and other activities 1999, Ontario Geological Survey, Open File Report* 6000, 10-1 to 10-4.

Macdonald, R., Thorpe, R. S., Gaskarth, J. W. & Grindrod, A. R. (1985). Multi-component origin of Caledonian lamprophyres of northern England. *Mineralogical Magazine*, vol. 50, 547-577.

Mahood, G. A. & Hildreth, W. (1983). Large partition coefficients for trace elements in high-silica rhyolites. *Geochimica et Cosmochimica Acta*, vol. 47, 11–30.

Marmont, S. & Corfu, F. (1989). Timing of gold introduction in the Late Archean tectonic framework of the Canadian shield: Evidence from U-Pb zircon geochronology of the Abitibi subprovince. *Economic Geology Monograph 6*, 101-111.

McDonough, W. F. & Sun, S.-S. (1995). The composition of the earth. *Chemical Geology*, vol. 120, 223-253.

McGuire, A. V., Dyar, M. D. & Ward, K. A. (1989). Neglected Fe^{3+}/Fe^{2+} ratios - a study of Fe^{3+} content of megacrysts from alkali basalts. *Geology*, vol. 17, 687-690.

McNeil, A. M. & Kerrich, R. (1986). Archean lamprophyre dykes and gold mineralization, Matheson, Ontario: the conjuncture of LILE-enriched mafic magmas, deep crustal structures, and Au concentration. *Canadian Journal of Earth Sciences*, vol. 23, 324-343.

Melluso, L., Morra, V. & Di Girolamo, P. (1996). The Mt Vulture volcanic complex (Italy): Evidence for distinct parental magmas and for residual melts with melilite. *Mineralogy and Petrology*, vol. 56, 225-250.

Miller, T. (1972). Potassium-rich alkaline intrusive rocks of western Alaska. *Geological Society of America Bulletin*, vol. 83, 2111-2128.

Mitchell, R. H. (1996). Undersaturated potassic plutonic complexes. In: *Undersaturated Alkaline Rocks: Minerology, Petrogenesis, and Economic Potential. Mineralogical Association of Canada, Short Course Series* 24, 193-216.

Mitchell, R. H. & Platt, R. G. (1978). Mafic mineralogy of ferroaugite syenite from the Coldwell alkalic complex, Ontario, Canada. *Journal of Petrology*, vol. 19, 627-651.

Mitchell, R. H. & Platt, R. G. (1979). Nepheline-bearing rocks from the Poohbah Lake complex, Ontario: Malignites and malignites. *Contributions to Mineralogy and Petrology*, vol. 69, 255-264.

Mitchel, R. H. & Vladykin, N. V. (1996). Compositional variation of pyroxene and mica from the Little Murun ultrapotassic complex, Aldan Shield, Russia. *Mineralogical Magazine*, vol. 60, 907-925.

Miyashiro, A. (1978). Nature of alkalic volcanic rock series. *Contributions to mineralogy and petrology*, vol. 66, 91-104.

Morimoto, N. (1989). Nomenclature of pyroxenes. *Canadian Mineralogist*, vol. 27, 143-456.

Mueller, W., Donaldson, J. A. & Doucet, P. (1994). Volcanic and tectono-plutonic influences on sedimentation in the Archean Kirkland basin Abitibi greenstone belt, Canada. *Precambrian Research*, vol. 68, 201-230.

Mueller, W. U., Daigneault, R., Mortensen, J. K. & Chown, E. H. (1997). Archean terrane docking: upper crust collision tectonics, Abitibi greenstone belt, Québec, Canada. *Tectonophysics*, vol. 265, 127-150.

Muller, D. & Groves, D. I. (2000). *Potassic igneous rocks and associated gold-copper mineralization*, 3rd updated and enlarged edition, Springer Verlag, Berlin, 252pp.

Nash, W. P. (1972). Apatite-calcite equilibria in carbonatites: Chemistry of apatite from Iron Hill, Colorado. *Geochimica et Cosmochimica Acta*, vol. 36, 1313-1319.

Nash, W. P. & Wilkinson, J. F. G. (1970). Shonkin Sag laccolith, Montana: Part 1. Mafic minerals and estimates of temperature, pressure, oxygen fugacity and silica activity. *Contributions to Mineralogy and Petrology*, vol. 25, 241-269.

Nelson, S. J. & Johnson, R. D. (1966). Geology of Hudson Bay Basin. *Bulletin of Canadian petrology and geology*, vol. 14, 520-578.

Nesse, W. D. (1991) *Introduction to optical mineralogy.* Second edition. Oxford University Press, 335 pp.

Neumann, E.-R. (1976). Compositional relations among pyroxenes, amphiboles and the other mafic phases in the Oslo region plutonic rocks. *Lithos*, vol. 9, 85-109.

Neumann, E.-R., Brunfelt, A. D. & Finstad, K. G. (1977). Rare earth elements in some igneous rocks in the Oslo Rift, Norway. *Lithos*, vol. 10, 311–319.

Neumann, H., Mead, J. & Vitaliano, C. J. (1954). Trace element variation during fractional crystallization as calculated from the distribution law. *Geochimica et Cosmochimica Acta*, vol. 6, 90-99.

Norris, A. W. (1993). Hudson Platform: Introduction. In: *The Geology of North America - Sedimentary cover of the craton in Canada, Geological Survey of Canada, The Decade of North American Geology*, vol. D1, 645-651.

Noyes, H. J., Wones, D. R. & Frey, F. A. (1983). A tale of two plutons: petrographic and mineralogical constraints of the Red Lake and Eagle Creek plutons, Central Sierra Nevada, California. *Journal of Geology*, vol. 91, 353-379.

Parsons, I. (1979). The Klokken gabbro-syenite complex, South Greenland: cryptic variation and origin of inversely graded layering. *Journal of Petrology*, vol. 20, 653-694.

Parsons, I. (1980). Alkali-feldspar and Fe-Ti oxide exsolution textures as indicators of the distribution and subsolidus effects of magmatic "water" in the Klokken layered syenite intrusion, South Greenland. *Transactions of the Royal Society of Edinburgh, Earth Sciences*, vol. 71, 1-12.

Pearce J. A. (1983). Role of the sub-continental lithosphere in magma genesis at active continental margins. In: *Continental basalts and mantle xenoliths.* C.J. Hawkesworth & M.J. Norry (eds.), Shiva, Nantwich, 230-249.

Peccerillo, A. (1985). Roman Comagmatic Province (central Italy): evidence for subduction related magma genesis. *Geology*, vol. 13, 103-106.

Peccerillo, A. (1990). On the origin of the Italian potassic magmas – comments. *Chemical Geology*, vol. 85, 183-186.

Peccerillo, A. (1992). Potassic and ultrapotassic rocks: Compositional characteristics, petrogenesis, and geological significance. *Episodes*, vol. 15, 243-251.

Peccerillo, A. (1998). Relationship between ultrapotassic and carbonate-rich volcanic rocks in central Italy: petrogenetic and geodynamic implications. *Lithos*, vol. 43, 267-279.

Peccerillo, A. (1999). Multiple mantle metasomatism in central-southern Italy: geochemical effects, timing and geodynamic implications. *Geology*, vol. 27, 315-318.

Percival, J. A. & Card, K. D. (1983). Archean crust as revealed in the Kapuskasing uplift, Superior Province, Canada. *Geology*, vol. 11, 323-326.

Percival, J. A. & Card, K. D. (1985). Structure and evolution of Archean crust in central Superior Province, Canada. In: *Evolution of Archean Supracrustal Sequences. Geological Association of Canada, Special Paper* 28, 179-192.

Perfit, M. R., Gust, D. A., Bence, A. E., Arculus, R. J. & Taylor, S. R. (1980). Chemical characteristics of island-arc basalts: Implications for mantle sources. *Chemical Geology*, vol. 30, 227-256.

Piilonen, P. C., McDonald, A. M. & Lalonde, A. E. (1998). The crystal chemistry of aegirine from Mont Saint-Hilaire, Québec. *Canadian Mineralogist*, vol. 36, 779-791.

Piroshco, D. W. & Kettles, K. (1991). Structural geology of Tisdale and Whitney townships, Abitibi greenstone belt, District of Cochrane, northeastern Ontario. *Ontario Geological Survey, Open File Report* 5768, 115 pp.

Platt, G. R. (1996). Nepheline syenite complexes - an overview. In *Undersaturated Alkaline Rocks: Minerology, Petrogenesis, and Economic Potential. Mineralogical Association of Canada, Short Course Series* 24, 63-99.

Pouchou, J. L. & Pichoir, F. (1984). Un nouveau modèle de calcul pour la microanalyse quantitative par spectrométrie de rayon X: Partie 1. Application à l'analyse d'échantillons homogènes. *Recherche Aérospaciale*, vol. 3, 13-38.

Powell, W.G., Carmichael, D.M. & Hodgson, C.J. (1995). Conditions and timing of metamorphism in the southern Abitibi greenstone belt, Quebec. *Canadian Journal of Earth Sciences*. vol. 32, 787-805.

Prest, V. K. (1951). Geology of Guibord Township. *Ontario Department of Mines, Annual Report*, vol. 60, part 9, 56pp.

Rhodes, J. M. (1981). Characteristics of primary basaltic magmas. In: *Basaltic volcanism on the terrestrial planets*, Pergamon, Oxford, 409-452.

Rieder, M., Cavazzini, G., D'Yakonov, Y. S., Frank-Kamenetskii, V. A., Gottardi, G., Guggenheim, S., Koval, P. V., Müller, G., Neiva, A. M. R., Radoslovich, E. W., Robert, J.-L., Sassi, F. P., Takeda, H., Weiss, Z. & Wones, D. R. (1998). Nomenclature of the micas. *Canadian Mineralogist*, vol. 36, 905-912.

Robert, F. (1990). Structural setting and control of gold-quartz veins of the Val D'Or area, southeastern Abitibi Subprovince. In: *Gold and base-metal mineralization in the Abitibi Subprovince, Canada, with emphasis on the Québec segment.* Short Course Notes, The University of Western Australia, Department of Geology, Publication No. 24, 167-209.

Robert, F. (2001). Syenite-associated disseminated gold deposits in the Abitibi greenstone belt, Canada. *Mineralium Deposita*, vol. 36, 503-516.

Rock, N. M. S. (1987). Nature of lamprophyres: an overview. In: *Alkaline igneous rocks. Geological Society of London Special Publication*, vol. 30, 191-226.

Rock, N. M. S. (1991). *Lamprophyres*, Blackie and Sons, London, 285pp.

Rogers, N. W., Hawkesworth, C. J., Parker, R. J. & Marsh, J. S. (1985). The geochemistry of potassic lavas from Vulsini, Central Italy, and implications for mantle enrichment processes beneath the Roman region. *Contributions to Mineralogy and Petrology*, vol. 90, 244-257.

Rogers, N. W., James, D., Kelley, S. P. & De Mulder, M. (1998). The Generation of Potassic Lavas from the Eastern Virunga Province, Rwanda. *Journal of Petrology*, vol. 39, 1223-1247.

Roksandic, M. M. (1987). The tectonics and evolution of the Hudson Bay region. In: *Sedimentary basins and basin-forming mechanisms, Atlantic Geoscience Society Special Publication* 5, 507-518.

Ropchan, J. C. (2000). Petrographic and geochemical studies of the alteration zones associated with gold mineralization at the Holloway Mine, southwestern Abitibi greenstone belt, Canada. *Unpublish M.Sc. thesis*, University of Ottawa, Ottawa, Ontario, 151pp.

Rowins, S. M. (1990). Mineralogy and geochemistry of the Murdock Creek intrusion, Kirkland Lake, Ontario. *Unpublish M.Sc. thesis*, University of Ottawa, Ottawa, Ontario, 196pp.

Rowins, S. M., Lalonde, A. E. & Cameron, E. M. (1989). Geology of the Archean Murdock Creek intrusion, Kirkland Lake, Ontario. In: *Geological Survey of Canada, Current Research Paper* 89-1C, Part C, 313-323.

Rowins, S. M., Lalonde, A. E. & Cameron, E. M. (1991). Magmatic oxidation in the syenitic Murdock Creek intrusion, Kirkland Lake, Ontario: evidence from the ferromagnesian minerals. *Journal of Geology*, vol. 99, 395-414.

Rowins, S. M., Cameron, E. M, Lalonde, A. E. & Ernst, R. E. (1993). Petrogenesis of the late Archean syenitic Murdock Creek pluton, Kirkland Lake, Ontario: evidence for an extensional tectonic setting. *Canadian Mineralogist*, vol. 31, 219-244.

Sabine, P. A. (1950). The optical properties and composition of acmitic pyroxenes. *Mineralogical Magazine*, vol. 29, 113-125.

Sanford, B. V., Norris, A. W. & Bostock, H. H. (1968). Geology of the Hudson Bay Lowlands. *Geological Survey of Canada, Paper* 78-10.

Satterly, J. (1947). Township of Michaud, District of Cochrane. *Ontario Department of Mines, Map No.* 1947-3, scale 1:12 000.

Satterly, J. (1949). Township of Garrison, District of Cochrane. *Ontario Department of Mines, Map No.* 1949-1, scale 1:12 000.

Shaw, C. S. J. (1996). The petrology and petrogenesis of Roman province-type lavas and ultrapotassic leucitites. In: *Undersaturated Alkaline Rocks: Minerology, Petrogenesis, and Economic Potential. Mineralogical Association of Canada, Short Course Series* 24, 193-216.

Shaw, D. M. (1968). A review of K-Rb fractionation trends by covariance analysis. *Geochimica et Cosmochimica Acta*, vol. 32, 573-601.

Singer, B. S., Myers, J. D. & Frost, C. D. (1992). Mid-Pleistocene lavas from the Seguam volcanic center, central Aleutian arc: closed-system fractional crystallization of basalt to rhyodacite eruptive suite. *Contribution to Mineralogy and Petrology*, vol. 110, 87-112.

Smith, A. R. & Sutcliffe, R. H. (1988). Plutonic rocks of the Abitibi subprovince, In: *Project 88-08, Ontario Geological Survey, Miscellaneous Paper* 141, 188-196.

Smith, D. & Lindsley, D. H. (1971). Chemical variations in pyroxenes and olivine from Picture Gorge basalt. *Carnegie Institution of Washington, Yearbook* 69, 269-274.

Smith, J. V. & Brown, W. L. (1988). *Feldspar Minerals*, Springer-Verlag, Berlin, 828 pp.

Stephenson, D. (1972). Alkali clinopyroxenes from the nepheline syenites of the South Qâroq centre, south Greenland. *Lithos*, vol. 5, 187-201.

Stollery, G., Borcsik, M. & Holland, H. D. (1971). Chlorine in intrusives: a possible prospecting tool. *Economic Geology*, vol. 66, 361-367.

Stolz, A. J., Varne, R., Wheller, G. E., Foden, J. D. & Abbott, M. J. (1988). The geochemistry and petrogenesis of K-rich alkaline volcanics from the Batu Tara volcano, eastern Sunda arc. *Contributions to Mineralogy and Petrology*, vol. 98, 374-389.

Streckeisen, A. (1976). To each plutonic rock its proper name. *Earth Science Review*, vol. 12, 1-33.

Sutcliffe, R. H., Smith, A. R., Doherty, W. & Barnett, R. L. (1990). Mantle derivation of Archean amphibole-bearing granitoid and associated mafic rocks: Evidence from the southern Superior province, Canada. *Contributions to mineralogy and petrology*, vol. 105, 255-274.

Taylor, J. K. (1987). *Quality Assurance of Chemical Measurements*. Lewis Publishers, Inc. Chelsea, Michigan.

Thirlwall, M. F. & Burnard, P. (1990). Pb-Sr-Nd isotope and chemical study of the origin of undersaturated and oversaturated shoshonitic magmas from the Borralan pluton, Assynt, NW Scotland. *Journal of the Geological Society, London*, vol. 147, 259-269.

Thompson, R. N. (1974). Some high-pressure pyroxenes. *Mineralogy Magazine*, vol. 39, 768-787.

Thompson, R. N. & Fowler, M. B. (1986). Subduction-related shoshonitic and ultrapotassic magmatism: a study of Siluro-Ordovician syenites from the Scottish Caledonides. *Contributions to Mineralogy and Petrology*, vol. 94, 507-522.

Thurston, P. C. (1991). Archean Geology of Ontario: Introduction. In: *Geology of Ontario, Ontario Geological Survey, Special Volume* 4, Part 1, 73-78.

Toogood, D. J. & Hodgson, C. J. (1986). Relationship between gold deposits and the tectonic framework of the Abitibi greenstone belt in the Kirkland Lake-Larder Lake area. In: *Geoscience Research Grant Program, Summary of the Research 1985-1986. Ontario Geological Survey, Miscellaneous Paper* 130, 79-86.

Troop, D. G. (1989). Geological investigations of the Destor-Porcupine Deformation Zone east of Matheson. In: *Summary of field work and other activities 1989, Ontario Geological Survey, Miscellaneous paper* 146, 136-143.

Troop, D. G. (1990). Gold mineralization and the Destor-Porcupine Deformation Zone east of Matheson - Investigations in Garrison Township. In: *Summary of field work and other activities 1990, Ontario Geological Survey, Miscellaneous paper* 151, 67-77.

Tracy, R. J. & Robinson, P. (1977). Zonal titanian augite in alkali olivine basalt from Tahiti and the nature of titanium substitutions in augite. *American Mineralogist*, vol. 62, 634-645.

Tyler, R. C. & King, B .C. (1967). The pyroxenes of the alkaline igneous complexes of eastern Uganda. *Mineralogical Magazine*, vol. 36, 5-21.

Ujike, O. (1985). Geochemistry of Archean alkalic volcanic rocks from the Crystal Lake area, east of Kirkland Lake, Ontario, Canada. *Earth and Planetary Science Letters*, vol. 73, 333-344.

Verhoogen, J. (1962). Distribution of titanium between silicates and oxides in igneous rocks. *American Journal of Science*, vol. 260, 211-220.

Voll, G. (1960). Recrystallization of quartz, biotite, and feldspars from Erstfeld to the Leventina Nappe, Swiss Alps, and its geological significance. *Schweizerische Mineralogische und Petrographische Mitteilungen*, vol. 56, 641-647.

Weill, D. F. & Drake, M. J. (1973). Europium anomaly in plagioclase feldspar: experimental results and semiquantitative model. *Science*, vol. 180, 1059-1060.

Wheller, G. E., Varne, R. & Foden, J. D. & Abbott, M. J. (1987). Geochemistry of Quaternary volcanism in the Sunda-Banda arc, Indonesia, and three-component genesis of island-arc basaltic magmas. *Journal of Volcanology and Geothermal Research*, vol. 32, 137-160.

Wilkinson, L., Cruden, A. & Krogh, T. E. (1999). Timing and kinematics of post-Timiskaming deformation within the Larder Lake-Cadillac deformation zone, southwest Abitibi greenstone belt, Ontario, Canada. *Canadian Journal of Earth Sciences*, vol. 36, 627-647.

Wolff, J. A. (1984). Variation in Nb/Ta during differentiation of phonolitic magma, Tenerife, Canary Islands. *Geochimica et Cosmochimica Acta*, vol. 48, 1345-1348.

Wood, B. J & Blundy, J. D. (2001). The effect of cation charge on crystal-melt partitioning of trace elements. *Earth and Planetary Science Letters*, vol. 188, 59-72.

Woolley, A. R. (1973). The pseudoleucite borolanites and associated rocks of the south-eastern tract of the Borralan Complex, Scotland. *Bulletin of the British Museum, Natural History (Mineralogy)*, vol. 2, 288-333.

Wörner, G., Beussen, J. M., Duchateau, N., Gijbels, R. & Schmincke, H. U. (1983). Trace element abundances and mineral/melt distribution coefficients in phonolites from the Laacher See Volcano (Germany). *Contributions to Mineralogy and Petrology*, vol. 84, 152-173.

Wyman, D. & Kerrich, R. (1988). Alkaline magmatism, major structures, and gold deposits: Implications for greenstone belt metallogeny. *Economic Geology*, vol. 83, 454-461.

Wyman, D. & Kerrich, R. (1989). Archean shoshonitic lamprophyres associated with Superior province gold deposits: distribution, tectonic setting, noble metal abundances, and significance for gold mineralization. *Economic Geology Monograph* 6, 651-667.

Wynne-Edwards, H. R. (1972). The Grenville Province. In: *Variations in tectonic styles in Canada. Geological Association of Canada, Special Paper* 11, 263-334.

Appendix 1

I. Whole-rock analyses
II. Mineral analyses
III. Sample location

I. Whole-rock analyses

	Emens											
Unit	B-Sye	B-Sye	B-Sye	B-Sye	B-Sye	B-Sye	B-Sye	B-Sye	B-Sye	B-Sye	B-Sye	M-Sye
Sample	083	084	157	159	171	173	175	176	177	178	043	045
SiO_2	50.80	52.88	50.21	47.11	48.98	48.83	53.43	50.11	47.50	49.78	45.09	39.85
TiO_2	1.08	0.87	0.64	0.92	0.92	0.83	0.91	0.84	0.87	0.76	2.03	1.28
Al_2O_3	15.43	14.80	13.92	12.93	16.87	16.62	17.43	16.89	16.58	16.78	17.73	7.25
Fe_2O_3	3.77	3.34	6.57	7.04	3.83	5.20	4.00	5.03	2.27	2.84	5.44	9.20
FeO	3.82	2.64	1.52	2.85	3.45	1.87	2.67	1.83	4.01	2.87	3.49	7.06
MnO	0.14	0.13	0.16	0.20	0.15	0.15	0.15	0.17	0.15	0.16	0.15	0.23
MgO	3.52	4.77	4.13	5.18	3.18	2.74	2.92	3.26	2.49	2.26	1.95	9.17
CaO	5.03	5.43	10.08	10.86	6.14	6.28	5.33	6.49	6.72	5.90	7.80	15.23
Na_2O	3.59	3.08	3.69	4.20	4.27	5.08	6.28	3.57	4.42	5.54	2.96	1.83
K_2O	7.39	8.20	5.11	3.70	5.69	4.90	3.30	5.79	5.94	4.95	5.90	3.11
BaO	0.22	0.22	0.33	0.19	0.19	0.19	0.12	0.21	0.20	0.20	>0.39	0.10
SrO	0.29	0.23	0.33	0.36	0.24	0.23	0.20	0.38	0.35	0.29	0.17	0.21
P_2O_5	0.31	0.53	0.61	0.93	0.47	0.43	0.44	0.41	0.40	0.35	0.32	2.19
CO_2	1.54	0.24	0.11	0.43	2.23	3.57	0.82	0.58	5.15	4.06	1.48	0.61
S	0.43	0.12	0.24	0.24	0.09	0.10	0.08	0.15	0.31	0.15	0.19	0.05
LOI	1.74	1.13	0.79	1.21	3.60	4.85	1.79	3.27	5.66	5.03	3.02	1.31
Total	97.13	98.24	98.09	97.68	97.97	98.20	98.97	98.25	97.56	97.71	96.43	98.02
Be (ppm)	*n.d.*	*n.d.*	*n.d.*	*n.d.*	5	5	3	5	5	7	4	4
Co	26	29	24	36	23	21	17	20	18	19	28	59
Cu	155	59	95	143	184	152	121	102	87	156	142	107
Mo	12	15	20	9	9	*n.d.*	9	8	10	*n.d.*	*n.d.*	*n.d.*
Ni	65	49	42	52	35	32	16	29	28	25	14	47
Sc	11	11	14	18	10	9	12	9	9	8	7	39
V	228	146	252	276	213	213	173	215	216	181	530	361
W	*n.d.*	*n.d.*	*n.d.*	*n.d.*	*n.d.*	*n.d.*	*n.d.*	*n.d.*	*n.d.*	*n.d.*	*n.d.*	*n.d.*
Zn	146	163	105	159	196	158	131	159	160	143	116	204
Ba	1935	1926	2960	1706	1663	1734	1089	1905	1770	1819	>3500	928
Cr	131	161	89	61	43	32	*n.d.*	27	27	25	12	46
Ga	20.14	22.90	16.48	18.70	20.84	21.98	25.11	22.06	23.18	22.00	21.63	16.68
Pb	12.26	9.76	10.22	7.24	10.92	13.86	20.25	10.78	18.22	17.78	5.34	9.84
Sn	*n.d.*	*n.d.*	*n.d.*	*n.d.*	*n.d.*	*n.d.*	*n.d.*	*n.d.*	*n.d.*	*n.d.*	4.8	*n.d.*
Rb	157.89	182.63	109.30	132.00	150.14	123.26	122.56	148.96	140.02	131.14	143.80	109.50
Sr	2481.8	1935.8	2811.4	3042.0	1988.3	1913.5	1674.0	3184.0	2989.3	2443.6	1395.8	1773.1
Nb	14.07	7.61	5.46	6.86	11.50	11.59	16.28	11.77	12.50	11.76	13.53	5.97
Cs	-	3.46	1.85	-	-	-	-	-	5.82	2.70	3.71	-
Hf	-	3.59	3.95	-	-	-	-	-	5.57	5.00	11.40	-
Ta	0.63	0.27	0.29	0.32	0.62	0.57	0.74	0.59	0.65	0.52	0.77	0.27
Th	7.11	8.00	7.09	6.78	8.45	10.33	12.94	9.32	11.93	11.57	10.60	9.15
U	-	1.67	1.03	-	-	-	-	-	1.93	2.93	3.95	-
Y	33.42	24.98	29.32	35.63	42.91	41.03	22.88	41.93	42.48	36.74	130.20	34.66
Zr	127.66	127.83	120.89	109.15	144.98	156.42	203.70	145.35	175.43	171.42	380.80	128.56
Au (ppb)	106	*n.d.*	*n.d.*	5	9	26	*n.d.*	7	6	17	*n.d.*	*n.d.*
Pt	*n.d.*	*n.d.*	*n.d.*	*n.d.*	*n.d.*	*n.d.*	*n.d.*	*n.d.*	*n.d.*	*n.d.*	*n.d.*	*n.d.*
Pd	*n.d.*	*n.d.*	*n.d.*	*n.d.*	*n.d.*	*n.d.*	*n.d.*	*n.d.*	*n.d.*	*n.d.*	*n.d.*	11.

continued

B-Sye Alkali-feldspar porphyritic biotite-syenite
M-Sye Melasyenite

	Emens							Pangea				
Unit	M-Sye	M-Sye	Sye	Sye	Sye	Sye	Sye	Hbdt	Hbdt	Hbdt	M-Sye	M-Sye
Sample	080	086	081	161	165	169	172	009	014	019	008	020
SiO_2	45.02	40.73	62.37	62.41	60.88	62.81	63.54	43.81	48.34	43.54	51.40	48.43
TiO_2	0.60	4.20	0.31	0.15	0.18	0.05	0.17	3.73	3.50	2.17	1.22	1.12
Al_2O_3	9.69	8.49	18.41	18.02	17.40	18.55	18.17	12.21	14.07	14.01	13.56	15.07
Fe_2O_3	3.07	13.96	1.22	0.76	1.02	0.87	0.87	8.37	4.75	7.04	6.13	5.90
FeO	4.84	5.71	0.80	0.26	1.22	0.49	0.47	11.84	3.26	9.92	4.38	3.67
MnO	0.13	0.27	0.03	0.01	0.06	0.02	0.04	0.25	0.13	0.23	0.23	0.18
MgO	16.67	4.91	0.46	0.25	1.60	0.26	0.56	6.04	2.14	6.05	3.20	3.08
CaO	7.81	10.13	1.00	1.13	1.77	0.70	1.71	7.96	7.66	9.94	8.25	7.87
Na_2O	1.76	3.38	4.33	3.26	3.78	3.65	6.25	1.85	2.45	2.93	3.71	2.51
K_2O	6.11	4.02	10.28	11.60	9.86	11.12	6.73	0.59	6.20	0.94	3.54	5.33
BaO	0.06	0.15	0.06	0.12	0.17	0.14	0.19	0.02	>0.39	0.02	0.23	>0.39
SrO	0.06	0.14	0.15	0.17	0.22	0.16	0.21	0.05	0.42	0.07	0.25	0.51
P_2O_5	0.29	0.85	0.02	0.01	0.11	0.01	0.04	0.48	0.26	0.18	0.53	0.55
CO_2	0.71	0.09	0.48	0.78	0.54	0.35	0.21	0.71	1.76	0.88	1.71	1.25
S	0.01	0.25	0.04	0.55	0.09	0.04	0.02	0.22	0.16	0.34	0.08	0.1
LOI	1.77	0.46	0.96	0.57	1.26	0.81	0.55	2.25	2.24	2.01	2.18	2.22
Total	97.87	97.40	100.40	98.72	99.53	99.64	99.50	99.46	95.42	99.05	98.81	96.44
Be (ppm)	*n.d.*	10	*n.d.*	*n.d.*	*n.d.*	*n.d.*	*n.d.*	3	4	3	5	4
Co	54	57	*n.d.*	*n.d.*	7	*n.d.*	*n.d.*	61	32	60	27	26
Cu	15	126	16	18	192	13	8	63	267	150	27	40
Mo	16	*n.d.*	13	10	11	13	13	*n.d.*	*n.d.*	*n.d.*	*n.d.*	9
Ni	429	36	*n.d.*	5	26	*n.d.*	9	63	16	123	16	17
Sc	23	40	*n.d.*	*n.d.*	4	*n.d.*	1	35	8	33	12	13
V	192	472	66	18	55	38	39	389	331	374	284	307
W	*n.d.*	*n.d.*	*n.d.*	*n.d.*	69	*n.d.*	*n.d.*	n.d.	n.d.	n.d.	n.d.	n.d.
Zn	117	230	29	22	65	23	30	221	114	193	236	146
Ba	514	1303	531	1067	1496	1249	1694	214	>3500	164	2045	>3500
Cr	>500	9	6	*n.d.*	35	5	14	26	*n.d.*	157	22	15
Ga	15.16	21.16	20.51	16.98	21.26	21.70	21.01	23.04	21.98	20.18	24.75	18.48
Pb	5.19	6.32	23.30	29.54	32.88	24.86	22.54	5.15	15.27	5.73	15.36	15.90
Sn	*n.d.*	4.8	*n.d.*	*n.d.*	*n.d.*	*n.d.*	*n.d.*	n.d.	5.8	*n.d.*	4.8	*n.d.*
Rb	236.62	138.98	164.54	172.35	157.12	203.96	104.81	16.63	91.62	26.75	51.75	75.80
Sr	466.6	1225.0	1277.4	1419.2	1889.3	1385.3	1745.3	448.8	3519.0	630.3	2141.3	4336.0
Nb	3.77	50.84	8.49	4.83	1.76	1.51	3.66	14.64	73.20	7.17	18.12	16.48
Cs	-	-	-	-	-	-	-	1.08	-	1.82	-	-
Hf	-	-	-	-	-	-	-	4.56	-	2.60	-	-
Ta	0.18	2.58	0.36	0.22	0.07	0.06	0.17	0.80	5.52	0.40	1.23	0.85
Th	5.19	18.55	7.34	2.93	2.30	7.54	1.95	0.93	13.43	2.17	17.04	9.28
U	-	-	-	-	-	-	-	0.24	-	0.70	-	-
Y	12.93	106.87	10.06	3.40	5.97	3.16	8.71	56.56	99.70	32.94	68.17	49.63
Zr	75.13	366.03	126.27	45.33	69.54	100.84	68.85	150.06	376.83	92.35	295.45	168.98
Au (ppb)	*n.d.*	*n.d.*	*n.d.*	*n.d.*	10	*n.d.*	*n.d.*	n.d.	n.d.	n.d.	n.d.	n.d.
Pt	*n.d.*	*n.d.*	*n.d.*	*n.d.*	*n.d.*	*n.d.*	*n.d.*	n.d.	9	*n.d.*	*n.d.*	*n.d.*
Pd	*n.d.*	*n.d.*	*n.d.*	*n.d.*	*n.d.*	*n.d.*	*n.d.*	n.d.	n.d.	n.d.	n.d.	n.d.

continued

M-Sye Melasyenite
Hbdt Pyroxene-bearing hornblendite
Sye Alkali-feldspar syenite

Pangea

Unit	M-Sye	Diorite	M-Sye	M-Sye	M-Sye	M-Sye	M-Sye	M-Sye	M-Sye	M-Sye	Sye	Sye	Sye
Sample	035	051	056	059	180	183	186	191	195	196	050	053B	193
SiO_2	46.42	48.66	42.24	45.78	48.88	49.42	51.28	52.20	54.04	48.59	53.88	65.15	57.26
TiO_2	1.39	1.05	1.09	1.69	1.25	0.82	1.18	0.71	0.83	0.81	1.00	0.39	0.37
Al_2O_3	9.52	17.57	13.39	16.88	15.31	13.90	15.61	15.00	13.69	13.17	17.10	15.64	17.71
Fe_2O_3	3.82	5.57	6.59	5.76	6.13	5.37	4.88	1.83	3.96	3.47	2.66	1.19	0.99
FeO	5.81	3.12	5.31	3.05	3.72	3.23	4.14	5.99	4.58	4.24	1.79	0.87	2.45
MnO	0.18	0.15	0.20	0.16	0.19	0.22	0.20	0.18	0.24	0.15	0.07	0.04	0.10
MgO	9.44	2.84	4.69	1.54	3.41	3.98	3.07	6.65	3.13	3.68	1.01	0.79	0.87
CaO	11.40	6.85	8.59	5.91	7.68	9.82	7.01	9.63	7.35	8.51	4.08	3.11	3.59
Na_2O	1.41	2.06	3.95	2.72	3.96	3.34	4.40	2.41	5.03	4.48	2.52	6.20	5.05
K_2O	4.66	6.63	4.42	7.11	4.12	4.34	3.91	2.65	3.07	3.63	9.27	2.19	6.64
BaO	0.20	0.29	0.13	0.25	0.17	0.18	0.23	0.05	0.32	0.21	>0.39	0.09	0.15
SrO	0.16	0.64	0.16	0.30	0.20	0.25	0.23	0.05	0.26	0.38	0.32	0.06	0.23
P_2O_5	0.79	0.37	1.01	0.30	0.58	0.80	0.41	0.06	0.80	0.82	0.12	0.23	0.16
CO_2	2.57	0.63	5.47	4.37	1.25	1.18	1.2	0.37	0.91	4.47	1.7	2.22	2.07
S	0.03	0.11	1.02	0.58	0.22	0.23	0.52	*n.d.*	0.87	0.04	0.12	0.35	0.02
LOI	3.71	1.78	5.07	4.80	2.88	2.48	1.74	1.86	0.78	5.92	2.42	2.99	3.18
Total	98.91	97.58	96.84	96.25	98.48	98.15	98.29	99.27	98.08	98.06	96.24	98.94	98.75
Be (ppm)	*n.d.*	4	5	4	4	4	5	*n.d.*	7	5	*n.d.*	*n.d.*	6
Co	55	28	38	30	26	26	30	41	27	25	15	8	7
Cu	64	32	188	270	159	50	127	11	378	106	96	12	59
Mo	*n.d.*	*n.d.*	*n.d.*	*n.d.*	9	8	9	8	8	*n.d.*	*n.d.*	10	9
Ni	61	23	22	11	30	45	39	89	24	26	11	15	9
Sc	33	9	21	6	13	15	13	30	13	14	4	4	2
V	252	277	308	358	314	276	261	236	200	206	160	46	106
W	*n.d.*	*n.d.*	*n.d.*	*n.d.*	*n.d.*	*n.d.*	*n.d.*	*n.d.*	*n.d.*	*n.d.*	*n.d.*	*n.d.*	*n.d.*
Zn	174	163	209	162	139	583	157	69	192	139	119	31	120
Ba	1774	2596	1176	2242	1482	1656	2064	436	2856	1845	>3500	832	1346
Cr	156	40	8	7	19	49	63	188	37	17	19	43	2
Ga	18.23	23.86	22.48	20.34	25.35	24.41	24.16	16.92	23.96	25.22	18.04	20.15	33.20
Pb	7.80	20.04	27.67	29.32	22.09	116.46	19.75	2.67	11.46	17.30	38.23	10.45	60.35
Sn	*n.d.*	3.3	*n.d.*	4.3	*n.d.*	*n.d.*	*n.d.*	*n.d.*	*n.d.*	*n.d.*	3.7	*n.d.*	*n.d.*
Rb	141.40	92.81	112.70	139.38	62.98	70.10	55.94	103.71	84.33	103.65	108.05	87.62	136.05
Sr	1340.6	5403.0	1346.1	2564.5	1702.2	2078.2	1946.0	451.1	2212.6	3207.0	2717.0	521.5	1934.6
Nb	8.38	17.82	8.40	29.44	13.11	9.77	14.20	2.19	13.58	15.83	23.76	9.15	31.86
Cs	-	-	-	-	1.54	-	1.14	-	-	-	-	-	1.24
Hf	-	-	-	-	8.67	-	8.57	-	-	-	-	-	9.94
Ta	0.38	0.79	0.25	1.56	0.68	0.46	0.77	0.13	0.49	0.54	1.31	0.54	0.75
Th	6.52	8.96	10.71	12.53	16.54	11.11	15.50	0.50	20.51	20.45	9.96	13.14	38.10
U	-	-	-	-	3.74	-	3.76	-	-	-	-	-	9.20
Y	27.39	51.77	37.76	88.87	48.69	42.09	49.25	16.07	46.07	48.58	47.06	14.13	34.16
Zr	124.63	211.79	218.53	335.83	299.08	163.18	287.44	54.58	336.52	346.41	181.35	204.82	431.09
Au (ppb)	*n.d.*	*n.d.*	719	5	*n.d.*	*n.d.*	*n.d.*	*n.d.*	9	*n.d.*	*n.d.*	9	*n.d.*
Pt	*n.d.*	*n.d.*	8	*n.d.*	*n.d.*	*n.d.*	*n.d.*	*n.d.*	*n.d.*	*n.d.*	*n.d.*	*n.d.*	*n.d.*
Pd	*n.d.*	*n.d.*	*n.d.*	*n.d.*	*n.d.*	*n.d.*	*n.d.*	*n.d.*	*n.d.*	*n.d.*	*n.d.*	*n.d.*	*n.d.*

continued

M-Sye Melasyenite
Sye Alkali-feldspar syenite

Iris

Unit	A-Sye	A-Sye	A-Sye	A-Sye	Monzo	Monzo	Monzo	Monzo	MD	MD	Hbdt	Hbdt	Hbdt
Sample	069	118	131	153	076	142	149	198	125	133	068	126	128
SiO_2	56.06	62.36	62.02	62.77	65.07	61.09	61.16	61.24	49.93	48.42	39.39	39.93	38.23
TiO_2	0.79	0.29	0.31	0.25	0.37	0.66	0.56	0.43	1.11	2.83	1.52	1.63	2.02
Al_2O_3	18.03	18.18	17.85	18.02	16.16	16.04	16.71	17.06	15.29	12.78	6.64	7.25	9.58
Fe_2O_3	4.01	1.85	1.87	1.36	2.30	3.54	3.54	2.93	5.77	6.13	11.49	11.14	9.89
FeO	1.94	0.80	0.86	0.81	1.45	2.38	2.30	1.75	5.32	8.44	8.54	8.91	9.74
MnO	0.13	0.03	0.03	0.04	0.06	0.10	0.08	0.09	0.20	0.30	0.26	0.27	0.28
MgO	1.52	0.48	0.50	0.40	1.01	1.69	1.92	1.36	4.76	4.94	9.45	9.71	10.19
CaO	5.05	1.58	2.03	1.55	3.80	3.71	4.74	2.40	7.86	9.85	15.62	14.77	12.81
Na_2O	5.95	8.29	8.41	7.79	7.13	6.89	4.74	7.49	3.51	2.62	1.43	1.62	2.15
K_2O	3.47	3.37	2.94	4.19	0.49	1.18	1.86	1.53	3.58	0.64	1.04	0.70	0.99
BaO	0.15	0.12	0.11	0.10	0.03	0.06	0.09	0.14	0.10	0.04	0.06	0.03	0.04
SrO	0.26	0.11	0.12	0.08	0.06	0.06	0.10	0.08	0.12	0.03	0.07	0.05	0.07
P_2O_5	0.22	0.06	0.06	0.05	0.12	0.18	0.23	0.15	0.50	0.30	1.90	1.13	1.17
CO_2	0.14	0.77	1.19	0.87	0.30	0.64	0.06	1.19	0.10	0.29	0.47	1.29	1.14
S	*n.d.*	0.01	*n.d.*	0.01	0.18	0.07	0.01	0.04	0.01	0.22	0.01	0.01	0.01
LOI	0.95	1.32	1.79	1.44	1.11	1.44	1.26	2.52	1.36	1.67	1.46	2.03	1.93
Total	98.52	98.84	98.90	98.85	99.16	99.02	99.29	99.17	99.42	98.99	98.87	99.18	99.09
Be (ppm)	*n.d.*	*n.d.*	*n.d.*	*n.d.*	*n.d.*	*n.d.*	*n.d.*	*n.d.*	3	4	3	4	4
Co	11	*n.d.*	*n.d.*	*n.d.*	5	10	13	8	36	52	64	59	62
Cu	6	*n.d.*	15	7	22	15	30	23	135	87	25	35	25
Mo	10	15	*n.d.*	*n.d.*	14	*n.d.*	*n.d.*	9	10	*n.d.*	*n.d.*	*n.d.*	*n.d.*
Ni	9	7	7	*n.d.*	9	13	15	12	30	78	56	60	59
Sc	6	2	2	2	5	8	8	6	25	36	43	48	55
V	130	50	49	47	63	105	126	98	288	500	465	538	529
W	*n.d.*	*n.d.*	*n.d.*	*n.d.*	*n.d.*	*n.d.*	*n.d.*	*n.d.*	*n.d.*	*n.d.*	*n.d.*	*n.d.*	*n.d.*
Zn	80	33	37	33	36	61	64	71	144	198	193	172	196
Ba	1318	1061	1024	930	288	516	811	1219	930	345	547	283	371
Cr	11	3	*n.d.*	*n.d.*	39	3	4	12	12	66	19	53	54
Ga	22.85	18.12	17.96	22.01	19.05	20.78	20.46	21.07	22.23	20.25	18.45	19.22	20.20
Pb	21.18	14.17	11.86	17.24	5.86	5.04	5.59	6.62	11.35	6.99	4.00	3.54	3.78
Sn	*n.d.*	*n.d.*	*n.d.*	*n.d.*	*n.d.*	*n.d.*	*n.d.*	*n.d.*	*n.d.*	*n.d.*	*n.d.*	*n.d.*	*n.d.*
Rb	62.21	38.31	36.55	76.07	9.10	25.06	36.40	30.98	102.30	14.32	22.58	15.28	9.93
Sr	2161.5	961.0	1012.7	653.6	477.1	545.0	811.7	706.9	1043.7	258.8	591.0	454.2	577.2
Nb	13.87	5.94	6.19	6.40	7.96	10.92	8.60	6.50	7.71	4.57	2.58	3.29	5.06
Cs	0.28	0.25	-	0.35	-	-	0.25	-	0.83	-	0.18	0.33	-
Hf	5.38	1.71	-	4.21	-	-	5.52	-	4.96	-	3.46	3.75	-
Ta	0.88	0.70	0.31	0.30	0.46	0.63	0.55	0.33	0.40	0.28	0.12	0.13	0.21
Th	8.57	2.78	2.93	7.92	6.35	6.34	6.82	6.12	7.87	0.45	4.06	2.69	2.20
U	1.74	0.85	-	2.18	-	-	1.05	-	1.96	-	1.02	0.72	-
Y	52.32	13.19	17.12	17.09	35.11	55.60	40.18	21.34	38.73	40.36	44.18	41.83	48.61
Zr	177.37	61.74	70.53	210.74	181.20	219.80	177.54	147.10	166.32	89.59	97.31	100.70	95.70
Au (ppb)	*n.d.*	*n.d.*	*n.d.*	*n.d.*	*n.d.*	*n.d.*	*n.d.*	9	*n.d.*	*n.d.*	*n.d.*	*n.d.*	*n.d.*
Pt	*n.d.*	*n.d.*	*n.d.*	*n.d.*	*n.d.*	*n.d.*	*n.d.*	*n.d.*	*n.d.*	*n.d.*	68	45	19
Pd	*n.d.*	*n.d.*	*n.d.*	*n.d.*	*n.d.*	*n.d.*	*n.d.*	*n.d.*	*n.d.*	*n.d.*	67	17	17

continued

A-Sye Antiperthite syenite
Monzo Monzonite
MD Monzodiorite
Hbdt Pyroxene-bearing hornblendite

Iris

Unit	Hbdt	Hbdt	Hbdt	P-Sye	P-Sye	P-Sye	Q-Sye	Q-Sye	Q-Sye	Q-Sye	Q-Sye	Q-Sye
Sample	129	151	154	116	120	121	103	104	105	106	107	108
SiO_2	41.09	50.17	39.35	64.96	65.67	65.09	67.01	65.02	66.00	67.24	65.87	66.31
TiO_2	1.72	0.99	1.88	0.26	0.25	0.25	0.09	0.21	0.12	0.13	0.14	0.12
Al_2O_3	9.55	5.96	9.70	17.86	17.80	17.42	18.23	17.02	18.16	18.24	18.59	18.09
Fe_2O_3	10.59	4.45	10.20	1.40	1.50	1.39	1.16	1.81	1.69	1.48	1.26	1.12
FeO	8.17	7.20	8.97	0.60	0.40	0.62	0.23	0.73	0.40	0.00	0.32	0.25
MnO	0.32	0.28	0.28	0.04	0.03	0.05	0.01	0.05	0.02	*n.d.*	0.02	0.01
MgO	8.54	10.42	9.81	0.42	0.30	0.43	0.14	0.47	0.29	0.12	0.22	0.15
CaO	12.70	16.77	13.47	1.01	0.57	1.22	0.34	1.45	0.19	0.12	0.36	0.16
Na_2O	2.64	1.67	1.85	8.42	9.74	8.95	10.42	9.71	10.79	10.82	9.54	9.38
K_2O	0.98	0.16	1.11	3.17	1.60	2.02	0.96	0.72	0.33	0.39	2.43	2.60
BaO	0.05	0.01	0.05	0.12	0.11	0.12	0.12	0.09	0.07	0.12	0.12	0.11
SrO	0.07	0.02	0.09	0.08	0.07	0.07	0.05	0.06	0.05	0.05	0.07	0.06
P_2O_5	1.33	0.08	0.68	0.07	0.06	0.07	0.02	0.08	0.02	0.01	0.03	0.01
CO_2	0.45	0.85	0.16	0.42	0.22	0.70	0.18	0.88	0.04	0.03	0.10	*n.d.*
S	0.01	0.04	0.01	0.02	0.04	0.06	0.06	0.02	0.01	0.16	0.02	0.01
LOI	1.36	1.44	1.01	1.07	0.81	1.35	0.60	1.50	0.57	0.78	0.55	0.50
Total	99.11	99.61	98.45	99.48	98.91	99.05	99.38	98.92	98.70	99.50	99.52	98.87
Be (ppm)	4	*n.d.*	4	*n.d.*	*n.d.*	*n.d.*	*n.d.*	*n.d.*	*n.d.*	*n.d.*	*n.d.*	*n.d.*
Co	59	47	65	*n.d.*	*n.d.*	*n.d.*	*n.d.*	*n.d.*	*n.d.*	*n.d.*	*n.d.*	*n.d.*
Cu	7	7	24	8	6	9	*n.d.*	17	8	6	9	6
Mo	*n.d.*	*n.d.*	*n.d.*	14	15	15	17	16	17	17	17	16
Ni	49	61	63	5	6	6	0	6	6	0	5	0
Sc	42	63	52	2	2	2	*n.d.*	2	1	*n.d.*	*n.d.*	*n.d.*
V	468	336	522	33	45	39	27	63	52	12	26	24
W	*n.d.*	*n.d.*	*n.d.*	*n.d.*	*n.d.*	*n.d.*	*n.d.*	*n.d.*	*n.d.*	*n.d.*	*n.d.*	*n.d.*
Zn	205	132	188	31	22	31	11	28	20	10	18	13
Ba	407	45	463	1065	1008	1095	1072	842	614	1117	1072	994
Cr	7	62	56	7	2	4	*n.d.*	2	1	*n.d.*	*n.d.*	*n.d.*
Ga	22.45	12.44	21.19	20.99	22.63	21.06	23.51	21.39	24.26	23.43	23.11	23.16
Pb	5.69	1.16	3.73	12.84	7.65	6.32	4.41	5.10	3.75	40.44	12.00	6.34
Sn	*n.d.*	*n.d.*	*n.d.*	*n.d.*	*n.d.*	*n.d.*	*n.d.*	*n.d.*	*n.d.*	*n.d.*	*n.d.*	*n.d.*
Rb	15.48	1.99	17.10	34.02	17.51	21.61	10.72	7.33	3.99	4.28	28.94	26.62
Sr	630.4	130.1	718.5	662.4	549.8	574.1	437.4	506.2	449.2	404.9	622.6	526.2
Nb	8.53	1.98	5.21	6.50	6.24	6.68	2.45	4.74	2.48	5.11	4.59	4.22
Cs	0.11	-	0.10	0.13	0.10	0.13	-	0.07	-	-	0.14	0.17
Hf	5.58	-	3.91	1.79	2.62	2.54	-	4.01	-	-	2.96	3.49
Ta	0.36	0.14	0.24	0.30	0.30	0.30	0.10	0.23	0.13	0.20	0.16	0.14
Th	5.06	0.89	2.46	2.44	4.50	4.26	6.52	5.00	3.06	3.58	5.59	6.33
U	1.17	-	0.60	0.81	1.47	1.63	-	1.51	-	-	2.02	2.81
Y	63.09	36.70	43.88	14.32	13.74	13.24	5.23	11.83	4.46	4.29	8.92	6.57
Zr	157.70	78.03	108.60	61.39	102.30	95.23	91.40	176.61	70.24	94.27	117.70	121.70
Au (ppb)	*n.d.*	*n.d.*	*n.d.*	*n.d.*	72	31	198	14	31	595	*n.d.*	6
Pt	11	*n.d.*	21	*n.d.*	*n.d.*	*n.d.*	*n.d.*	*n.d.*	*n.d.*	*n.d.*	*n.d.*	*n.d.*
Pd	8	*n.d.*	19	*n.d.*	*n.d.*	*n.d.*	*n.d.*	*n.d.*	*n.d.*	*n.d.*	*n.d.*	*n.d.*

continued

Hbdt Pyroxene-bearing hornblendite
P-Sye Alkali-feldspar porphyritic syenite
Sye Alkali-feldspar syenite

Iris

Unit	Q-Sye	Q-Sye	Q-Sye	Q-Sye	Q-Sye	Q-Sye	Q-Sye	Q-Sye	Q-Sye	Q-Sye	Q-Sye	Q-Sye
Sample	109	110	111	112	113	114	115	117	119	122	123	124
SiO_2	65.49	65.50	65.49	65.47	66.96	65.82	65.84	66.64	66.04	66.85	66.92	66.25
TiO_2	0.31	0.15	0.16	0.22	0.13	0.11	0.10	0.05	0.14	0.10	0.10	0.11
Al_2O_3	17.86	18.06	18.15	17.89	18.36	18.58	18.26	18.03	18.37	18.01	18.27	18.33
Fe_2O_3	3.44	1.12	1.44	1.49	1.04	0.92	1.07	0.97	1.48	0.94	0.96	1.28
FeO	0.23	0.26	0.27	0.46	0.24	0.30	0.32	0.23	0.00	0.23	0.24	0.24
MnO	0.01	0.01	0.02	0.02	0.01	0.01	0.01	*n.d.*	*n.d.*	0.02	*n.d.*	0.01
MgO	0.05	0.16	0.20	0.35	0.12	0.20	0.15	0.11	0.13	0.14	0.09	0.16
CaO	0.10	0.20	0.47	0.18	0.17	0.25	0.25	0.13	0.13	0.15	0.14	0.17
Na_2O	10.96	8.45	10.10	8.62	10.39	10.27	8.76	9.78	10.90	10.33	10.72	9.51
K_2O	0.15	3.79	1.54	3.28	1.23	1.58	3.61	1.97	0.58	1.13	0.62	2.44
BaO	0.07	0.12	0.11	0.09	0.12	0.10	0.10	0.11	0.07	0.12	0.09	0.07
SrO	0.01	0.07	0.05	0.05	0.06	0.05	0.07	0.05	0.04	0.05	0.06	0.05
P_2O_5	0.01	0.03	0.04	0.04	0.02	0.02	0.01	0.01	0.01	0.01	0.01	0.02
CO_2	0.06	0.05	0.25	0.04	0.09	0.12	0.08	0.10	0.06	0.03	0.06	0.09
S	0.31	0.01	0.08	0.11	0.06	0.15	0.02	0.13	0.32	0.15	0.06	0.01
LOI	0.64	0.60	0.71	0.74	0.53	0.67	0.54	0.70	0.84	0.58	0.52	0.58
Total	99.33	98.52	98.75	98.90	99.39	98.88	99.09	98.77	98.73	98.66	98.74	99.22
Be (ppm)	4	*n.d.*	*n.d.*	*n.d.*	*n.d.*	*n.d.*	*n.d.*	*n.d.*	*n.d.*	*n.d.*	*n.d.*	*n.d.*
Co	*n.d.*	*n.d.*	*n.d.*	*n.d.*	*n.d.*	*n.d.*	*n.d.*	*n.d.*	*n.d.*	*n.d.*	*n.d.*	*n.d.*
Cu	19	12	11	*n.d.*	6	20	*n.d.*	7	10	7	9	*n.d.*
Mo	14	15	15	13	14	15	15	16	17	16	18	17
Ni	0	0	0	0	0	0	0	0	0	0	0	5
Sc	*n.d.*	*n.d.*	*n.d.*	*n.d.*	*n.d.*	*n.d.*	*n.d.*	*n.d.*	*n.d.*	*n.d.*	*n.d.*	*n.d.*
V	96	21	32	36	22	15	21	11	13	16	19	34
W	*n.d.*	*n.d.*	*n.d.*	*n.d.*	*n.d.*	*n.d.*	*n.d.*	*n.d.*	*n.d.*	*n.d.*	*n.d.*	*n.d.*
Zn	11	15	17	25	11	14	15	12	12	12	10	15
Ba	617	1052	966	794	1097	857	920	958	636	1089	806	665
Cr	*n.d.*	*n.d.*	1	*n.d.*	*n.d.*	*n.d.*	*n.d.*	*n.d.*	*n.d.*	*n.d.*	*n.d.*	2
Ga	41.17	22.59	24.81	24.28	22.91	22.97	21.66	22.34	23.42	21.93	22.88	23.72
Pb	14.29	6.47	7.80	10.97	4.43	6.19	11.51	6.97	7.10	4.56	3.71	5.00
Sn	*n.d.*	*n.d.*	*n.d.*	*n.d.*	*n.d.*	*n.d.*	*n.d.*	*n.d.*	*n.d.*	*n.d.*	*n.d.*	*n.d.*
Rb	1.13	40.49	17.29	40.62	13.78	18.11	43.65	22.75	4.80	11.71	5.46	29.08
Sr	109.9	583.1	435.5	416.6	529.8	442.9	560.1	390.7	361.1	437.4	480.8	403.6
Nb	8.41	3.81	6.46	6.02	3.67	3.24	3.16	1.92	3.59	2.27	2.39	3.81
Cs	-	0.20	-	-	0.14	-	-	0.13	-	-	-	-
Hf	-	2.80	-	-	3.03	-	-	2.12	-	-	-	-
Ta	0.49	0.17	0.22	0.26	0.15	0.12	0.11	0.05	0.51	0.11	0.10	0.14
Th	43.46	5.40	7.89	9.79	8.17	4.44	3.43	4.60	4.79	4.22	4.14	5.10
U	-	2.32	-	-	1.93	-	-	2.39	-	-	-	-
Y	24.95	7.21	9.82	10.80	6.30	5.88	6.08	4.63	6.01	4.23	4.01	7.78
Zr	706.07	106.03	133.24	205.26	94.74	85.52	74.72	92.17	105.17	69.69	73.02	126.14
Au (ppb)	598	6	44	247	15	809	106	626	80	256	571	141
Pt	*n.d.*	*n.d.*	*n.d.*	*n.d.*	*n.d.*	*n.d.*	*n.d.*	*n.d.*	*n.d.*	*n.d.*	*n.d.*	*n.d.*
Pd	*n.d.*	*n.d.*	*n.d.*	*n.d.*	*n.d.*	*n.d.*	*n.d.*	*n.d.*	*n.d.*	*n.d.*	*n.d.*	*n.d.*

continued

Q-Sye Alkali-feldspar quartz-syenite

	Iris		Ludgate		Garrison					
Unit	Q-Sye	Q-Sye	Q-Sye	Q-Sye	HQM	HQM	HQM	HQM	HQM	HQM
Sample	132	156	088	091	097	098	099	100	101	102
SiO_2	64.10	61.88	64.98	63.58	65.16	64.01	59.00	68.80	68.98	68.08
TiO_2	0.30	0.51	0.20	0.25	0.28	0.34	0.65	0.19	0.22	0.21
Al_2O_3	17.71	16.64	16.60	16.53	16.04	16.61	16.27	15.25	15.15	16.00
Fe_2O_3	1.66	2.80	1.34	1.51	1.66	1.63	3.77	1.12	1.29	1.15
FeO	0.83	1.69	0.31	0.48	1.11	1.36	2.62	0.45	0.53	0.62
MnO	0.04	0.07	0.03	0.05	0.05	0.05	0.14	0.03	0.03	0.03
MgO	0.70	1.01	0.57	1.03	1.12	1.24	2.11	0.57	0.68	0.74
CaO	1.33	2.34	1.37	2.06	1.72	2.54	5.57	1.21	1.26	1.29
Na_2O	8.22	7.76	7.83	8.33	5.81	5.59	5.31	5.57	5.63	5.79
K_2O	2.89	2.38	3.85	3.54	4.73	4.64	2.22	4.82	4.94	4.80
BaO	0.09	0.14	0.13	0.12	0.13	0.21	0.08	0.11	0.12	0.13
SrO	0.08	0.06	0.11	0.09	0.15	0.19	0.10	0.11	0.12	0.13
P_2O_5	0.06	0.15	0.08	0.09	0.17	0.18	0.26	0.08	0.11	0.12
CO_2	0.71	1.13	0.78	0.71	*n.d.*	0.04	0.29	*n.d.*	0.04	*n.d.*
S	0.02	0.01	0.08	0.05	0.02	*n.d.*	0.08	*n.d.*	*n.d.*	*n.d.*
LOI	1.44	1.77	1.32	1.13	0.52	0.38	1.05	0.44	0.41	0.49
Total	99.44	99.20	98.72	98.79	98.65	98.96	99.15	98.76	99.46	99.58
Be (ppm)	*n.d.*	*n.d.*	*n.d.*	3	4	*n.d.*	*n.d.*	*n.d.*	4	4
Co	*n.d.*	8	*n.d.*	*n.d.*	5	7	16	*n.d.*	*n.d.*	*n.d.*
Cu	54	6	11	14	7	9	15	*n.d.*	5	15
Mo	13	9	16	16	18	14	13	15	15	15
Ni	5	12	11	16	16	16	17	7	9	12
Sc	2	5	2	3	4	4	11	2	2	3
V	55	115	42	68	50	48	137	27	33	31
W	*n.d.*	*n.d.*	*n.d.*	*n.d.*	*n.d.*	*n.d.*	*n.d.*	*n.d.*	*n.d.*	*n.d.*
Zn	37	75	35	61	75	57	76	45	54	49
Ba	779	1248	1204	1070	1173	1856	758	1015	1045	1130
Cr	12	13	20	24	30	49	11	9	12	11
Ga	18.30	22.77	25.34	25.23	21.26	20.78	21.68	19.45	20.02	20.58
Pb	8.47	9.16	16.17	13.73	115.25	22.76	5.67	33.75	34.76	32.06
Sn	*n.d.*	*n.d.*	*n.d.*	*n.d.*	*n.d.*	*n.d.*	*n.d.*	3.4	*n.d.*	*n.d.*
Rb	47.83	37.55	66.10	64.53	131.25	119.83	38.24	117.18	147.92	153.60
Sr	650.2	535.7	894.2	778.9	1252.7	1579.3	815.5	966.6	991.8	1127.3
Nb	6.54	11.37	6.79	6.08	10.13	9.60	9.35	6.63	8.41	8.61
Cs	-	-	0.48	0.47	2.40	1.39	-	-	-	2.39
Hf	-	-	3.51	1.54	6.53	5.72	-	-	-	5.18
Ta	0.35	0.65	0.34	0.23	0.63	0.60	0.54	0.42	0.52	0.53
Th	5.37	5.74	5.48	1.58	11.30	5.80	7.83	6.67	10.69	11.07
U	-	-	1.49	0.63	2.08	1.53	-	-	-	1.88
Y	16.87	52.70	9.18	8.58	13.46	15.12	44.10	6.31	7.75	9.53
Zr	106.36	240.22	114.79	43.36	234.48	216.78	187.95	146.00	165.51	180.82
Au (ppb)	*n.d.*	*n.d.*	*n.d.*	*n.d.*	5	*n.d.*	*n.d.*	*n.d.*	*n.d.*	*n.d.*
Pt	*n.d.*	*n.d.*	*n.d.*	*n.d.*	*n.d.*	*n.d.*	*n.d.*	*n.d.*	*n.d.*	*n.d.*
Pd	*n.d.*	*n.d.*	*n.d.*	*n.d.*	*n.d.*	*n.d.*	*n.d.*	*n.d.*	*n.d.*	*n.d.*

Q-Sye Alkali-feldspar quartz-syenite
HQM Hornblende quartz-monzonite

II. Mineral analyses

A. Pyroxene

	Emens			Pangea			Iris					
Unit	M-Sye	M-Sye	M-Sye	M-Sye	Hbdt	Hbdt	A-Sye	A-Sye	A-Sye	A-Sye	MD	MD
Sample	45-11	45-31	86-31	008-31	26-11	26-31	69-11	69-12	69-21	69-33	125-11	125-12
SiO_2	53.24	53.11	52.89	51.30	51.28	51.50	50.68	50.99	51.89	51.33	51.35	50.62
TiO_2	0.03	0.04	0.06	0.19	0.54	0.54	0.51	0.37	0.33	0.35	0.35	0.59
Al_2O_3	1.37	1.35	1.01	1.50	2.08	2.19	2.69	2.38	1.72	1.66	3.06	3.24
Cr_2O_3	0.02	0.00	0.00	0.00	0.00	0.00	0.01	0.00	0.00	0.00	0.04	0.00
MgO	6.67	7.11	5.23	11.14	15.17	14.97	11.75	11.69	12.47	12.33	12.98	14.19
CaO	11.02	11.56	8.88	22.99	23.98	23.99	22.14	21.98	22.63	22.43	22.41	23.13
MnO	0.16	0.21	0.23	0.66	0.12	0.14	0.66	0.69	0.78	0.84	0.35	0.17
FeO	0.98	2.24	1.97	8.56	2.75	3.24	6.27	5.87	6.71	6.12	6.49	4.42
Fe_2O_3	19.22	16.60	21.43	2.67	3.60	3.32	4.06	4.93	3.01	4.01	2.11	3.29
NaO	7.90	7.26	8.74	0.74	0.27	0.28	1.09	1.25	0.97	0.98	0.70	0.33
K_2O	0.02	0.03	0.03	0.00	0.01	0.00	0.00	0.00	0.01	0.01	0.00	0.01
Total	100.63	99.51	100.47	99.75	99.80	100.17	99.86	100.15	100.52	100.06	99.84	99.99
Chemical folmulae calculated based on 4 cations												
Si^{4+}	1.983	1.997	1.988	1.943	1.898	1.901	1.904	1.912	1.932	1.924	1.915	1.879
Al^{3+}	0.017	0.003	0.012	0.057	0.091	0.095	0.096	0.088	0.068	0.073	0.085	0.121
Fe^{3+}	0.000	0.000	0.000	0.000	0.011	0.004	0.000	0.000	0.000	0.003	0.000	0.000
Sum T	2.000	2.000	2.000	2.000	2.000	2.000	2.000	2.000	2.000	2.000	2.000	2.000
Al^{3+}	0.043	0.057	0.033	0.010	0.000	0.000	0.023	0.017	0.007	0.000	0.049	0.021
Fe^{3+}	0.539	0.470	0.606	0.076	0.089	0.088	0.115	0.139	0.084	0.110	0.059	0.092
Ti^{4+}	0.001	0.001	0.002	0.005	0.015	0.015	0.014	0.010	0.009	0.010	0.010	0.016
Cr^{3+}	0.001	0.000	0.000	0.000	0.000	0.000	0.000	0.000	0.000	0.000	0.001	0.000
Mg^{2+}	0.370	0.399	0.293	0.629	0.837	0.824	0.658	0.653	0.692	0.689	0.721	0.785
Fe^{2+}	0.030	0.070	0.062	0.271	0.059	0.073	0.190	0.181	0.208	0.191	0.160	0.086
Sum M1	0.984	0.997	0.996	0.991	1.000	1.000	1.000	1.000	1.000	1.000	1.000	1.000
Mg^{2+}	0.000	0.000	0.000	0.000	0.000	0.000	0.000	0.000	0.000	0.000	0.000	0.000
Fe^{2+}	0.000	0.000	0.000	0.000	0.026	0.027	0.007	0.003	0.001	0.001	0.043	0.051
Ca^{2+}	0.440	0.466	0.358	0.933	0.951	0.949	0.891	0.883	0.903	0.901	0.895	0.920
Na^{+}	0.570	0.529	0.637	0.054	0.019	0.020	0.079	0.091	0.070	0.071	0.051	0.024
Sum M2	1.010	0.995	0.995	0.987	0.996	0.996	0.977	0.977	0.974	0.973	0.989	0.995
Mol. % end-member												
Wo	31.79	33.00	27.00	48.34	48.10	48.20	47.34	46.94	47.20	46.88	47.38	47.47
En	26.73	28.26	22.10	32.59	42.34	41.85	34.96	34.72	36.17	35.85	38.17	40.48
Fs	41.47	38.74	50.91	19.07	9.56	9.95	17.69	18.34	16.62	17.27	14.45	12.07

continued

M-Sye Melasyenite
Hbdt Pyroxene-bearing hornblendite
A-Sye Antiperthite syenite
M Monzodiorite

A. Pyroxene *(continued)*

	Iris									Ludgate			Garrison
Unit	MD	Hbdt	Hbdt	Hbdt	Hbdt	Hbdt	Hbdt	Hbdt	Hbdt	Q-Sye	Q-Sye	Q-Sye	HQM
Sample	125-21	126-11	126-12	126-21	126-31	126-32	129-31	129-32	129-21	91-11	91-12	91-21	101-21
SiO_2	51.56	49.31	49.85	49.00	50.16	50.10	51.72	50.46	51.26	52.51	53.39	52.78	51.99
TiO_2	0.46	0.73	0.74	0.73	0.55	0.63	0.47	0.74	0.46	0.09	0.04	0.05	0.20
Al_2O_3	2.30	4.26	4.13	4.41	3.59	3.49	2.08	3.61	2.52	0.38	0.44	0.32	0.37
Cr_2O_3	0.00	0.02	0.02	0.00	0.01	0.01	0.01	0.01	0.00	0.04	0.03	0.01	0.02
MgO	14.78	13.49	12.77	12.71	13.42	13.17	14.49	12.28	11.88	8.50	8.64	6.14	4.52
CaO	23.38	23.17	23.29	23.12	23.09	23.34	23.11	22.84	22.47	17.61	17.80	14.44	9.99
MnO	0.19	0.21	0.25	0.24	0.25	0.26	0.23	0.28	0.38	0.43	0.45	1.50	0.52
FeO	4.28	4.49	5.53	5.18	5.07	4.92	5.25	6.28	6.93	7.60	6.97	6.08	5.72
Fe_2O_3	2.77	3.67	2.91	3.36	3.26	3.46	2.42	2.88	3.05	8.78	8.51	13.14	18.41
NaO	0.28	0.32	0.47	0.42	0.47	0.51	0.34	0.75	1.05	3.71	3.96	5.63	7.60
K_2O	0.00	0.00	0.01	0.00	0.01	0.00	0.00	0.00	0.01	0.03	0.00	0.00	0.00
Total	100.00	99.67	99.97	99.17	99.88	99.89	100.12	100.13	100.01	99.68	100.23	100.09	99.34
Chemical folmulae calculated based on 4 cations													
Si^{4+}	1.908	1.841	1.860	1.843	1.868	1.868	1.916	1.883	1.919	1.997	2.011	2.011	2.002
Al^{3+}	0.092	0.159	0.140	0.157	0.132	0.132	0.084	0.117	0.081	0.003	0.000	0.000	0.000
Fe^{3+}	0.000	0.000	0.000	0.000	0.000	0.000	0.000	0.000	0.000	0.000	0.000	0.000	0.000
Sum T	2.000	2.000	2.000	2.000	2.000	2.000	2.000	2.000	2.000	2.000	2.011	2.011	2.002
Al^{3+}	0.008	0.028	0.042	0.039	0.026	0.021	0.007	0.042	0.030	0.014	0.020	0.014	0.017
Fe^{3+}	0.077	0.103	0.082	0.095	0.091	0.097	0.067	0.081	0.086	0.251	0.241	0.377	0.534
Ti^{4+}	0.013	0.020	0.021	0.021	0.015	0.018	0.013	0.021	0.013	0.003	0.001	0.001	0.006
Cr^{3+}	0.000	0.001	0.001	0.000	0.000	0.000	0.000	0.000	0.000	0.001	0.001	0.000	0.001
Mg^{2+}	0.816	0.751	0.710	0.713	0.745	0.732	0.800	0.683	0.663	0.482	0.485	0.349	0.260
Fe^{2+}	0.086	0.097	0.144	0.132	0.123	0.132	0.113	0.173	0.208	0.242	0.219	0.194	0.182
Sum M1	1.000	1.000	1.000	1.000	1.000	1.000	1.000	1.000	1.000	0.993	0.967	0.935	1.000
Mg^{2+}	0.000	0.000	0.000	0.000	0.000	0.000	0.000	0.000	0.000	0.000	0.000	0.000	0.000
Fe^{2+}	0.046	0.043	0.029	0.031	0.035	0.021	0.050	0.023	0.009	0.000	0.000	0.000	0.002
Ca^{2+}	0.927	0.927	0.931	0.932	0.921	0.933	0.917	0.913	0.901	0.718	0.718	0.589	0.412
Na^{+}	0.020	0.023	0.034	0.031	0.034	0.037	0.024	0.054	0.076	0.274	0.289	0.416	0.568
Sum M2	0.993	0.993	0.994	0.994	0.990	0.991	0.991	0.990	0.986	0.992	1.007	1.005	0.982
Mol. % end-member													
Wo	47.34	48.08	48.90	48.77	47.89	48.52	46.93	48.51	47.95	42.06	42.81	37.80	29.28
En	41.68	38.95	37.29	37.31	38.74	38.07	40.94	36.29	35.28	28.24	28.92	22.40	18.48
Fs	10.98	12.97	13.81	13.92	13.36	13.42	12.13	15.20	16.76	29.70	28.26	39.79	52.24

MD	Monzodiorite
Hbdt	Pyroxene-bearing hornblendite
Q-Sye	Alkali-feldspar quartz-syenite
HQM	Hornblende quartz-monzonite

B. Amphibole

	Pangea										
	M-Sye 008-41	M-Sye 008-21	Hbdt 009-11	Hbdt 009-21	Hbdt 009-31	Hbdt 019-11	M-Sye 020-21	M-Sye 020-31	M-Sye 035-11	M-Sye 035-31	M-Sye 035-41
SiO_2	40.63	55.83	42.45	41.67	42.76	42.17	53.66	53.81	53.51	54.35	52.53
TiO_2	1.49	0.05	2.34	2.86	2.44	2.68	0.03	0.00	0.02	0.13	0.05
Al_2O_3	10.38	0.51	10.09	10.40	9.49	11.10	2.04	1.40	1.60	0.89	1.87
Cr_2O_3	0.00	0.00	0.00	0.01	0.03	0.06	0.00	0.01	0.16	0.01	0.03
MgO	9.67	17.35	8.46	8.45	8.10	9.48	15.02	16.11	17.03	17.38	14.33
CaO	11.27	12.39	10.63	10.40	10.55	10.70	12.01	12.28	12.61	12.45	11.90
MnO	0.62	0.59	0.22	0.21	0.22	0.19	0.75	0.64	0.24	0.28	0.48
FeO	15.37	8.93	15.43	14.70	16.28	12.34	10.61	9.35	8.95	8.53	11.55
Fe_2O_3	4.23	1.47	6.25	7.04	6.04	7.74	3.30	3.21	1.89	2.07	3.69
Na_2O	2.86	0.28	2.26	2.40	2.05	1.98	0.54	0.41	0.45	0.37	0.53
K_2O	1.64	0.07	0.72	0.67	0.88	0.72	0.12	0.05	0.11	0.07	0.20
F	0.47	0.13	0.00	0.03	0.09	0.05	0.03	0.07	0.22	0.14	0.07
Cl	0.08	0.00	0.04	0.02	0.04	0.00	0.00	0.01	0.01	0.00	0.00
H_2O	1.72	2.05	1.99	1.97	1.94	2.00	2.07	2.05	1.97	2.02	2.02
O=F	-0.20	-0.05	0.00	-0.01	-0.04	-0.02	-0.01	-0.03	-0.09	-0.06	-0.03
O=Cl	-0.02	0.00	-0.01	0.00	-0.01	0.00	0.00	0.00	0.00	0.00	0.00
Total	100.20	99.59	100.87	100.81	100.85	101.19	100.16	99.97	98.67	98.64	99.22
Chemical formulae calculated based on 13 (Si^{4+}, Ti^{4+}, Al^{3+}, Fe^{3+}, Cr^{3+}, Fe^{3+}, Mg^{2+}, Mn^{2+})											
Si^{4+}	6.217	7.940	6.379	6.266	6.447	6.247	7.711	7.750	7.726	7.820	7.673
Al^{3+}	1.783	0.060	1.621	1.734	1.553	1.753	0.289	0.250	0.272	0.151	0.322
Ti^{4+}	0.002	0.014	0.005								
Sum T	8.000	8.000	8.000	8.000	8.000	8.000	8.000	8.000	8.000	7.985	8.000
Al^{3+}	0.089	0.025	0.166	0.109	0.133	0.185	0.056	-0.013	0.000	0.000	0.000
Ti^{4+}	0.171	0.005	0.264	0.323	0.277	0.299	0.003	0.000	0.000	0.000	0.000
Cr^{3+}	0.000	0.000	0.000	0.001	0.004	0.007	0.000	0.002	0.018	0.001	0.003
Fe^{3+}	0.487	0.157	0.707	0.797	0.685	0.863	0.357	0.348	0.205	0.225	0.406
Mg^{2+}	2.206	3.679	1.895	1.894	1.821	2.094	3.218	3.459	3.666	3.728	3.120
Fe^{2+}	1.966	1.062	1.939	1.848	2.052	1.529	1.275	1.126	1.081	1.027	1.411
Mn^{2+}	0.080	0.071	0.028	0.027	0.028	0.023	0.091	0.078	0.029	0.019	0.059
Sum C	4.999	4.999	4.999	4.999	5.000	5.000	5.000	5.000	4.999	5.000	4.999
Mn^{2+}	0.001	0.015									
Ca^{2+}	1.848	1.888	1.711	1.676	1.704	1.698	1.849	1.895	1.951	1.919	1.862
Na^+	0.152	0.077	0.289	0.324	0.296	0.301	0.151	0.105	0.049	0.066	0.138
Sum B	2.000	1.965	2.000	2.000	2.000	2.000	2.000	2.000	2.000	2.000	2.000
Na^+	0.697	0.000	0.369	0.376	0.303	0.268	0.000	0.009	0.077	0.037	0.012
K^+	0.320	0.013	0.138	0.129	0.169	0.136	0.021	0.009	0.020	0.013	0.037
Sum A	1.017	0.013	0.507	0.505	0.472	0.404	0.021	0.018	0.097	0.050	0.049
Mg#	0.529	0.776	0.494	0.506	0.470	0.578	0.716	0.754	0.772	0.784	0.689

Continued

M-Sye Melasyenite
Hbdt Pyroxene-bearing hornblendite

B. Amphibole *(continued)*

	Iris					Ludgate			Garrison	
	MD 125-41	MD 125-51	Hbdt 126-22	Hbdt 129-11	Hbdt 129-41	Q-Sye 088-31	Q-Sye 088-32	Q-Sye 091-31	HQM 097-11	HQM 097-21
SiO_2	39.47	40.14	40.33	39.95	39.92	55.52	55.62	55.53	49.61	48.49
TiO_2	2.65	2.59	2.30	2.48	2.46	0.05	0.08	0.03	0.86	0.96
Al_2O_3	12.33	11.70	13.40	13.33	13.40	0.61	0.41	0.50	5.41	5.73
Cr_2O_3	0.01	0.04	0.00	0.00	0.00	0.03	0.01	0.01	0.01	0.01
MgO	8.48	9.01	12.51	11.81	11.99	10.91	10.29	9.86	14.25	14.08
CaO	11.23	11.40	11.90	11.71	11.87	2.32	0.91	0.21	11.31	11.21
MnO	0.46	0.49	0.20	0.31	0.22	0.16	0.12	0.06	0.54	0.54
FeO	16.43	16.55	10.66	10.90	10.27	9.00	7.89	8.09	10.98	10.66
Fe_2O_3	2.92	2.53	1.94	2.86	3.60	12.89	15.77	16.13	2.75	3.39
Na_2O	2.38	2.49	2.59	2.33	2.06	5.98	6.60	7.09	1.98	2.08
K_2O	1.87	1.87	1.59	1.74	1.76	0.17	0.09	0.10	0.62	0.75
F	0.10	0.25	0.12	0.19	0.15	0.00	0.14	0.21	0.84	0.85
Cl	0.11	0.13	0.02	0.02	0.04	0.00	0.03	0.00	0.04	0.05
H_2O	1.88	1.82	1.95	1.90	1.92	2.07	2.00	1.97	1.66	1.63
O=F	-0.04	-0.11	-0.05	-0.08	-0.06	0.00	-0.06	-0.09	-0.35	-0.36
O=Cl	-0.02	-0.03	0.00	0.00	-0.01	0.00	-0.01	0.00	-0.01	-0.01
Total	100.26	100.88	99.46	99.45	99.58	99.70	99.90	99.71	100.49	100.06
Chemical formulae calculated based on 13 (Si^{4+}, Ti^{4+}, Al^{3+}, Fe^{3+}, Cr^{3+}, Fe^{3+}, Mg^{2+}, Mn^{2+})										
Si^{4+}	6.038	6.103	6.023	5.993	5.971	8.027	8.027	8.038	7.199	7.092
Al^{3+}	1.962	1.897	1.977	2.007	2.029	0.801	0.908			
Ti^{4+}										
Sum T	8.000	8.000	8.000	8.000	8.000	8.027	8.027	8.038	8.000	8.000
Al^{3+}	0.261	0.200	0.381	0.350	0.333	0.104	0.070	0.085	0.124	0.080
Ti^{4+}	0.305	0.296	0.258	0.280	0.277	0.005	0.009	0.003	0.094	0.106
Cr^{3+}	0.001	0.005	0.000	0.000	0.000	0.003	0.001	0.001	0.001	0.001
Fe^{3+}	0.336	0.290	0.218	0.323	0.405	1.402	1.713	1.757	0.300	0.373
Mg^{2+}	1.934	2.042	2.785	2.641	2.674	2.351	2.214	2.128	3.083	3.070
Fe^{2+}	2.102	2.105	1.332	1.367	1.284	1.088	0.952	0.980	1.332	1.304
Mn^{2+}	0.060	0.062	0.025	0.039	0.027	0.020	0.015	0.007	0.066	0.066
Sum C	4.999	5.000	4.999	5.000	5.000	4.973	4.974	4.961	5.000	5.000
Mn^{2+}	0.001	0.001	0.001							
Ca^{2+}	1.841	1.857	1.904	1.882	1.902	0.359	0.141	0.033	1.758	1.757
Na^+	0.159	0.142	0.096	0.118	0.097	1.641	1.847	1.967	0.242	0.242
Sum B	2.000	2.000	2.000	2.000	2.000	2.000	1.988	2.000	2.000	2.000
Na^+	0.547	0.592	0.654	0.560	0.500	0.035	0.000	0.023	0.315	0.348
K^+	0.365	0.363	0.303	0.333	0.336	0.031	0.017	0.018	0.115	0.140
Sum A	0.912	0.955	0.957	0.893	0.836	0.066	0.017	0.041	0.430	0.488
Mg#	0.479	0.492	0.676	0.659	0.676	0.684	0.699	0.685	0.698	0.702

continued

MD Monzodiorite
Hbdt Pyroxene-bearing hornblendite
Q-Sye Alkali-feldspar quartz-syenit
HQM Hornblende quartz-monzonite

B. Amphibole *(continued)*

	Garrison			
	HQM 098-11	HQM 098-21	HQM 101-11	HQM 101-12
SiO_2	48.04	49.33	56.49	54.63
TiO_2	0.92	0.68	0.09	0.03
Al_2O_3	6.22	5.04	0.39	0.38
Cr_2O_3	0.00	0.00	0.01	0.04
MgO	13.67	13.81	16.28	8.61
CaO	11.35	11.66	4.08	0.48
MnO	0.54	0.54	0.53	0.35
FeO	9.73	11.01	6.54	10.15
Fe_2O_3	5.14	3.64	5.25	15.10
Na_2O	1.50	1.33	6.33	6.82
K_2O	0.69	0.51	1.34	0.13
F	0.49	0.12	1.76	0.07
Cl	0.00	0.00	0.00	0.00
H_2O	1.82	1.99	1.27	2.00
O=F	-0.21	-0.05	-0.74	-0.03
O=Cl	0.00	0.00	0.00	0.00
Total	99.90	99.62	99.62	98.76
Chemical formulae calculated based on 13 (Si^{4+}, Ti^{4+}, Al^{3+}, Fe^{3+}, Cr^{3+}, Fe^{2+}, Mg^{2+}, Mn^{2+})				
Si^{4+}	7.025	7.224	8.055	8.060
Al^{3+}	0.975	0.776		
Ti^{4+}				
Sum T	8.000	8.000	8.055	8.060
Al^{3+}	0.097	0.094	0.066	0.066
Ti^{4+}	0.101	0.075	0.010	0.003
Cr^{3+}	0.000	0.000	0.001	0.005
Fe^{3+}	0.565	0.402	0.563	1.676
Mg^{2+}	2.980	3.015	3.461	1.894
Fe^{2+}	1.190	1.348	0.780	1.253
Mn^{2+}	0.067	0.066	0.064	0.044
Sum C	5.000	5.000	4.945	4.941
Mn^{2+}	0.001			
Ca^{2+}	1.778	1.829	0.623	0.076
Na^+	0.222	0.170	1.377	1.924
Sum B	2.000	2.000	2.000	2.000
Na^+	0.203	0.208	0.373	0.027
K^+	0.129	0.095	0.244	0.024
Sum A	0.332	0.303	0.617	0.051
Mg#	0.715	0.691	0.816	0.602

HQM Hornblende quartz-monzonite

C. Mica

	Pangea				Iris		Emens				
	M-Sye 015-11	Hbdt 026-41	M-Sye 035-21	Sye 050-11	A-sye 069-31	A-sye 069-32	B-Sye 043-11	M-Sye 045-12	B-Sye 083-11	B-Sye 084-21	M-Sye 086-21
SiO_2	36.26	36.81	35.94	37.80	35.77	35.39	35.50	40.74	36.12	37.57	36.83
TiO_2	2.94	3.89	2.66	0.84	3.27	3.04	1.74	0.23	1.75	1.48	2.29
Al_2O_3	14.94	14.44	14.79	15.14	14.89	14.97	18.03	12.70	15.15	14.17	13.92
Cr_2O_3	0.00	0.00	0.00	0.00	0.00	0.00	0.00	0.00	0.00	0.13	0.00
MgO	11.40	13.54	12.52	14.23	11.38	11.56	7.72	20.54	12.03	16.10	12.61
CaO	0.01	1.57	0.00	0.03	0.03	0.06	0.01	0.07	0.02	0.00	0.02
MnO	0.20	0.26	0.31	0.65	0.93	0.98	0.59	0.25	0.44	0.49	0.62
FeO	20.44	15.97	19.28	16.39	20.32	20.36	21.79	10.60	19.73	15.75	19.45
Na_2O	0.06	0.02	0.02	0.03	0.12	0.08	0.02	0.00	0.03	0.02	0.06
K_2O	9.93	9.03	9.75	10.04	9.43	9.35	9.69	10.14	9.92	10.23	9.77
F	0.27	0.39	0.30	0.32	0.22	0.22	0.20	0.70	0.21	0.29	0.29
Cl	0.02	0.01	0.00	0.00	0.02	0.01	0.00	0.00	0.00	0.00	0.00
H_2O	3.79	3.80	3.76	3.82	3.81	3.79	3.77	3.77	3.79	3.86	3.78
O=F	-0.11	-0.16	-0.13	-0.13	-0.09	-0.09	-0.08	-0.29	-0.09	-0.12	-0.12
O=Cl	0.00	0.00	0.00	0.00	0.00	0.00	0.00	0.00	0.00	0.00	0.00
Total	100.14	99.56	99.21	99.15	100.09	99.72	98.98	99.45	99.11	99.97	99.51
Chemical formulae calculated based on 12 anions [10 O + 2 (OH^-, F^-, Cl^-)]											
Si^{4+}	2.770	2.769	2.759	2.856	2.738	2.722	2.751	2.977	2.782	2.817	2.821
Al^{3+}	1.230	1.231	1.241	1.144	1.262	1.278	1.249	1.023	1.218	1.183	1.179
Sum T	4.000	4.000	4.000	4.000	4.000	4.000	4.000	4.000	4.000	4.000	4.000
Al^{3+}	0.115	0.049	0.097	0.204	0.081	0.079	0.398	0.071	0.157	0.069	0.078
Ti^{4+}	0.169	0.220	0.154	0.048	0.188	0.176	0.101	0.013	0.101	0.083	0.132
Cr^{3+}	0.000	0.000	0.000	0.000	0.000	0.000	0.000	0.000	0.000	0.008	0.000
Mn^{2+}	0.013	0.017	0.020	0.042	0.060	0.064	0.039	0.015	0.029	0.031	0.040
Fe^{2+}	1.306	1.005	1.238	1.036	1.301	1.310	1.412	0.648	1.271	0.988	1.246
Mg^{2+}	1.298	1.518	1.433	1.603	1.299	1.326	0.892	2.238	1.381	1.800	1.440
Sum M	2.901	2.809	2.942	2.933	2.929	2.955	2.842	2.985	2.939	2.979	2.936
Ca^{2+}	0.001	0.127	0.000	0.002	0.002	0.005	0.001	0.005	0.002	0.000	0.002
K^+	0.968	0.867	0.955	0.968	0.921	0.917	0.958	0.945	0.975	0.979	0.955
Na^+	0.009	0.003	0.003	0.004	0.018	0.012	0.003	0.000	0.004	0.003	0.009
Sum I	0.978	0.997	0.958	0.974	0.941	0.934	0.962	0.950	0.981	0.982	0.966
Fe/Fe+Mg	0.502	0.398	0.464	0.393	0.500	0.497	0.613	0.225	0.479	0.354	0.464

continued

Hbdt	Pyroxene-bearing hornblendite
M-Sye	Melasyenite
Sye	Alkali-feldspar syenite
A-Sye	Antiperthite syenite
B-Sye	Alkali-feldspar porphyritic biotite-syenite

C. Mica *(continued)*

	Emens						
	M-Sye 086-32	Sye 161-21	B-Sye 164-21	B-Sye 164-32	B-Sye 178-31	B-Sye 178-31	B-Sye 178-41
SiO_2	40.52	35.86	37.69	38.17	37.18	34.69	36.96
TiO_2	0.51	2.20	1.38	0.56	1.57	1.67	1.75
Al_2O_3	12.34	17.15	15.96	17.19	16.77	19.00	16.16
Cr_2O_3	0.00	0.03	0.01	0.02	0.03	0.01	0.01
MgO	16.08	11.23	14.19	13.42	12.10	10.36	11.33
CaO	0.15	0.00	0.01	0.04	0.03	0.02	0.01
MnO	0.64	0.76	0.57	0.56	0.64	0.63	0.55
FeO	15.97	18.35	14.99	14.95	17.30	19.20	17.98
Na_2O	0.26	0.02	0.06	0.03	0.00	0.04	0.09
K_2O	9.98	10.19	9.95	10.07	10.40	10.21	9.78
F	0.59	0.00	0.03	0.25	0.33	0.06	0.31
Cl	0.00	0.00	0.02	0.00	0.00	0.00	0.00
H_2O	3.76	3.94	3.97	3.89	3.83	3.90	3.77
O=F	-0.25	0.00	-0.01	-0.11	-0.14	-0.03	-0.13
O=Cl	0.00	0.00	0.00	0.00	0.00	0.00	0.00
Total	100.55	99.73	98.81	99.05	100.04	99.76	98.57
Chemical formulae calculated based on 12 anions [10 O + 2 (OH^-, F^-, Cl^-)]							
Si^{4+}	3.006	2.727	2.834	2.855	2.799	2.648	2.826
Al^{3+}	0.994	1.273	1.166	1.145	1.201	1.352	1.174
Sum T	4.000	4.000	4.000	4.000	4.000	4.000	4.000
Al^{3+}	0.085	0.264	0.249	0.370	0.287	0.357	0.282
Ti^{4+}	0.028	0.126	0.078	0.031	0.089	0.096	0.101
Cr^{3+}	0.000	0.002	0.001	0.001	0.002	0.001	0.001
Mn^{2+}	0.040	0.049	0.036	0.035	0.041	0.041	0.036
Fe^{2+}	0.991	1.167	0.943	0.935	1.089	1.226	1.150
Mg^{2+}	1.778	1.273	1.591	1.496	1.358	1.179	1.291
Sum M	2.922	2.881	2.898	2.868	2.866	2.900	2.861
Ca^{2+}	0.012	0.000	0.001	0.003	0.002	0.002	0.001
K^+	0.945	0.989	0.955	0.961	0.999	0.994	0.954
Na^+	0.037	0.003	0.009	0.004	0.000	0.006	0.013
Sum I	0.994	0.992	0.965	0.968	1.001	1.002	0.968
Fe/Fe+Mg	0.358	0.478	0.372	0.385	0.445	0.510	0.471

M-Sye Melasyenite
B-Sye Alkali-feldspar porphyritic biotite-syenite
Sye Alkali-feldspar syenite

D. Feldspar

	Ludgate								
Unit	Q-sye	Q-sye	Q-sye	Q-sye	Q-sye	Q-sye	Q-sye	Q-sye	Q-sye
Sample	88-1.1	88-1.2	88-1.3	88-1.4	88-1.5	88-21	88-22	88-23	88-24
SiO_2	65.94	63.69	66.78	66.74	67.19	66.63	67.78	67.04	66.87
TiO_2	0.00	0.02	0.00	0.00	0.00	0.00	0.00	0.00	0.00
Al_2O_3	19.53	19.01	19.40	19.40	19.44	18.45	18.65	18.60	18.56
CaO	0.54	3.05	0.63	0.39	0.29	0.01	0.01	0.01	0.00
FeO	0.14	0.22	0.14	0.16	0.42	0.36	0.32	0.33	0.31
SrO	0.23	0.40	0.32	0.32	0.27	0.02	0.00	0.13	0.01
BaO	0.70	0.09	0.36	0.32	0.37	0.20	0.05	0.13	0.07
Na_2O	8.59	9.97	9.94	9.58	10.12	6.96	8.38	7.86	6.75
K_2O	4.27	1.71	2.31	2.97	2.52	7.54	4.85	5.93	7.44
Total	99.94	98.15	99.89	99.89	100.62	100.17	100.04	100.03	100.02
Chemical formulae calculated based on 8 oxygen									
Si^{4+}	2.954	2.904	2.966	2.969	2.968	2.997	3.012	3.000	3.003
Ti^{4+}	0.000	0.001	0.000	0.000	0.000	0.000	0.000	0.000	0.000
Al^{3+}	1.031	1.021	1.016	1.017	1.012	0.978	0.977	0.981	0.982
Ca^{2+}	0.026	0.149	0.030	0.018	0.014	0.000	0.000	0.000	0.000
Fe^{2+}	0.005	0.008	0.005	0.006	0.016	0.014	0.012	0.012	0.012
Sr^{2+}	0.006	0.011	0.008	0.008	0.007	0.001	0.000	0.003	0.000
Ba^{2+}	0.012	0.002	0.006	0.006	0.006	0.004	0.001	0.002	0.001
Na^{+}	0.746	0.882	0.856	0.826	0.867	0.607	0.722	0.682	0.587
K^{+}	0.244	0.099	0.131	0.169	0.142	0.433	0.275	0.339	0.426
Sum	5.025	5.076	5.019	5.020	5.031	5.033	4.998	5.020	5.013
Mol. % end member									
Ab	73.4	78.1	84.2	81.5	84.8	58.4	72.4	66.8	57.9
Or	24.0	8.8	12.9	16.7	13.9	41.6	27.6	33.2	42.1
An	2.6	13.2	2.9	1.8	1.4	0.0	0.0	0.0	0.0

continued

Q-Sye Alkali-feldspar quartz-syenite

D. Feldspar *(continued)*

	Iris					Ludgate				
Unit	Q-sye	Q-sye	Q-sye	Q-sye	Q-sye	Q-sye	Q-sye	Q-sye	Q-sye	Q-sye
Sample	108-21	108-22	108-23	108-24	108-25	91-41	91-42	91-43	91-44	91-45
SiO_2	66.46	66.85	65.99	65.18	66.32	66.72	65.03	66.58	66.54	67.88
TiO_2	0.01	0.03	0.00	0.51	0.01	0.02	0.01	0.02	0.00	0.01
Al_2O_3	18.58	18.71	18.73	18.38	18.45	18.68	18.52	18.68	18.67	19.06
CaO	0.21	0.10	0.29	0.09	0.08	0.01	0.03	0.09	0.00	0.00
FeO	0.23	0.35	0.32	0.25	0.25	0.29	0.16	0.28	0.27	0.23
SrO	0.06	0.11	0.00	0.00	0.00	0.11	0.16	0.18	0.14	0.01
BaO	0.08	0.01	0.12	0.09	0.11	0.16	0.36	0.16	0.16	0.01
Na_2O	5.93	6.99	5.85	4.97	5.57	8.45	5.28	9.82	7.91	10.90
K_2O	8.60	6.88	8.86	10.01	9.22	5.03	9.23	3.21	5.80	1.39
Total	100.16	100.04	100.17	99.48	100.02	99.49	98.78	99.00	99.48	99.49
Chemical formulae calculated based on 8 oxygen										
Si^{4+}	2.995	2.997	2.982	2.977	2.999	2.994	2.986	2.988	2.994	2.998
Ti^{4+}	0.000	0.001	0.000	0.018	0.000	0.001	0.000	0.001	0.000	0.000
Al^{3+}	0.987	0.988	0.997	0.989	0.983	0.988	1.002	0.988	0.990	0.992
Ca^{2+}	0.010	0.005	0.014	0.004	0.004	0.001	0.002	0.004	0.000	0.000
Fe^{3+}	0.009	0.013	0.012	0.009	0.010	0.011	0.006	0.010	0.010	0.009
Sr^{2+}	0.002	0.003	0.000	0.000	0.000	0.003	0.004	0.005	0.004	0.000
Ba^{2+}	0.001	0.000	0.002	0.002	0.002	0.003	0.007	0.003	0.003	0.000
Na^+	0.518	0.608	0.513	0.440	0.488	0.735	0.470	0.855	0.690	0.933
K^+	0.495	0.393	0.511	0.583	0.532	0.288	0.541	0.184	0.333	0.078
Sum	5.017	5.009	5.031	5.022	5.019	5.023	5.018	5.037	5.023	5.011
Mol. % end member										
Ab	50.6	60.4	49.4	42.8	47.7	71.8	46.4	82.0	67.4	92.3
Or	48.4	39.1	49.2	56.8	52.0	28.1	53.4	17.6	32.6	7.7
An	1.0	0.5	1.3	0.4	0.4	0.1	0.2	0.4	0.0	0.0

continued

Q-Sye Alkali-feldspar quartz-syenite

D. Feldspar *(continued)*

	Garrison				
Unit	HQM	HQM	HQM	HQM	HQM
Sample	101-31	101-32	101-33	101-34	101-35
SiO_2	64.19	65.14	63.93	64.47	64.52
TiO_2	0.00	0.01	0.02	0.00	0.02
Al_2O_3	18.62	19.04	18.70	18.78	18.55
CaO	0.17	0.36	0.15	0.28	0.18
FeO	0.13	0.17	0.17	0.14	0.14
SrO	0.22	0.22	0.24	0.29	0.21
BaO	1.08	0.64	0.93	0.94	0.85
Na_2O	2.79	6.07	3.20	4.11	3.10
K_2O	12.50	7.94	12.32	10.60	12.28
Total	99.70	99.60	99.66	99.61	99.85
Chemical formulae calculated based on 8 oxygen					
Si^{4+}	2.971	2.964	2.961	2.967	2.976
Ti^{4+}	0.000	0.000	0.001	0.000	0.001
Al^{3+}	1.016	1.021	1.021	1.019	1.008
Ca^{2+}	0.009	0.018	0.008	0.014	0.009
Fe^{3+}	0.005	0.007	0.007	0.005	0.005
Sr^{2+}	0.006	0.006	0.007	0.008	0.006
Ba^{2+}	0.020	0.011	0.017	0.017	0.015
Na^{+}	0.250	0.535	0.287	0.366	0.277
K^{+}	0.738	0.461	0.728	0.622	0.722
Sum	5.015	5.023	5.035	5.018	5.020
Mol. % end member					
Ab	25.1	52.8	28.1	36.5	27.5
Or	74.0	45.5	71.2	62.1	71.6
An	0.9	1.8	0.8	1.4	0.9

HQM Hornblende quartz-monzonite

E. Garnet

	Pangea			Emens						
Unit	M-Sye	M-Sye	M-Sye	B-Sye	B-Sye	M-Sye	M-Sye	B-Sye	B-Sye	M-Sye
Sample	041-11	041-21	041-31	043-21	043-31	045-21	045-41	083-21	083-31	086-11
SiO_2	35.45	34.89	35.30	34.65	35.26	33.91	36.28	35.63	34.75	35.30
TiO_2	2.70	3.52	2.62	1.66	1.00	3.63	0.74	1.44	3.21	2.22
Nb_2O_5	0.03	0.00	0.06	0.00	0.00	0.00	0.02	0.00	0.00	0.08
ZrO_2	0.13	0.05	0.12	0.25	0.04	0.28	0.00	0.03	0.15	0.00
Al_2O_3	6.60	5.88	6.31	3.13	2.74	2.39	5.74	6.22	2.31	3.83
Cr_2O_3	0.03	0.12	0.03	0.01	0.01	0.01	0.01	0.02	0.00	0.00
MgO	0.25	0.22	0.24	0.17	0.01	0.26	0.02	0.00	0.13	0.02
V_2O_5	0.23	0.52	0.20	0.45	0.38	0.31	0.18	0.45	0.50	0.25
Y_2O_3	0.00	0.09	0.09	0.19	0.14	0.00	0.00	0.00	0.01	0.03
CaO	32.16	31.83	32.17	33.02	33.01	32.19	33.59	33.95	32.32	33.29
MnO	0.62	0.69	0.60	0.46	0.40	0.32	0.40	0.54	0.45	0.55
^1FeO	3.01	3.87	4.04	0.68	0.97	2.44	0.88	0.59	3.22	1.45
$^1Fe_2O_3$	18.52	18.52	17.47	24.18	24.91	23.27	21.23	20.32	21.78	22.38
Na_2O	0.04	0.02	0.02	0.00	0.00	0.09	0.01	0.03	0.05	0.03
K_2O	0.00	0.00	0.00	0.00	0.00	0.01	0.00	0.01	0.00	0.00
Total	99.77	100.22	99.30	98.85	98.87	99.11	99.10	99.23	98.88	99.43
Chemical formulae calculated based on 12 anions and 8 cations										
Si^{4+}	2.914	2.873	2.948	2.921	2.973	2.871	2.998	2.939	2.939	2.944
Ti^{4+}	0.167	0.218	0.165	0.105	0.063	0.231	0.046	0.089	0.204	0.139
Nb^{5+}	0.001	0.000	0.002	0.000	0.000	0.000	0.001	0.000	0.000	0.003
Zr^{4+}	0.005	0.002	0.005	0.010	0.002	0.011	0.000	0.001	0.006	0.000
Al^{3+}	0.639	0.571	0.621	0.311	0.272	0.238	0.559	0.605	0.230	0.376
Cr^{3+}	0.002	0.008	0.002	0.000	0.001	0.001	0.001	0.002	0.000	0.000
Mg^{2+}	0.031	0.027	0.030	0.021	0.001	0.033	0.002	0.000	0.016	0.003
V^{5+}	0.012	0.028	0.011	0.025	0.021	0.017	0.010	0.024	0.028	0.013
Y^{3+}	0.000	0.004	0.004	0.009	0.006	0.000	0.000	0.000	0.000	0.001
Ca^{2+}	2.832	2.808	2.789	2.983	2.982	2.920	2.974	3.000	2.929	2.975
Mn^{2+}	0.043	0.048	0.042	0.033	0.029	0.023	0.028	0.038	0.032	0.039
Fe^{3+}	0.207	0.266	0.282	0.048	0.173	0.173	0.061	0.040	0.228	0.101
Fe^{3+}	1.146	1.148	1.098	1.534	1.482	1.482	1.320	1.261	1.386	1.405
Na^+	0.006	0.003	0.003	0.000	0.000	0.015	0.001	0.004	0.009	0.004
K^+	0.000	0.000	0.000	0.000	0.000	0.001	0.000	0.001	0.000	0.000
Mol. % end-member										
Prp	1.0	0.9	1.0	0.7	0.0	1.1	0.1	0.0	0.5	0.1
Adr	70.3	75.1	68.9	87.6	87.0	92.7	71.0	71.2	90.4	82.8
Alm	6.7	8.5	9.0	1.6	2.2	5.5	2.0	1.3	7.1	3.4
Uv	0.1	0.4	0.1	0.0	0.1	0.1	0.1	0.1	0.0	0.0
Sps	1.4	1.5	1.3	1.1	0.9	0.7	0.9	1.2	1.0	1.3
Grs	20.6	13.6	19.8	9.1	9.8	0.0	26.0	26.2	1.0	12.6

B-Sye Alkali-feldspar porphyritic biotite-syenite
M-Sye Melasyenite
[1] Estimated assuming ideal stoichiometry

III. Sample location

Sample	Intrusion	Location[1]	Rock type	PTS	WRC	REE	Probe
LMP-99-001	Hislop	E:552634 N:5371290	Sye	X	-	-	
LMP-99-002	Hislop	E:552497 N:5371498	Sye	X	-	-	
LMP-99-008	Pangea	G94-66 166.4 m	M-sye	X	X	-	Px, Amp, Epi
LMP-99-009	Pangea	G94-66 174.4 m	Hbdt	X	X	X	Amp, Hem, Mag
LMP-99-011	Pangea	G94-66 199.2 m	Sye	X	-	-	
LMP-99-014	Pangea	G94-66 218.1 m	Hbdt	-	X	-	
LMP-99-015	Pangea	G94-66 227.3 m	M-sye	X	-	-	Mica, Epi
LMP-99-019	Pangea	G94-66 240.5 m	Hbdt	X	X	X	Amp
LMP-99-020	Pangea	G94-66 245.1 m	M-sye	X	X	-	Amp, Epi
LMP-99-023	Pangea	G94-66 269.4 m	M-sye	X	-	-	
LMP-99-026	Pangea	G94-66 295.7 m	M-sye	X	-	-	Px, Mica, Epi
LMP-99-035	Pangea	G94-27 206.4 m	M-sye	X	X	-	Amp, Mica
LMP-99-039	Pangea	G94-27 309.9 m	Sye	X	-	-	
LMP-99-040	Pangea	G94-27 342.0 m	Diabase	X	-	-	
LMP-99-041	Pangea	G94-27 325.6 m	M-sye	X	-	-	Gar
LMP-99-042	Emens	MDM89-01 191.1 m	Diorite	X	-	-	
LMP-99-043	Emens	MDM89-01 234.4 m	B-Sye	X	X	-	Mica, Gar, Ti
LMP-99-044	Emens	MDM89-01 267.9 m	Sye	X	-	-	
LMP-99-045	Emens	MDM89-01 269.0 m	M-sye	X	X	X	Px, Mica, Gar
LMP-99-046	Pangea	G94-11 46.0 m	Sye	X	-	-	
LMP-99-048	Pangea	G94-11 207.5 m	M-sye	X	-	-	
LMP-99-050	Pangea	G94-11 223.1 m	Sye	X	X	-	Mica, Chl
LMP-99-051	Pangea	G94-11 231.4 m	Diorite	X	X	-	
LMP-99-053b	Pangea	G94-52 108.8 m	Sye	-	X	-	
LMP-99-056	Pangea	G94-52 207.9 m	M-sye	X	X	-	
LMP-99-057	Pangea	G94-52 242.5 m	M-sye	X	-	-	
LMP-99-059	Pangea	G94-52 272.3 m	M-Sye	-	X	-	
LMP-99-060	Pangea	G94-52 307.2 m	Sye	X	-	-	
LMP-99-064	Pangea	FE94-04 102.4 m	Sye	X	-	-	
LMP-99-065	Pangea	FE94-04 109.3 m	Sye	X	-	-	
LMP-99-068	Iris	E:590489 N:5367381	Hbdt	-	X	X	
LMP-99-069	Iris	E:590493 N:5367379	A-Sye	X	X	X	Px, Mica
LMP-99-070	Iris	E:590488 N:5367374	Blue Amp. Vein	X	-	-	
LMP-99-072	Iris	E:590481 N:5367392	Monzo	X	-	-	
LMP-99-076	Iris	E:590388 N:5367511	Monzo	X	X	-	
LMP-99-079	Emens	M87-08 160.0 m	Sye	X	-	-	
LMP-99-080	Emens	M87-08 166.4 m	M-sye	-	X	-	
LMP-99-081	Emens	M87-08 170.7 m	Sye	-	X	-	
LMP-99-082	Emens	M87-08 193.2 m	M-sye	X	-	-	
LMP-99-083	Emens	M87-08 198.1 m	B-Sye	X	X	-	Mica, Gar

Continued

B-Sye Alkali-feldspar porphyritic biotite-syenite
M-Sye Melasyenite
Sye Alkali-feldspar syenite
Hbdt Pyroxene-bearing hornblendite
HQM Hornblende quartz-monzonite
A-Sye Antiperthite syenite
MD Monzodiorite
P-Sye Alkali-feldspar porphyritic syenite
Q-Sye Alkali-feldspar quartz-syenite
[1]Hole number and depth, or UTM NAD 27 zone 17

III. Sample location *(continued)*

Sample	Intrusion	Location[1]	Rock type	PTS	WRC	REE	Probe
LMP-99-084	Emens	M87-08 218.2 m	B-Sye	X	X	X	
LMP-99-086	Emens	M87-08 240.2 m	M-sye	X	X	-	
LMP-99-088	Ludgate	E:566924 N:5370427	Q-Sye	X	X	-	Amp, Feld
LMP-99-089	Ludgate	E:566842 N:5370561	Q-Sye	X	-	-	
LMP-99-090	Ludgate	E:566842 N:5370561	Q-Sye	X	-	-	
LMP-99-091	Ludgate	E:566807 N:5370432	Q-Sye	X	X	X	Px, Amp, Feld
LMP-99-092	Pangea	G94-66 242.5 m	Blue Amp. in Sye.	X	-	-	
LMP-99-093	Emens	M87-08 114.9 m	Sye	X	-	-	
LMP-99-095	Iris	E:590449 N:5367412	IMS Syenite	X	-	-	
LMP-99-097	Garrison	E:577488 N:5369835	HQM	X	X	X	Amp
LMP-99-098	Garrison	E:590810 N:5367600	HQM	X	X	X	Amp
LMP-99-099	Garrison	E:590844 N:5367615	HQM	X	X	-	
LMP-99-100	Garrison	E:578759 N:5369223	HQM	X	X	-	
LMP-99-101	Garrison	E:578750 N:5369218	HQM	X	X	-	Px, Amp, Feld
LMP-99-102	Garrison	E:578188 N:5369018	HQM	X	X	X	
LMP-99-103	Iris	E:590461 N:5367414	Q-Sye	X	X	-	
LMP-99-104	Iris	E:590443 N:5367454	Q-Sye	X	X	X	
LMP-99-105	Iris	E:590443 N:5367421	Q-Sye	-	X	-	
LMP-99-106	Iris	E:590378 N:5367379	Q-Sye	-	X	-	
LMP-99-107	Iris	E:590395 N:5367361	Q-Sye	-	X	X	
LMP-99-108	Iris	E:590383 N:5367394	Q-Sye	X	X	X	Feld, Hem
LMP-99-109	Iris	E:590483 N:5367396	Q-Sye	-	X	-	
LMP-99-110	Iris	E:590428 N:5367389	Q-Sye	X	X	X	
LMP-99-111	Iris	E:590469 N:5367390	Q-Sye	-	X	-	
LMP-99-112	Iris	E:590458 N:5367364	Q-Sye	-	X	-	
LMP-99-113	Iris	E:590398 N:5367414	Q-Sye	X	X	X	
LMP-99-114	Iris	E:590331 N:5367341	Q-Sye	-	X	-	
LMP-99-115	Iris	E:590350 N:5367440	Q-Sye	-	X	-	
LMP-99-116	Iris	E:590415 N:5367499	P-Sye	X	X	X	
LMP-99-117	Iris	E:590351 N:5367363	Q-Sye	-	X	-	
LMP-99-118	Iris	E:590313 N:5367324	A-Sye	X	X	X	
LMP-99-119	Iris	E:590320 N:5367339	Q-Sye	-	X	-	
LMP-99-120	Iris	E:590398 N:5367469	P-Sye	-	X	X	
LMP-99-121	Iris	E:590423 N:5367494	P-Sye	X	X	X	
LMP-99-122	Iris	E:590418 N:5367439	Q-Sye	-	X	-	
LMP-99-123	Iris	E:590451 N:5367446	Q-Sye	-	X	-	
LMP-99-124	Iris	E:590343 N:5367414	Q-Sye	-	X	-	
LMP-99-125	Iris	E:590476 N:5367379	MD	X	X	X	Px, Amp

Continued

B-Sye	Alkali-feldspar porphyritic biotite-syenite	A-Sye	Antiperthite syenite
M-Sye	Melasyenite	MD	Monzodiorite
Sye	Alkali-feldspar syenite	P-Sye	Alkali-feldspar porphyritic syenite
Hbdt	Pyroxene-bearing hornblendite	Q-Sye	Alkali-feldspar quartz-syenite
HQM	Hornblende quartz-monzonite	[1]Hole number and depth, or UTM NAD 27 zone 17	

III. Sample location *(continued)*

Sample	Intrusion	Location[1]	Rock type	PTS	WRC	REE	Probe
LMP-99-126	Iris	E:590488 N:5367365	Hbdt	X	X	X	Px, Amp
LMP-99-128	Iris	E:590348 N:5367332	Hbdt	-	X	-	
LMP-99-129	Iris	E:590349 N:5367319	Hbdt	X	X	X	Px, Amp, Hem, Mag
LMP-99-131	Iris	E:590318 N:5367324	A-Sye	-	X	-	
LMP-99-132	Iris	E:590334 N:5367329	A-Sye	-	X	-	
LMP-99-133	Iris	E:590333 N:5367434	MD	-	X	-	
LMP-99-139	Iris	E:590463 N:5367356	MD	X	-		
LMP-99-142	Iris	E:590302 N:5367417	Monzo	-	X	-	
LMP-99-149	Iris	E:589626 N:5367048	Monzo	-	X	X	
LMP-99-151	Iris	E:589602 N:5367044	Hbdt	-	X	-	
LMP-99-153	Iris	E:589276 N:5367247	A-Sye	-	X	X	
LMP-99-154	Iris	E:589283 N:5367244	Hbdt	-	X	X	
LMP-99-156	Iris	E:589243 N:5367424	Q-Sye	-	X	-	
LMP-99-157	Emens	M87-08 295.7 m	B-Sye	-	X	X	
LMP-99-159	Emens	M87-08 314.2 m	B-Sye	-	X	-	
LMP-99-161	Emens	M87-08 344.7 m	Sye	X	-	-	Mica, Chl
LMP-99-164	Emens	M87-08 416.4 m	B-Sye	X	-	-	Mica
LMP-99-165	Emens	M87-08 413.3 m	Sye	-	X	-	
LMP-99-168	Emens	M87-13 117.0 m	B-Sye	X	-	-	
LMP-99-169	Emens	M87-13 125.9 m	Sye	-	X	-	
LMP-99-171	Emens	M87-13 171.0 m	B-Sye	-	X	-	
LMP-99-172	Emens	M87-13 194.2 m	Sye	-	X	-	
LMP-99-173	Emens	M87-13 224.3 m	B-Sye	-	X	-	
LMP-99-175	Emens	M87-13 235.6 m	B-Sye	-	X	-	
LMP-99-176	Emens	M87-13 269.7 m	B-Sye	-	X	-	
LMP-99-177	Emens	M87-13 280.7 m	B-Sye	-	X	X	
LMP-99-178	Emens	M87-13 298.7 m	B-Sye	X	X	X	Mica
LMP-99-180	Pangea	G95-101 59.7 m	M-Sye	X	X	X	
LMP-99-183	Pangea	G95-101 86.7 m	M-Sye	-	X	-	
LMP-99-186	Pangea	G95-101 113.5 m	M-Sye	-	X	X	
LMP-99-191	Pangea	G95-101 152.6 m	M-Sye	-	X	-	
LMP-99-193	Pangea	G95-101 169.7 m	Sye	X	X	X	
LMP-99-195	Pangea	G95-101 188.5 m	M-Sye	-	X	-	
LMP-99-196	Pangea	G95-101 225.0 m	M-Sye	-	X	-	
LMP-99-198	Iris	E:590443 N:5367494	Monzo	-	X	-	

B-Sye Alkali-feldspar porphyritic biotite-syenite
M-Sye Melasyenite
Sye Alkali-feldspar syenite
Hbdt Pyroxene-bearing hornblendite
HQM Hornblende quartz-monzonite
A-Sye Antiperthite syenite
MD Monzodiorite
P-Sye Alkali-feldspar porphyritic syenite
Q-Sye Alkali-feldspar quartz-syenite
[1]Hole number and depth, or UTM NAD 27 zone 17

Appendix 2

Published reports

I. [1]Pigeon, L., Lalonde, A. E. & Berger, B. (1999). Petrogenesis of syenitic magmatism associated with gold meneralization along the Destor-Porcupine fault zone near Matheson, Ontario. In: *Summary of field work and other activities 1999, Ontario Geological Survey Open File Report* 6000, 12-1 to 12-4.

II. [1]Pigeon, L., Lalonde, A. E. & Berger, B. (2000). Petrogenesis of syenitic magmatism associated with gold meneralization along the Destor-Porcupine fault zone near Matheson, Ontario. In: *Summary of field work and other activities 2000, Ontario Geological Survey Open File Report* 6032, 8-1 to 8-6.

III. [1]Pigeon, L., Lalonde, A. E. & Berger, B. (2001). Meneralogy of pyroxene, amphibole and mica in syenitic rocks of the Porcupine-Destor deformation zone near Matheson, Ontario. In: *Summary of field work and other activities 2001, Ontario Geological Survey Open File Report 6070*, 11-1 to 11-8.

[1] Summary of field work articles included in this thesis are reproduced with the permission of the Ontario Geological Survey, Ontario Ministry of Northern Development and Mines.

I.

12. Petrogenesis of Syenitic Magmatism Associated With Gold Mineralization Along the Destor-Porcupine Fault Zone Near Matheson, Ontario

L. Pigeon[1], A. E. Lalonde[1], B. Berger[2]

[1]Ottawa-Carleton Geoscience Centre, University of Ottawa, Ottawa, Ontario
[2]Ontario Geological Survey

The association of alkaline syenitic magmatism and gold mineralization have long been recognized along the Larder Lake-Cadillac fault in the Kirkland Lake area (Cameron and Hattori 1987; Rowins et al. 1991). A similar association has only recently been discovered along the Destor-Porcupine fault zone (DPFZ) east of Matheson, Ontario. Despite the similarities with the Kirkland Lake camp, no studies have yet been undertaken to describe the mineralogy, geochemistry and petrogenesis of these syenite intrusions. In addition, the possible genetic links between the syenitic intrusions and the gold mineralization of this region remain to be investigated.

The purpose of this project is to study the syenitic rocks that occur near the DPFZ in Guibord, Michaud, Garrison and Harker townships and to explore the potential genetic relationships between these intrusions and the gold mineralization.

Four specific objectives are defined: 1) to determine the petrogenetic evolution and emplacement conditions of the intrusions, 2) to delineate the geochemical evolution of the intrusive suites, 3) to investigate the mineral chemistry of the principal ferromagnesian minerals in order to evaluate the redox conditions that prevailed during the crystallization of the magmas, and 4) to characterize the postmagmatic alteration associated with the intrusions.

This project involves the collaboration of the Department of Earth Sciences at the University of Ottawa and the Ontario Geological Survey (OGS). It consists of a M.Sc. thesis by L. Pigeon and poster presentations to be given at the Northeastern Regional Symposiums to be held in the spring of 2000 and 2001.

The 1999 field season started in early June and extended to the end of August. Five intrusions of syenite or syenitic rock were studied. Samples were obtained in the field wherever possible, or taken from diamond drill core stored locally. The five intrusions are from east to west 1) Iris syenite, 2) Garrison stock, 3) Emens Lake intrusion, 4) Ludgate syenite, and 5) Pangea intrusion (Figure 12.1). The following is a summary of fieldwork done on each of these intrusions.

Iris syenite

The Iris syenite is located approximately 4 km east of Highway 672 at the south boundary of Harker Township (Figure 12.1) and is owned by Alex Perron, a local prospector. A considerable amount of work was performed on the Iris syenite since it is the best-exposed intrusion of the region. Both a detailed map at a scale of 1:100 of the 350 m by 250 m stripped outcrop (the final map will be at a scale of 1:500) and a more general map at the scale of 1:2500 of the surrounding metavolcanic rocks of the Kinojevis assemblage were produced. The major intrusive rock types encountered on the Iris property are: a)

Summary of Field Work and Other Activities 1999,
Ontario Geological Survey, Open File Report 6000, p.12-1 to 12-4.

coarse-grained pink quartz syenite, b) medium- to coarse-grained quartz-syenite containing 30-40% 1 to 3 cm size euhedral alkali feldspar phenocryts, c) medium-grained equigranular syenite, d) xenolith-rich monzonite, e) diorite, f) medium- to coarse-grained equigranular hornblendite and g) fine-grained hornblendite with large 1 to 2 cm hornblende phenocrysts. The metavolcanic rocks are predominantly pillowed and massive basalts, silicified massive basalts and rhyolite. All the phases of the intrusion and surrounding metavolcanic rocks were extensively sampled for petrological analyses and whole-rock geochemistry (total of about 65 specimens). Nepheline was not observed in the Iris syenite; however, numerous late fractures filled with asbestiform blue alkali-amphibole were observed. Such amphibole-filled fractures are typical of alkaline intrusions.

Ludgate Lake syenite

The northern tip of the Ludgate Lake syenite is located approximately 2 km south of Perry Lake in Michaud Township (Figure 12.1). The property visited is owned by Pentland Firth Ventures Ltd. and occurs at the southern boundary of the intrusion. It consists of a stripped outcrop of about 30 m by 80 m in dimension. The principal rock type found on the property is coarse-grained purplish-pink syenite locally exhibiting a trachytic texture defined by the alignment of 1 to 3 cm long euhedral alkali feldspar laths. Four specimens were taken for petrological and geochemical analyses.

Emens Lake intrusion

The Emens Lake intrusion is located northeast of the Ludgate Lake syenite and is approximately 2 km southeast of Perry Lake in Michaud Township (Figure 12.1). The southwestern portion of this intrusion is in contact with the Ludgate Lake syenite and may represent a mafic unit of the same intrusion. The pluton, which is only visible in diamond drill core, is situated on property owned by Moneta-Porcupine Mines Ltd. Three drill holes were logged and sampled (total of about 30 samples). The rock types encountered vary from medium-grained melanosyenite showing abundant euhedral 2 to 5 cm long alkali feldspar phenocrysts to equigranular melanosyenite to fine-grained pyroxene-bearing mafic units.

Garrison intrusion

The Garrison intrusion is located approximately 2.5 km south of the intersection of Garrison Creek with Highway 101 in Garrison Township (Figure 12.1). The property visited, called New Buffonta, is owned by Alex Perron and is located at the western margin of the intrusion. Five samples were collected on a small traverse. The intrusion is homogenous and is composed of medium-grained equigranular quartz monzonite. The samples were taken for geochemistry and petrological analyses.

Pangea intrusion

The Pangea intrusion is located approximately 1 km southeast of the intersection of Little Pike River with Highway 101 in Guibord Township and extends about 2 km into Michaud Township (Figure 12.1). The intrusion is situated on a property owned by Pangea Goldfields Inc. but can only be studied in diamond drill core because of the lack of surface exposure. A total of six diamond drill holes were logged and sampled. Approximately 80 samples were taken for geochemical and petrological analyses. The rocks encountered were found to be extremely heterogeneous and often without sharp contacts. The major rock types were megacrystic alkali feldspar syenite, medium-grained equigranular melanosyenite and hornblendite. Large euhedral crystals of pseudoleucite, up to 5 cm in diameter and with trapezohedral outline, were observed at numerous locations in the diamond drill core (Figure 12.2). The

occurrence of pseudoleucite in these syenites corroborates their ultra-potassic alkaline character and reinforces their similarity with the rocks of the Kirkland Lake area.

References

Cameron, E.M. and Hattori, K. 1987. Archean gold mineralization and oxidized hydrothermal fluids; Econ. Geol., v. 82, p. 1177-1191.

Rowins, S.M., Lalonde, A.E. and Cameron, E.M. 1991. Magmatic oxidation in the syenitic Murdock Creek intrusion, Kirkland Lake, Ontario: evidence from the ferromagnesian silicates; Journal of Geology, v. 99, p. 395-414.

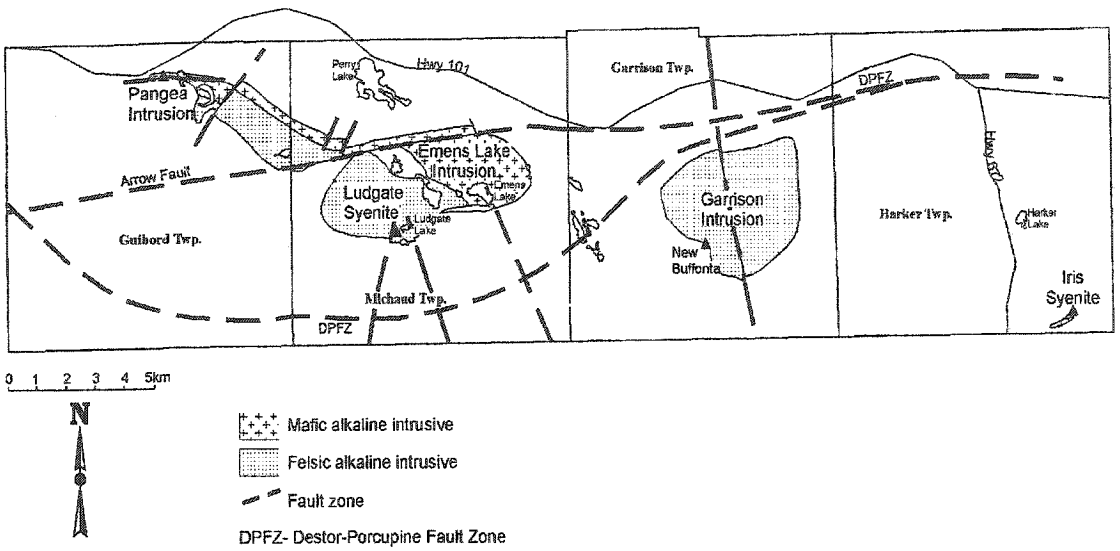

Figure 12.1. Location map.

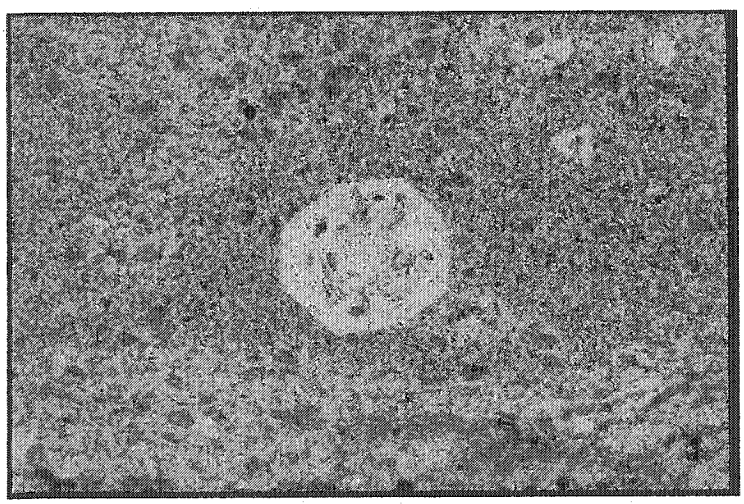

Figure 12.2. Photomicrograph of melanosyenite from the Pangea intrusion showing euhedral trapezohedral phenocryst of pseudoleucite. Plane-polarized light, field of view = 2.5 mm (*photo by B. Berger, OGS*).

II.

8. Project Unit 99-026. Petrogenesis of Syenitic Magmatism Associated with Gold Mineralization Along the Destor–Porcupine Fault Zone Near Matheson, Ontario

L. Pigeon[1], A.E. Lalonde[1], B. Berger[2]

[1]Ottawa-Carleton Geoscience Centre, University of Ottawa, Ottawa, Ontario
[2]Precambrian Geoscience Section, Ontario Geological Survey

We describe the petrography, mineralogy and geochemistry of a suite of small intrusions of syenite and related rocks that are closely associated with gold mineralization in the Destor–Porcupine zone, near and east of Matheson, Ontario. The intrusions studied are from east to west, the Iris, Garrison, Emens Lake, Ludgate and Pangea (Figure 8.1).

The objectives of this study, which constitutes part of an M.Sc. project at the University of Ottawa are: 1) to determine the petrogenetic evolution and emplacement conditions of the intrusions, 2) to delineate the geochemical evolution of the suite, 3) to investigate the mineral chemistry of the principal ferromagnesian minerals in order to gain insight into the redox conditions that prevailed during crystallization, and 4) to characterize the postmagmatic alteration associated with these rocks.

In this paper, we summarize some of the salient geochemical features that are apparent at this early stage of the project. All the fieldwork was accomplished during the summer of 1999. A large amount of work has yet to be accomplished, primarily in the fields of petrography and mineral chemistry, before announcing any definitive interpretations. However, based on the available geochemical data, we can recognize certain common features among some of the intrusions, and group these together for the

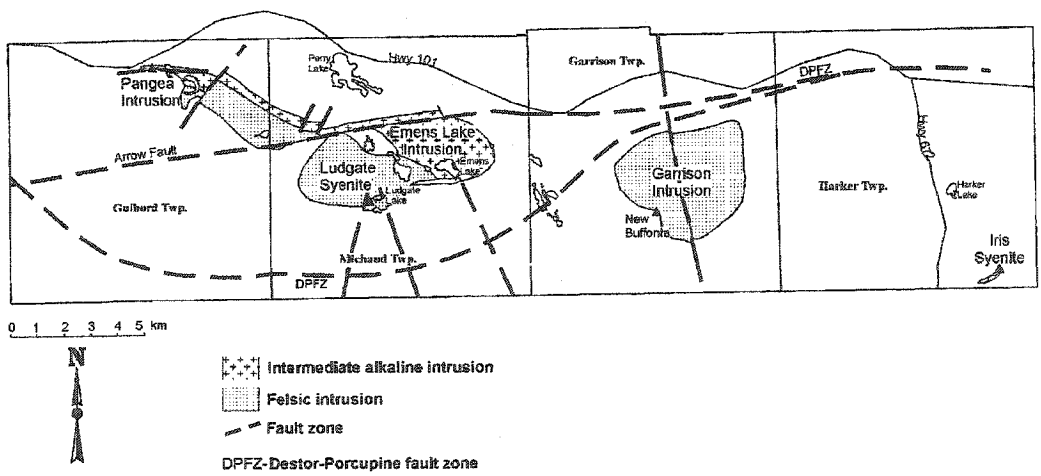

Figure 8.1. Location map of study area.

Summary of Field Work and Other Activities 2000,
Ontario Geological Survey, Open File Report 6032, p.8-1 to 8-6.

purpose of our discussion. Three groups were defined as follows: 1) the Emens and Pangea intrusions, 2) the Iris and Ludgate intrusions and 3) the Garrison intrusion. The most important compositional distinction between these groups is their alkaline nature. The Emens and Pangea intrusions both have high alkaline affinities, with the majority of their analyses plotting in the undersaturated field of the total alkali-silica diagram of Le Bas et al. (1986), whereas the Iris and Ludgate intrusions both have the majority of their analyses plotting in the SiO_2 saturated portion of the diagram. The analyses from the Garrison intrusion also plot in the SiO_2 saturated portion of the diagram but the geochemical properties of this intrusion differ considerably from the Iris and Ludgate intrusions (Figure 8.2).

The Emens and Pangea Intrusions

Rocks of the Emens and Pangea intrusions are principally feldspar-porphyritic hornblende and/or clinopyroxene melanosyenites. Both intrusions also contain a minor syenite component. These two intrusions are grouped together because of their common alkaline nature. This is especially true for the Emens intrusion for which all the samples analysed (n=21) yielded normative nepheline ($\bar{x}$ = 6.15 wt %), with some samples also displaying normative leucite. Similarly, the Pangea melanosyenite also yielded normative nepheline but not as commonly as the Emens melanosyenite. No analysis from the Emens intrusion showed normative quartz. The majority of the samples analysed are of intermediate composition with an average SiO_2 content of 51.20 wt.% ± 2.07 (n=42, α=0.05)[3]. Both intrusions show a wide range of K_2O/Na_2O values with an average of 1.54 ± 0.32 (n=42, α=0.05) (Figure 8.3). All analyses of the

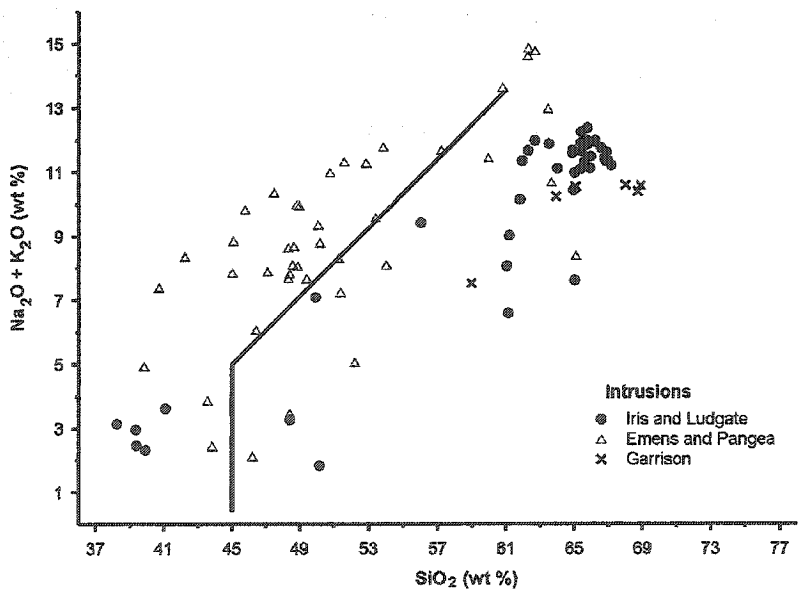

Figure 8.2. Total alkali silica-diagram (Le Bas et al. 1986) illustrating the more pronounced alkaline nature of the Emens and Pangea intrusions.

[3] Confidence intervals on averages are calculated using: $\bar{x} \pm t_{\alpha/2,n-1}\, s/\sqrt{n}$

syenite from the Emens intrusion are potassium enriched (K_2O/Na_2O average value of 2.53) and nepheline normative, whereas those from Pangea are sodium enriched ($\bar{x}$ = 0.52) and may also be nepheline normative.

The chondrite normalized rare earth element (REE) diagram for the Emens and Pangea melanosyenites shows a strong enrichment in the LREE (up to 600 times chondrite) and a more moderate enrichment in the HREE (10 to 50 times chondrite) (Figure 8.4). The patterns have a pronounced negative slope with an average La/Lu ratio of 31.70 ± 11.64 (n=8, α=0.05). Two samples of hornblendite from the Pangea intrusion have nearly flat patterns with a moderate enrichment in the LREE and HREE (20 to 60 times chondrite) and an average La/Lu ratio of 2.23.

The Iris and Ludgate Intrusions

The Iris and Ludgate intrusions are composed mainly of coarse-grained alkali-feldspar syenites, however, mafic and intermediate rocks are also present at Iris. The syenites from the two intrusions are quartz normative with an average quartz content of approximately 2 wt %. Nepheline is not present in the norm of the felsic rocks but some mafic rocks at Iris show minor amounts of normative nepheline. The SiO_2 content of these intrusions is quite variable, ranging from 40 wt % in the mafic rocks to 68 wt % in the syenites. The average SiO_2 content of all rocks from both intrusions is 60.47 wt % ± 2.87 (n=41, α=0.05). Numerous samples show an important and significant enrichment in sodium which is reflected in an average K_2O/Na_2O value of 0.30 ± 0.07 (n=41, α=0.05) (Figure 8.5). The syenites are especially sodic in nature with an average Na_2O content of 8.95 wt % ± 0.53 (n=33, α=0.05).

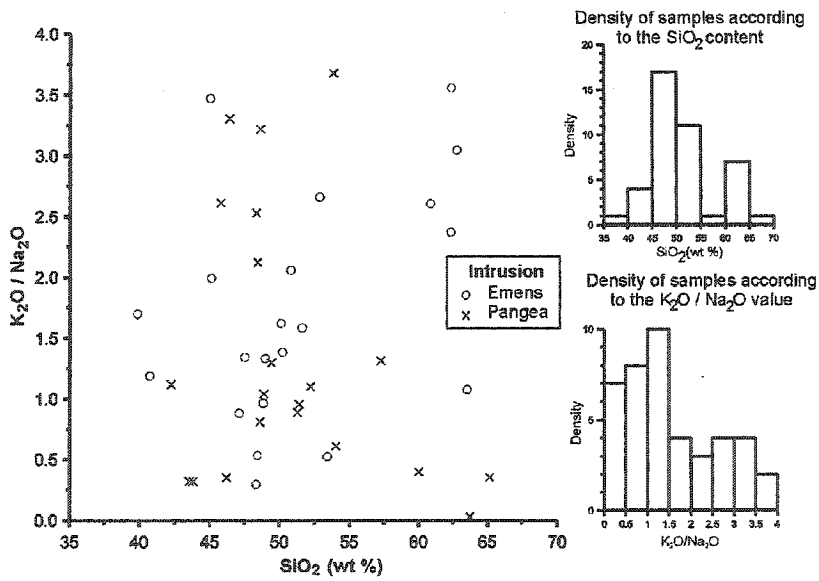

Figure 8.3. K_2O/Na_2O(wt % ratio) as a function of SiO_2 content in rocks from the Emens and Pangea intrusions.

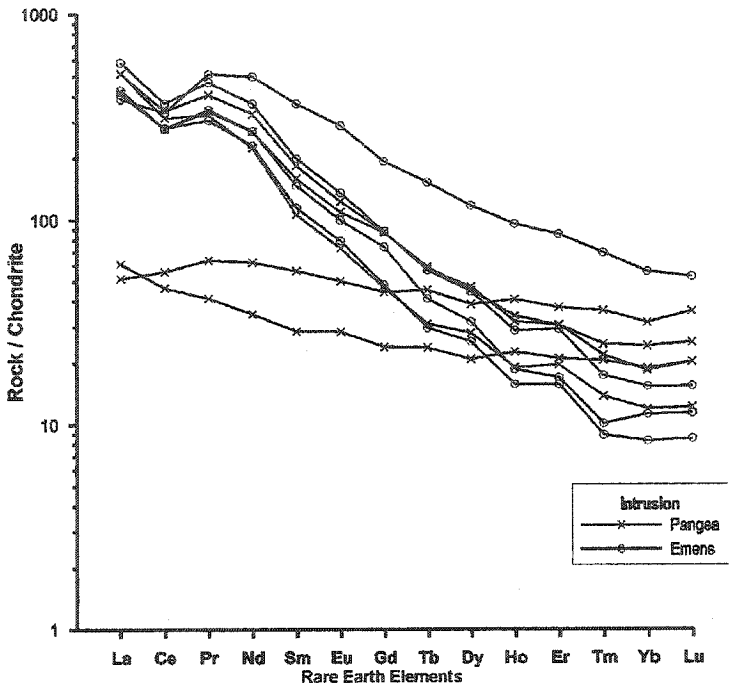

Figure 8.4. Chondrite normalized REE diagram for the Emens and Pangea intrusions. Chondrite values from McDonough and Sun (1995).

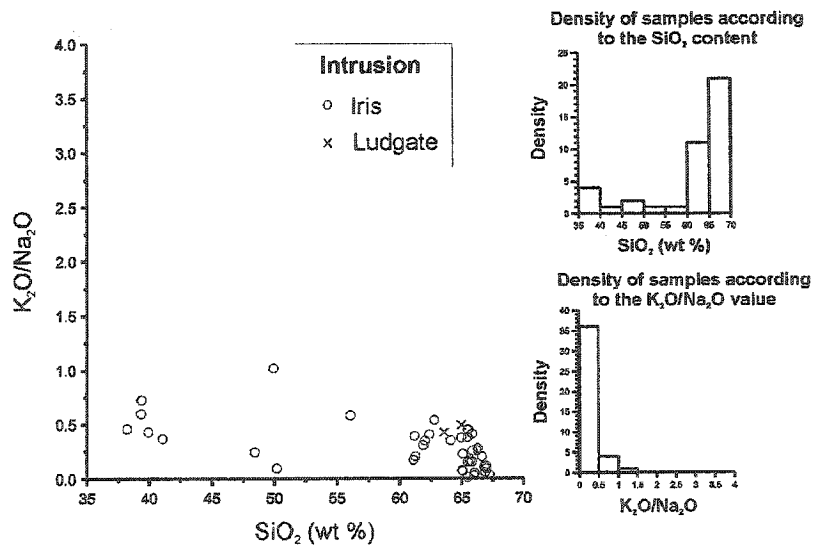

Figure 8.5. K_2O/Na_2O (wt % ratio) as a function of SiO_2 content in rocks from the Iris and Ludgate intrusions.

The chondrite normalized REE diagram of the Iris and Ludgate intrusions are presented in Figure 8.6. The mafic rocks of Iris are more enriched in REE than the felsic ones. They show a strong enrichment in the LREE (150 to 300 times chondrite) and a moderate enrichment in the HREE (20 to 35 times chondrite). The patterns have moderate negative slopes with an average La/Lu of 8.55± 2.20 (n = 7, α = 0.05). The cause of the relative REE enrichment that is observed in the mafic rocks of the Iris intrusion is not well understood. The high modal abundance of accessory titanite in these mafic rocks, in contrast to the near absence of this mineral in the more felsic syenites, may be a likely cause. The syenites are moderately enriched in LREE (30 to 100 times chondrite) and slightly enriched in the HREE (3 to 15 times chondrite). The REE patterns of the syenites have a peculiar curved shape, they show decreasing abundances from La to Tb and then slight increases from Tb to Lu. The average La/Lu ratio is 7.96 ± 1.30 (n = 11, α = 0.05). The Ludgate syenites are enriched in LREE (90 to 110 times chondrite) and are slightly enriched in HREE (3.5 to 4 times chondrite). The patterns have strong negative slopes with an average La/Lu ratio of 27.33.

The Garrison Intrusion

The Garrison intrusion is composed of medium-grained hornblende-biotite monzonite to quartz monzonite. The samples from Garrison are all quartz normative ($\bar{x}$ = 11.31 wt %) and nepheline is never present in the norm. The average SiO_2 content of all samples analysed is 65.67 wt % ± 4.04 (n=6, α=0.05).

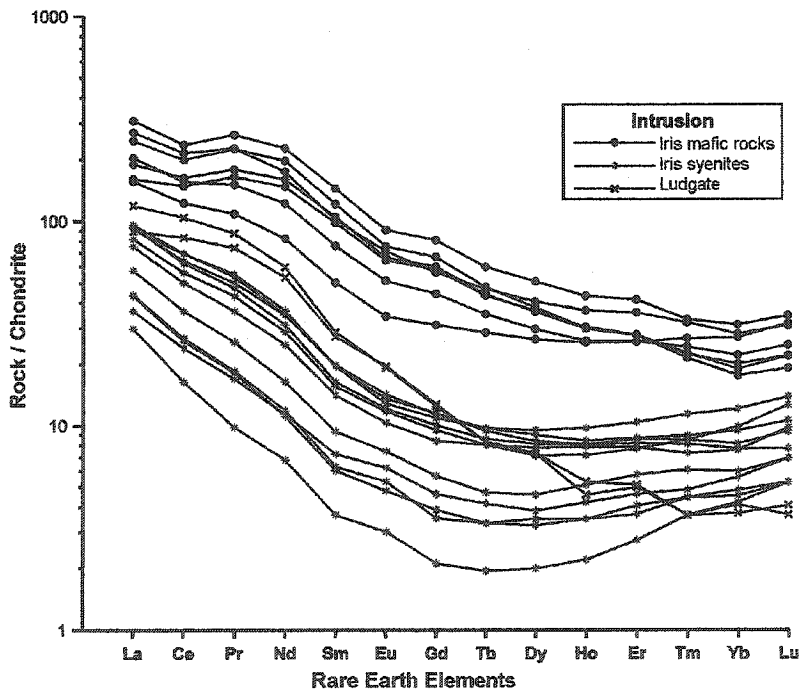

Figure 8.6. Chondrite normalized REE diagram for the Iris and Ludgate intrusions. Chondrite values from McDonough and Sun (1995).

The average K_2O/Na_2O value is 0.77 ± 0.18 ($n=6$, $\alpha=0.05$). Samples from Garrison are enriched in the LREE (160 to 220 times chondrite) and slightly enriched in HREE (5 to 7 times chondrite). The patterns have a pronounced negative slope with an average La/Lu ratio of 32.46.

The suite of intrusions studied showed considerable variations in their geochemical compositions. The Emens and Pangea intrusions exhibited undersaturated characteristics, with the majority of their samples displaying normative nepheline. In contrast, the samples from the Iris and Ludgate intrusions have a more saturated nature, with most of them showing normative quartz. Furthermore, the Iris and Ludgate intrusions were highly enriched in sodium whereas the Emens and Pangea intrusions have a more potassic signature. The samples from the Garrison intrusion were all quartz normative and showed no significant enrichment in sodium.

The intrusions of the Destor–Porcupine fault zone share numerous geochemical and petrological properties in common with those of the Cadillac–Larder Lake fault zone in the Kirkland Lake region to the south. For example, the association of quartz-bearing and feldspathoid-bearing suites, identified here in the Iris–Ludgate and Emens–Pangea groups was also recognized in the Kirkland Lake region by Levesque et al. (1991). Given the close spatial association of these intrusions with the gold mineralization along both fault zones, our current efforts on the Destor–Porcupine intrusive rocks will focus on documenting the relative redox state under which the magmas evolved by means of mineral-chemical studies in order to better evaluate the potential contribution these magmas may have made to the mineralization process.

REFERENCES

Le Bas, M.J., Le Maitre, R.W., Streckeisen, A. and Zanettin, B. 1986. A chemical classification of volcanic rocks based on the total alkali-silica diagram; Journal of Petrology, v.27, p.745-750.

Levesque, G.S., Cameron, E.M. and Lalonde, A.E. 1991. Duality of magmatism along the Kirkland Lake-Larder Lake fault zone, Ontario; Current research, part C, Geological Survey of Canada, paper 91-1C, p.17-24.

McDonough, W.F. and Sun, S.-s. 1995. The composition of the earth; Chemical Geology, v.120, p.223-253.

III.

11. Project Unit 99-026. Mineralogy of Pyroxene, Amphibole and Mica in Syenitic Rocks of the Porcupine–Destor Deformation Zone near Matheson, Ontario

L. Pigeon[1], A.E. Lalonde[1] and B.R. Berger[2]

[1]Ottawa–Carleton Geoscience Centre, University of Ottawa, Ottawa
[2]Ontario Geological Survey, Sudbury

INTRODUCTION

We describe the occurrence and composition of the principal mafic minerals in a suite of small intrusions of syenite and related rocks that are closely associated with gold mineralization in the Porcupine–Destor deformation zone, near and east of Matheson, Ontario. The intrusions studied are, from east to west, the Iris, Garrison, Emens Lake, Ludgate and Pangea intrusions (Figure 11.1).

The objectives of this paper, which constitutes part of an MSc project at the University of Ottawa and an Ontario Geological Survey–University of Ottawa Graduate Thesis Agreement, are 1) to describe the occurrence, textural relationships and paragenesis of the principal ferromagnesian minerals in syenite intrusions; 2) to delineate the mineral chemistry and compositional evolution of these minerals in order to gain insight into the redox conditions that prevailed during crystallization; and 3) to characterize the postmagmatic alteration of these minerals. This is a continuation of work that was initiated in 1999 (Pigeon, Lalonde and Berger 1999, 2000).

Mineral analyses were carried out by wavelength-dispersive X-ray spectrometry on a Cameca electron microprobe at the Geoscience Laboratories, Ontario Geoservices Centre, Sudbury. Operating conditions were set to 20 kV and 20 nA using a beam diameter of 3 to 12 μm, the diameter dependent upon the mineral analyzed. Counting times varied from 10 to 15 seconds per element. All analyses were corrected with the PAP procedure.

Pyroxene formulae and nomenclature are based on the recommendations of the International Mineralogical Association (IMA) (Morimoto 1989). Estimations of Fe^{2+} to Fe^{3+} contents were done by charge-balance considerations. Amphibole formulae were calculated on the basis of 13 cations (Si^{4+}, Al^{3+}, Cr^{3+}, Ti^{4+}, Fe^{2+}, Fe^{3+}, Mg^{2+}, Mn^{2+}) and assuming that (OH^-, Cl^-, F^-) equal 2. Assignments of cations and nomenclature of the amphiboles were done according to the current IMA recommendations (Leake et al. 1997). Here again, estimations of Fe^{2+} to Fe^{3+} contents were done by charge-balance considerations. Micas were calculated on the basis of 12 anions [10 oxygens + 2 (OH^-, Cl^-, F^-)]. Classification and site assignments for the micas were also done according to current IMA recommendations (Rieder et al. 1998). The following results are based on 23 analyses of pyroxene from 10 different samples, 24 analyses of amphibole from 12 samples, and 19 analyses of mica from 15 samples.

Summary of Field Work and Other Activities 2001,
Ontario Geological Survey, Open File Report 6070, p.11-1 to 11-8.

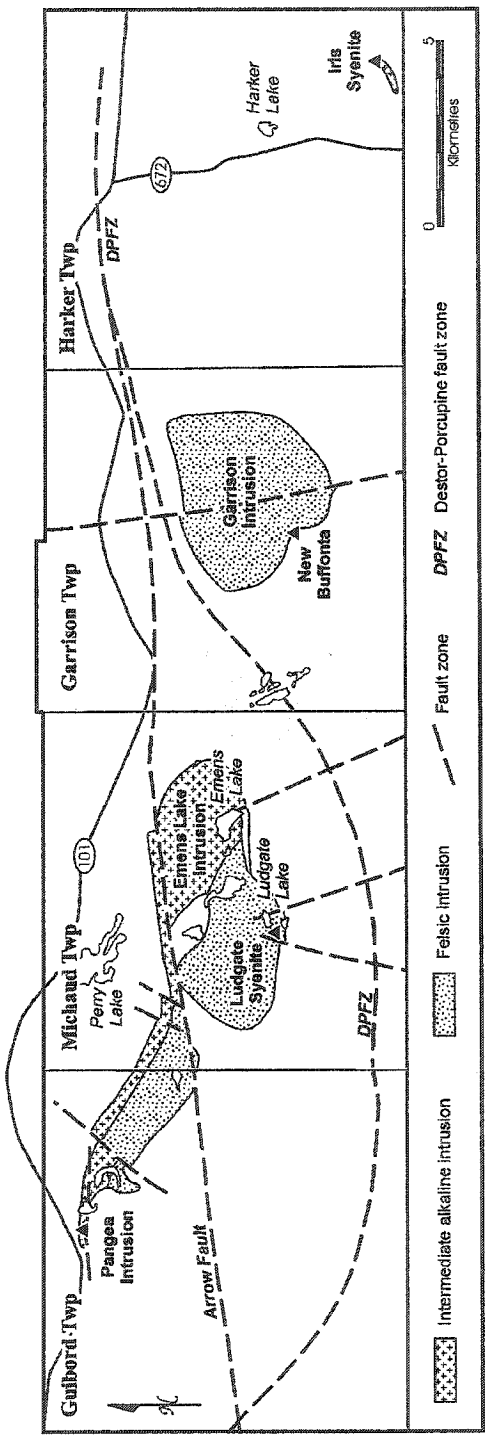

Figure 11.1. Location map of study area.

11-2

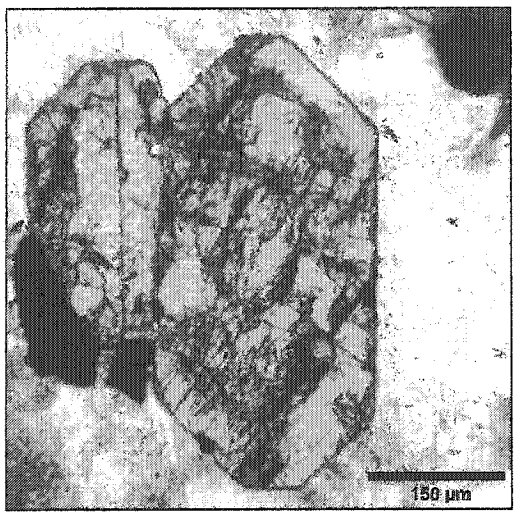

Figure 11.2. Basal section of euhedral crystals of diopside in syenite from the Iris intrusion. Plane-polarized light.

MINERALOGY AND MINERAL CHEMISTRY

Pyroxene

Pyroxene is found in all the intrusions studied, however, in the Garrison intrusion, pyroxene occurs only in minor amounts (<1%), and, in the Ludgate intrusion, only one sample contains pyroxene.

In the Iris intrusion, pyroxene is more common in the hornblendite and diorite units (20 to 40%), but is also present as a minor phase in the medium-grained syenite unit (5 to 10%). Pyroxene from the hornblendite and medium-grained syenite is commonly subhedral to euhedral. In the diorite unit, it is anhedral to subhedral. When subhedral or euhedral, the pyroxene crystals show long prismatic or equant basal sections, suggesting a primary magmatic origin (Figure 11.2).

The pyroxene in the hornblendite and medium-grained syenite is fresh with only minor alteration. In the diorite unit, pyroxene is commonly rimmed by amphibole. In all rocks, the pyroxene is light green and displays minor or no pleochroism. Three representative analyses of pyroxene from the Iris and other intrusions are listed in Table 11.1. All analyses of pyroxene from the Iris intrusion plot in the diopside field of the pyroxene quadrilateral diagram (Figure 11.3a).

Fresh pyroxene is not common in the samples from the Pangea and Emens intrusions. When present in these rocks, the pyroxene is found in the centre of amphibole clusters, suggesting that the amphibole replaced the primary pyroxene. In the Pangea intrusion, pyroxene is present in hornblendite and melanosyenite units; and in the melanosyenite unit in the Emens intrusion. Pyroxene occurs as anhedral crystals that are light green with minor or no pleochroism. All pyroxene from the Pangea intrusion is diopside, however, the pyroxene in the Emens intrusion is distinctly more sodic (Figure 11.3b) and corresponds to aegirine-augite.

Table 11.1. Mineral chemistry of representative pyroxene, amphibole and mica.

	Pyroxene			Amphibole				Mica	
Intrusion	**Iris** [a]	**Iris** [a]	**Emens** [b]	**Pangea** [c]	**Iris** [d]	**Pangea** [e]	**Ludgate** [f]	**Iris** [g]	**Emens** [h]
Sample No.	**125-1-2**	**126-1-1**	**45-1-1**	**009-21**	**126-22**	**035-41**	**088-32**	**069-32**	**086-21**
SiO_2	50.62	49.31	53.24	41.67	40.33	52.53	55.62	35.39	36.83
TiO_2	0.59	0.73	0.03	2.86	2.30	0.05	0.08	3.04	2.29
Al_2O_3	3.24	4.26	1.37	10.40	13.40	1.87	0.41	14.97	13.92
Cr_2O_3	0.00	0.02	0.02	0.01	0.00	0.03	0.01	0.00	0.00
MgO	14.19	13.49	6.67	8.45	12.51	14.33	10.29	11.56	12.61
CaO	23.13	23.17	11.02	10.40	11.90	11.90	0.91	0.06	0.02
MnO	0.17	0.21	0.16	0.21	0.20	0.48	0.12	0.98	0.62
FeO	4.42	4.49	0.98	14.70	10.66	11.55	7.89	20.36	19.45
Fe_2O_3 [i]	3.29	3.67	19.22	7.04	1.94	3.69	15.77	–	–
Na_2O	0.33	0.32	7.90	2.40	2.59	0.53	6.60	0.08	0.06
K_2O	0.01	0.00	0.02	0.67	1.59	0.20	0.09	9.35	9.77
F	0.00	0.08	0.04	0.03	0.12	0.07	0.14	0.22	0.29
Cl	0.01	0.00	0.00	0.02	0.02	0.00	0.03	0.01	0.00
H_2O [j]	–	–	–	1.97	1.95	2.02	2.00	3.79	3.78
O=F	0.00	-0.03	-0.02	-0.01	-0.05	-0.03	-0.06	-0.09	-0.12
O=Cl	0.00	0.00	0.00	0.00	0.00	0.00	-0.01	0.00	0.00
Total	100.00	99.72	100.65	100.81	99.46	99.22	99.90	99.72	99.51
Based on:		4 cations			24 anions and 13 cations			12 anions	
Si^{4+}	1.879	1.841	1.983	6.266	6.023	7.673	8.027	2.722	2.821
Ti^{4+}	0.016	0.020	0.001	0.323	0.258	0.005	0.009	0.176	0.132
Al^{3+}	0.142	0.187	0.060	1.843	2.358	0.322	0.070	1.357	1.257
Cr^{3+}	0.000	0.001	0.001	0.001	0.000	0.003	0.001	0.000	0.000
Mg^{2+}	0.785	0.751	0.370	1.894	2.785	3.120	2.214	1.326	1.440
Ca^{2+}	0.920	0.927	0.440	1.676	1.904	1.862	0.141	0.005	0.002
Mn^{2+}	0.005	0.007	0.005	0.027	0.025	0.059	0.015	0.064	0.040
Fe^{2+}	0.137	0.140	0.030	1.848	1.332	1.411	0.952	1.310	1.246
Fe^{3+}	0.092	0.103	0.539	0.797	0.218	0.406	1.713	–	–
Na^{+}	0.024	0.023	0.570	0.700	0.750	0.150	1.847	0.012	0.009
K^{+}	0.000	0.000	0.001	0.129	0.303	0.037	0.017	0.917	0.955
F^{-}	0.000	0.009	0.005	0.014	0.057	0.032	0.064	0.054	0.070
Cl^{-}	0.001	0.000	0.000	0.005	0.005	0.000	0.007	0.001	0.000

Notes: *a*, diopside; *b*, aegirine-augite; *c*, magnesiohastingsite; *d*, pargasite; *e*, actinolite; *f*, magnesioriebeckite; *g*, phlogopite; *h*, annite; *i*, calculated Fe^{2+} and Fe^{3+} values; *j*, calculated assuming OH + Cl + F = 2.

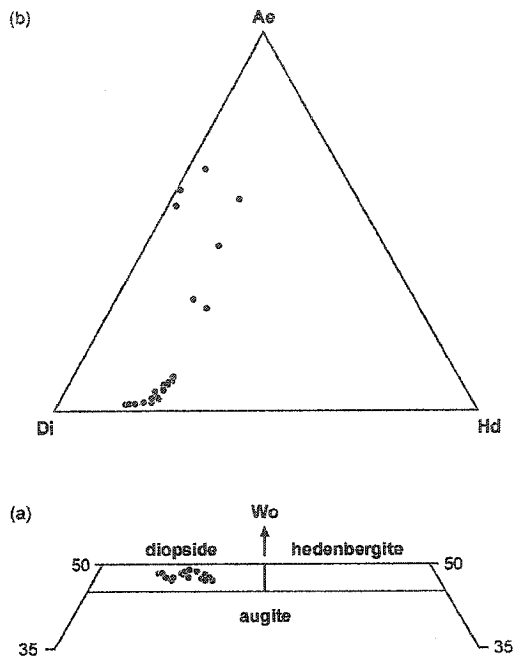

Figure 11.3. Composition of pyroxenes from all the studied intrusions plotted on a) part of the pyroxene quadrilateral, and b) the aegirine-diopside-hedenbergite triangular diagram.

Pyroxene at the Ludgate intrusion was observed in a single sample of syenite. This pyroxene occurs as anhedral to subhedral crystals that are fresh and that display a light pleochroism from yellowish green to pale green. Crystal size varies from approximately 0.5 to 1 mm. Pyroxene at the Ludgate intrusion is aegirine-augite.

Samples of the Garrison intrusion contain minor (<1%), but ubiquitous, small (<1 mm) anhedral pyroxene crystals. The pyroxene is fresh in appearance and displays distinct pleochroism from light yellowish green to darker green. Pyroxene at the Garrison intrusion is aegirine-augite.

Amphibole

Amphibole is a major phase in the mafic rocks of the Iris and Pangea intrusions, and a minor, but ubiquitous, phase in the Garrison and Ludgate intrusions.

Amphibole from the Pangea intrusion is abundant in the hornblendite (~15 to 40%) and melanosyenite units (~15 to 20%). In these 2 rock units, the amphibole is both a primary magmatic phase and a later alteration product. Primary amphibole occurs predominantly as small (~0.5 to 0.8 mm) anhedral crystals displaying light to dark olive green pleochroism. Large (2 to 8 mm) anhedral megacrysts displaying light olive green to brownish orange pleochroism are common. These megacrysts are interpreted to have formed late in the crystallization sequence since they commonly contain numerous inclusions of apatite, magnetite and pyroxene. Secondary deuteric actinolite commonly replaces subhedral to euhedral crystals of pyroxene. A representative analysis of a megacryst from the hornblendite unit, and 3 amphiboles from other intrusions, are given in Table 11.1. The megacrysts are

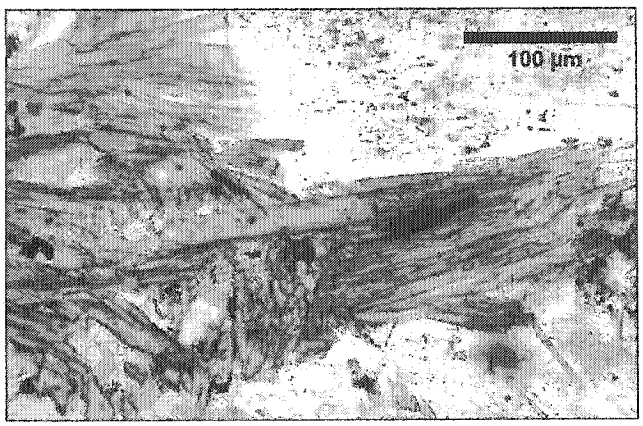

Figure 11.4. Subhedral acicular crystals of magnesioriebeckite in syenite from the Ludgate intrusion. Plane-polarized light.

magnesiohastingsite and tschermakite. Hastingsite and ferrotschermakite were also identified in the Pangea intrusion.

Amphibole is abundant in the hornblendite (~30 to 50%) and the diorite (~15%) units from the Iris intrusion, and is a primary magmatic mineral in both cases. In the diorite, the amphibole crystals are small (0.5 to 0.8 mm), anhedral and light olive green. In the hornblendite unit, amphibole occurs as large (2 to 8 mm) subhedral megacrysts with numerous inclusions of apatite, magnetite, pyroxene and plagioclase which is evidence of late magmatic crystallization. The megacrysts have typically light to dark olive green to brownish orange pleochroism. The small anhedral amphibole crystals of the diorite unit were classified as hastingsite, and the megacrysts in the hornblendite unit vary in composition from pargasite to magnesiohastingsite.

Amphibole in rocks of the Garrison intrusion occurs as small (0.5 to 1 mm), anhedral to subhedral crystals that account for 5 to 10 % of the rock. This amphibole has light yellowish green to light green pleochroism. Both richterite (sodic-calcic group) and magnesioriebeckite (sodic group) were identified in the Garrison intrusion. These sodium-rich amphiboles most likely crystallized from a late sodium-enriched deuteric fluid.

Amphibole in the Ludgate intrusion occurs as small (0.2 to 0.5 mm), subhedral to euhedral acicular crystals (Figure 11.4). The pleochroism varies from light blue to bluish green and purplish blue. Minor crystals of larger (0.8 to 1 mm) anhedral bluish green amphibole are also present. The amphibole from the Ludgate syenite is magnesioriebeckite.

Mica

Biotite is a common mineral in the Emens (20 to 30%) and Pangea (15 to 20%) intrusions. However, no biotite was identified in the Garrison and Ludgate intrusions, and only one sample from the Iris intrusion contained minor amounts of biotite (<1%). Biotite in the samples of the Emens and Pangea intrusions occurs as small (0.5 to 1 mm), anhedral crystals that commonly contain numerous small inclusions of acicular rutile crystals. In general, the crystals are fresh, but chlorite alteration is common in the samples from the Pangea intrusion. Pleochroism varies from light olive green to dark green to brown. Biotite crystals in the Iris intrusion are small (0.5 to 0.8 mm), anhedral and chloritized. The pleochroism varies from light brown to dark brown.

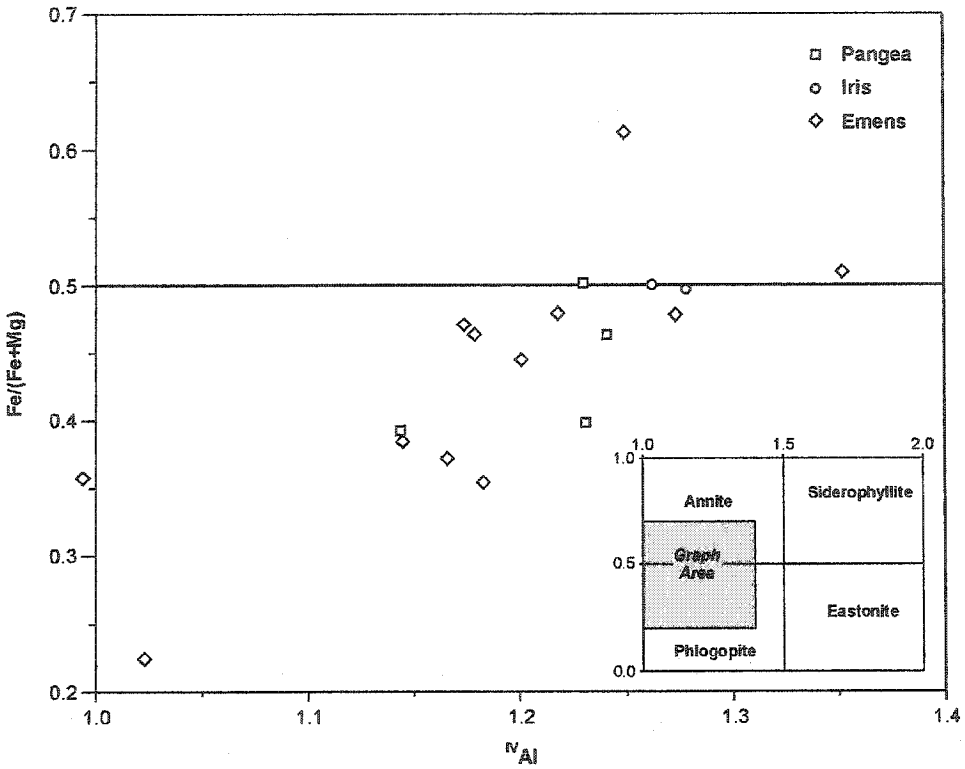

Figure 11.5. Composition of trioctahedral micas from the Pangea, Iris and Emens intrusions plotted on part of the phlogopite-annite-eastonite-siderophyllite quadrilateral diagram.

Two representative analyses of mica are given in Table 11.1. Most mica analyses, apart from 4 analyses described below, are phlogopite (Figure 11.5) in the sense of the IMA nomenclature for the mica group [i.e., Fe/(Fe+Mg) < 0.5]. One analysis from the Emens intrusion plotted within the annite field and 3 analyses plotted in the annite field on the border with the phlogopite field.

DISCUSSION

Our preliminary study of the ferromagnesian silicate minerals in the syenitic rocks of the Porcupine–Destor deformation zone allows us to determine a general paragenetic sequence for these rocks. In general, calcium-rich clinopyroxene is the first mafic mineral to crystallize. It is a primary magmatic phase and has a magnesium-rich composition (diopside) despite whole-rock compositions that are moderately iron rich. This leads us to postulate that, at the time of crystallization, the iron was most likely present as Fe^{3+} because of oxidizing conditions in the melt and, therefore, the iron partitioned into oxide mineral phases, such as magnetite or hematite, rather than mafic silicate minerals. Sodic pyroxene is also observed as a primary magmatic phase in some of the intrusions, indicating that some of the magmas achieved relatively alkaline compositions.

Amphibole is also observed as a primary magmatic phase in numerous units of the suite. The composition of this primary amphibole is variable and corresponds to pargasite, hastingsite, magnesiohastingsite, tschermakite and ferrotschermakite. Secondary amphiboles are also present. These include deuteric actinolite and sodic-calcic and sodic amphiboles, such as richterite and magnesioriebeckite. These sodium-rich amphiboles demonstrate the presence of late sodium-rich volatiles, a feature common in alkaline intrusions.

Trioctahedral micas in the studied rocks are all magnesium rich, again, possibly a consequence of oxidizing conditions. These micas, phlogopites in the sense of the IMA, are for the most part late-magmatic or post-magmatic phases. In many instances, they replace earlier pyroxenes or amphiboles. In many rocks, they coexist with unidentified accessory barium sulphates (most likely barite), once again, evidence of late oxidation.

Our initial findings indicate that ferromagnesian minerals in the syenitic rocks of the Porcupine–Destor deformation zone are directly comparable in paragenesis and mineral chemistry with those of similar syenitic rocks of the Larder–Cadillac deformation zone further to the south, where magmatic and postmagmatic oxidation have been well documented (Rowins , Lalonde and Cameron 1991; Lévesque 1994). Given the close spatial association of these intrusions with the gold mineralization along both fault zones; our current efforts on the intrusive rocks in the area of the Porcupine–Destor deformation zone are focussed on documenting the relative redox state under which the magmas evolved by means of mineral–chemical studies. These studies will help to better evaluate the potential contribution these magmas may have made to the gold mineralization process.

REFERENCES

Leake, B.E., Woolley, A.R., Arps, C.E.S., Birch, W.D., Gilbert, M.C., Grice, J.D., Hawthorne, F.C., Kato, A., Kisch, H.J., Krivovichev, V.G., Linthout, K., Laird, J., Mandarino, J.A., Maresch, W.V., Nickel, E.H., Rock, N.M.S., Schumacher, J.C., Smith, D.C., Stephenson, N.C.N., Ungaretti, L., Whittaker, E.J.W. and Youzhi, G. 1997. Nomenclature of amphiboles: report of the subcommittee on amphiboles of the International Mineralogical Association, Commission on New Minerals and Mineral Names; The Canadian Mineralogist, v.35, p.219-246.

Levesque, G. 1994. Duality of magmatism at Kirkland Lake, Ontario, Canada. unpublished MSc thesis, University of Ottawa, Ottawa, Ontario, p.226.

Morimoto, N. 1989. Nomenclature of pyroxenes; The Canadian Mineralogist, v.27, p.143-156.

Pigeon, L., Lalonde, A.E. and Berger, B. 1999. Petrogenesis of syenitic magmatism associated with gold mineralization along the Destor–Porcupine fault zone near Matheson, Ontario; *in* Summary of Field Work and Other Activities, Open File Report 6000, p.12-1 to 12-4.

——— 2000. Petrogenesis of syenitic magmatism associated with gold mineralization along the Destor–Porcupine fault zone near Matheson, Ontario; *in* Summary of Field Work and Other Activities, Open File Report 6032, p.8-1 to 8-6.

Rieder, M., Cavazzini, G., D'Yakonov, Y.S., Frank-Kamenetskii, V.A., Gottardi, G., Guggenheim, S., Koval, P.V., Müller, G., Neiva, A.M.R., Radoslovich, E.W., Robert, J.-L., Sassi, F.P., Takeda, H., Weiss, Z. and Wones, D.R. 1998. Nomenclature of the micas; The Canadian Mineralogist, v.36, p.905-912.

Rowins, S.M., Lalonde, A.E. and Cameron, E.M.I. 1991. Magmatic oxidation in the syenitic Murdock Creek intrusion, Kirkland Lake, Ontario: evidence from the ferromagnesian silicates; Journal of Geology, v.99, p.395-414.